Magnetic and structural properties of ultra-thin metallic layers upon hydrogen exposure

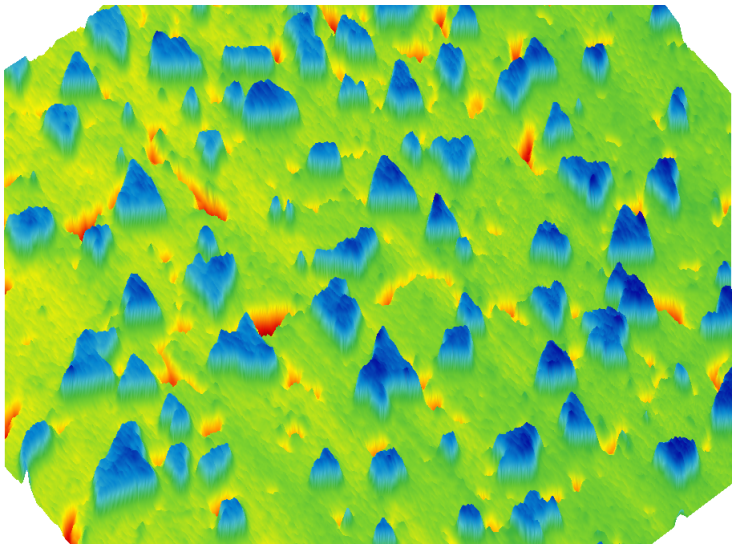

Benito Santos Burgos

Universidad Autónoma de Madrid

A dissertation submitted to the Universidad Autónoma de Madrid
in fulfillment of the thesis requirement for the degree of Doctor of Philosophy in Physics
Madrid, 2011

Abstract

In this thesis I present the most relevant results obtained about the growth, structure, magnetization of Pd, Mg and Co thin films on Ru(0001), and the effects of hydrogen exposure on the same films. The experimental techniques used were low energy electron microscopy (LEEM), spin-polarized LEEM (SPLEEM) and scanning tunneling microscopy (STM).

We studied the growth and the structure of Pd films by LEEM and LEED-IV fits in two different regimes: thin films up to 6 ML on Ru(0001), and thicker films up to 20 ML on Ru(0001) and W(110). The incorporation of hydrogen into the palladium films and the influence of CO in the process was studied by LEEM. We determined that significant hydrogen population of the palladium films sub-surface positions was only achieved in ultra-high vacuum under atomic hydrogen in the presence of carbon monoxide.

We followed our study by giving a description of the growth and the structure of thin Mg films (up to 10 ML) on Ru(0001), whose surface was characterized by LEEM and STM. The formation of a Mg-hydride was studied by means of LEEM and thermal desorption spectroscopy.

Finally, we studied the growth and magnetic domain structure of Co on Ru(0001) by means of LEEM, SPLEEM and STM. The magnetic structure of three-layers thick Co islands was found to depend on the stacking sequence of the islands. Hydrogen induced an spin-reorientation transition (SRT) on 2 ML thick Co films, studied by means of SPLEEM in real space. Finally the effect of a Pd capping on the magnetic properties of Co films on Ru was studied.

Prólogo

En esta tesis muestro los resultados más relevantes obtenidos en el estudio del crecimiento, la estructura, la imanación (en su caso) de películas metálicas delgadas de Pd, Mg y Co crecidas sobre Ru(0001), así como el efecto de exponer dichas películas a hidrógeno. Las técnicas usadas fueron la microscopía de electrones lentos con y sin polarización de espín (SPLEEM y LEEM, respectivamente) y la microscopía de efecto túnel (STM).

El primer lugar estudiamos el crecimiento y la estructura de películas de Pd en dos regímenes diferentes: películas delgadas hasta 6 capas atómicas sobre Ru(0001), y películas de Pd más gruesas de hasta 20 capas crecidas en Ru(0001) y W(110). Las películas fueron caracterizadas por LEEM, y ajustes de LEED-IV. También estudiamos, mediante LEEM la incorporación de hidrógeno en dichas películas y las influencia de CO en este proceso. Sólo utilizando H atómico y CO fue posible poblar las posiciones de la sub-superficie de las películas de Pd con hidrógeno en condiciones de ultra alto vacío.

A continuación se llevó a cabo un estudio del crecimiento y la estructura de películas delgadas de Mg (de hasta 10 capas atómicas) crecidas sobre Ru(0001). La superficie de las películas fue caracterizada mediante LEEM y STM. Finalmente se observó a escala nanométrica la formación de hidruro de Mg mediante la exposición de las películas anteriores a hidrógeno atómico.

Por último estudiamos Co/Ru(0001). Por medio de LEEM, SPLEEM y STM hemos estudiado el crecimiento de películas delgadas de Co hasta 3 capas, nuestros resultados muestran que la estructura magnética de las películas de 3 capas depende de la secuencia de apilamiento. Hemos visto que la adsorción de hidrógeno induce una reorientación de espín en las películas de Co de 2 capas atómicas. Por medio de SPLEEM hemos podido seguir en espacio real dicho proceso.

Para terminar hemos estudiado los efectos que produce un recubrimiento de Pd en las propiedades magnéticas del Co.

A mis padres

Contents

Chapter 1

Hydrogen adsorption on metal films and magnetism

1.1 Hydrogen adsorption on metallic surfaces

Hydrogen is the simplest atom, and the most abundant element in the universe. In the world of the interaction of gases and surfaces, hydrogen holds a prominent place [1]: due to its unique electron, hydrogen is the simplest reacting adsorbate known in nature[1]. But more recently hydrogen has also risen in popularity due to the technological need to find non-carbon based energy carriers. Hydrogen has some useful properties as an energy vector: it has a large heat of combustion [2] and it is obviously abundant. Several works have announced a future world that relies on hydrogen in what has been termed the "hydrogen economy" [3]. However hydrogen as an energy carrier has unsolved issues related to generation, storage, and transport.

Materials science has been called to solve the storage problem. For real industrial applications a hydrogen storage material needs to satisfy the following requirements:

[1] Although the small size of hydrogen and the fact that is has only one electron sometimes makes its use as a model gas adsorbate questionable.

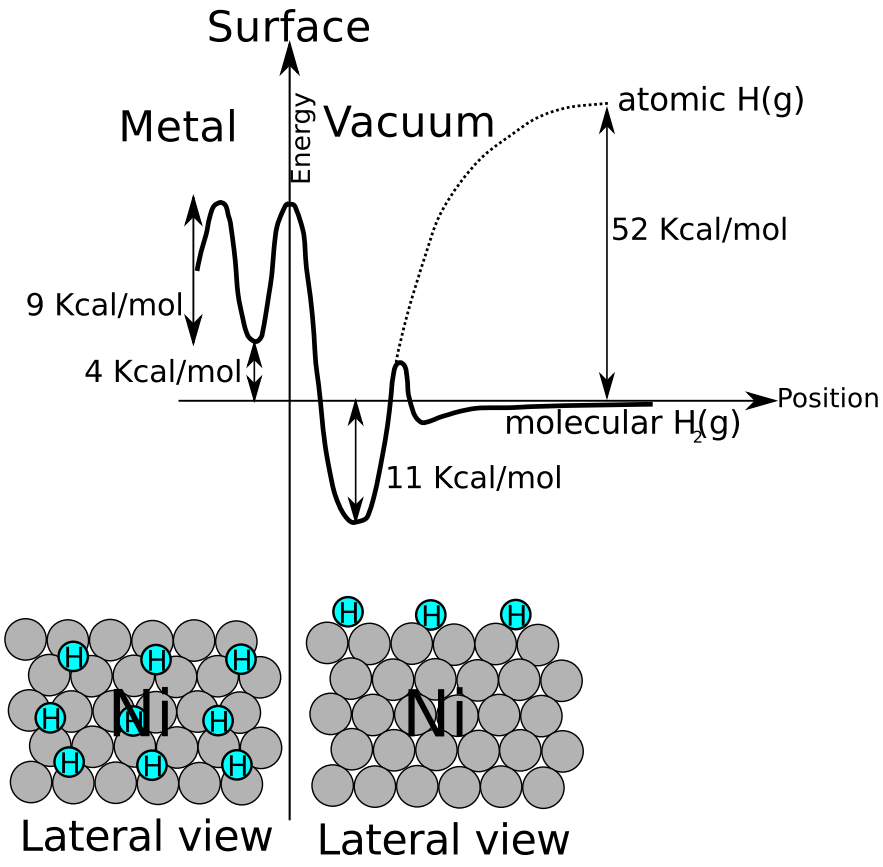

Figure 1.1 Hydrogen potential diagram in Ni. Figure adapted from [11].

- The storage material must be able to store hydrogen in excess of 6.5% in weight [4].
- The kinetics of absorption and desorption must be within a time scale of minutes.
- The hydrogen desorption temperature must be in the range of 240–400 K [4, 5].

Metallic hydrides [6–9] are good candidates, with densities of hydrogen larger than the density of molecular hydrogen in its liquid phase [10].

In the reaction of hydrogen and a metal, several steps occur before a metal hydride is formed. The potential energy landscape that the molecule sees when approaching a metal surface is shown in figure 1.1. First, the hydrogen molecule is adsorbed on the metal surface. The hydrogen molecule has a large dissociation energy of 4.52 eV/molecule [12–18]. If the hydrogen atoms that

form the molecule are going to travel into the metal, the molecule has to dissociate into two hydrogen atoms. This sometimes involves crossing an energy barrier (in which case the dissociation is said to be activated), and sometimes can happen without a kinetic barrier (non-activated dissociation). The most energetically favorable position for hydrogen on a metal is often the adsorbed position on the surface. In some metals, there are sites below the surface that have a similar energy to the adsorbed positions (although in most metals those positions have a higher energy [19]). For example, for Ni, the adsorbed hydrogen atom must overcome a 24 kcal/mol (1.03 eV/atom) potential barrier to diffuse inside the metal, much larger than the average energy of hydrogen at RT [11]. However, if hydrogen has enough energy to overcome that potential barrier, it can diffuse into the metal. Once the atomic hydrogen is inside the metal, the equilibrium lattice position is determined by the potential energy. Most metals can incorporate a given concentration of hydrogen as a solid solution, due to the small size of the hydrogen atom. This is usually called the α phase of the corresponding metal hydride. It produces a slight expansion of the lattice of the host metal. But much larger hydrogen concentrations are possible, as often ordered compounds of the metal and hydrogen exist, such as PdH or MgH_2. The phase transformation from the diluted α phase to an ordered hydride is a first order transformation in which the lattice spacing of of the hydride can change abruptly by a large fraction. In a bulk material, this can fracture it.

The first problem encountered when planning research on hydrogen interacting with metal surfaces is how to detect it. As hydrogen has one electron (in neutral form), its scattering power is much smaller than metal atoms so a direct observation by low-energy electron diffraction (LEED) is often impossible [20]. Typical electron spectroscopies do not fare much better, as Auger electron spectroscopy or X-ray photoelectron spectroscopy are also blind to hydrogen. Even in scanning tunneling microscopy, hydrogen detection is very difficult. The problem is complicated by the fact that most surface science experiments take place in an ultra-high vacuum that is composed mostly of hydrogen. A reactive surface at a pressure of 1×10^{-10} Torr, which is usually considered

a "good" vacuum, will be covered with hydrogen in less than three hours.

However, hydrogen absorption on metals produces structural or electronic changes in the metal atoms that might be simpler to detect than hydrogen itself. For example, as mentioned before, hydrogen absorption induces an expansion of the lattice parameter of the crystal, which is typically proportional to the amount of hydrogen incorporated in the lattice. This suggests that crystallographic techniques capable of measuring the average lattice spacing of a film, such as low-energy electron diffraction or surface X-ray diffraction [21] can be used to follow the fate of hydrogen in a metal film.

Hydrogen also produces changes in the electronic structure and the magnetic properties of metals. Hydrogen does not have core levels, but it changes the valence band of the metal. Greuter et al. [22] showed that the metal d band shifted downwards in energy respect to the Fermi level because of increased bonding with the hydrogen $1s$ band [23]. It was also shown in Fe films on V [24] that hydrogen adsorption modifies the occupation of the d bands of the metal.

Finally, both the changes in the electronic structure of a ferromagnetic metal or its strain can change drastically its magnetic properties, opening another method to follow the incorporation of hydrogen in a metal film. For example, hydrogen induces an spin reorientation transition on ultrathin Ni films [25]. Other work reported that the magnetic moment of magnetic surfaces is reduced upon hydrogen adsorption [26].

In this thesis we have studied the response to hydrogen exposure by three different metallic films, Pd, Co and Mg on the same substrate, Ru(0001). The substrate is chosen because hydrogen does not go into the bulk of Ru nor it easily forms an hydride. Furthermore, it is easy to clean by flashing and annealing cycles, and it is a substrate that does not alloy strongly with the metals to be grown on top, at least at the temperature range where the metals show islands large enough to be detected in low-energy electron microscopy. The three metal films selected span a range of behavior with hydrogen: Pd is the prototypical metal that absorbs hydrogen, Mg forms an stable

ordered hydride and Co films supposedly only adsorb hydrogen on the surface. All the experiments described were performed under ultra-high vacuum conditions. The metal films were grown by molecular beam epitaxy in the same chamber where their structure was characterized, and they were later exposed to hydrogen. Hydrogen exposure was performed by filling the experimental chambers with molecular hydrogen, or in some cases, by using an atomic hydrogen source.

The main technique used through this thesis is low-energy electron microscopy (LEEM). In its standard form, LEEM is not a chemical characterization tool. Besides, we have already commented that spectroscopies are not too useful with hydrogen. We resort to using some special capabilities of LEEM to locate hydrogen: the LEEM ability to acquire low-energy electron reflectivity, and low-energy electron diffraction data, or to image in real space magnetic domain patterns. But LEEM has a limited laterial resolution. In some cases, we have used STM to further characterize the metal films. The LEEM experiments have been performed through collaborations with Andreas K. Schmid of Berkeley National Laboratory, and Kevin F. McCarty of Sandia National Laboratories. The STM experiments have been performed in a home built system constructed during this thesis.

In the following chapters we first describe the experimental systems used. Then we devote two chapters to discuss the structure of Pd films on Ru, and their interaction with hydrogen. A large part of these two chapters relies on the LEEM measurement and subsequent fit of LEED intensity vs energy data, in collaboration with Dr. J. Cerda from ICMM. The same plan is repeated with Mg, where instead of LEED-IV, STM data has been acquired. Finally, magnetic domains in Co films are characterized and the effect of hydrogen determined (the structure of Co films had already been published by El Gabaly et al [27]). The thesis closes with a summary of the work.

In order to introduce the results presented in this thesis, some ideas of on the interaction of hydrogen and metals, and thin film magnetism are presented. For a more detailed description the reader is referred to different textbooks [28–33].

1.1.1 Dissociative vs non dissociative adsorption on surfaces

The first step on the interaction of a hydrogen molecule and a metal surface is the adsorption of the molecule, defined as the bonding to a surface called adsorbent. Depending on the nature of the bonding we can distinguish between physisorption or chemisorption. In the first case the electronic structure of the adsorbate and that of the surface do not change significantly and there is not a "chemical bond". In this case the adsorption occurs, for example, by van der Waals forces. In chemisorption, the electronic structure of the adsorbate and the surface is significantly altered, yielding a real chemical bond between them. In the case of a molecule like H_2, it is also necessary to differentiate between non-dissociative adsorption, when the molecule is adsorbed on surface with no changes on its components, and dissociative adsorption, where the molecule breaks the bond between its atoms and each component is adsorbed on the surface. At the temperatures considered in this work (usually room temperature, except the Pd experiments that were performed at 100 K) hydrogen adsorption is dissociative. The rate of adsorption and dissociation varies as a function of the surface termination and the nature of the metal in the periodic table. Hydrogen adsorption is dissociative in the transition metals (in particular Pd and Co) while molecular hydrogen is not adsorbed on metals (i.e. it does not dissociate) from the first two columns (Mg), or on the coinage metals.

To understand the dissociative adsorption we just consider that the potential energy curve that describes the physisorption process of the H_2 molecule crosses at some point the energy curve of the dissociated (chemisorbed) molecule. Each potential is considered to depend to a first approximation on the distance to the surface as shown in figure 1.2 (more realistic potentials need to take into account many more degrees of freedom, from rotation to incidence angle [34]. At long distances from the surface, the dissociated hydrogen atoms have an energy higher than the molecular hydrogen. At small distances from the surface $\sim$1–2 Å [20, 35, 36], both species interact with the surface lowering their energy.

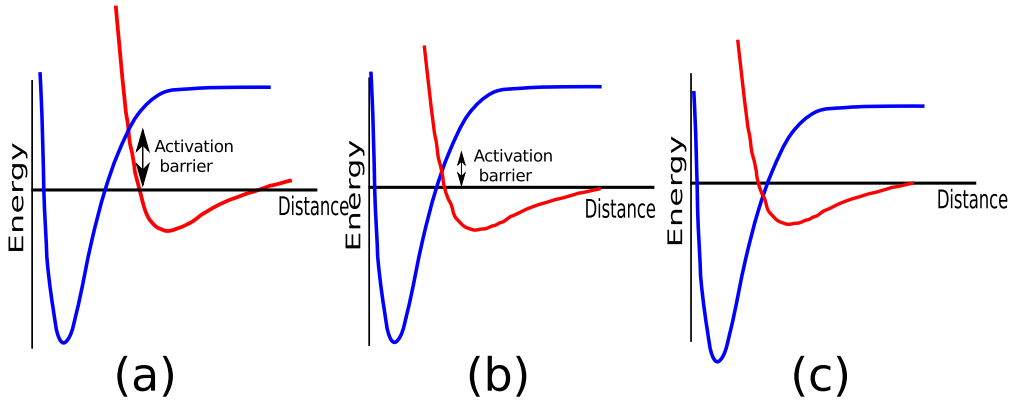

Figure 1.2 Different types of adsorption on surfaces, depending on the relative energy curves for molecular adsorption (red) and dissociated adsorption (blue): (a) molecular adsorption (b) activated dissociative adsorption (c) pure dissociative adsorption. Adapted from [31].

A hydrogen molecule approaches the surface following the red line. As it gets close to the surface, the molecule can cross the activation barrier (the minimum difference between molecular and dissociated energy curves) entering in this way the potential of the atomic hydrogen i.e. becoming two dissociated atoms of hydrogen adsorbed on the surface. The difference between dissociative and non dissociative adsorption will be given by the height of the energy barrier between the molecular and dissociative states of the molecule. Depending on the height of the activation barrier, the molecule will (a) be unable to dissociate on the surface, (b) will encounter a barrier so the dissociation will depend strongly on the temperature or (c) the molecule will dissociate directly upon adsorption (c).

1.1.2 Dissociative adsorption of hydrogen on transition metals

Hydrogen adsorption on transition metals is dissociative at 100 K [31, 37], in particular on Pd or Co. However, dissociative hydrogen adsorption is not possible on 1s or 2s metals such as Mg or Be [38–41]. Detailed calculations show that the activation barrier of hydrogen dissociation is much lower in metals with the d-bands partially filled (for example the dissociation barrier

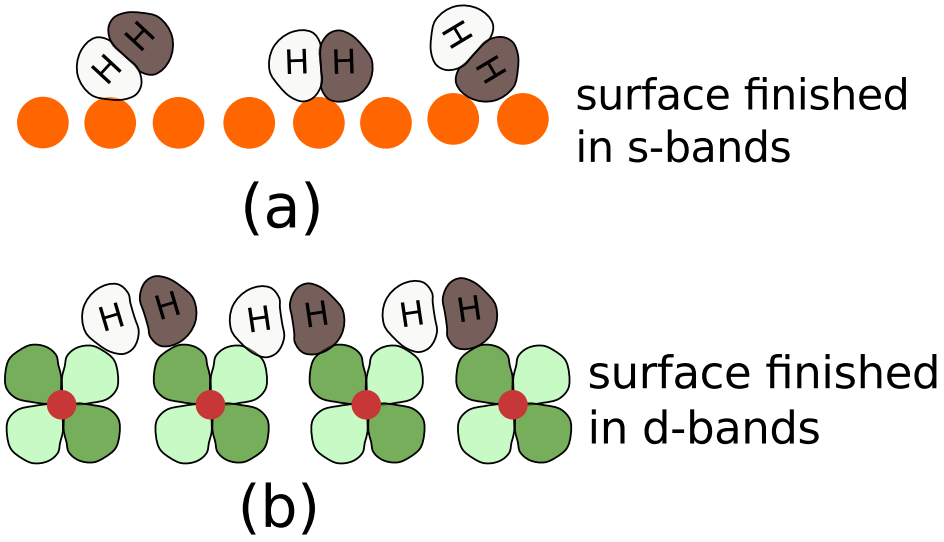

Figure 1.3 Representation of the anti-bonding orbital of hydrogen with (a) a surface terminated in a *s*-band metal and (b) a surface terminated in *d*-band metal. The dark/light colors indicate the sign of each orbital part. Adapted from [31].

is 14 Kcal/mol (0.60 eV) lower on Pt than on Cu). The reason for the ability of half-full d-bands to dissociate hydrogen is related to the presence of empty anti-bonding orbitals. Using quantum mechanic arguments, to break a bond within a molecule, electrons have to be removed from the bonding orbitals or the anti-bonding ones have to be filled. The first case is not possible for hydrogen because transition metals are not electronegative enough to remove electrons from the hydrogen. So to break the hydrogen molecule the anti-bonding orbitals have to be filled up, and experimentally this is easier with surfaces made of elements with an unfilled d-band.

In figure 1.3 we present a schematic diagram of the bonding between the hydrogen molecule and two different different surfaces, one surface terminated in *s*-orbitals, while the other is terminated in *d*-orbitals. In figure 1.3 we represent the anti-bonding σ^* orbital of H_2, which has a positive and a negative lobe. The interaction between the surface atoms and the adsorbed molecule increases with the overlap of the wavefunctions. When H_2 reaches the surface terminated with s orbitals, no matter the orientation of the molecule the two lobes of the σ^* orbital cannot overlap simultaneously with the surface s orbitals, inhibiting the dissociation of the molecule. The situation

is different for adsorption on the half-filled d-metal. In this case the change of sign of the lobes of the d-orbital makes it possible to provide the change in sign required for a proper overlap with the H_2 σ^* orbital, favoring the breaking of the molecule.

1.2 Some aspects of magnetism

In this chapter we introduce some concepts of magnetism in thin films. We start explaining the different contributions to the magnetic anisotropy and we finish with the magnetic structure observed in ferromagnetic films. For a more complete description the reader is referred to different textbooks [28–30].

1.2.1 Magnetic anisotropy

During the last decades the number of studies dealing with magnetic materials has increased due to the versatility of these materials for technological applications such as actuators [42,43], magnetic data storage [44] or nonvolatile random access memories [44,45]. Independently of the particular application, a important issue in magnetic materials is their magnetization easy-axis direction, and the ability an tailor it. In absence of an external magnetic field (i.e. in remanence), the magnetization of a ferromagnetic film tends to lie along one preferential axis. A certain energy is needed to change the magnetization direction from the preferred axis. This energy needed to turn the easy-axis of magnetization to a given orientation is defined as the magnetic anisotropy energy (MAE). There are several contributions to this MAE. It can be expressed as a sum of different contributions to the free energy density of a magnetic system E_{ani}:

$$E_{ani} = \sum_{i,j,k} K_{i.j.k} \alpha^i \alpha^j \alpha^k \tag{1.1}$$

These contributions in E_{ani} are often expanded into a series of components α_i of the unit vec-

tor pointing into the direction of magnetization. The parameters $K_{i.j.k}$ are called the magnetic anisotropy constants, and they can be measured experimentally with techniques such as magneto-optical Kerr effect (MOKE), torsion oscillating magnetometry (TOM) or vibrating sample magnetometry (VSM).

In context of this thesis, we will introduce the three principal contributions to the anisotropy. To put them in perspective, we comment first on the exchange interaction. This is the largest magnetic interaction, with a typical energy of $\sim$1 eV/atom. It provides the alignment of a spin system at finite temperature and is, thus, responsible for the existence of ferromagnetic order in magnetic materials. The origin of this interaction is the repulsive interaction between electrons (i.e. Coulomb interaction) together with the symmetrization postulate that makes the electron wave function antisymmetric. In a system with only two spins, the exchange is defined as the energy difference between the parallel and antiparallel spin alignment. In a simple model, the exchange energy J provides the system energy by considering the relative orientation of each spin S in the Heisenberg hamiltonian:

$$H_{ex} = -2\sum_{i<j} J_{ij} S_i S_j \tag{1.2}$$

The contributions to the magnetic anisotropy are:

- The magneto-crystalline anisotropy (MCA). This term describes the coupling between the electron spin and its surroundings, giving a dependence of the magnetic energy and the crystallographic directions of the material. Its origin is the spin-orbit coupling. This magnetic anisotropy energy is typically $\sim$10–100 μeV/atom in the bulk.

- The shape anisotropy. The magnetization of a sample induces a magnetic stray field in its surroundings. This field has associated a magnetostatic energy. It depends on the shape of the sample and the relative orientation between the magnetization of the sample and the

sample shape and arises from the dipolar interaction. In the case of a continuous flat film with homogeneous magnetization, the total contribution to the dipolar interaction arises from the demagnetizing field created by the uncompensated magnetic moments at the surface of the film. This energy from the stray field is given by:

$$E_d = \frac{1}{2}\mu_0 M_s^2 cos^2\theta \tag{1.3}$$

where M_s is the value of the saturation magnetization and θ is the angle with the film normal. The shape anisotropy energy is minimized for when the magnetization of the sample is in-plane. In other words, the stray field is reduced when the magnetization of the sample M_s keeps the magnetic flux lines in the film plane. The shape anisotropy is responsible for the in-plane easy-axis in thin films. The shape anisotropy energy per atom is usually slightly larger than the magneto-crystalline anisotropy energy.

Other contributions to the magnetic anisotropy that may play a role in thin films are:

- The surface (interface) anisotropy. This is a loose term which refers to the contributions from atoms close to the surface (interface) of a film, where the reduced symmetry gives rise to contributions which differ from the ones from bulk atoms. The relative importance of the surface anisotropy (interface) decreases when compared with other volume contributions when the film thickness increases.

  As the contribution of the atoms close to the surface of the film to the total MAE of the thin film can be substantial, it should not be surprising that depositing either non-magnetic metals or other adsorbates such as hydrogen on the surface of a ferromagnetic film can modify not only the absolute value of the MAE, but the magnetization easy-axis itself.

- The magnetoelastic anisotropy. It arises from the coupling between the magnetization of the sample and its strain. It is often observed in thin films, as they can present large strains.

Theoretical calculations [46] have predicted that the magnetoelastic anisotropy energy is in the range of μeV/atom [42].

Taking into account all the contributions to the magnetic anisotropy energy, the magnetization easy axis has been found to change as a function of temperature, thickness, or adsorbate coverage. The most common magnetization easy-axis configuration for a thin film is in-plane, because it minimizes the shape anisotropy contribution which often dominates the magneto-crystalline one. But in particular cases, the surface and/or interface contributions to the magnetic anisotropy energy can make the out-of-plane magnetization direction the preferred one (i.e. perpendicular magnetic anisotropy, PMA [47]). Material science researchers are on the lookout for such systems with PMA. In most cases, this orientation only occurs for a thickness range, as for larger thickness the surface or interface contribution responsible for the PMA is overwhelmed by the shape anisotropy.

One standing problem in the field of magnetic anisotropy is that often the contributions are too small to be reliable calculated. Even if they can be calculated at all (the increase in computer power makes now feasible to do first-principles calculations of the MAE in films several layers thick as long as the in-plane units cells are small), it is often very hard to interpret the results in terms of a simple dependence on strain, or other parameters. However, this predictive problems mean that there is still a large field for a pure experimental approach to studies of the magnetic anisotropy.

1.2.2 Magnetic domains and domain walls

The concept of magnetic domain was postulated by Weiss [48] at the beginning of the 20^{th} century to explain that ferromagnetic materials do not present a uniform magnetization. In the ground state, a ferromagnet presents regions where the magnetic moments are aligned parallel to each other i.e. different oriented magnetic domains, due to the exchange interaction. The magnetic domains are created by the system to reduce the magnetic stray field generated outside the magnet. To understand the origin of the magnetic domains it is instructive to start with a sample with uniform

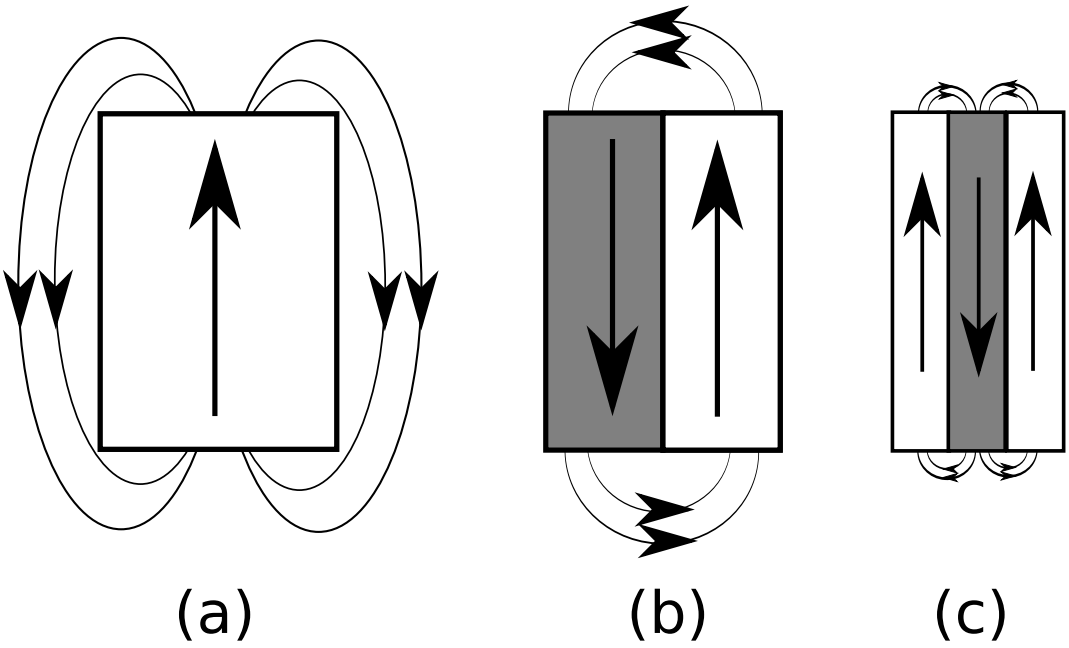

Figure 1.4 Domain wall creation from a uniform magnetized material.

magnetization like the one shown in figure 1.4 (a). Associated with the uniform magnetization there is an external magnetic field created by the sample, with an associated magnetostatic energy. To reduce the total energy of the system, the external field can be reduced by creating magnetic domains with opposite magnetization directions [figure 1.4 (b)-(c)]. But this process cannot be done indefinitely because boundary regions between two magnetic domains, i.e. domain walls, have an energy cost. Magnetic domains will be created until an equilibrium is reached between the external magnetostatic energy and the energy required to create the domain walls. Within the domain wall, the magnetization rotates continuously from one domain to the other. Several types of domain walls are possible with the more common being Bloch walls [figure 1.5 (a)] and Néel walls [figure 1.5 (b)].

In a Bloch wall the magnetization rotates parallel to the plane of the wall i.e. the magnetization rotates in the plane x–z. In a Néel wall the magnetization rotates within the plane defined by the surface of the material, i.e. the magnetization rotates in the plane x–y. In ultra-thin films the

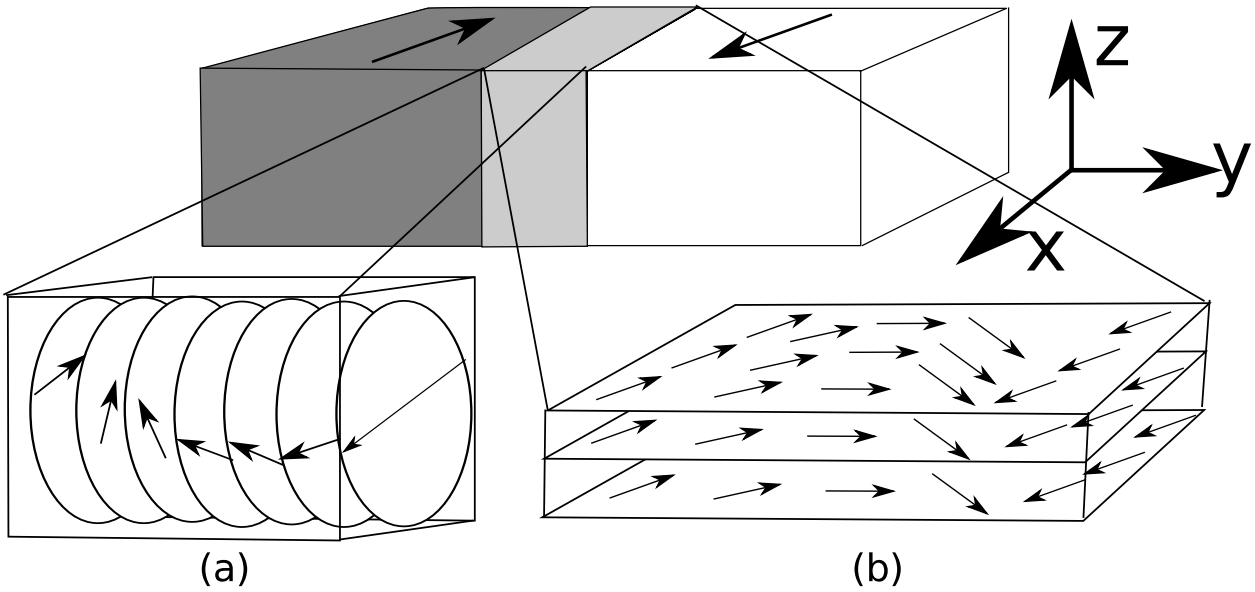

Figure 1.5 Schematic representation of (a) a Bloch wall, and (b) a Néel wall. In both cases the magnetization rotates 180° between adjacent magnetic domains.

surface stray field is minimized by rotating the magnetization within the surface plane [28]. In consequence Néel walls are more common in very thin magnetic films.

A domain wall has a finite width given by the the competition between the exchange energy (that tends to make the wall as wide as possible) and the anisotropy energy (that tends to make the wall as thin as possible). The exchange contribution to the total surface energy density is given by the relation:

$$\sigma_{exch} \sim JS^2 \frac{\pi^2}{Na} \tag{1.4}$$

Where J is the exchange constant, S the spin number, N the number of atoms and a is the lattice constant. The anisotropy energy density is given by:

$$\sigma_{anis} \sim K_2 Na \tag{1.5}$$

where K_2 is the uniaxial magnetic anisotropy. In equilibrium, the wall thickness is given by the minimization of the sum $\sigma_{exch} + \sigma_{anis}$ [49, 50]. Since in the domain wall the magnetization

rotates in a continuous way from one magnetic domain to the adjacent domain, there is no unique definition of the domain wall width. When electrons are used to image magnetic domains, the projection of the magnetization within a domain wall is observed and the width of a domain wall is defined as [51]:

$$w \sim \sqrt{\frac{A}{K}} \tag{1.6}$$

where w is the domain wall width, A is the exchange constant and K is the anisotropy constant, (which for Néel walls refers to the in-plane anisotropy constant). Not all ferromagnetic samples present magnetic domains. If the domain wall width is larger than the lateral size of the particle, the particle will be in a single domain state. This phenomenon very often occurs in thin ferromagnetic islands [52, 53].

1.2.3 Stripe domain patterns

In two dimensional magnetic systems, near the spin reorientation transition (SRT) the competition between the short-range exchange interaction and the long-range magnetic dipole interaction results in many interesting self-organized magnetic domain patterns [54, 55]. The dynamics and the shape of this stripe pattern phase depends sensitively on both internal and external conditions such as on the anisotropy constants or external magnetic field [54, 56, 57]. Different works reported that the stripe domain width increases exponentially far from the SRT point [54, 57]. Recent studies show that there are still unsolved critical issues regarding the stability of the stripe domain phase and the formation mechanism of domain boundary [58, 59]. Theoretical calculations based on Monte-Carlo simulations [55] shown that the stripe domain phase at the SRT point minimizes the total energy by changing not only the stripe width but also the magnitude of the perpendicular magnetization. In this region, the domain wall width becomes comparable to the domain width itself becoming a static spin wave with a sinusoidal variance of the perpendicular magnetization.

This stripe magnetic pattern will be discussed in more detail in chapter 8.

Chapter 2

Experimental details

2.1 General introduction

In the next sections of this chapter we will describe the experimental techniques used during the thesis. We have used mostly two different instruments low-energy electron microscopes (LEEM): the one at Sandia National Laboratories in California (USA), under the supervision of Dr. Kevin F. McCarty, and the spin-polarized LEEM (SPLEEM) at Berkeley National Laboratory, also in California (USA), under the supervision of Dr. Andreas K. Schmid. LEEM is a very powerful technique to acquire images in real time of crystalline surfaces with a resolution of 10 nm. Additionally, SPLEEM provides information of the magnetic microstructure of the films.

As in some cases the lateral resolution achieved by LEEM-SPLEEM is not enough to characterize the morphology of the films, scanning tunneling microscopy (STM) has also been used. To such end, we have built an ultra-high vacuum (UHV) STM following the design described in Ref. [60]. The STM head was mounted during my stay at the University of New Hampshire under the supervision of Prof. Karsten Pohl.

We start by discussing the electron energy range that is most used in LEEM, the parts of a

LEEM system, and some details of the Sandia and the Berkeley instruments. We then comment on the use of LEEM for the adquisition of low energy electron diffraction (LEED) data. We finish by describing the STM instrument in Madrid.

2.2 The low-energy electron microscope (LEEM)

The low-energy electron microscope relies on the interaction of low-energy electrons (0–500 eV) with a crystalline surface. Electron beam energies in that range are often used to study surfaces. To understand why low electron energies are used, the interaction of electrons with matter has to be considered, as discussed in Ref. [61]. As the energy of an electron beam is decreased, forward scattering processes are less relevant and inelastic scattering and elastic backscattering become increasingly important. In the solid state, the periodic distribution of the atoms in a crystal gives rise to an electronic band structure. In the band structure there are forbidden energy regions due to discontinuities at Brillouin zone boundaries and due to the splitting of the energy bands at band crossings [62, 63]. An electron beam whose energy is in the forbidden region will not find allowed states in the crystal and, thus, it will be reflected by the first few atomic layers.

The mean free path of the electrons at low energies is determined by their interaction with the substrate. At low energies many inelastic processes which involve inner shell electrons do not take place because the incoming electrons do not have sufficient energy to excite them. The predominant interactions take place through inelastic processes involving outer shell electrons. At high electron energies, the attenuation due to inelastic scattering is dominant over the one due to elastic backscattering. The energy threshold between the two regimes is given by the plasmon excitation energy E_t. Consequently, for beam energies $E > E_t$ the sampling depth is determined mostly by inelastic scattering, with a mean free path ranging from 0.3 nm to 1 nm. For beam energies $E < E_t$ the inelastic mean free path increases rapidly. The resulting mean free path presents

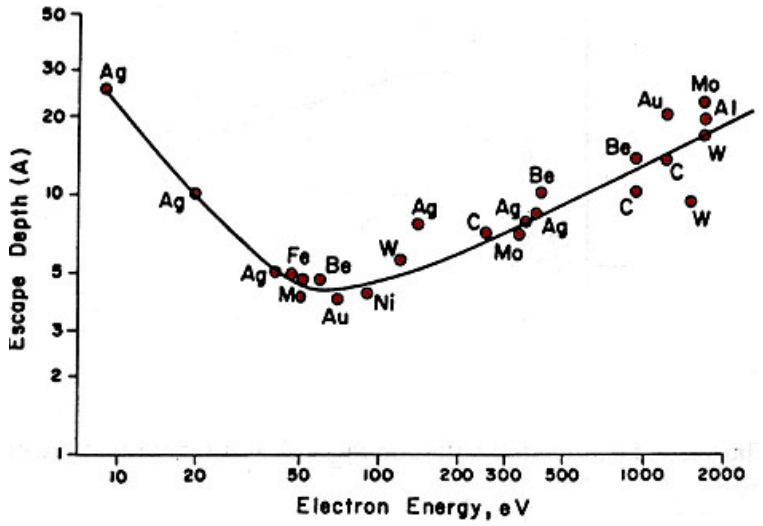

Figure 2.1 Universal mean free path curve for electrons in a crystal as a function of the electron energy. The calculated curved and the experimental mean free path data for each elements are plotted versus the energy. Imagen taken from Ref. [64].

small changes with the Fermi energy of the sample or with its electron density giving as a result the universal inelastic mean free path curve that is widely used in surface analysis with electrons [figure 2.1]. In LEEM, the most used energy range lies below the plasmon limit, typically 0–20 eV

.

The LEEM instrument is related to the transmission electron microscope TEM [65–67]. It uses an low-energy electron beam to illuminate the sample but instead of using the transmitted electrons, it uses the electrons reflected from the surface to create a real-space image. The first LEEM prototype was built by E. Bauer in 1962. But it was only in the 80's that the first successful operating instruments were built. In the 90's the first commercial company was founded (Elmitec, the manufacturer of the Sandia LEEM which we have used in this PhD thesis), and the Berkeley LEEM was designed and built [68] at IBM.

There are some technical issues that have delayed the development of LEEM instrumentation. For example, as the incident and outgoing beam share the same path, a magnetic prism is placed after the objective to separate both beams into the illumination and the imaging columns. Sometimes

overlooked detail is that the samples must be as flat as possible and must withstand an electric field of $\sim$20 kV/mm.

LEEM components

There are several tens of LEEM instruments in the world. Most of them belong to a couple of commercial designs, together with a few "custom" systems. The Sandia LEEM belongs to the first group, while the Berkeley LEEM belongs to the second.

In LEEM, an electron beam is used to illuminate the sample, and the reflected electrons are detected. While the electrons travel at 10–20 keV energies within the LEEM, they are decelerated before interaction with the sample down to energies of a few eV. All the different LEEM instruments contain the same components [illustrated in figure 2.2 for the Sandia LEEM]: an illumination system that provides a parallel electron beam, a beam separator that separated the electrons going from the sample from the electrons reflected from it, and an imaging system that provides the amplified distribution of reflected electrons on a phosphor screen.

- Illumination system. It is composed of an electron gun which generates an electron beam. The beam is demagnified and collimated by several magnetic or electrostatic lens.

- Beam separator. It is composed by a magnetic prism that separates the incident and the reflected beams that share the same path through the objective. The prism works by applying a magnetic field that bends the incident electron beam from the illumination system onto the objective, and the reflected electrons coming from the sample through the objective onto the imaging column.

- Objective. The objective lens is composed, starting from the sample, by the sample itself, an electrode to accelerate the reflected electrons and at the same time deccelarate the illuminating electrons, and either an electrostatic (Berkeley) or an magnetostic (Sandia) lens that

forms the first amplified image of the reflected electrons.

- Imaging system. It is composed first of a lens that can either provide an amplified image of the distribution of reflected electrons coming from the beam separator in real-space (normal imaging mode), or in reciprocal-space (diffraction mode). Then a series of projection lenses can to increase the magnification of the final image. The electrons impinge on a microchannel plate with a high gain, and reach a phosphor screen. A CCD camera records the images on the phosphor screen. These images are then processed by a computer.

Contrast modes in LEEM

Contrast in LEEM arises from differences in the electron reflectivity of different parts of the sample. The differences in electron reflectivity can have several origins:

- Composition contrast. Due to differences in the band structure, the electron reflectivity differs among different elements and compounds. In general, it is necessary to scan the electron energy to select experimentally the energy were the largest composition contrast is obtained for a given couple of materials.

- Step contrast: At low energies, the wavelength of the electrons is comparable with atomic step heights (0.2–0.6 nm). Thus, electrons reflected from different terraces separated by atomic steps will interfere giving a Fresnel diffraction pattern. Due to aberrations in the system lens, only a single line is observed instead of an oscillatory pattern located at the step edge. Figure 2.3 (a) shows a LEEM image acquired on clean Ru(0001). The black lines corresponds to the position of the substrate atomic steps.

- Electron interference effects in thin films. This effect arises from the interference between electron waves reflected from the surface of a thin film and from its interface with the substrate. It gives a modulation of the reflected electron intensity as a function of the energy and

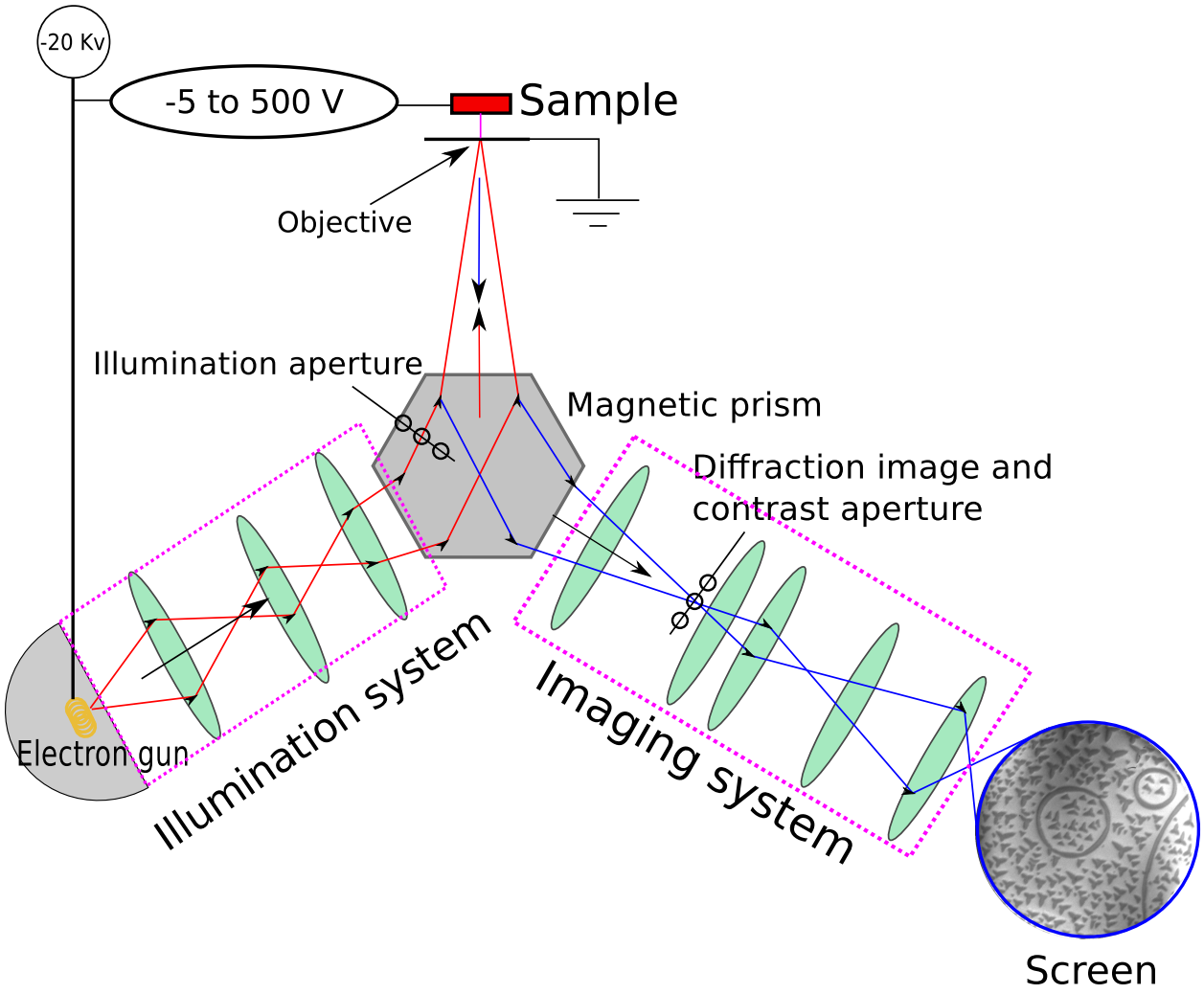

Figure 2.2 Schematic representation leem optics. Image adapted from [69].

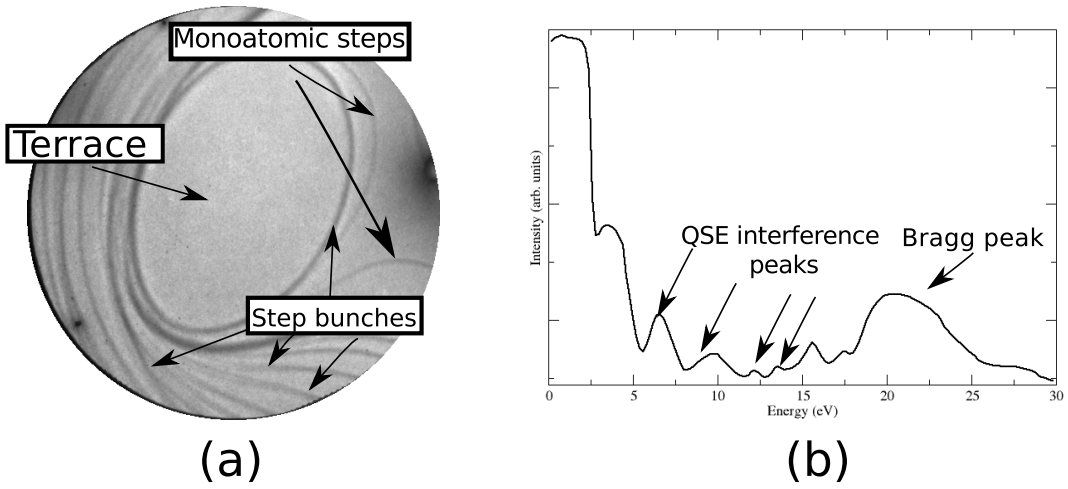

Figure 2.3 (a) Typical LEEM image of the clean surface of Ru(0001). A dark grey line is observed in the atomic step position. The FOV is 7μm, beam energy is 5 eV. (b) Reflectivity curve acquired on 5 ML of Pd on Ru(0001)

the thickness of the film. This contrast mode is very useful to detect film areas with different thicknesses. Figure 2.3 (b) shows a low-energy electron reflectivity curve acquired on a thin Pd films. The modulation in the reflectivity due to phase contrast can be observed.

Magnetic contrast

The local sample magnetization can be another source of contrast in special circumstances. The usual method is to use a spin-polarized electron beam as illumination (spin-polarized LEEM, or SPLEEM). When a spin-polarized beam reaches a magnetic surface, the number of elastically reflected electrons depends on three factors: the elastic scattering between the incoming polarized electrons and the material electrons, the relative orientation of the spin incident beam and the surface magnetization and the inelastic electron-electron collisions that make the mean free path spin dependent [70]. Both the scattering potential and the differences in the spin mean free path make the number of backscattered electrons decrease as the energy of the incident beam is increased. In consequence, low-energy electrons (3–7 eV) are used for maximum contrast. To remove all

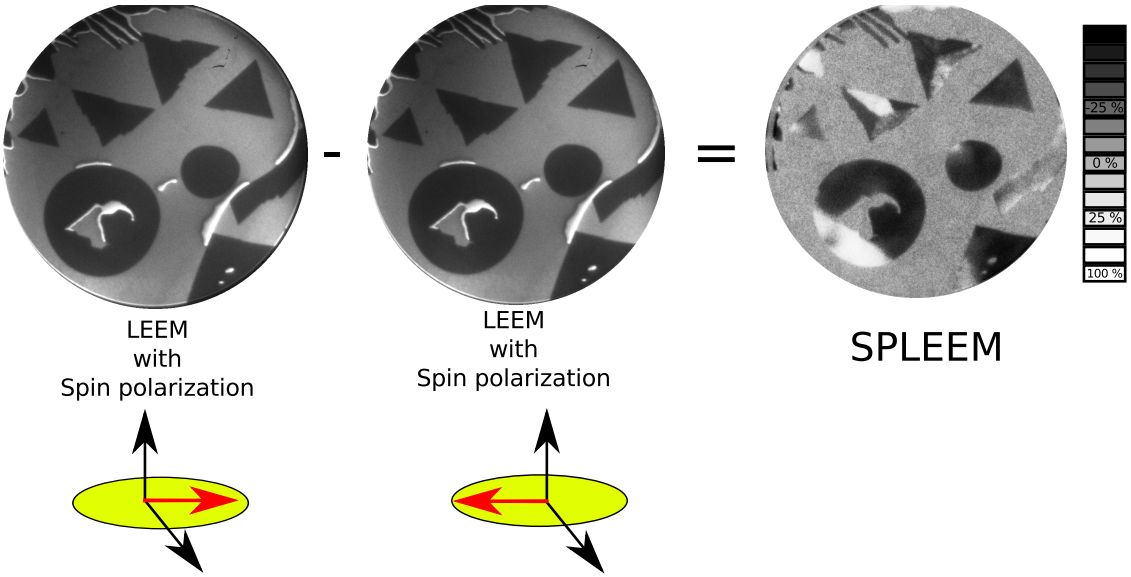

Figure 2.4 To acquire a SPLEEM image, we first acquire two consecutive images with opposite spin polarizations of the illumination electron beam, which are then substracted. In the LEEM images, triangular islands of 3 ML of Co/Ru(0001) appear dark gray. The beam energy is 7.2 eV. FOV is 8μm, and the spin-polarization was within the film plane.

non-magnetic contrast, two consecutive images are acquired with opposite spin-polarization directions. Then, the asymmetry image I_{SPLEEM} (what we call a SPLEEM image) is computed by a pixel-by-pixel image substation:

$$I_{SPLEEM} = \frac{I_{\uparrow} - I_{\downarrow}}{I_{\uparrow} + I_{\downarrow}} \tag{2.1}$$

The difference in the numerator of equation 2.1 eliminates all the non-magnetic features obtained in a conventional LEEM image, and the sum in the denominator of the equation 2.1 normalizes the result.

Figure 2.4 shows such a SPLEEM image computed from the two LEEM images acquired with opposite spin-polarizations. The SPLEEM is a gray scale image where white (black) areas correspond to areas of the surface were the local magnetization direction is along (opposite) the spin-polarization direction of the illumination beam in the first LEEM image ($I_{\uparrow}$). If the component

of the magnetization along the illuminating spin-polarization direction is 0, the image will present a medium gray level. For example in figure 2.4 a film with 3 ML Co islands on a continuous 2 ML Co film on Ru(0001) is shown. In the LEEM images, the dark areas correspond to 3 ML thick Co islands. Only those areas show in-plane magnetic contrast, indicating that their magnetization is within the film plane. In contrast, the rest of the film, 2 ML thick, has a medium gray level in the SPLEEM image, indicating that its magnetization is 0 along the in-plane direction of the spin-polarization of the LEEM images.

2.2.1 The LEEM at Sandia

In figure 2.5 we show pictures of the commercial Elmitec III LEEM [71] located at Sandia National Laboratories. In this system the lateral resolution is close to 10 nm. In the Elmitec III design, the prism is attached to the objective through a valve, and the illumination and imaging systems are attached to the prism. Different dosers can be attached to the sample main chamber by $2^{3/4}$" CF flanges. The incidence angle to the dosers is 16° relative to the surface normal, and the dosers can reach the sample thanks to holes in the objective electrode. The LEEM employs magnetostatic lenses, and is well suited to perform low-energy electron diffraction (LEED).

The sample manipulator has two independent tilt angles, and when in LEEM observation the sample is floating at 20 kV relative to system ground. The sample can be heated to 1500 K by electron bombardment or cooled down to 200 K by cooling the manipulator with liquid nitrogen. The sample holder is equipped with a type C thermocouple and a wolframium filament. The base pressure in the main chamber during the experiments was $\sim 10^{-10}$ Torr.

By means of a transfer bar the sample can be moved from the LEEM chamber to a preparation chamber. An Auger electron spectrometer (AES) and a parking system, where different samples are stored under UHV conditions, complete the system.

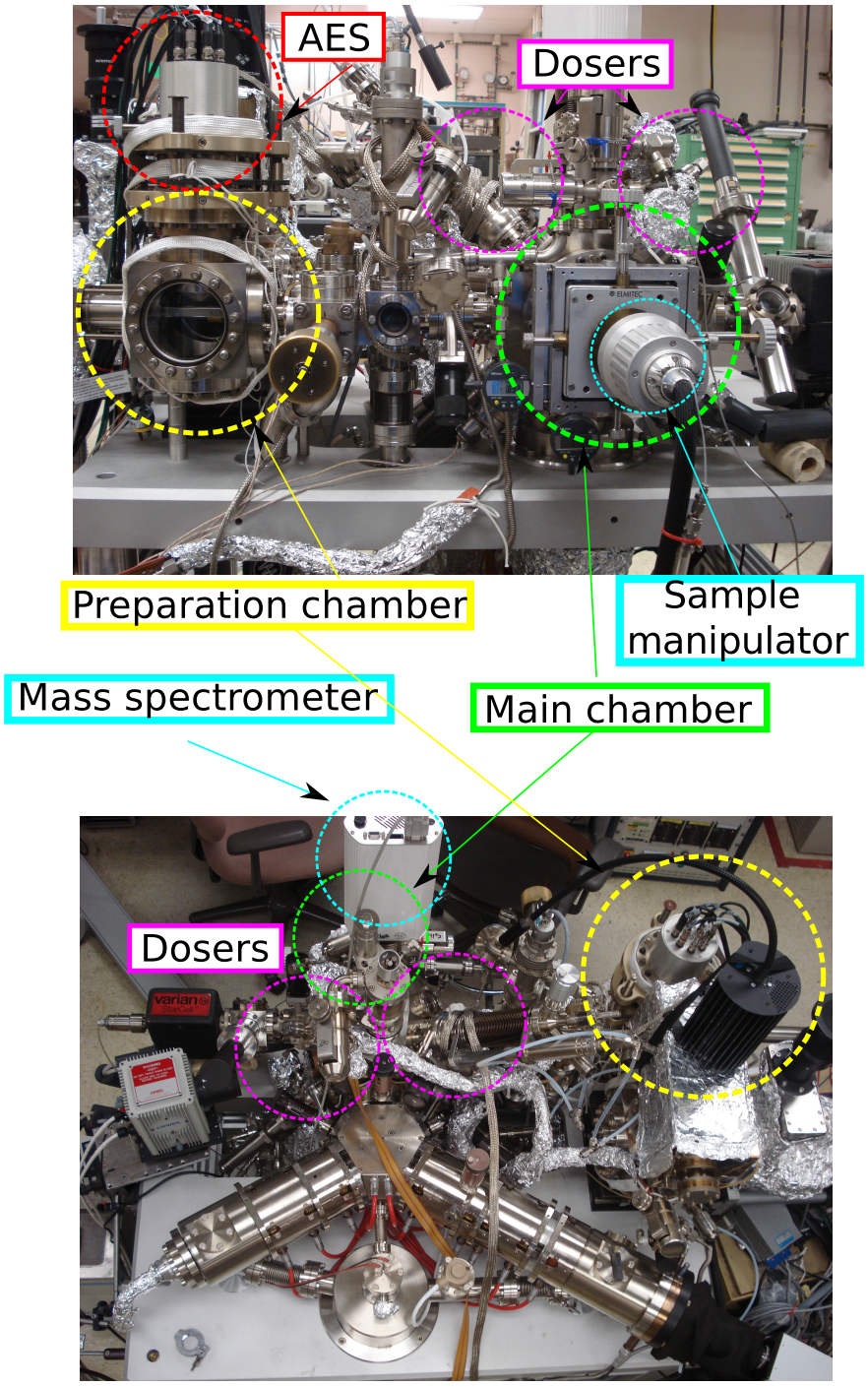

Figure 2.5 Photography of Elmitec III LEEM located at Sandia National Laboratories. Top picture shows a lateral view of the system. Bottom picture presents a top view of the LEEM and the optics, with the different elements marked.

2.2.2 The SPLEEM at Berkeley

The design differences between the Sandia and the Berkeley LEEMs are due to the fact that the later [68] is designed for magnetic studies [70]. In addition to the spin-polarized electron source, it uses electrostatic lenses, as magnetic lenses change the spin-direction of an electron beam. The beam separator also employs a system of magnetic prisms that is spin-neutral. Due to problems to move the contrast aperture, it cannot be used at present to image the diffraction pattern of the reflected electrons.

A standard method [72] to obtain a beam of spin-polarized electrons is to use a GaAs cathode illuminated by a circular-polarized laser (in our case a 800 nm laser beam [73]). If the laser is tuned to near the band-gap energy of GaAs, the electrons at the bottom of the conduction band are excited with a polarization of near 50% (the limit is given by the degeneracy of two electronic levels at the valence band edge and can increased by employing strained GaAs layers). The excited electrons are 2.5 eV below the vacuum level. To lower the work function, Cs and oxygen are coadsorbed on the surface of the cathode [74–76]. The adsorption of molecules on the surface of the cathode changes the work function of the cathode decreasing the intensity of the beam. In order to have a high current electron beam the layer of Cs oxide must be regenerated daily. To that end the GaAs crystal is flashed up to 800 K and then a few layers of cesium oxide are grown again on the surface. Typical beam currents obtained by this method are in the range of 5μA. The spin-direction of extracted electrons is perpendicular to the surface of the GaAs cathode and can be rotated 180° very rapidly from up ($\uparrow$) to down ($\downarrow$) by changing the helicity of the laser beam.

The SPLEEM also includes a spin manipulator [77] that combines electric and magnetic fields in order to adjust the spin direction of the electron beam. The spin manipulator is located between the electron source and the illumination column.

Figure 2.6 illustrates how the spin manipulator works. The electrons extracted from the GaAs cathode reach an electromagnetic deflector, where a radial electric (E=E_r) field bends the beam

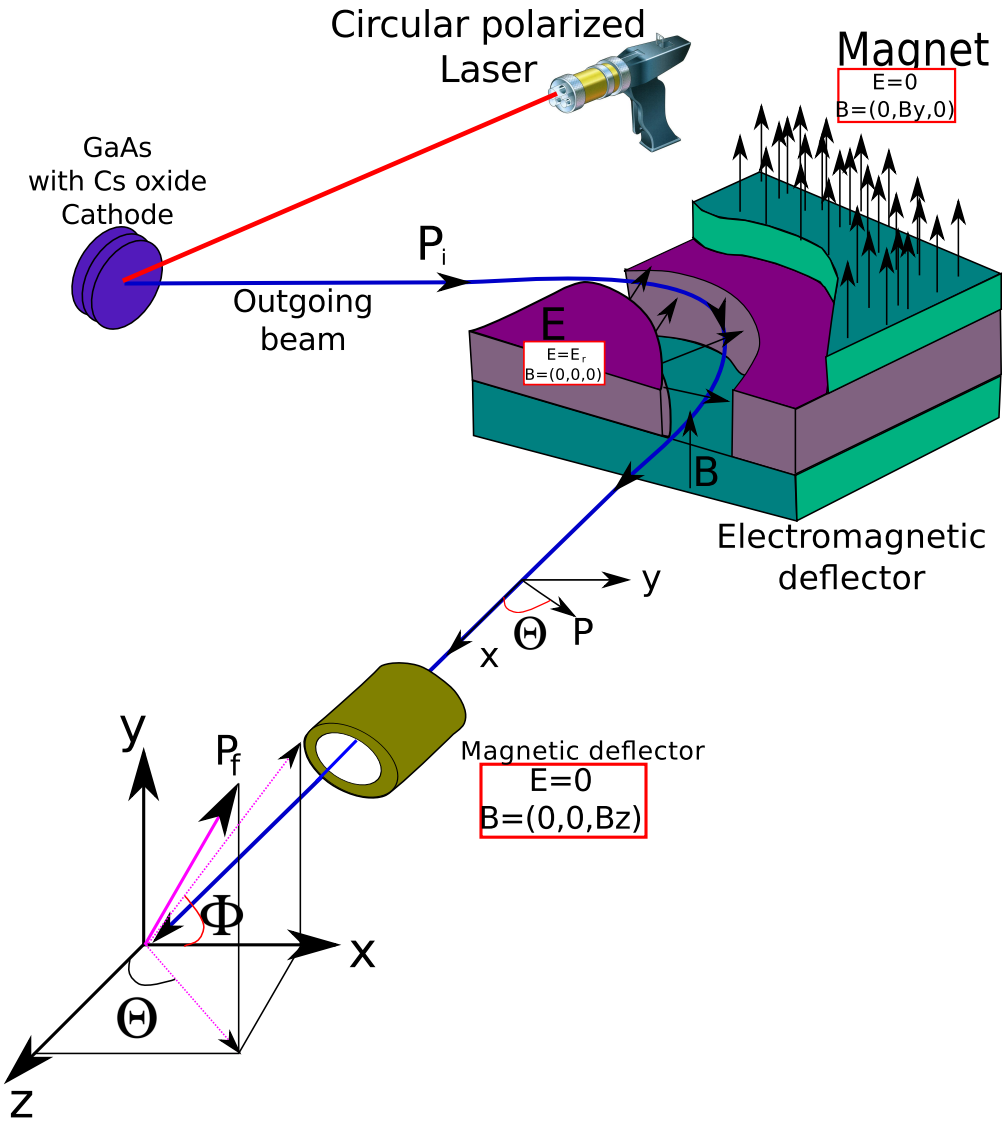

Figure 2.6 Schematics of the spin manipulator and the final polarization of the beam [77]. The electrons are extracted by illuminating the cathode with a laser. The electrons are guided to an electromagnetic deflector where their spin direction is rotated in the horizontal plane (x,y). Finally the beam is rotated in the vertical plane (z,x). Adapted from [73]

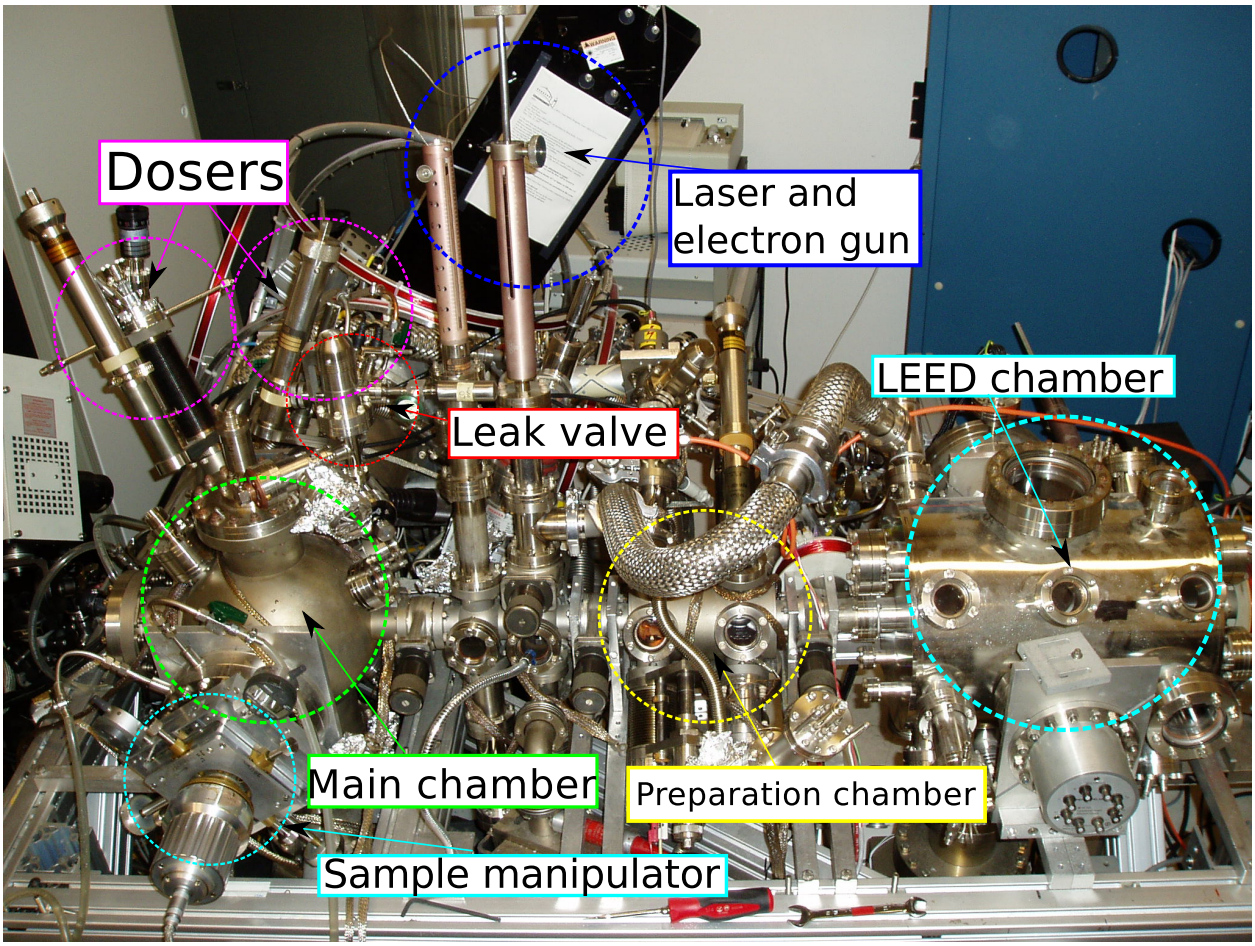

Figure 2.7 General view of the SPLEEM chamber at Berkeley

trajectory by 90°. Within the deflector a perpendicular magnetic field B=(0,B_y,0) is also applied in order to rotate the spin of the electron beam in the horizontal plane (z,x). This deflector enables to turn the spin direction of the polarized electrons from perpendicular to the sample surface (Θ=0°) to parallel to the sample surface (Θ=90°). Finally the beam passes through a magnetic lens where a collinear magnetic field rotates the beam spin in the vertical plane (x,y).

Figure 2.7 shows a general view of the SPLEEM system at Berkeley. As all the lenses are electrostatic, the full LEEM system is quite compact and is mounted on a 6" CF flange to the main chamber together with several metal evaporators. The base pressure of the main chamber is in the $\sim 10^{-11}$ Torr range. The sample holder and the sample design is the same as in the

Sandia LEEM and it is held in a similar manipulator. Unlike the Sandia LEEM, the sample in the Berkeley instrument is close to ground. The sample can also be heated up to 1500 K by electron bombardment or cooled down to 150 K with liquid nitrogen. Attached to the main chamber there is a preparation chamber where O_2 can be dosed to clean the sample without contaminating the GaAs cathode. Finally, attached to the preparation chamber there is a chamber that holds a conventional LEED diffractometer and an Auger electron spectrometer.

2.3 Low-energy electron diffraction

Low Energy Electron Diffraction (LEED) is the standard surface crystallographic tool [78,79]. By examining the LEED diffraction pattern it is possible to determine both the absolute dimensions of the surface unit cell and the unit cell symmetry. However the determination of the atoms that form the unit cell and their positions is more involved. For such studies, LEED intensity versus energy (LEED-IV) analysis has been developed. In LEED-IV analysis, the intensity of each diffracted beam that forms the LEED pattern is acquired as a function of the incident beam energy, typically in the range 50–400 eV. To perform a LEED-IV structural determination it is necessary to propose a model of the surface unit cell. Obviously, to elaborate the starting model the more information about the surface the better.

By means of a multiple scattering formalism, a set of theoretical LEED-IVs are calculated for the starting model. In our case, the multiple-scattering LEED IV calculations were performed with a modified version of the van Hove-Tong package [80–83] in collaboration with Dr. J. I. Cerda from ICMM, using the renormalized forward scattering approach. Then, as shown in Figure 2.8, the computed LEED-IVs are compared with the experimental ones. For quantifying the comparison, a goodness-of-fit factor, i.e. a number that quantifies the similarity between the experimental and the computed LEED IVs, is calculated. In LEED-IV the peak positions are more relevant to the

structural determination of the unit cell. As a consequence, a comparison factor that disregards the peak heights is usually employed, such as Pendry's R-factor (Rp) [84]. In the case of the Pendry factor Rp, the lower the value, the more similar the calculated and the experimental LEED IVs are. Values below 0.2–0.1, depending on the complexity of the model, are considered to give an acceptable agreement. If the agreement between the model and the measured LEED-IV is not good, the model structure is modified and the LEED IVs are re-calculated and compared again with the experimental ones. This process is repeated until a good agreement between experiment and theory is reached. We note that the main problem of a LEED IV determination is to have a model close enough to the real one that the latter can be reached from the starting one.

When properly applied, LEED-IV can provide the unit cell atomic positions of the 3–4 topmost atomic layers in a crystal with an accuracy of 0.01 Åin the out-of-plane directions. In our case (see chapters 3 and 4), the parameters we were more interested in were the interlayer spacings of our metal films. In such case, they were explored by calculating the IV curves over 3D parameter grid sweeping the interlayer spacings over wide ranges. The error bars were estimated for each parameter from the variance of the Pendry factor. Correlations between the structural parameters were taken into account for the estimation of the error limits. All the structural parameters derived present well-defined minima in the their respective R_p factor plots.

2.3.1 LEED in LEEM

In all the presented LEED and LEED-IV data, the instrument that has been used to acquired the data was a low-energy electron microscope instead of a traditional LEED diffractometer [85, 86]. LEEM is a very useful instrument for the exploration of electron diffraction patterns, an advantage it shares with TEM. As illustrated in figure 2.9, a diffraction pattern of the reflected electrons is formed at the back-focal plane of the objective. By changing the power of the lenses in the imaging system, either a real-image of the distribution of the reflected electrons or a reciprocal-space image

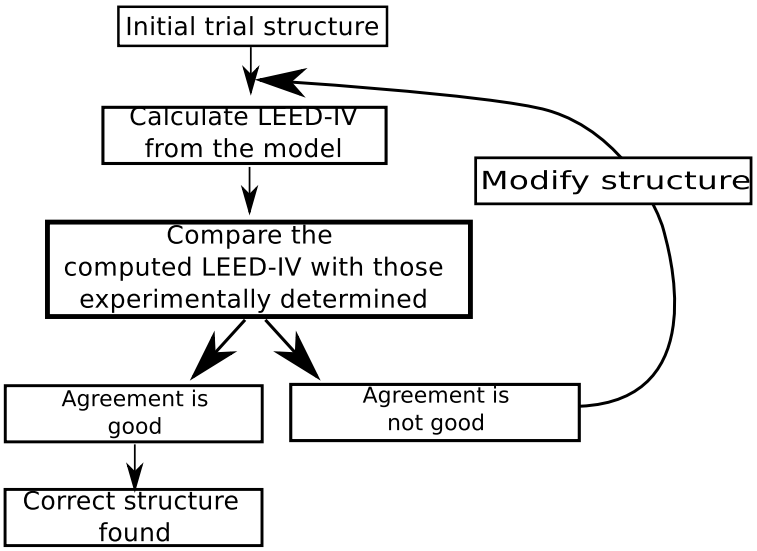

Figure 2.8 Flux diagram for optimal structure determination in LEED-IV

of the same electrons can be imaged in the LEEM phosphor screen.

There are several advantages when acquiring LEED data with a LEEM. First, the incident and the reflected beam are separated by the beam separator so nothing blocks the specular beam. It is possible to acquire LEED patterns at very low energies (only a few eV). In contrast with conventional LEED diffractometers, the position of the LEED beams does not change when the energy of the beam is changed, due to the accelerating field between the sample and the objective. And most important, by using a small illumination aperture it is also possible to acquire a LEED pattern from selected areas of the sample as small as 0.2 μm in diameter. This allows the acquisition of a LEED pattern from a single terrace of a substrate or a single island of a film.

There are some disadvantages of using LEEM as a LEED diffractometer. One is that the LEED pattern is distorted in far-off-axis regions. This means that, in practice, only up to the second order beams can be acquired. Also, in non-energy filtered LEEMs, the inelastically scattered electrons are not filtered so the diffraction pattern is superimposed with a bright broad spot formed by the secondary electrons.

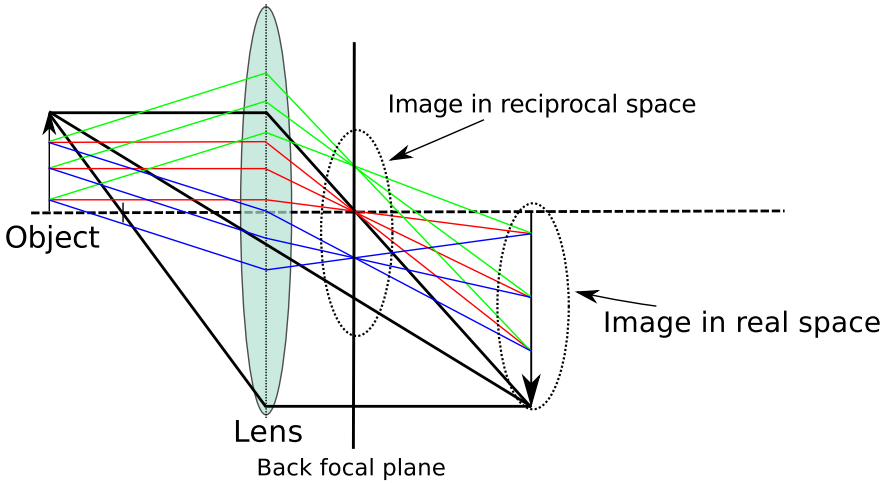

Figure 2.9 Schematic representation of the formation of an image by an electron lens. In addition to the real-space image, the electrons that leave the sample at a given angle are focused into a single point at the backfocal plane of the lens, i.e. a LEED pattern is formed for electrons a the backfocal plane of the objective. Image adapted from [69].

2.4 The scanning tunneling microscope (STM)

The STM was invented and developed by G. Binning and H. Rohrer at the IBM laboratories in Zurich in 1981 [87–89]. Five years later this invention was awarded with the Nobel prize. In figure 2.10 we present a simplified STM schematic. The STM works based on the principle of the quantum mechanical tunnel effect. When a voltage difference is applied between a tip and a surface and the distance between them is small enough, the electrons can tunnel between them. By means of a piezoelectric scanner the surface is explored and the current is measured [90, 91]. The tunnel current is proportional to:

$$I \sim exp\left(-Az\sqrt{\frac{\Phi_s + \Phi_t + V}{2}}\right) \tag{2.2}$$

where Φ_s is the work function of the sample and Φ_t is the work function of the tip. The distance between sample and tip is z and the applied bias is V. The tunnel current is determined by the overlap of the sample and tip wavefunctions. The current decays exponentially with the distance between

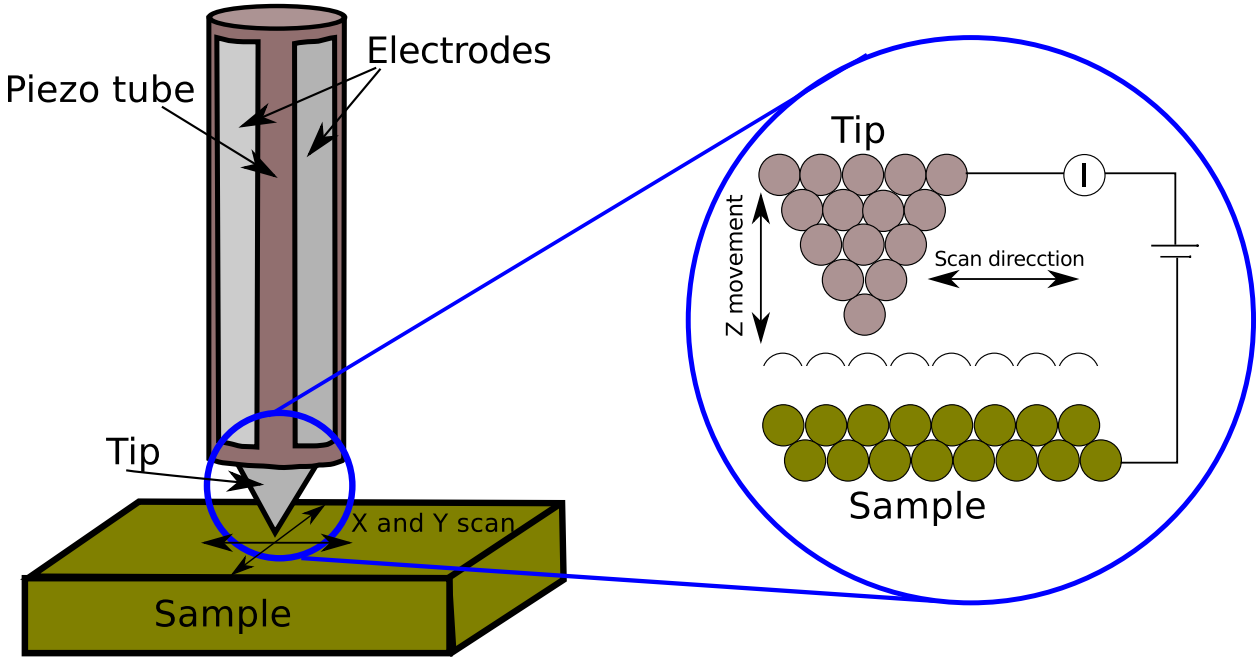

Figure 2.10 Schematics of an STM. A piezoelectric tube is used to control the position of a metallic tip close to a surface. The distance to the sample is changed in order to keep the tunneling current constant. The topographic representation of the surface is obtained plotting the voltage corrections applied to the piezoelectric scanner to keep the tunneling current constant. Adapted from [92]

tip and sample due to the exponential decay of the wave functions inside a potential barrier.To operate the STM a feedback loop is used to maintain a constant current by changing the distance between sample and tip. The topographic images of the surface are obtained by representing the corrections to the vertical position of the piezoelectric scanner.

STM has a lateral resolution of 0.02 nm and a vertical resolution that can be better than 0.001 nm. This implies that the distance between tip and sample has to be controlled in the range of a tenth of an Å. To that end piezoelectric ceramics are used.

2.4.1 The Madrid STM head

We describe now the STM that has been built during this thesis at the Instituto de Química-Física "Rocasolano" (together with the full UHV chamber that houses it). It is based on the design described in [60]. Figure 2.11 shows a cross section (a) and a photograph (b) of the assembled head. The housing of the STM was made of tantalum or gold-coated invar® [93, 94] [like the housing shown in figure 2.11 (b)]. The head has cylindrical symmetry in order to minimize lateral thermal drifts. The STM head houses the piezoelectric scanner and the coarse-approach motor stage. The STM head rests on a sample holder via three glass balls that decouple the head thermally and electrically from the sample holder. The three glass balls fit in a kinematic mount machined in the sample holder. Thanks to the kinematic mount, the position of the STM with respect to the sample can be fixed with an accuracy of a few micrometers. As the azimuthal angle of the scanner can be fixed, it is then possible to reach the same area of the sample after transferring the sample out of the STM and back (this control of the azimuthal angle can be done by rotating the sapphire tube that holds the scanner by means of the coarse-approach stack, as explained below). The access to the sample holder is accomplished by raising the STM head by means of a manipulator.

The coarse approach motor stage

The approach motor consists of two parts: a sapphire tube that carries the piezoelectric scanner, and the shear piezo stacks that are mounted in the STM housing and hold the sapphire tube that comprise the coarse-approach stage. Figure 2.12 (a)-(b) shows a top and a lateral view of two of the stacks of the same side of the STM housing. The sapphire tube is held in place with a spring that pushes the sapphire tube against the piezo stacks. The contact between the spring and the sapphire tube is made by alumina half-cylinders glued to the piezo stacks with Loctite® Hysol 1C epoxy resin [95] and oriented with the cylinder axis perpendicular to the STM housing axis to minimize the contact area with the sapphire tube. The piezo stacks in pairs and the spring are mounted

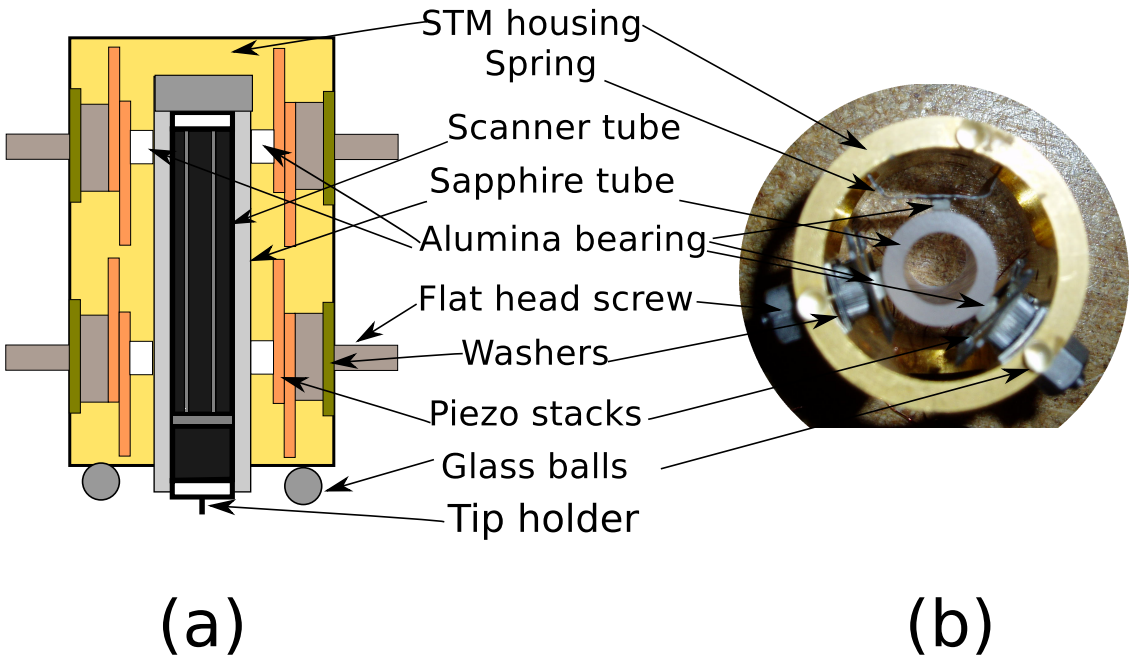

Figure 2.11 (a) Cross section of the STM head (b) Top view of the housing with the motor approach stage and the sapphire tube.

120° within the STM housing. Each of the four piezo stacks is composed of two piezo plates glued together with epotek® H27D conductive-epoxy resin [96] at right angles to one another on a flat-head screw. The piezo plates are made of EBL-4 PZT with nickel electrodes from Staveley Sensors [97] with dimensions 0.200" x 0.100" x 0.020". At room temperature these piezos move by 0.50 nm/V [98].

The motor employs a stick-slip mechanism. When a voltage is applied slowly to the piezo stacks, the sapphire tube moves along with them due to friction between them. Then a sudden decrease of the applied voltage makes the piezo stacks go back to their original position while the tube stays in the same place due to its inertia. A sequence of steps is generated by applying a sawtooth voltage to the stacks. Depending on the electrical connections to the two piezo plates of each stack the sapphire tube will move either up/down or will rotate. Figure 2.12 (c)-(d) shows the wiring schematics to obtain the two different motions of the sapphire tube. In order to obtain

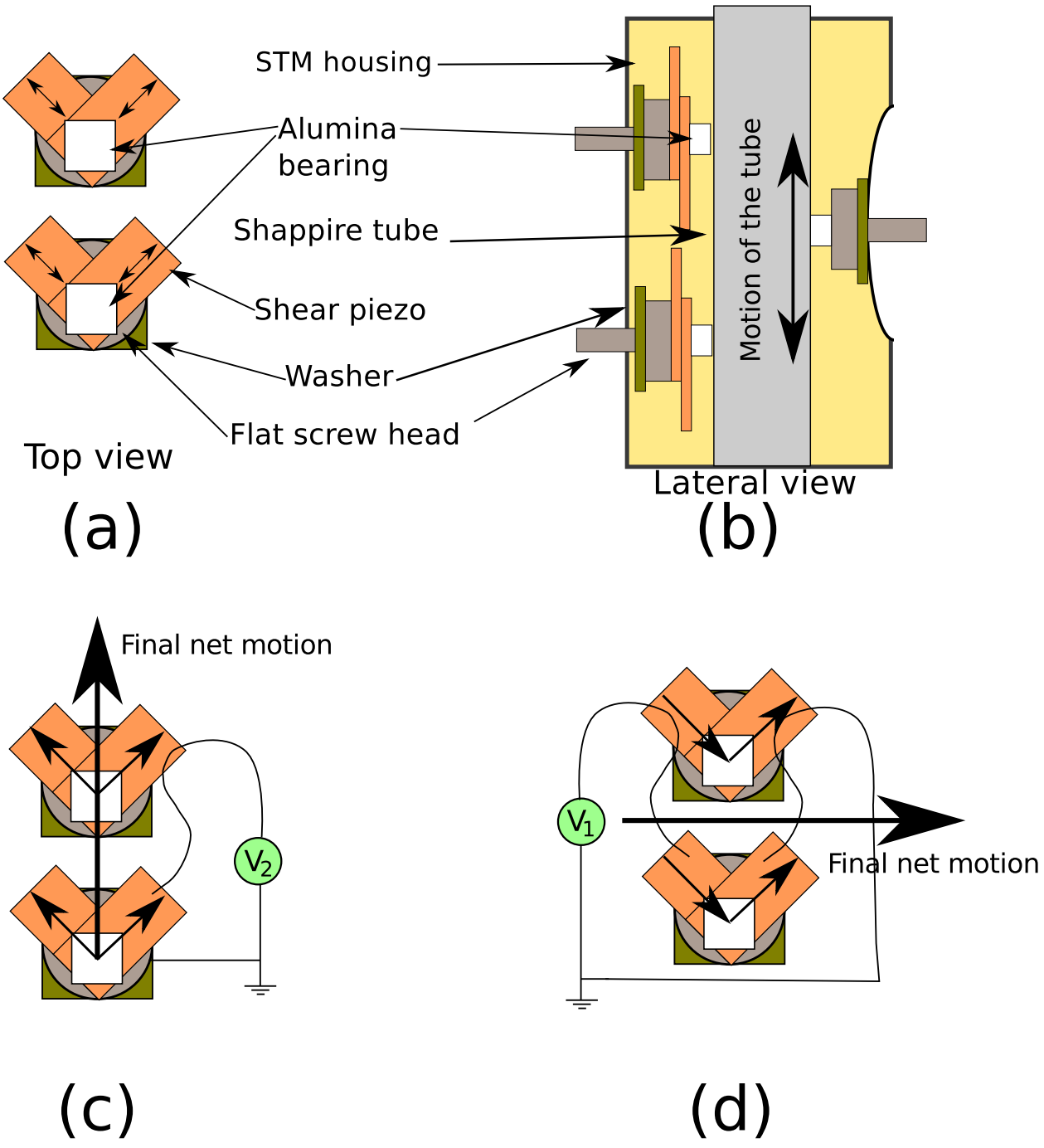

Figure 2.12 (a)-(b) Top and lateral view of two piezo stacks. (c) Wiring connection to move the tube up and down (d) Wiring diagram to obtain a net motion for rotation.

an up-down motion of the sapphire the voltage is applied between the upper electrode of the top piezo of the stack and the bottom electrode of the lower piezo i.e. there is an applied electric field with the same sense across both shear piezo plates of the stack. As a result the two plates will shear in the same direction and the vectorial sum of the two displacement vectors of each piezo will yield a net motion of the top of the stack up or down [figure 2.12 (c)]. To obtain a rotation of the tube, the electrical connections are changed: the voltage is applied between the lower electrode of the top piezo plate (and also to the top electrode of the lower piezo plate, as the two piezos are glued together with conductive epoxy) and the upper electrode of the upper piezo short-circuited to the bottom of the lower piezo. In this case, the electric fields across the plates are the same in magnitude but have opposite directions [figure 2.12 (d)]. The vectorial sum of the displacement vectors yields a net motion perpendicular to the STM housing. The other stacks generate the same net motion creating a torque that rotates the sapphire tube. With only three electrical connections, the coarse approach motor can then move up/down or rotate the scanner tube.

The scanner tube

As mentioned at the beginning of the section, the STM requires a fine control of the distance between sample and tip in the X, Y and Z axis. To such end we use a PZT hollow tube. Figure 2.13 (a) shows all the parts of the scanner just before the final assembly. The tube scanner (from Staveley Sensors [97] with dimensions 0.125" outer diameter, 0.020" wall thickness and 0.750" length) outer electrode is sectioned into 4 sectors. The assembly of the scanner tube is done in two steps: first, the tube is glued to a stainless steel base and attached to the sapphire tube. Second the tip holder is mounted at the lower end of the piezo tube. To isolate the PZT scanner tube from its base, they are glued together with an alumina washer in between. To hold the tube, washer and the base together while the resin cures, a screw is used and later removed. The tip holder is a piece of stainless steel tube glued to a T-shaped alumina which is glued to the bottom end of

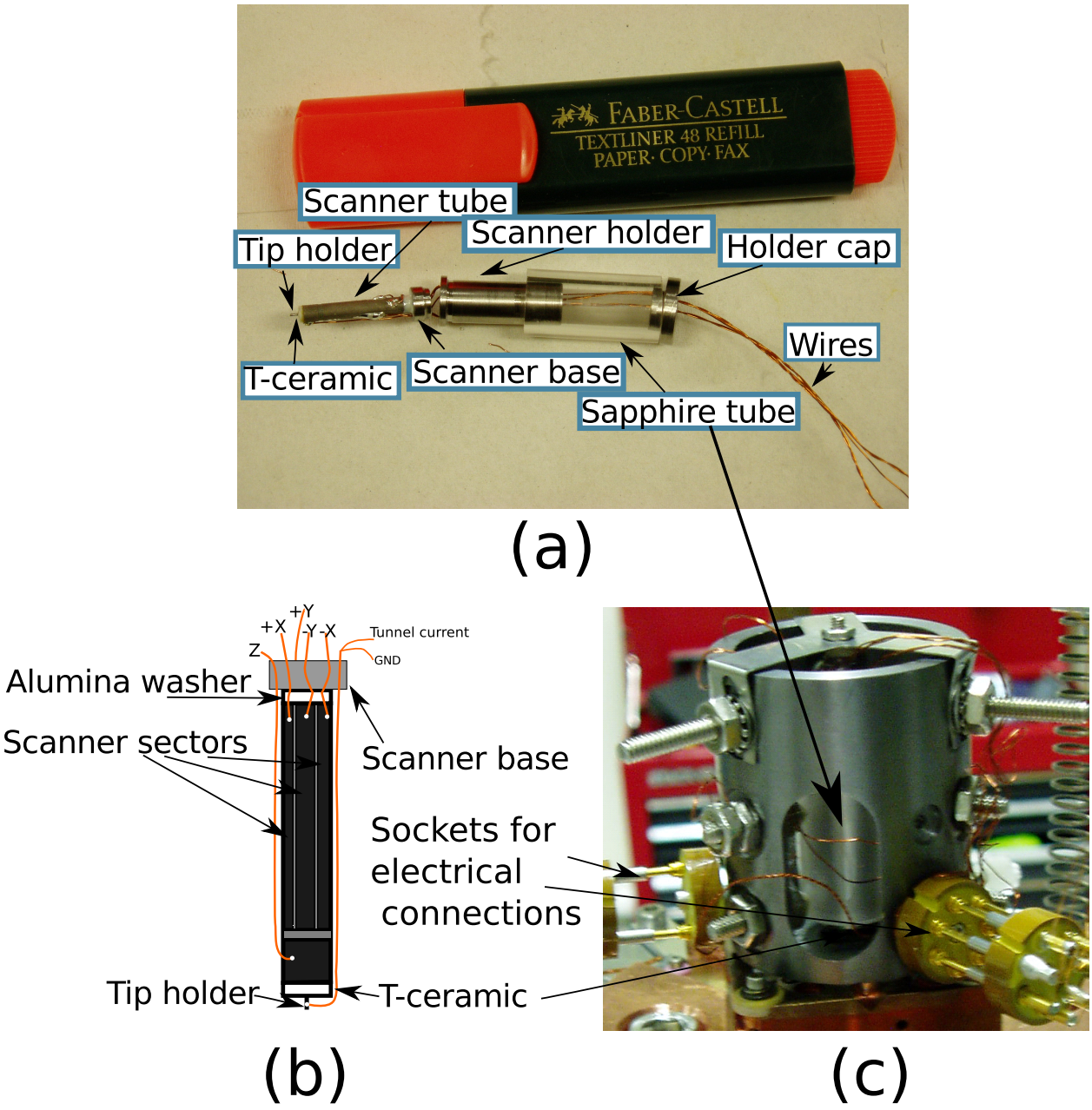

Figure 2.13 (a) Final steps for the assembly of the scanner tube inside the sapphire tube. (b) Closer view of the scanner and wiring schematics of the scanner tube. (c) Lateral view of a finished head.

the scanner tube. The current is carried by a shielded wire that is soldered to the tip holder (the shield is grounded). Figure 2.13 (b) illustrates the electrical connections of the final assembly. The scanner holder fits into the sapphire tube and is held in place with one screw and a holder cap.

STM test images

The tests of the STM gave good results, although it was deemed necessary to provide the UHV chamber with pneumatic legs for low frequency vibration insulation. Three examples of STM images from the STM built during the thesis is shown in figure2.14. (b)–(c) the images are raw experimental data. Image (a) is smoothed to reduce the noise. During most of the thesis, an RHK STM-100 electronics was used to control the STM together with the Omicron MSCU unit for driving the coarse approach stage, all under the control of a modified Gxsm software [99, 100]. For analysis, we used the Gwyddion package [101]. Latter we have used the STM with an Specs Nanonis control electronics [see figure 2.14(b)].

2.4.2 UHV STM chamber system

The STM is placed in a vibration isolation system and mounted into a custom built UHV chamber. Figure 2.15 (a) shows a lateral view of the chamber and the STM head mounted on the vibration isolation system [figure 2.15 (b)]. The sample holder and the STM rests on a copper disc attached to an Al block. The copper disc holds the electrical connections to the sample holder. The copper disc and the Al block are electrically isolated but thermally connected by a sapphire wafer. The Al block hangs by 4 stainless-steel springs for vibrational isolation. The springs are damped by an eddy current system made with 12 Sm-Co magnets protruding between fins machined in the Al block. The sample can be flashed to 2000 K by electron bombardment without the STM head or heated to moderate temperatures (up to 500 K) with the STM in operation. The Al block can be cooled down to 100 K by pushing it against a cold finger refrigerated by LN_2. The chamber is

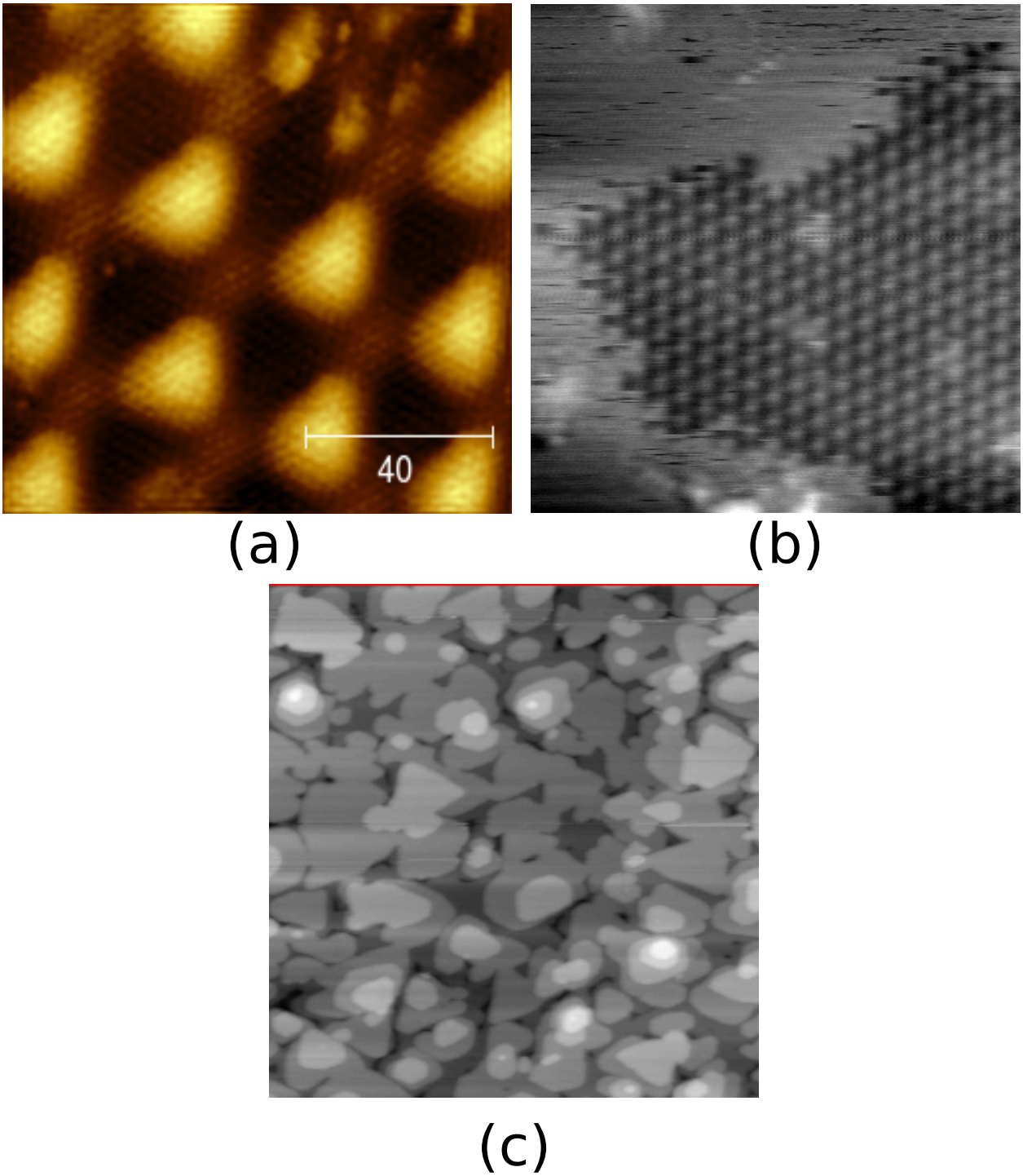

Figure 2.14 (a)13nm x 13nm STM acquired on graphene on Ru(0001). (b) 16nm x 16nm STM image, acquired on 2x2 O/Ru(0001). (c) 300nm x 300nm STM image acquired on 4 ML Pd/Ru(0001).

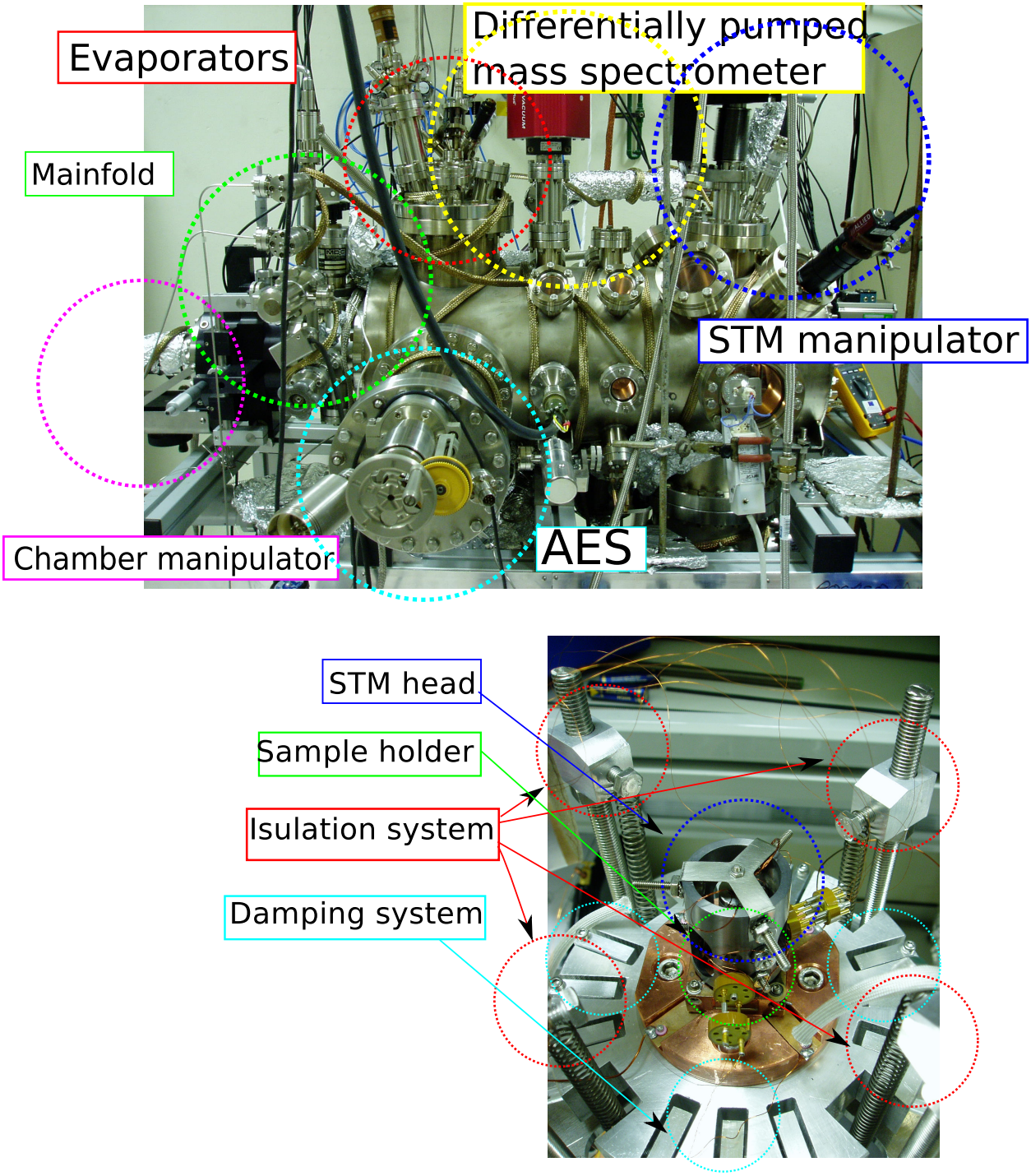

Figure 2.15 Lateral view of the chamber at Rocasolano-CSIC lab, Madrid. Image of the STM head resting on the sample holder and details of the vibration isolation system.

equipped with a linear motion manipulator that allows to move and rotate the sample within the horizontal axis of the vacuum chamber. The chamber is also equipped with an Auger spectrometer, a LEED diffractometer, an ion gun and a fast-entry system. Up to five different dosers can be attached to the chamber. The chamber, dosers, an hydrogen cracker and and the fast-entry system were designed by us and built at the SEGAINVEX workshop at the Universidad Autónoma de Madrid.

2.5 Sample preparation, metal and atomic hydrogen dosers

Ru(0001) single crystal was cleaned by exposure to $1x10^{-8}$ Torr of O_2 at 890 K in order to remove carbon (graphene) segregated to the surface, followed by brief flashes to 1600 K to remove the oxygen. The W(110) crystal was cleaned by exposure to O_2 followed by repeated flashes to 2200 K. High-purity H_2 and CO were dosed from lecture bottles through leak valves. The molecular hydrogen and CO doses were estimated from the vacuum chamber's ionization pressure gauge corrected for the molecular sensitivities of 0.46 and 1.0, respectively [102]. The nominal atomic hydrogen doses are indicated assuming a 100% dissociation efficiency and neglecting the line-of-sight nature of the source.

Cobalt, Pd and Mg were deposited from pure-element rods (about 5mm in diameter and 25 mm long with a purity of 99.99%) heated by electron bombardment. Figure 2.16 (a) shows a general view of a Co rod and the filament before the final assembly into the water-cooling jacket. For the electron bombardment, high voltage is applied to the metal rod. The electrons are extracted from a W filament 0.125 mm in diameter (typical current 2–3 A) and accelerated towards the rod resulting in the metal being heated. Typical conditions for Co deposition were a high voltage at the Co rod of 900 V, 2.5 A filament current and 25 mA emission, with a typical deposition rates of 0.3 ML/min. For Pd , typical evaporation conditions were 1000 V at the Pd row, 2.5 A filament current and 35

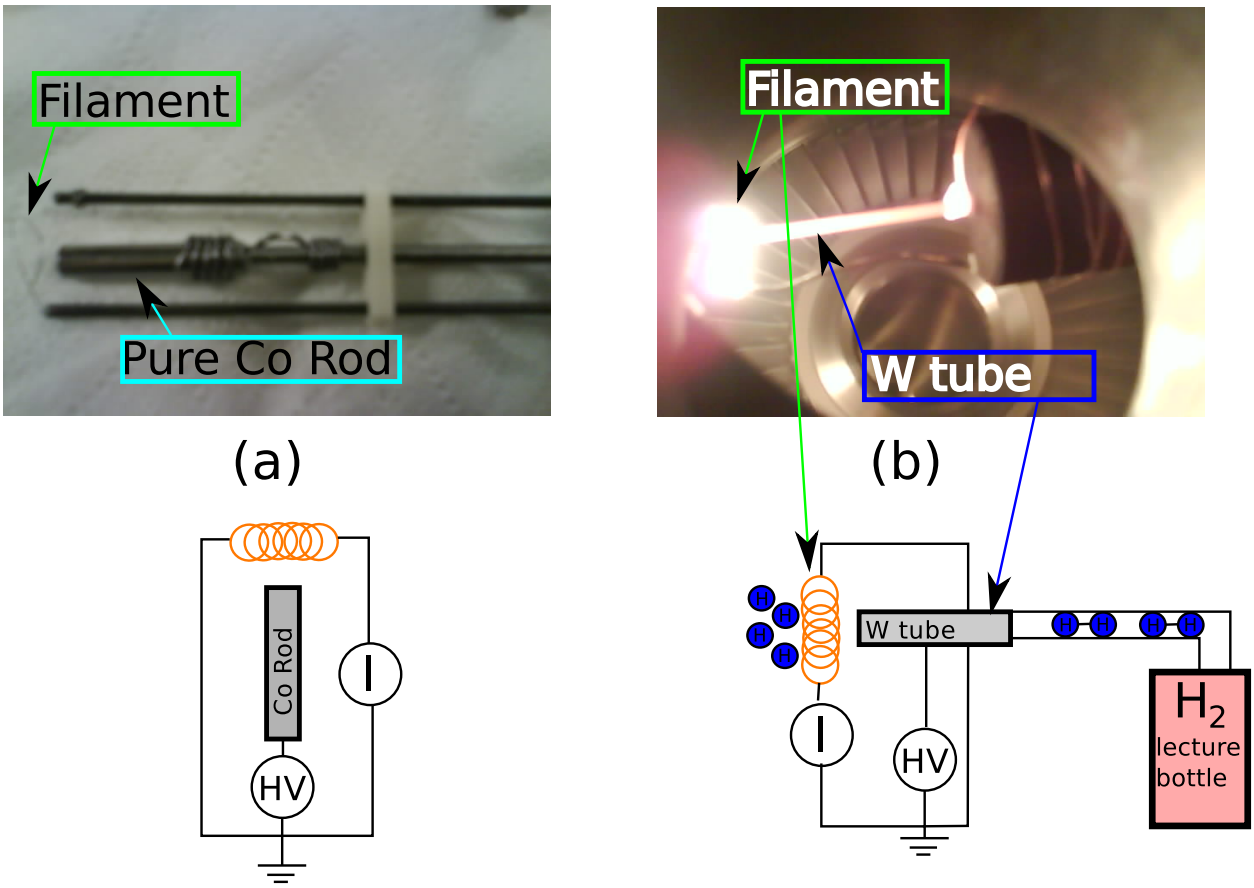

Figure 2.16 (a) General view of a pure Co rod and the filament used for metal deposition. The electrical schematics are shown below. (b) Picture acquired while the W capillary was heated to 2000 K, schematic and wiring connections are shown below.

mA emission. In the case of Mg deposition, typical conditions were 200 V, a filament current of 4.3 A and 12 mA emission. During growth the pressure remained in the 10^{-10} Torr range in both SPLEEM and LEEM chambers while it reached 2x10^{-9} Torr in the STM chamber.

Two atomic hydrogen sources were used:

- At Sandia, a commercial thermal hydrogen cracker was used from Createc [103]. This hydrogen source consists of a hot tungsten filament in a water-cooled tube through which molecular hydrogen was leaked. The manufacturer's reported efficiency of the cracker is $\sim$70% at pressures in the 10^{-6} Torr range. The cracker was throughly degassed by running the filament for several days until the chamber returned to its base pressure.

- During the last year a home-made atomic hydrogen source based on the cracker described by Bischler et al. [104] was designed and built. The cracker consists of a W tube 50 mm in length, 0.6 mm inside diameter, 1.6 mm outside diameter and with a purity of 99.95% from Goodfellow [105]. One side of the W tube is connected to the molecular hydrogen lecture bottle by through a leak valve and electrically isolated from the rest of the chamber by a Macor tube. The other side of the W tube is heated up to 2000 K [104, 106]. Molecular hydrogen is introduced into the W tube, which dissociates at the hot end. For the final assembly the W tube is mounted inside a water-cooling jacket. The efficiency of the cracker in the preliminary tests by means of quadrupole mass spectrometer was 40% at pressures in the 10^{-8} Torr range. Figure 2.16 (b) shows a picture acquired while the cracker was tested, together with an schematic of the design and the electrical connections is shown below.

Chapter 3

Growth and Structure of Pd films

3.1 Introduction

Palladium is a component of many structural materials, electronic materials and commercial catalysts [107]. The functionality of these materials is engineered in several ways, including the use of nanocrystalline or nanoparticle forms and by combining Pd with other metals, either in an alloy or in core-shell structures. In addition, the properties can be optimized by inducing strain and defects such as stacking faults. Some such "modified" forms of Pd have been experimentally confirmed to present ferromagnetic order [108, 109]. Ferromagnetism in Pd has been shown in theoretical studies to be greatly affected by stacking faults and twin boundaries [110]. Given this background, it is important to completely characterize the structure of Pd in various forms.

Here we explore the structural properties of Pd as ultra-thin films supported on metal Ru(0001). Thin films offer several advantages in structural characterization, relative to, for example, core-shell or alloy nanoparticles. Specifically, low-energy electron diffraction (LEED) can be used to determine the surface structure.

The contest of this chapter has been published in B. Santos et al. [111], from where it has been

reused with permission.

We present a detailed LEED and low-energy electron microscopy characterization of both thin films, in the range of 2–6 monolayers Pd on Ru(0001), as well as of the surface of thicker films, ∼20 ML thick, grown on both Ru(0001) and W(110). The latter could be considered structurally as a proxy for bulk Pd(111) surfaces.

Pd on Ru(0001) has been studied previously by several groups, focusing on the monolayer limit. A Pd monolayer on Ru(0001) is pseudomorphic with the substrate. Alloying is not detected if the growth is performed at room temperature (RT) or below [112]. At higher temperatures, alloying can occur. For example, at 870 K alloying at the edge of the growing Pd islands hinders further growth, producing distinctive labyrinthine islands [113]. Further annealing to 1150 K produces a uniform bidimensional alloy of PdRu [112]. Thicker films do not grow layer- by-layer [114] at RT or below. In the same study using reflection high-energy electron diffraction, x-ray photoelectron spectroscopy and x-ray photoelectron diffraction, the three-dimensional growth of Pd/Ru presented a twinned fcc structure with an unusual subsurface expansion of up to 7% in the second and third Pd layers in a film of 5 ML average thickness.

The surface of Pd(111) single crystals has been the subject of several structural studies [115, 116]. Unlike most transition metals, LEED experimental determinations of the last-layer interlayer spacing give a slight expansion instead of a contraction. This expansion could be caused by residual hydrogen adsorbed on the surface, as suggested for several transition metals [117]. We also compare our thin-film interlayer separations with ab-initio calculations.

3.2 The growth of 2 to 6 ML of Pd on Ru

LEED IV has the fewest possible interpretations if the diffraction data is obtained from a uniformly thick film on a single substrate terrace. The fcc structure of bulk Pd has an in-plane (111) spacing

of 2.75 Å, which is 1.7% larger than the Ru(0001) in-plane spacing [118]. This lattice mismatch should promote three dimensional (3D) growth, and prevent the formation of uniform-thickness, smooth films. Such 3D growth has been reported at room or lower temperatures [114]. However, the lattice mismatch might to able to be accommodated elastically in films up to several layers thick on Ru(0001). There is agreement that monolayer Pd films on Ru(0001) are pseudomorphic [112, 113]. Thicker films are expected to eventually relax towards the bulk in-plane value.

There are several strategies to obtain flat films in systems that prefer to grow 3D islands. One is to tailor the growth parameters and use large terraces on the substrate, taking advantage of the kinetic limitation to nucleate new layers on top of existing islands [119]. Another method is to dose the film material at room or lower temperature, producing a rough and disordered but continuous film. After the growth the film is annealed to improve the smoothness and crystallinity. With care, the film can be smoothed before its dewets and forms three-dimensional islands [120].

Using the in-situ and real-time ability of LEEM allows us to explore the parameters that promote smooth films, including the flux and/or temperature for thin films or the time and temperature during annealing of thicker RT-grown films. We first discuss thin-film growth, and then present the results on the thicker, annealed films.

3.2.1 Growth

By growing Pd on Ru terraces a few micrometers in width, a layer-by-layer growth front can be achieved using a substrate temperature of 750 K and a flux rate of 0.25 ML/min. Figure 3.1 shows frames from a continuous movie selected to show the nucleation of each new layer up to 7 ML thick. The initial substrate, figure3.1(a), presents a terrace of nearly 8 μm across (thicker gray lines indicate step bunches around the central terrace, while thinner gray lines correspond to monatomic steps).

The growth starts by Pd islands decorating the substrate steps and by the nucleation of roughly

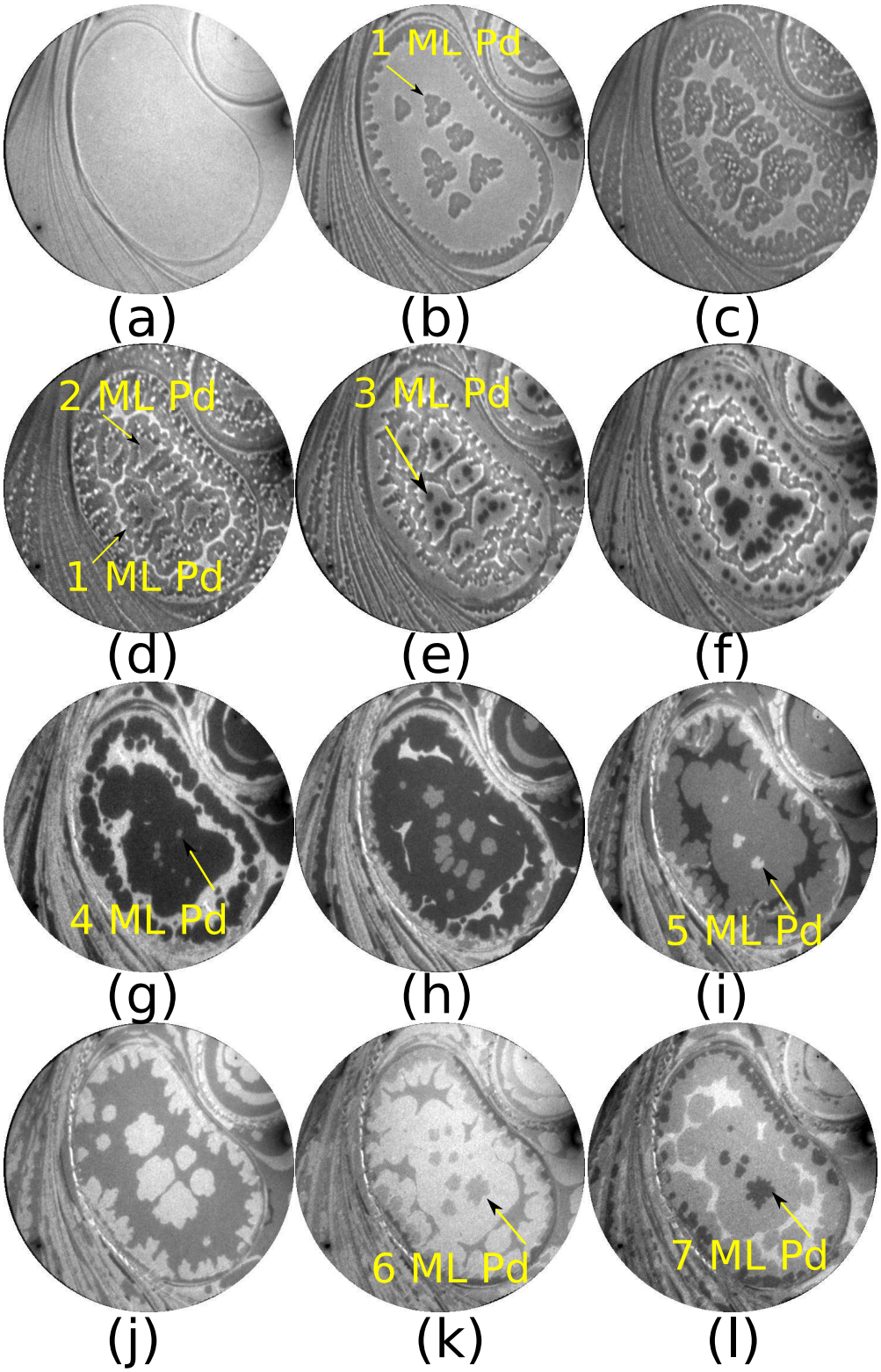

Figure 3.1 (a)-(l) LEEM images selected from a real-time movie acquired during the growth of Pd on Ru(0001). The field of view is 9.3 μm.

triangular islands in the middle of the terrace (figure 3.1(b)). Before the first layer is completed, the second and third layer (black islands in figure 3.1(e)) start to nucleate on top of the first and second layer, respectively (figure 3.1(d-f)). The dendritic shape of the edges of the 1^{st} layer islands probably result from some alloying at island edges [113]. Thicker islands have smoother edges (figure 3.1(g-l)).

The contrast between film regions of different thickness is due to a quantum size effect on the electron reflectivity [61]. To quantify those changes, we present in figure 3.2 the complete electron reflectivity of areas between 2 and 6 ML thick, acquired in different films (as the films only expose at most three different layers each). The reflectivity is dominated by a broad peak around 20 eV. This peak is attributed to the forbidden gap of the (222) Bragg reflection [121]. The smaller peak that appears in all the films close to 15.6 eV is probably due to a bulk-band crossing [121], although it has also been assigned to a Tamm resonance [122] or an anisotropy effect in electron inelastic scattering [123]. The other oscillations detected in the thinner regions correspond to quantum size effects (QSE) due to interference between electron reflection at the film surface and at the Pd/Ru interface. The sharpness of the oscillations suggests that the later interface is abrupt and free of significant alloying.

3.2.2 LEED IV

In figure 3.3 we present the LEED pattern acquired from a uniformly thick region of 6 ML on a single Ru terrace. The selected-area LEED patterns of all the thicknesses from 2 to 6 ML Pd show only integer (first-order)(1×1) spots at the same positions as the original substrate spots within our experimental resolution, which we estimate to be $\pm 2\%$. Since the in-plane lattice spacings of bulk Pd and bulk Ru differ by 1.7%, this resolution is insufficient to prove that the films have the same exact lattice spacing as the substrate. Nevertheless, the 2–6 ML films do not have satellite beams, which would be expected from multiple scattering between differently sized Pd and Ru lattices.

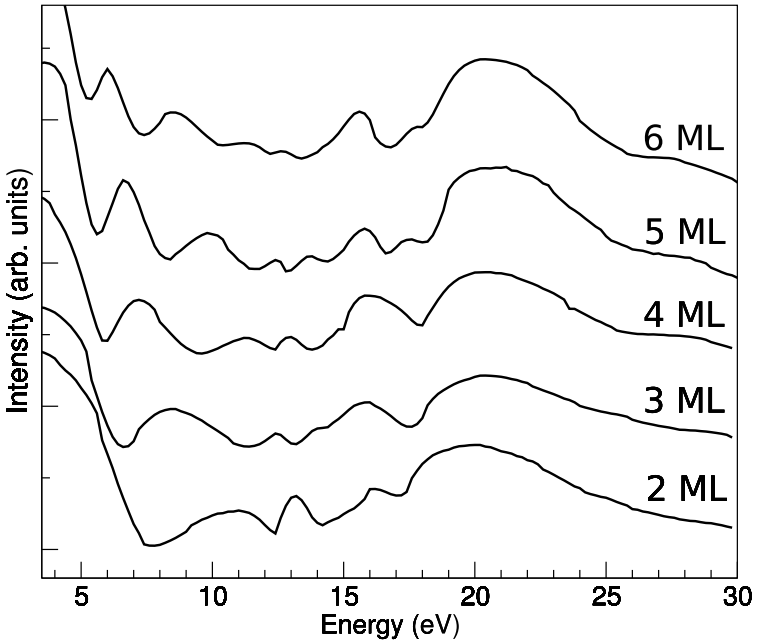

Figure 3.2 Electron reflectivity curves acquired on areas of labeled Pd thickness of Ru(0001).

A further proof of the in-plane matching of the films to the substrate comes from LEED IV, as discussed below. Thus, the films are pseudomorphic with the substrate i.e., the palladium unit cell is distorted in plane in order to obtain a one-by-one correspondence with the substrate atoms. This implies that Pd films up to 6 ML on Ru are under 1.7% compressive strain. This compression should expand the film's interlayer spacing relative to the bulk value. A simple estimate of the effect can be made by assuming that the Pd layers want to maintain the bulk nearest-neighbor distance to the atoms in adjacent layers even though they are compressed in-plane. This model predicts an interlayer separation of 2.26 Å for the strained films, slightly larger than the bulk value of 2.25 Å.

Even if Pd is fcc in bulk, there is the possibility of having different stacking sequences or stacking faults when in thin-film form. This possibility is more likely given that the Ru(0001) substrate is hcp, and that the first Pd layer grows following the same sequence [112]. The symmetry of the LEED pattern is three-fold for all thicknesses from 2–6 ML. However, this three-fold symmetry

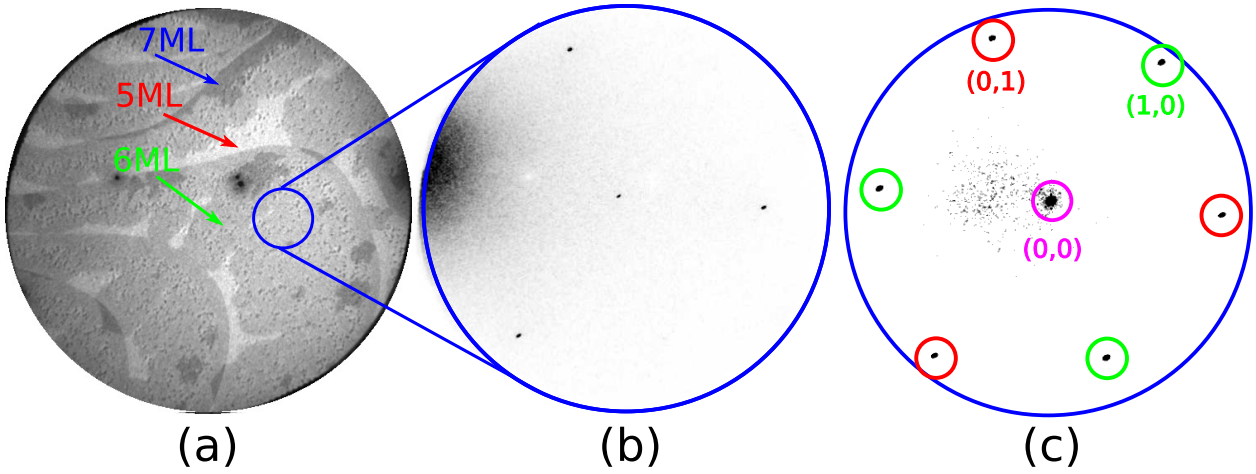

Figure 3.3 (a) LEEM image taken after the growth of Pd on Ru(0001). The field of view is 14.5 μm. (b) At 141 eV the LEED pattern of a 6 ML Pd area on a single Ru(0001) terrace, marked in (a) with a circle, has 3-fold symmetry. (c) At 132 eV the LEED pattern from the same Pd region has roughly 6-fold symmetry.

alone does not allow distinguishing between fcc and hcp Pd. We next use the LEED-IV data to determine the layer stacking sequence in the Pd films. We will use the common naming scheme of a, b, c to indicate each of the three possible hexagonal layers for a close-packed structure. When needed, we will denote the substrate layers with upper case labels ABAB, and the film layers with lower case acba, with the rightmost letter always indicating the topmost layer. For example, we will denote an fcc structure by acb and its twin (mirror fcc) as bca.

Since LEED IV curves (see figure 3.4) were obtained from regions of uniform thickness on a single substrate terrace, we can directly determine how Pd is stacked on Ru. We start discussing the bilayer of Pd, the film most likely to deviate in layer stacking from bulk Pd due to substrate interactions. Considering both possible terminations for a Ru terrace: BABA or ABAB , together with all possible sequences of Pd layers, the best fit found corresponds to ABAB/ac,with R_p=0.15 (all the other models result in a much worse $R_p > 0.50$). The fit shows a strong sensitivity to the bulk Ru orientation, allowing us to establish unambiguously the ABAB termination of the Ru terrace where the LEED pattern was acquired. The interlayer spacings for the 2 ML case are shown

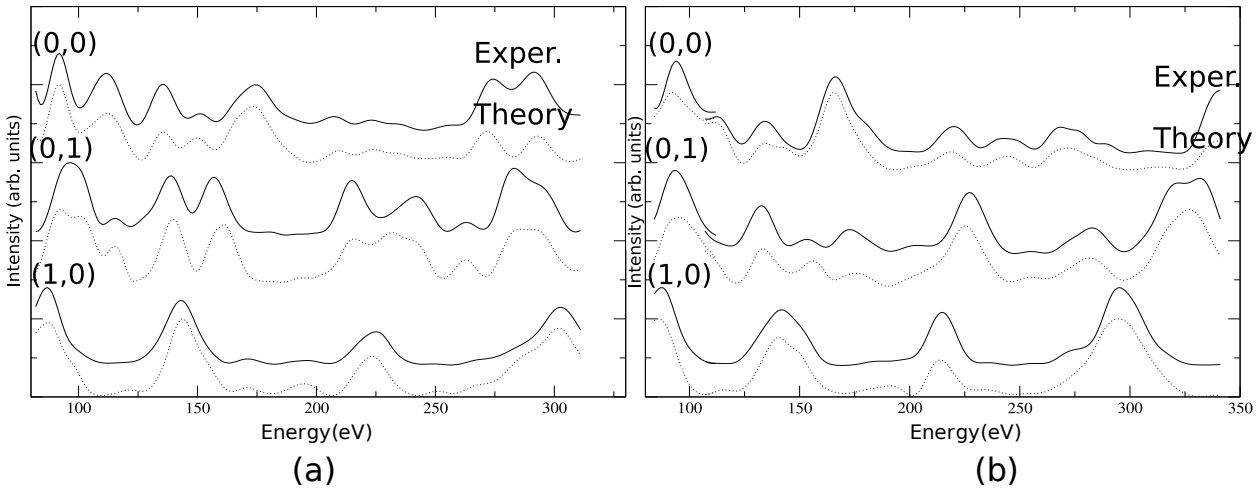

Figure 3.4 LEED IV data and best fit to: (a) 2 ML Pd/Ru(0001), (b) 6 ML Pd/Ru(0001).

the Table 3.1. It is noteworthy that the topmost two Ru layers are contracted by 4% relative to bulk Ru, similar to bare Ru(0001) [124]. The distance between Pd layers is very close to the value for a slightly compressed Pd layer that we estimated above. Thus, even just two layers of Pd behave as expected for thicker films pseudomorphic with Ru.

For 3 ML the best fit is ABAB/acb , with R_p=0.16. In the same way, for films up to 6 ML Pd, the best fit always corresponds to a fcc stacking sequence. The interlayer spacings are reported in Table 3.2. For all the films, the interlayer spacings of the topmost two layer are not contracted (or very slightly, and well within the error bar) relative to deeper layers. This lack of contraction is similar to previous Pd(111) LEED results [115, 116] that indicated no significant contraction of the last Pd layer, in contrast with other transition metals [117]. To check for possible hydrogen contamination that could potentially remove the last Pd layer contraction [125], we acquired LEED-IV's for a 6 ML Pd film at 480 K. Hydrogen is known to desorb from Pd at temperatures far below 480 K [126]. The interlayer spacing for the first layer was still 2.27 Å.

As a further check on the in-plane lattice spacing of the Pd films, we performed a LEED-IV fit to the data from the 6 ML Pd film varying the in-plane Pd spacing. (The previous fits were all performed at the Ru in-plane spacing). This film is the best candidate for detecting any in-plane

	2 ML Pd/Ru
	ABac
Pd_1Pd_2	2.26±0.02
Pd_2Ru_1	2.22±0.04
Ru_1Ru_2	2.04±0.05
R_p	0.15±0.03

Table 3.1 Structural parameters for the LEED I-V best-fit for 2 ML of Pd on Ru(0001). Interlayer spacings are given in Ångstrom. The subscripts number the Pd layers starting from the surface and the Ru layers starting from the film/substrate interface.

	3 ML Pd/Ru	4 ML Pd/Ru	5 ML Pd/Ru	6 ML Pd/Ru
	ABacb	ABacba	ABacbac	ABacbacb
Pd_1Pd_2	2.29±0.02	2.26±0.03	2.28±0.03	2.27±0.02
Pd_2Pd_3	2.27±0.05	2.28±0.05	2.28±0.05	2.27±0.05
Pd_3Pd_4		2.24±0.06	2.26±0.06	2.28±0.06
R_p	0.16±0.04	0.14±0.03	0.18±0.05	0.17±0.04

Table 3.2 LEED IV best-fit structural results for the interlayer spacing for different Pd areas. All distances are in Ångstrom.

relaxation [1]. As figure 3.5 shows, the fit has a well-defined minimum at about 2.70 Å, close to the in-plane spacing of bulk Ru (2.704 Å) but well-resolved from the spacing of bulk Pd (2.75 Å). Using the LEED patterns and the LEED-IV fits to the experimental data we find that the films grown layer-by-layer are pseudomorphic up to at least six atomic layers.

The ab-initio calculations predict geometries very similar to those determined from the experimental LEED IV data. The lowest energy configuration for 2 to 4 ML Pd on Ru(0001), with the

[1] We have not considered an energy dependence of the real part of the inner potential [127]. In any case, we are not approaching the 0.01 Å error level where such omission gives rise to systematic errors.

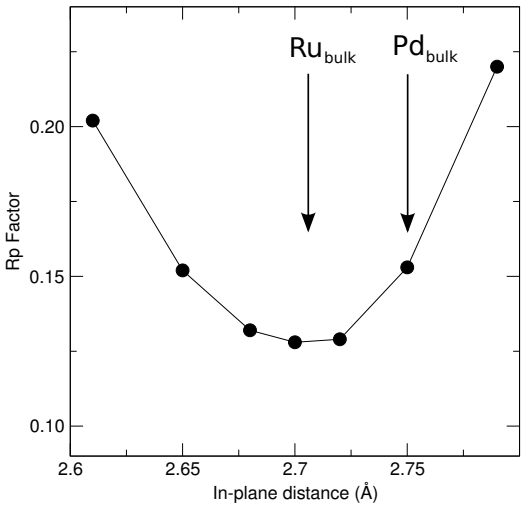

Figure 3.5 Pendry R_p factor describing the fit quality for varying in-plane distance of a 6 ML Pd region on Ru(0001). The lines are a guide to the eye.

in-plane Ru lattice spacing, is a fcc stacking within the Pd layers, with a very small expansion of the last Pd layer. The interlayer distances are presented in Table 3.3. Thus, both experiment and theory lead us to conclude that the last-layer slight expansion of Pd films is not a contamination effect but rather is an intrinsic property of the clean Pd surface.

Even if the layer stacking we detect by LEED-IV is a unique fcc sequence on a single terrace, we next establish that the film has a twinned fcc microstructure due to the substrate. The Ru substrate is hcp, i.e., ABAB, so the exposed basal plane alternates at adjacent terraces separated by monatomic steps. That is, the Ru termination is either A or B. This causes the preferred fcc stacking of the Pd to rotate by 180° across consecutive substrate terraces, giving a LEED pattern that also rotates by 180° [124]. On a ABAB terrace, the Pd stacking sequence as determined by LEED is ABAB/acb . On the adjacent ABABA terraces, the stacking sequence is ABABA/bca (so the Pd first layer is always in a “hcp” sequence relative to the substrate, . The acb and the bca Pd sequences are a mirror image of one another, i.e., twins. Thus, a twin boundary extends from each

	2 ML Pd/Ru	3 ML Pd/Ru	4 ML Pd/Ru
	ABac	ABacb	ABacba
Pd_1Pd_2	2.27	2.29	2.28
Pd_2Pd_3	2.20	2.27	2.27
Pd_3Pd_4		2.21	2.27
Pd_4Pd_5			2.21
PdRu	2.09	2.09	2.09

Table 3.3 Interlayer spacing from DFT calculations for different thickness; distances are in Ångstroms. "PdRu" refers to the the layer separation at the film/substrate interface.

substrate step, through the film, up to its surface.

3.2.3 Stacking faults

A way to directly image the twin microstructure of a Pd film in LEEM is to combine dark-field and bright-field imaging of the same area. Figure 3.6(a) presents a LEEM image from a film with Pd regions that are 6, 7 and 8 ML thick. Each different thickness has a different gray level due to the quantum size effect on the electron reflectivity mentioned before (figure 3.2). Dark-field imaging is sensitive to fcc twins. An bca sequence gives the same diffraction pattern as a acb sequence, but rotated by 180°. So the (01) and (10) beams will be exchanged by going from one twin to the other. If an energy is selected where a three-fold symmetric pattern is observed, as in figure 3.3, then only one set of twins will be observed if the (01) beam is used for dark-field imaging while the other set of twins on the surface will be imaged if the (10) beam is used. This effect can be observed in figure 3.6(c-d).

In contrast, bright-field imaging is not sensitive to the two types of fcc stacking. Figure 3.6(b) provides an example. To reduce the QSE contrast, the image was acquired very close to the for-

bidden gap corresponding to the (222) Bragg reflection, at an energy of 18.5 eV. With the contrast from film thickness minimized, it is easy to see that the twin fcc structures on the different Ru terraces have the same contrast. However, bright-field imaging can be sensitive to stacking mistakes in the Pd film on a given Ru terrace. Figure 3.6(b) shows an example. The only area with a markedly different contrast is the small region of 8 ML Pd marked with an arrow. Such regions occur with very low density. The schematic of figure 3.6(e) presents a model of the stacking fault that makes the region special [2]. As it has a non-fcc structure, its vertical periodicity is different from the fcc areas, and the forbidden gap corresponding to the (0002) hcp structure appears at a different energy than the rest of the fcc film. A similar effect has been observed in Co islands on Ru(0001) [128]. The stacking-fault region also has contrast in the dark-field images. In figure 3.6(c), for example, the region has roughly the same contrast (bright) as the 7 ML Pd on the higher terrace to the immediate left. The similar contrast is explained by the same stacking sequence of the last two layers of the stacking-fault region and of the Pd on the *upper* terrace with a twin fcc structure [see figure 3.6(e)]. One effect observed in the thicker pseudomorphic films is the presence of linear defects, as best seen in the bright-field images in figure 3.6(a-b). These defects are likely the precursor of a dislocated interface layer, or they might even be small film regions with a dislocated interface layer.

In summary, thin films of up to 6 ML Pd on Ru(0001) grown at elevated temperature have the in-plane lattice spacing of Ru(0001). They present a twinned fcc microstructure, where each substrate terrace has a single twin, except for rare stacking faults. The substrate steps are then replicated into twin boundaries, which run through the film. The film's vertical lattice spacing is slightly expanded, as expected due to the in-plane compressive strain. No significant last-layer contraction is detected, in agreement with ab-initio calculations and with previous reports on single-crystal

[2] The stacking-fault schematic shows only the topmost Pd layer being faulted compared to the Pd on the same Ru terrace. The fault can possibly lie deeper into the film.

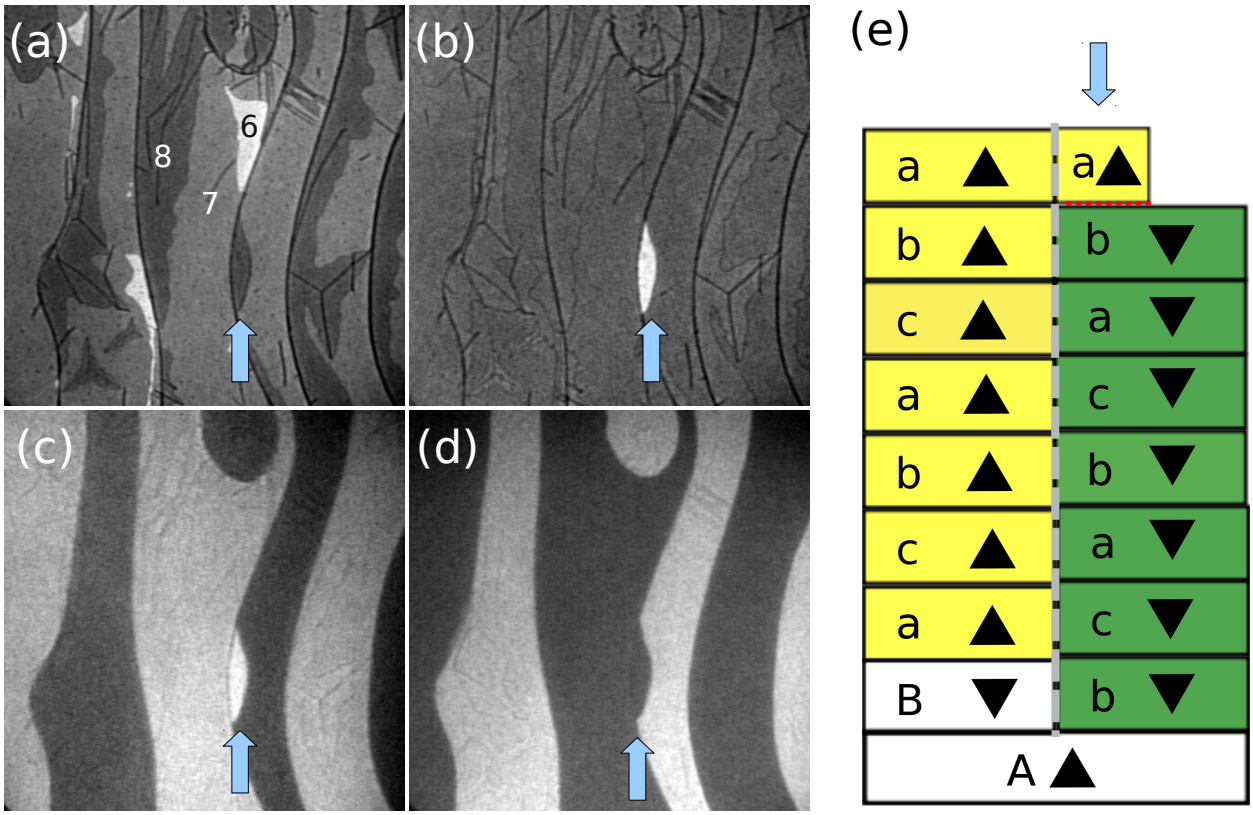

Figure 3.6 Same region imaged for different microscope parameters. Field of view is 10 μm. (a) Bright-field LEEM image of a Pd film with 6, 7 and 8 ML exposed at an electron energy of 6.5 eV. Representative thicknesses are labeled. (b) Bright-field LEEM image at an electron energy of 18.5 eV. (c) Dark-field view image formed from a (10) beam at an electron energy of 39 eV. (d) Dark-field image from a (01) beam at 39 eV. (e) Schematic of the film stacking that gives rise to the observed dark- and bright-field contrast. For discussion see text.

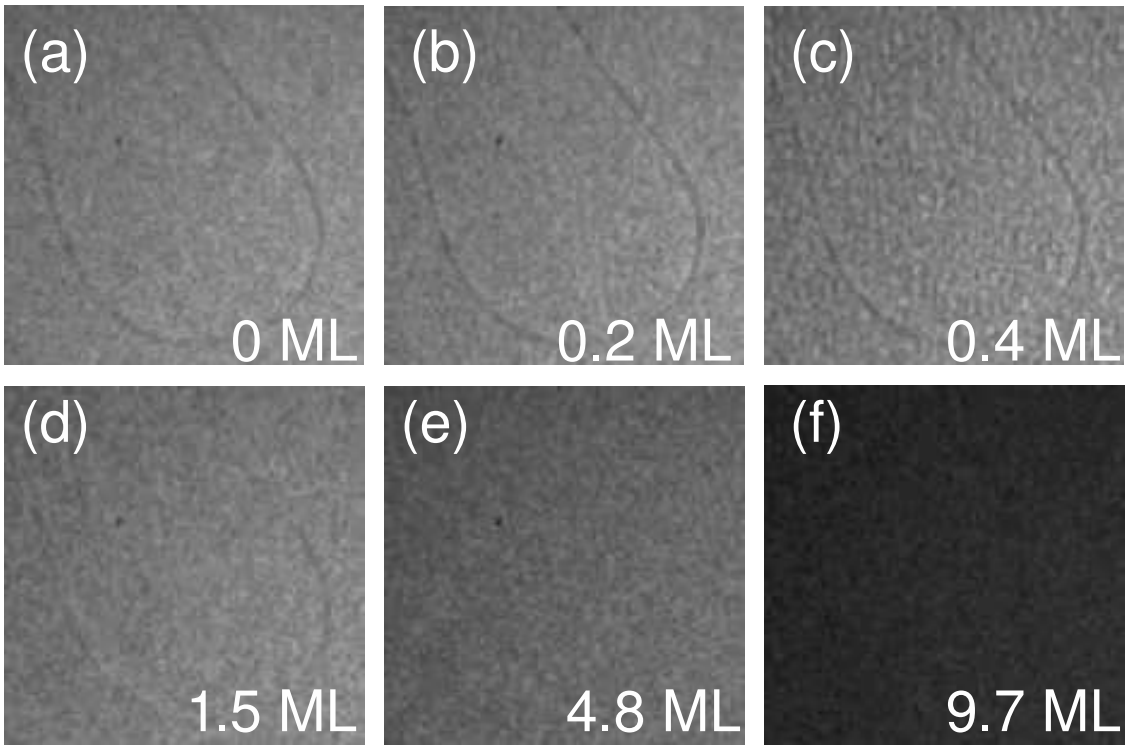

Figure 3.7 LEEM image acquired during initial stage of depositing ∼20 ML Pd on a RT Ru(0001) substrate at a rate of 0.60 ML/min. The image size is 2.25 μm. The same image contrast is used for all the images.

Pd(111) surfaces [115, 116].

3.3 Relaxed Pd films on Ru(0001)

To obtain a surface more akin to a Pd(111) single crystal, ∼20 ML Pd layers were deposited at RT on Ru(0001). The initial stages of the growth are followed in figure 3.7. During dosing up to half a monolayer a granular texture was observed in the LEEM images, which probably results from islands smaller than the in-plane resolution of LEEM (10 nm). With further deposition, the reflected electron intensity gradually decreases due to increased film roughness. This is the same effect observed when Co was deposited on Ru(0001) at RT.

After the growth the film was annealed to 880 K and cooled back to RT while imaging (fig-

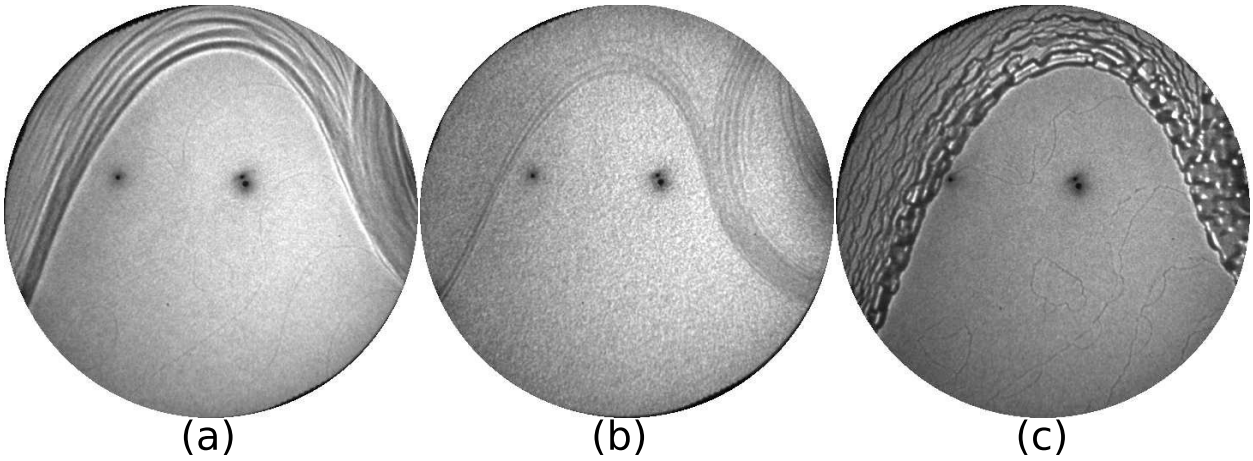

Figure 3.8 LEEM images of the same area: (a) before Pd growth at RT, (b) after ∼20 ML Pd growth at RT and, (c) after annealing to 890 K. The image size is 14.5 μm.

ure 3.8). At the end of the procedure the surface of the film is quite flat, having monatomic Pd steps separated by nearly a micrometer.

3.3.1 LEED IV

As the film is continuous, the diffracting electrons do not see the Ru substrate. Thus, the LEED patterns only provide information for the topmost Pd layers. If acquired on a single substrate terrace, the pattern is still three-fold symmetric, as shown in figure 3.9(a). In the LEED IV fits, all the models with the three different possible stacking of hexagonal layers of Pd where first explored, initially with a Pd-bulk in-plane lattice spacing. The best fit is an acb termination, with a R-factor R_p =0.12. (The other models yielded $R_p > 0.60$). The structural parameters are shown in the Table 3.4. The first interlayer spacing shows again a very small expansion, with 2.26 Å (within the error bars of the bulk value of 2.24 Å). This is the same result that was previously reported by Van Hove et. al [115, 116] for a Pd(111) single-crystal surface.

The in-plane lattice spacing of the thick, annealed Pd film was determined by finding the value in the multiple-scattering calculations that best fit the experimental LEED-IV curves. Figure 3.10

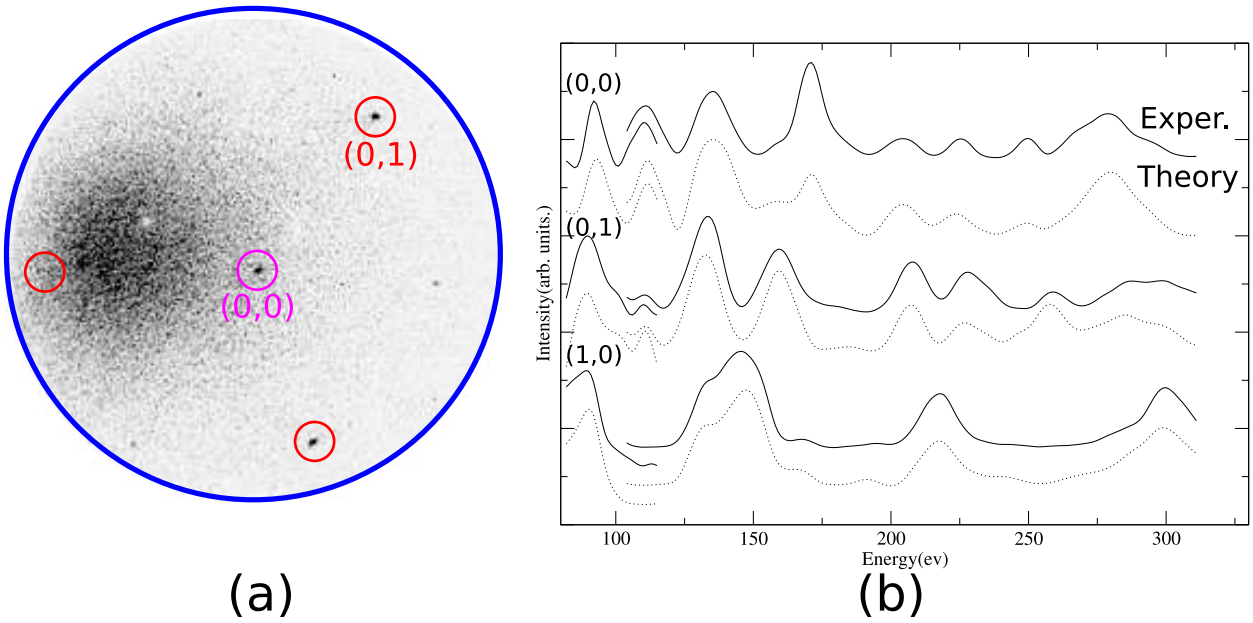

Figure 3.9 (a) LEED pattern of thick ∼20 ML Pd film on Ru(0001) at 53 eV, acquired from a single Ru terrace. Note the three-fold symmetry. (b) Experimental LEED-IV curves and best fits

shows that the Pendry R_p factor is optimized at about 2.75 Å i.e. the value for bulk Pd within the error limits of the fits. Thus, the thick film is relaxed in-plane, unlike the thinner films grown at elevated temperature, which had the Ru in-plane spacing (about 2.704 Å).

3.3.2 Stacking faults

After the annealing some of the surface film steps are located at positions close to the substrate steps. This observation is revealed by comparing the location of the bare Ru steps [the thin, dark lines in figure 3.11(a)] and the Pd steps [the thin, dark lines in figure 3.11(b)]. In addition, new Pd steps are located at other locations of the surface. It was interesting to see the conformal nature of the film, with many of its steps nearly over substrate steps through 20 film layers.

Twin structures are still expected in the thick film since the two twin-related fcc stacking sequences of Pd layers have the same energy. To check for their presence dark-field LEEM im-

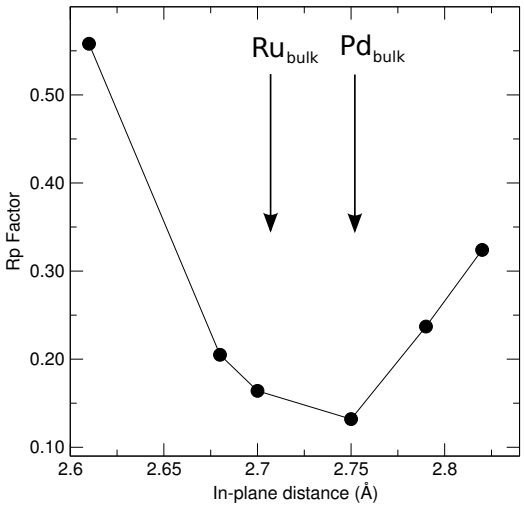

Figure 3.10 Pendry R_p factor describing the fit quality of a thick ∼20 ML annealed Pd film on Ru(0001) for varying in-plane distance.

ages were acquired at the same location as the bright-field images of figure 3.11(a) and (b). Figure 3.11(d) shows dark-field LEEM images acquired with two different energies. Inspection shows that the regions of bright/dark contrast uniquely correspond to Ru terraces separated by monoatomic Ru steps. Thus, like the thinner films, the thick film also has a single unique stacking of Pd layers on each Ru terrace. Substrate steps are replicated into the film as twin boundaries. While the substrate steps were smooth, the twin boundaries are more jagged, probably because they have lower energy for selected orientations. The observation that the underlying substrate terraces still dictates the twin distribution is surprising for two reasons. First, small twins within a single Ru terrace might be expected to form when growing the film at low temperature. Second, as the films relax to the in-plane lattice spacing, a network of lattice dislocations near the film/substrate interface should develop. This network adapts the lattice spacing of the substrate to the lattice spacing of the film. A misfit dislocation network would be expected to decouple the stacking sequence of the Ru substrate and the Pd film. Yet, after annealing, each Ru terrace has a

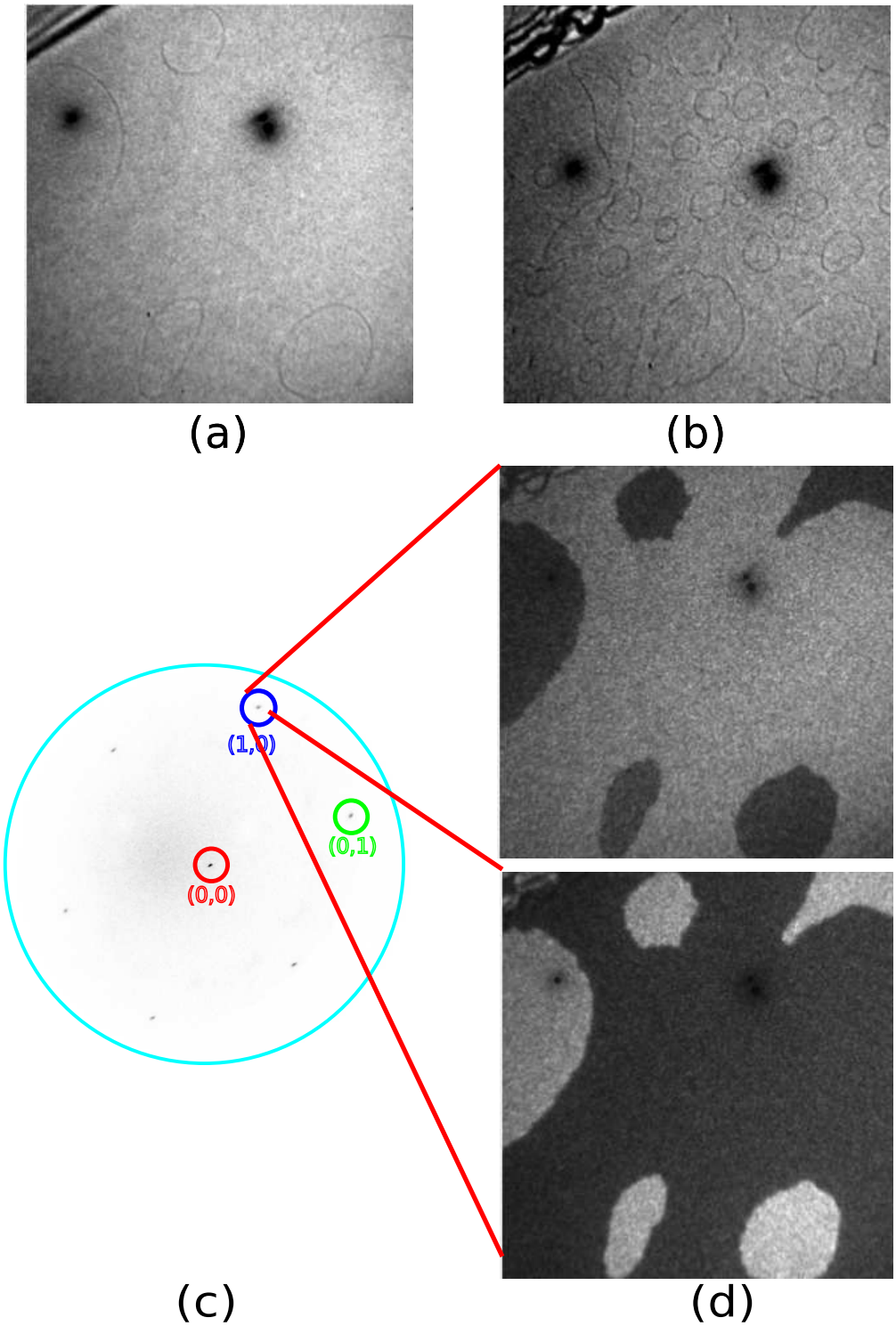

Figure 3.11 (a) LEEM image of the Ru(0001) substrate before Pd deposition. The image size is 8.9 μm. (b) LEEM image after depositing ~20 ML of Pd and annealing. (c) LEED pattern of a single substrate terrace. (d) Dark-field LEEM images of the same area taken with the (10) spot using two different energies that reverse the contrast (upper, 29.3 eV and lower, 42.5 eV).

	∼20 ML Pd/Ru
	acb
Pd_1Pd_2	2.26±0.02
Pd_2Pd_3	2.22±0.04
Pd_3Pd_4	2.26±0.05
R_p	0.12±0.02

Table 3.4 Interlayer spacing and stacking sequence of a uniform thickness region of a ∼20 ML Pd film on Ru(0001), as determined from the best LEED-IV fit. Distances are in Angstroms.

single, unique stacking of Pd layers.

The film is too thick to show in LEED any sign of such a dislocation network. This in turn leaves open the question of whether the dislocation network adapts the lattice spacing abruptly at the Pd/Ru interface, as has been observed for Cu/Ru(0001) [129] and Co/Ru(0001) [128], or through a layer of intermediate density, like in Ag/Ru(0001) [130]. The latter is more probable given that Pd/Ru is under compressive stress like Ag/Ru(0001) [130]. Further work, likely with information provided by scanning tunneling microscopy, is needed to address the structure of the relaxed Pd/Ru(0001) interface.

In a summary, thick films grown at RT and annealed present an in-plane lattice spacing very close to bulk-Pd. The behavior of the last layer expansion agrees well with the results for Pd(111) single crystals [115, 116], which have few fcc twins. In contrast, Pd films on Ru have very high densities of fcc twins: each substrate step has a twin boundary above it, which separates fcc twins on adjacent substrate terraces. The abundance of twins merits further study regarding their possible influence on Pd ferromagnetism [110], especially given the relaxed in-plane spacing of these films.

3.4 Relaxed Pd films on W(110)

W(110), the most compact surface of bcc tungsten that consequently usually presents the largest terraces [131], has often been used for Pd growth [132–134]. The growth is known to proceed through an interface layer with a complex arrangement [132] that acts as buffer between the (110) bcc and the (111) fcc structures of W and Pd, respectively. Attempting to grow thicker films layer-by-layer will produce 3D islands on top of the interface layer. In order to obtain continuous films, we follow the same recipe as for thick Pd films on Ru(0001): depositing Pd at RT, followed by a brief annealing to 880 K.

Figure 6.5(a) shows the LEED pattern acquired from the area of a 20 ML film circled in figure 6.5(b). The LEED pattern is six-fold symmetric. The LEEM images are dominated by wide, diffuse dark lines that form closed loops. They do not show any clear relationship with the pre-existing substrate steps. They also look thicker than the Pd steps observed on Ru(0001) [see figure 3.11(b)] and present a high curvature. We used dark-field imaging to identify the origin of these lines. A dark-field image from the same area, figure 6.5(c), exhibits bright and dark regions, which result from fcc twins. The contrast is reversed at a different electron energy [figure 6.5(d)]. Inspection of figure 6.5 shows that the wide lines of the bright-field image are the boundaries between fcc twins in the dark-field images. Higher temperature annealing led to larger twin domains. Thus, Pd films on both W(110) and Ru(0001) contain high twin densities.

The twins also explain the six-fold symmetry of the LEED pattern in figure 6.5(a) – the selected area contains both twin types. To perform a multiple-scattering calculation fit, the LEED IV curves were acquired from the full area of figure 6.5(b). The (10) and (01) beams, shown in figure 3.13, are very similar, indicating that the two twin structures have similar abundance. The fit was performed by averaging incoherently the two twin-fcc stacking sequences, with their ratio as a free parameter. The best fit (R_p =0.13) yields a relative twin population of 40$\pm$20% in the film. For comparison, the ratio observed in dark-field LEEM images is $\approx$55%, in good agreement with the estimate from

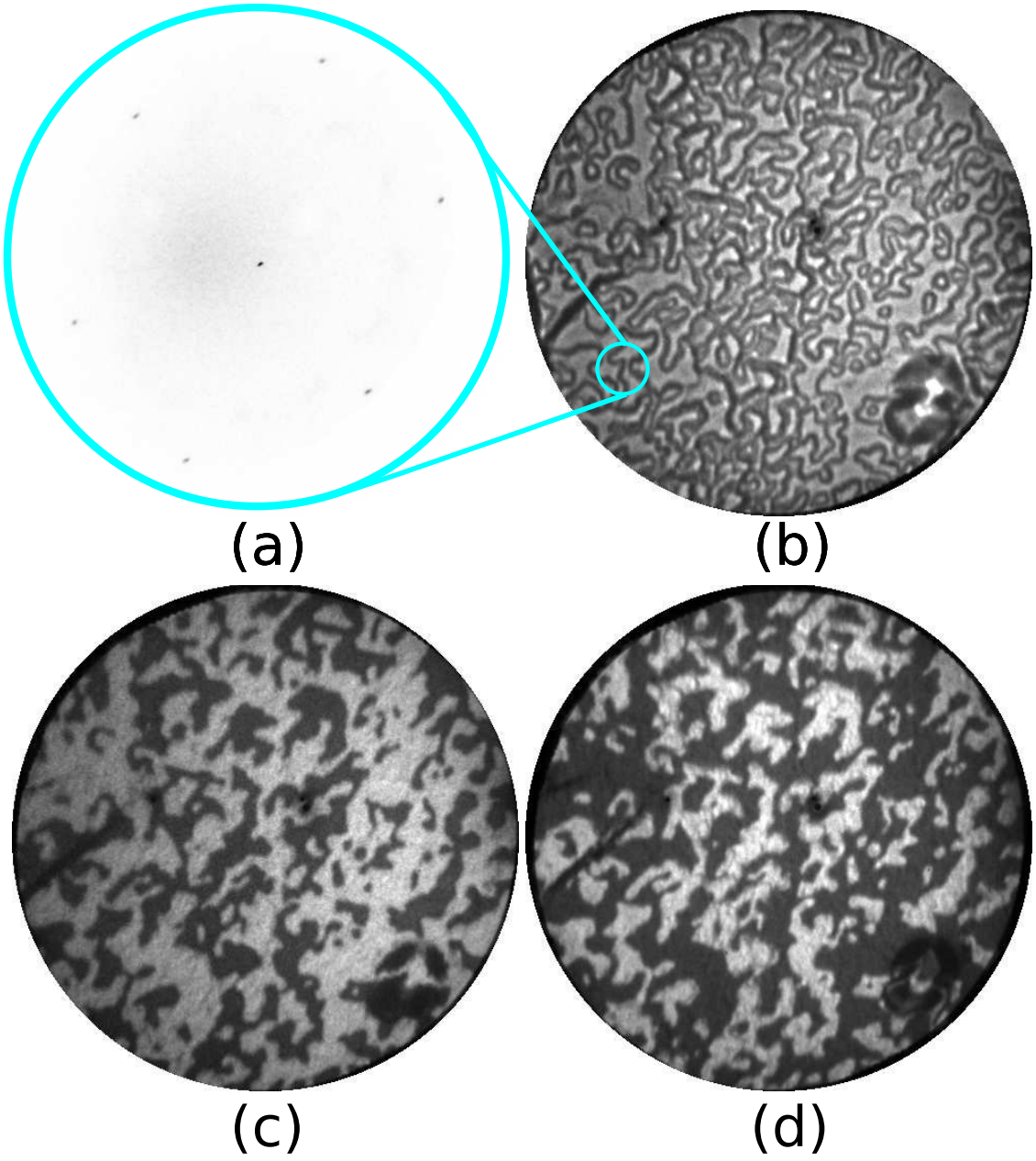

Figure 3.12 Characterization of thick (∼20 ML) Pd film on W(110). (a) LEED pattern. (b) 7μm LEEM image. (c-d) Dark field images of the same region formed from the (1,0) beam at 58.5 eV and 67.3 eV.

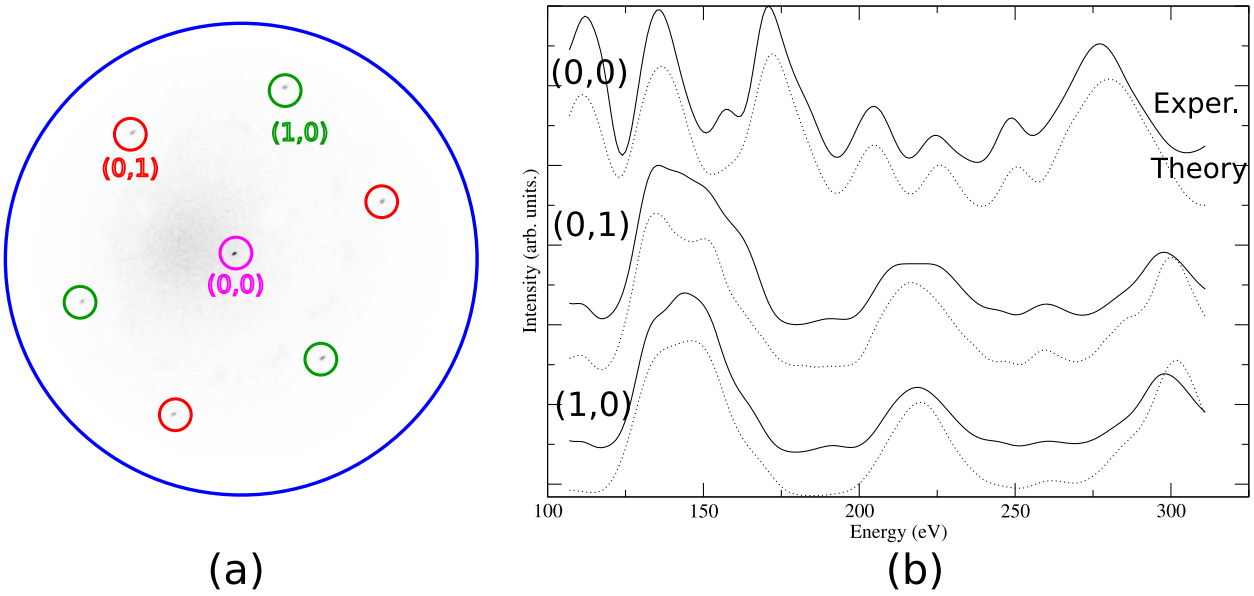

Figure 3.13 (a) LEED pattern of thick Pd film on W(110) at 53 eV. Note the six-fold symmetry. (b) LEED IV data and best fits.

the LEED-IV data. The structural parameters for the fit are shown in Table 3.5. The interlayer spacing of the two topmost layers, 2.25±0.03 Å, presents a slight expansion (+0.5% compared with bulk Pd interlayer spacing, and within the error limits of no expansion), in line with single-crystal Pd(111) [115, 116] or the films on Ru(0001) presented previously (see tables 3.2 and 3.4).

The distribution of twins, as shown in the schematic of figure 3.14(c), can be explained by considering the nucleation of Pd islands on top of the Pd interface layer. The difference in structure between the interface layer and the subsequent hexagonal layers is so large that the nucleation of the two types of twins is essentially random (a similar behavior has been reported for other close-packed metals on W(110), such as Dy or Er [135]). During the initial RT growth, there is a 50% probability of growing one twin or the other. When the film is later annealed there is a fine distribution of small twins all over the film. The annealing makes the twins coarsen, driven by minimizing the length of twin boundary. (The twins themselves have the same energy.) This is in contrast with the case of the Pd films on Ru(0001), where the two types of substrate terraces

	20 ML Pd/W
	acb+abc
Pd_1Pd_2	2.25±0.03
Pd_2Pd_3	2.20±0.06
Pd_3Pd_4	2.24±0.07
R_p	0.13±0.03

Table 3.5 Structural parameters for the best LEED IV fit to the ∼20 ML Pd film on W(110).

provides a preference for one type of twin. In Pd/W(110) the twin distribution evolves very slowly giving rise to the observed microstructure.

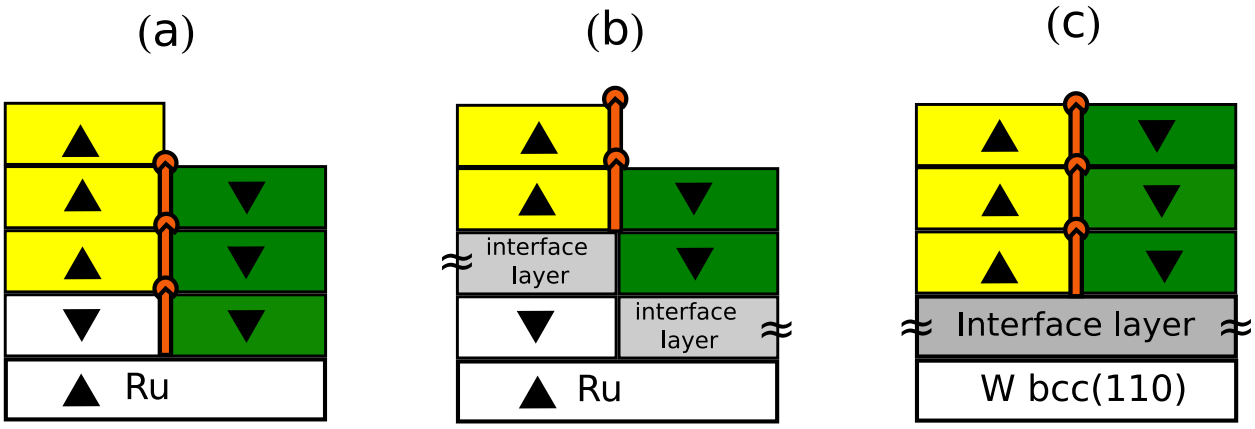

Figure 3.14 Schematics of the film microstructures. (a) Pseudomorphic Pd films on Ru(0001). The red line represents a planar twin boundary that starts at the substrate step and runs through the film. (b) Relaxed Pd films on Ru(0001). (c) Relaxed Pd films on W(110).

3.5 Conclusions

We have grown and characterized ultra-thin films of Pd on Ru(0001) and W(110). The structure of the different films is summarized in figure 3.14. By depositing Pd on Ru(0001) at elevated temperatures, pseudomorphic films can be grown to thicknesses of at least 6 ML. The Pd microstructure replicates the Ru substrate, with an fcc twin on each substrate terrace. Twin boundaries extend from the substrate steps to the film surface. The separation of the topmost Pd layers of each pseudomorphic film is essentially the bulk value. This lack of interlayer contraction is different than the behavior of other transition metal surfaces and does not result from hydrogen adsorption. Thicker films ($\sim$20 ML) were grown at RT and post annealed, both on Ru(0001) and W(110). This procedure provides films with their in-plane spacing relaxed to the bulk Pd value. The microstructure of thick films on Ru is similar to the thin, pseudomorphic films: a single twin is detected on each substrate terrace, despite the presumed presence of a misfit dislocation network at the Pd/Ru interface. Again the twin boundaries of the film replicate the step distribution of the substrate. On the other hand, films grown on W(110) present interlocked twins that are difficult to coarsen, and whose distribution has little relation to the substrate steps.

These results indicate that Pd(111) films on Ru(0001) and W(110) are a rich system where the number and location of twin boundaries can be modified or even selected by a proper substrate nanostructuring. We look forward to further studies of the magnetic and chemical properties of these films, specially given the predicted influence of twin boundaries on the magnetic properties of Pd(111) surfaces [110].

Chapter 4

Hydrogen on Pd films

4.1 Introduction

The interaction of hydrogen and the Pd(111) surface has been a model system of gas-solid interactions since the start of modern surface science [136, 137]. Hydrogen readily adsorbs dissociatively on Pd(111) [1] at temperatures as low as 65 K [138]. But the system's true importance comes from how readily H incorporates into the Pd bulk [116, 139, 140]. At low concentrations, H occupies bulk octahedral sites as a solid solution, the α phase [141]. The hydride PdH, the β phase with a rock-salt structure, forms by a first-order phase transition at high concentrations [142]. These attributes enable important applications for the storage and purification of hydrogen and catalysis.

One incompletely answered question is the precise location of sub-surface H in Pd. This H is believed to participate directly in catalytic reactions [143, 144]. The distribution of the absorbed H between the near surface and the bulk is known to depend strongly on the absorption temperature [139, 145]. H binds more strongly to the Pd(111) surface than to the bulk, where theory indicates that H is most strongly bonded between the topmost two Pd layers and is less strongly bonded between the second and third layers [146–148]. Indeed, some experimental evidence suggests that

the absorbed H preferentially resides between the topmost two Pd layers [116, 140, 149]. Getting the direct structural characterization needed to answer the location question has challenged surface science for several reasons. First, as we have mentioned before, hydrogen is difficult to detect by the usual surface probes. Second, the pressure limitations of traditional ultrahigh vacuum (UHV) systems hinder achieving significant H concentrations in macroscopic Pd specimens, particularly since the sticking coefficient of hydrogen on Pd(111) decreases many orders of magnitude when the coverage approaches saturation [138, 150]. One way to overcome this problem is using atomic hydrogen, as the energy of an incident H atom is higher than any expected barrier to absorption [11, 149].

Another approach to increase H concentration is to limit the sample volume using ultra-thin Pd films. But this approach is not necessarily straightforward because the literature suggests that reduced dimensionality can significantly affect H absorption. As Pd grains are reduced to nanoscale dimensions, the hydrogen miscibility gap decreases [151]. In thin films, the temperature at which the α and β phases become indistinguishable, the critical temperature, has been reported to decrease dramatically with decreasing film thickness [152]. However, in other cases no significant effect has been observed [150]. As in bulk specimens, there is also much debate about reduced-size effects on the sub-surface H populations in ultra-thin films [21]. Reducing Pd consumption or engineering chemical/mechanical properties by replacing bulk Pd with thin films or nanoparticles also requires understanding reduced dimensionality.

The final aim of this chapter is to understand how carbon monoxide affects the interaction of H with Pd(111). The combination of H plus CO is relevant to gas sensors, superconductivity [153], energy storage and heterogeneous catalysis [144, 154–156]. In fact, CO can block H sorption and desorption [126, 157] and also changes the barrier to H_2 dissociation [158, 159]. Furthermore, CO has been convincingly demonstrated to displace adsorbed H on Pd(111), driving the H below the surface [159–162]. Here we address the question of the location of the displaced, sub-surface

hydrogen.

As explained in the previous sections we have used the techniques available in a low-energy electron microscope (LEEM) [61, 163] to study the incorporation of molecular and atomic H into thin Pd films with and without CO co-adsorption. From the quantitative analysis of low-energy electron diffraction (LEED) data, we have measured the expansion of the near-surface Pd layers caused by H sorption [21, 116, 136]. Even though the giving the difficulty to locate H directly by diffraction methods [164], we have used the measured interlayer Pd spacings, as validated by first-principles calculations, to infer the location of sorbed H. Exposing Pd films at 170 K to large doses of molecular and atomic hydrogen yields adsorbed H but no detectable sub-surface H. Co-dosing with CO and atomic H leads to a CO-covered surface. Based on the expansion of the topmost two Pd layers, we have concluded that the H displaced into the sub-surface by the CO is concentrated between the topmost two Pd layers. We have used the strong dependence of low-energy electron reflectivity on adsorbate identity and concentration to image adsorbed H being displaced by adsorbing CO.

4.2 Effects of molecular hydrogen

Figure 4.1 (a) shows a typical LEEM image of a 6 ML Pd film on Ru(0001) after growth and before H dosing. The dark curved lines result from steps and step bunches in the substrate. The three different film thicknesses present, 5, 6 and 7 ML, each have a different contrast due to the dependence of the reflected electron intensity on film thickness [165, 166]. At 10 eV, figure 4.1 (b), the different thicknesses have less contrast. Figure 4.1 (c) shows the film for this imaging condition after exposure at 170 K to 10^{-6} Torr of molecular hydrogen for 20 minutes, a total dose of 9 KL_{H_2}. Being one Langmuir (1L) the dose exposure of a surface to a gas pressure of 10^{-6} torr for one second. Outside of an overall intensity change described below, dosing H_2 did not

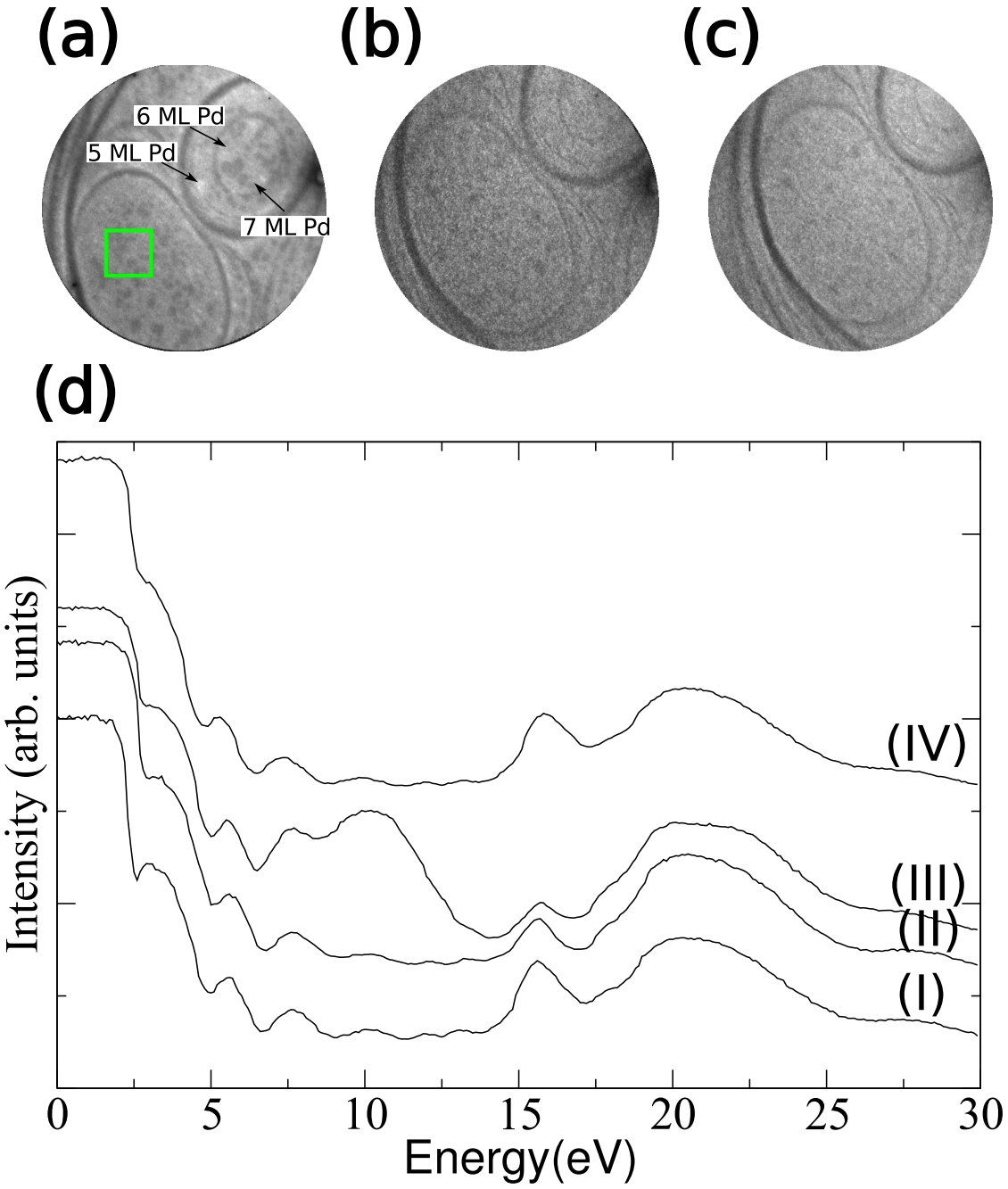

Figure 4.1 (a)–(c) LEEM images of a pseudomorphic 6 ML Pd/Ru(0001) film, with a field of view (FOV) of 9.3 μm. (a) Clean film at 5.3 eV with Pd thicknesses marked. The area whose reflected intensity is marked with a green box. (b) & (c) LEEM images at 10 eV before and after dosing 9 KL_{H_2}, respectively. (d) Low-energy electron reflectivity (I) clean film at room temperature, (II) clean films at 170 K, (III), after hydrogen dosing, (IV) and after heating the sample to 464 K. The curves have been offset for clarity.

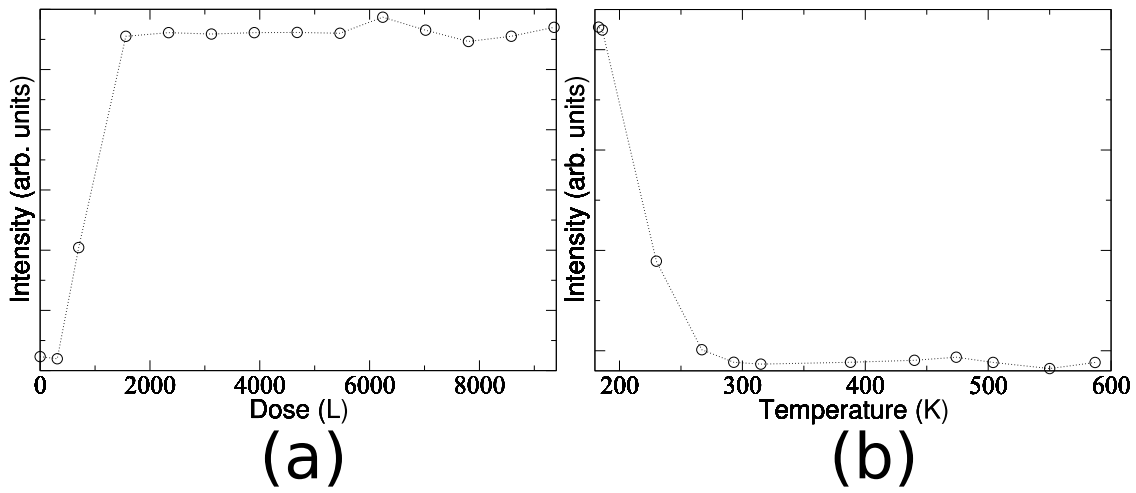

Figure 4.2 Intensity of 10 eV electrons reflected from a single substrate terrace of a 6 ML Pd film (see figure 4.1). (a) Reflectivity change while dosing H_2. (b) Reflectivity change while desorbing H.

noticeably change the images.

Figure 4.1 (d) shows how the intensity of electrons reflected from the area marked by the green box in figure 4.1 (a) changes with electron energy. The lowest curve corresponds to the reflectivity of the bare (clean) Pd film. When their electron energy is below the vacuum level of the sample, electrons are reflected before reaching the surface, giving the maximum reflected intensity. Images acquired in this energy range correspond to so-called mirror-mode microscopy [61]. At slightly over 2.5 eV, the intensity decreases and then oscillates several times due to the formation of quantum well states in the unoccupied band structure of the film [165, 166]. There is a sharp feature at 15.4 eV and a broad peak at 21 eV. The latter is attributed to the band gap formed by the (222) Bragg reflection of Pd [167]. The former is characteristic not only of Pd(111) but also of other fcc (111) metals [167]. It has been attributed to a band-crossing gap in the unoccupied bulk band structure although other explanations have been proposed [122, 123].

The reflected intensity increases between 8–11 eV after dosing molecular H, (see curve III in figure 4.1 (d)). Figure 4.2 (a) plots the intensity at 10 eV as a function of H_2 exposure. The feature

clearly saturates, although the time resolution was inadequate to determine if the saturation occurs at the exposure expected to saturate the Pd(111) with H, a few Langmuir [168]. The electron reflectivity increase around 8–11 eV is consistent with the results of Pfnür et al. [169, 170] for H on Ru(0001). Their theoretical calculations suggested that the increased reflectivity resulted from H adsorption removing a surface state.

Heating removes the 8–11 eV spectral feature, returning the reflectivity spectrum to its pre-dosing state (see top spectra in figure 4.1(d)). As a further check on the origin of the spectral feature, we have monitored the intensity during heating. Figure 4.2 (b) shows that the spectral feature vanishes at about $\sim$270 K. Given our slow heating rate, this temperature agrees reasonably well with the literature value of 295 K [116, 140] for the temperature needed to desorb adsorbed H.

In a separate experiment we have monitored the LEED pattern while dosing H_2. The LEED pattern remained unchanged, with no changes in spot positions and no new spots after 9 KL_{H_2}. We have evaluated whether H penetrated into the sub-surface using LEED-IV. The best-fits of the data indicate no change in the stacking of the Pd layers and only a 1% expansion between the topmost two Pd layers, to 2.30$\pm$0.03 Å (with a R_p=0.17) for the case of 6 ML of Pd on Ru(0001), no expansion was detected in deeper layers in this case the interlayer spacing for second and third layer was d_{23}=2.28$\pm$0.06 Å. for the third and fourth layers was d_{34}=2.27$\pm$0.02 Å. comparing this result with the bare 6 ML Pd film value where the interlayer spacing for the first layer is 2.27$\pm$0.02 Å. figure 4.3 shows the best LEED-IV fit and a schematic of the model used. We have observed the same relative results for films up to 20 ML. These changes are much smaller than the expansion expected for PdH formation, which has been predicted and measured experimentally to be close to 3% [150]. Thus, the observed expansion is unlikely the result of significant sub-surface H or hydride formation.

To explore the origin of the observed last-layer expansion of Pd, first-principles calculations

	2 ML	3 ML	4 ML
Stacking	BA/bcα	BA/bcaβ	BA/bcabγ
Pd_1Pd_2	2.32	2.31	2.30
Pd_2Pd_3	2.24	2.29	2.29
Pd_3Pd_4		2.22	2.28
Pd_4Pd_5			2.22
Ru_1Ru_2	2.09	2.09	2.09

Table 4.1 Interlayer spacing in angstroms from DFT calculations with a complete hydrogen layer adsorbed on Pd films 2, 3 and 4 ML thick on Ru(0001). The symbols give the lowest-energy stacking sequence of the layers. The a,b,c labels indicate the three possible stackings of the close-packed layers, with uppercase for the Ru layers and lowercase for the Pd layers [166].The Greek letters indicate the H positions, being α position a,β position b and γ position c.

evaluated adsorbed H on Pd films on Ru. The calculations predict that a complete layer (1x1) of hydrogen in fcc hollow sites expands the last interlayer palladium distance by $\approx$1%, the same as in experiment. Table 4.1 shows the results for 2, 3 and 4 ML of Pd on Ru. This consistency gives us confidence that the small surface expansions observed result from adsorbed H.

In summary, exposing 2–20 ML Pd films on Ru(0001) at 170 K to 10 KL_{H_2} of H_2 increases the electron reflectivity between 8–11 eV and causes the separation between the topmost two Pd layers to increase by a small amount, $\sim$1%. Deeper layers exhibit no measurable expansion. These results, together with first-principles calculations, are consistently interpreted as H adsorption without significantly populating sub-surface hydrogen or forming near-surface PdH. Indeed, extrapolating the bulk phase diagram to 10^{-6} Torr and 200 K gives a H concentration of $\sim$1% [157], below our LEED-IV detection limit. We note that the change in reflected intensity around 8–11 eV can be used as a fingerprint of adsorbed hydrogen, as initially proposed by Schmid et al. [171]. After a straightforward calibration, the approach would yield spatial maps of the adsorbed hydrogen

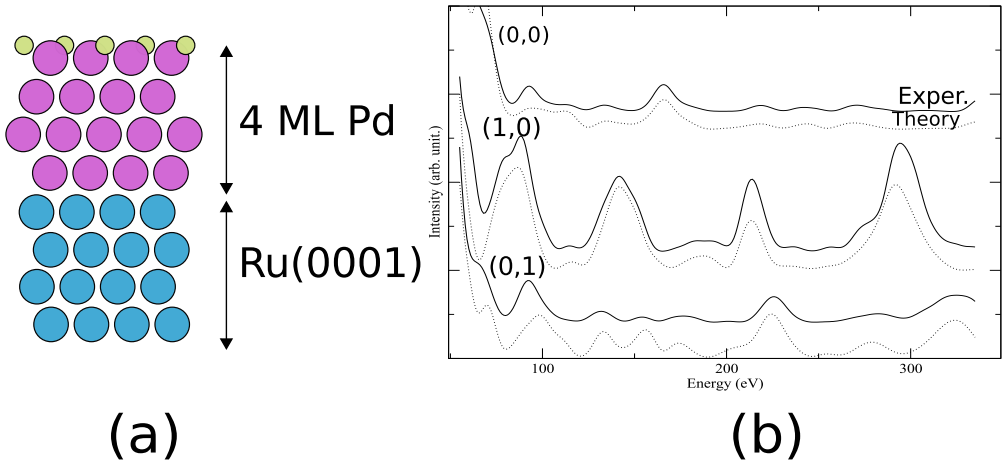

Figure 4.3 (a) Schematic of the slab employed for the ab-initio calculation of the Pd interlayer separations with adsorbed hydrogen. (b) LEED-IV experimental data and best-fits to multiple-scattering calculations of a 6 ML Pd film exposed to 9 kL_{H_2} .

concentration, as recently done for carbon adatoms on Ru(0001) [172]. Here we found no spatial variations in the adsorbed H, confirming the 2-dimensional gas behaviour expected for ready dissociation [1, 138] and high surface mobility.

4.3 Effects of atomic hydrogen

Using atomic H is an approach to overcoming the limits of dosing molecular H in UHV conditions. Atomic H has been used successfully to produce interstitial H in metals such as Ni that have significant barriers to absorption [11]. Here we explore whether atomic H can introduce significant H concentrations into ultra-thin Pd films.

Figure 4.4 (a) shows a LEEM image acquired after the growth of 6 ML Pd film on Ru(0001). At 6.6 eV we observe zones with different contrast due to the the presence of three different film thicknesses, light-grey areas correspond to Pd film 5 ML thick, the majority dark-grey areas corresponds to Pd film 6 ML thick, finally, areas that show a black contrast correspond to islands 7 ML thick. Figure 4.4 (b) shows a LEEM image of the sample acquired at 10 eV before atomic hydrogen exposure. At this energy, the areas of the film with different thicknesses present less contrast however it is still possible to distinguish between them. Figure 4.4 (c) shows a LEEM image after dosing 5x10^{-6} Torr H_H for 5 minutes, for a total dose of 3.2 KL_H at 170 K. After atomic hydrogen dose, LEEM images again show only a uniform change in electron reflectivity at selected energies. Figure 4.4 (d) shows the low energy electron reflectivity (acquired on the area marked in (a)) acquired on the bare Pd surface (curve I) and the low energy electron reflectivity acquired on the same area after 3.2 KL_H. Comparing both curves I and II, we observe the same effect that was obtained when dosing molecular hydrogen i.e. 3.2 L_H atomic hydrogen only gives an intensity increase around 8–11 eV.

To check for H incorporation into the film, LEED-IV data was acquired after the atomic H

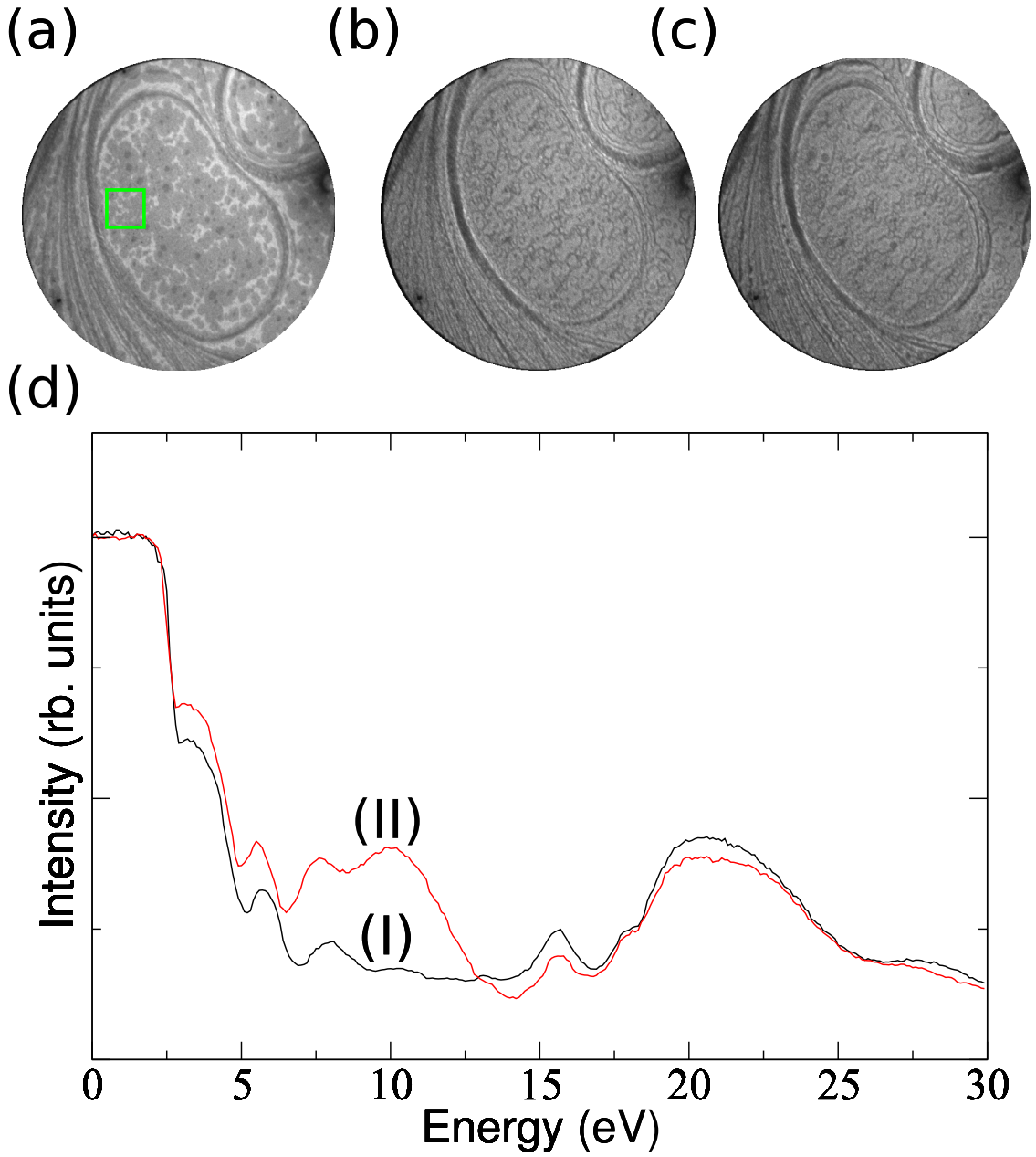

Figure 4.4 (a)–(c) LEEM images of a 6 ML Pd film. The field of view is 9.3 μm. (a) Bare film at an electron energy of 6.6 eV. The green box marks the area used to measure the reflected electron intensity in (d). (b), (c) Images at 10 eV acquired before and after the dose, respectively, of 3.2 kL_H at 170 K. d) Low-energy electron reflectivity (I, black) before and (II, red) after atomic H exposure.

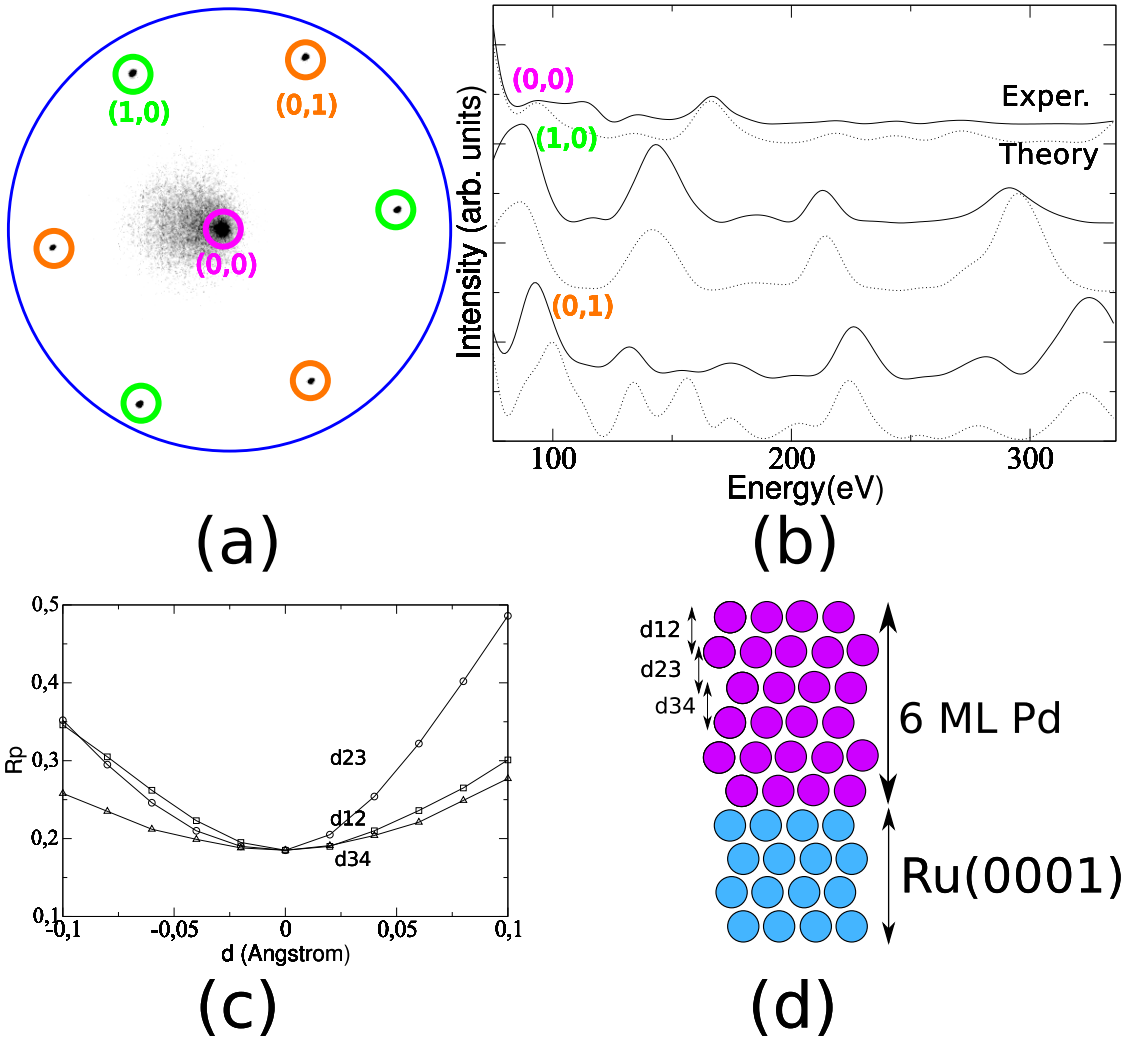

Figure 4.5 (a) LEED pattern of a 6 ML Pd film on Ru(0001). (b) LEED-IV and best-fit multiple scattering calculation for the 6 ML film of Pd/Ru after exposure to 3kL of atomic hydrogen. (c) $\triangle$Rp vs. variation of the interlayer spacing for each Pd layer d_{12}, d_{23}, d_{34}, for a fixed in-plane lattice parameter, where d=0 is the minimum interlayer spacing found in the LEED-IV fit. (d) Schematic of the slab used for the multiple scattering calculations.

dose. A representative LEED pattern, the IV curves and their fits are shown in figure 4.5. The best-fit of the multiple-scattering calculations to the experimental data yields an expansion of the last layer to 2.30 ± 0.03 Å (R_p=0.20), the same value as for molecular hydrogen. This result shows that does not result in a measurable concentration of sub-surface H.

That sub-surface H cannot be detected at all after substantial exposure to atomic H is unexpected. It might be related to either substrate or clamping effects in our thin films. We find no change in the morphology of the films after H dosing. A similar lack of evidence of H incorporation (studied by structural techniques) has been reported for a Pd bilayer on Pt when H was loaded by electrochemical methods [21].

4.4 Effects of atomic hydrogen and CO

Our study of the influence of the simultaneous presence of CO on the adsorption of hydrogen on Pd was motivated by the results obtained when Pd films were exposed to very large hydrogen doses. Even after rigorous cleaning methods, we found that these large doses led to CO adsorption, a well-known problem with H crackers[1]. As we show below, co-dosing atomic H and CO leads to significant concentrations of sub-surface H. Before reporting this finding, we show how CO alone affects Pd interlayer separations and electron reflectivity. We then show how we can use the latter to image CO displacing adsorbed H.

4.4.1 Effects of CO

CO on Pd(111) presents many ordered structures as a function of coverage and temperature [174]. For coverages between 0.5 and 0.66 ML, a c(4x2) diffraction pattern is observed. For coverages

[1] We made large efforts to minimize the CO contamination, including thoroughly degassing the hydrogen cracker and filtering the H_2 through a Pd foil acting as a semi-permeable membrane [173]

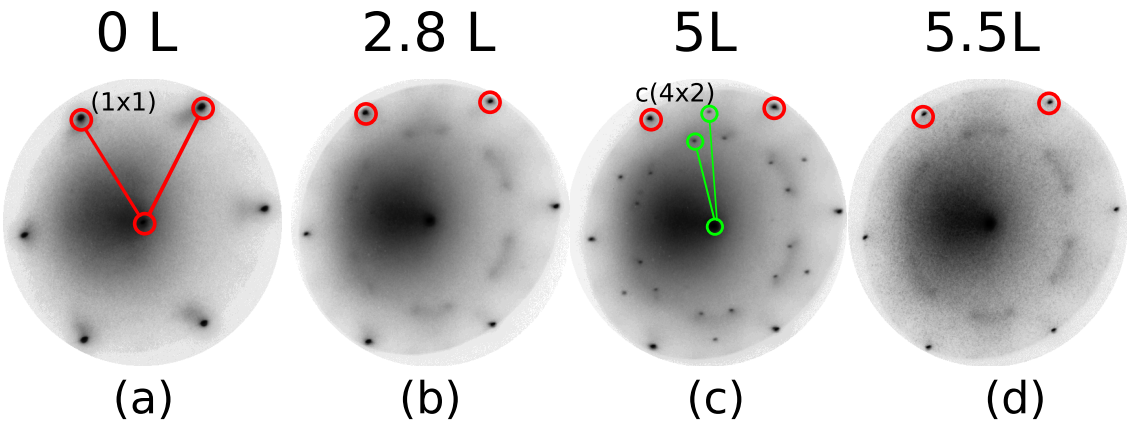

Figure 4.6 LEED patterns acquired at 32 eV while dosing CO on a 6 ML Pd film on Ru(0001) at 170 K. (a) Bare Pd film, (b) after 2.8 L_{CO}, (c) after 5 L_{CO}, and (d) 14 minutes after the CO dose. The first-order Pd spots are marked with red circles. Green circles in c) mark c(4x2) spots.

above $\geq$0.66 a (2x2) pattern [174] is observed. Figure 4.6 shows how LEED from a 6 ML Pd/Ru film evolved while CO was dosed at 170 K. Figure 4.6(a) shows the 1x1 pattern of the clean film. Dosing first gives a faint superstructure arc, as seen in figure 4.6(b). Dosing to 5 L_{CO} gives the distinctive c(4x2) pattern shown in figure 4.6(c), indicating a CO coverage between 0.5 and 0.55 ML [174]. The CO valve was then closed, as the CO is slowly pumped from the chamber, the CO adsoprtion continued for a few minutes. The c(4x2) LEED pattern transformed into a blurry arc pattern shown in figure 4.6(d). Our interpretation is that the new pattern obtained is coverage intermediate to the next ordered overlayer. Dosing more CO after the arc pattern forms does not restore the c(4x2) LEED pattern [126].

Low-energy reflectivity data extracted from real-space images acquired from the same film are shown in figure 4.7. The lowest curve corresponds to the bare Pd film. The reflectivity changes markedly with CO dose. First, the broad feature at 22 eV is gradually removed while a new feature appeared at lower energy ($\sim$16 eV). A similar effect has been reported on Pt(100) [171]. Comparing the doses needed for each LEED pattern shows that the initial decrease in the Bragg peak at 22 eV is associated with the initial diffraction arc, figure 4.6 (b), while the c(4x2) LEED

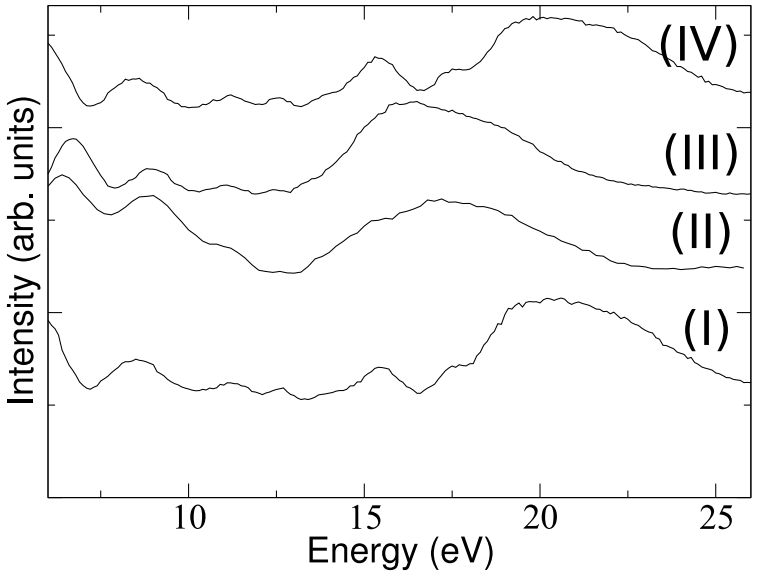

Figure 4.7 Effect of CO on low-energy electron reflectivity from. (I) a 6 ML Pd film on Ru(0001) at room temperature, (II) after 3 L of CO, (III) after 5.5 L of CO, (IV) 6 ML Pd film after heating to 500K. The curves are offset for clarity.

pattern, figure 4.6 (c), is related to the appearance of the 16 eV peak. Given its rich dependence on CO dose, the low-energy electron reflectivity could be used to determine the local CO coverage after a simple calibration.

We also measured the electron reflectivity while the film was heated. Around 400 K, the new peak at 16 eV disappears and the peak at 22 eV is restored to its original intensity, as shown in the top curve of figure 4.7. This temperature dependence agrees with the desorption temperature of CO from Pd [175], confirming the interpretation of the reflectivity changes as signatures of adsorbed CO.

LEED-IV data were also acquired after CO exposure. A multiple-scattering calculation of a Pd/Ru slab was fitted to the intensities of the 1x1 diffraction spots to estimate how adsorbed CO affects the Pd interlayer distances. The best-fit yields a slight expansion of the topmost Pd layer to a separation of 2.31$\pm$0.03Å, with R_p=0.19. DFT calculations confirm that the expansion obtained in the LEED-IV fits is due to the adsorption of CO on the surface. In the calculations, considering

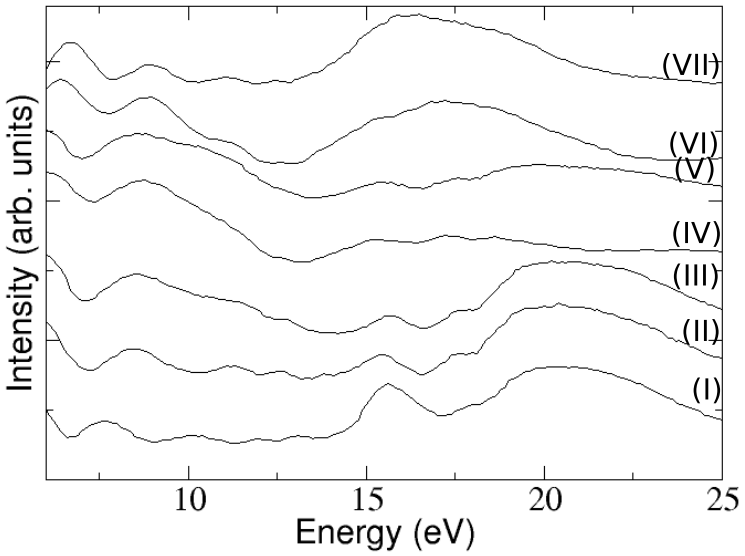

Figure 4.8 Low-energy electron reflectivity of a 6 ML Pd film acquired from a sequence of LEEM images. (I) Bare Pd film at 170 K. (II) After exposing to 22 L_{H_2}). (III), (IV), (V), (VI) and (VII) after exposure to 6, 9, 58, 60 and 63 L_{CO} respectively subsequently to the hydrogen dose. Curves are offset for clarity.

1/3 of ML of CO in hcp position is enough to expand the last layers to 2.31Å. This result also agrees well with previous work of how CO adsorption affects the Pd spacing [115, 176, 177]. As a summary CO adsorption expands the last two Pd layers by the same amount as adsorbed H. Low-energy reflectivity, however, can distinguish between the two adsorbates and measure their concentration, as we next show.

4.4.2 Imaging CO displacing adsorbed hydrogen

We next use electron reflectivity to image CO displacing adsorbed H. We first saturated a 6 Pd film with H by exposure to 22 L_{H_2} at 170 K, giving the broad reflectivity peak between 8–11 eV shown in figure 4.8. We then dosed CO while imaging and scanning the incident electron energy. As seen in figure 4.8, dosing CO results in a decrease of the intensiity of the Bragg peak at 22

eV. When this peak reached minimum intensity, the reflectivity at 16 eV started increasing. As this new CO-derived feature grew (curve VII), the shoulder at 8–11 eV vanished, indicating the removal of surface H.

In addition to the spatially averaged results presented in figure 4.8, we can also follow the local reflectivity changes. The LEEM image in figure 4.9(a) shows a large substrate terrace covered by patches of 5, 6 and 7 ML Pd. In figure 4.9(b) we measure the reflectivity from the 6 ML region marked "zone B" and the 5 ML region marked "zone A" as the H-covered surface was exposed to CO. We separately plot the H and CO concentrations from the reflectivities at 10 eV and 16 eV, respectively. In both zones the reflectivity was more or less constant until the 8–11 eV component decreased and the 16 eV component increased. Thus, the local concentration of adsorbed H decreased and, at the same time, the concentration of adsorbed CO increased. The change occurred earlier in zone A, which is closer to the edge of the substrate terrace. We interpret these changes as CO displacing the adsorbed H.

To illustrate more directly this displacement in real space, we present in figure 4.10 a sequence of composite images made by merging two images obtained using different electron energies. The red channel corresponds to the image intensity at 10 eV, i.e., H-covered areas. The green channel corresponds to the image intensity at 16 eV, i.e., CO-covered areas. The time sequence reveals some detailed behaviour. The changes in the CO and H coverages do not occur uniformly across the surface. Rather, CO-rich areas nucleate and grow from the edges of film steps, in particular at the boundary of the large Ru terrace. Zone A is closest to this boundary and H is displaced earlier there than in Zone B, accounting for the different dose dependencies in figure 4.9. Likely the sharp spatial boundaries in the 16 eV channel corresponds to transitions between dense CO phases, such as the c(4x2) phases. Our findings are consistent with the literature reports of CO displacing H above 150 K [159–161].

LEED-IV data was acquired at the end of the CO exposure figure 4.11 shows the LEED pattern

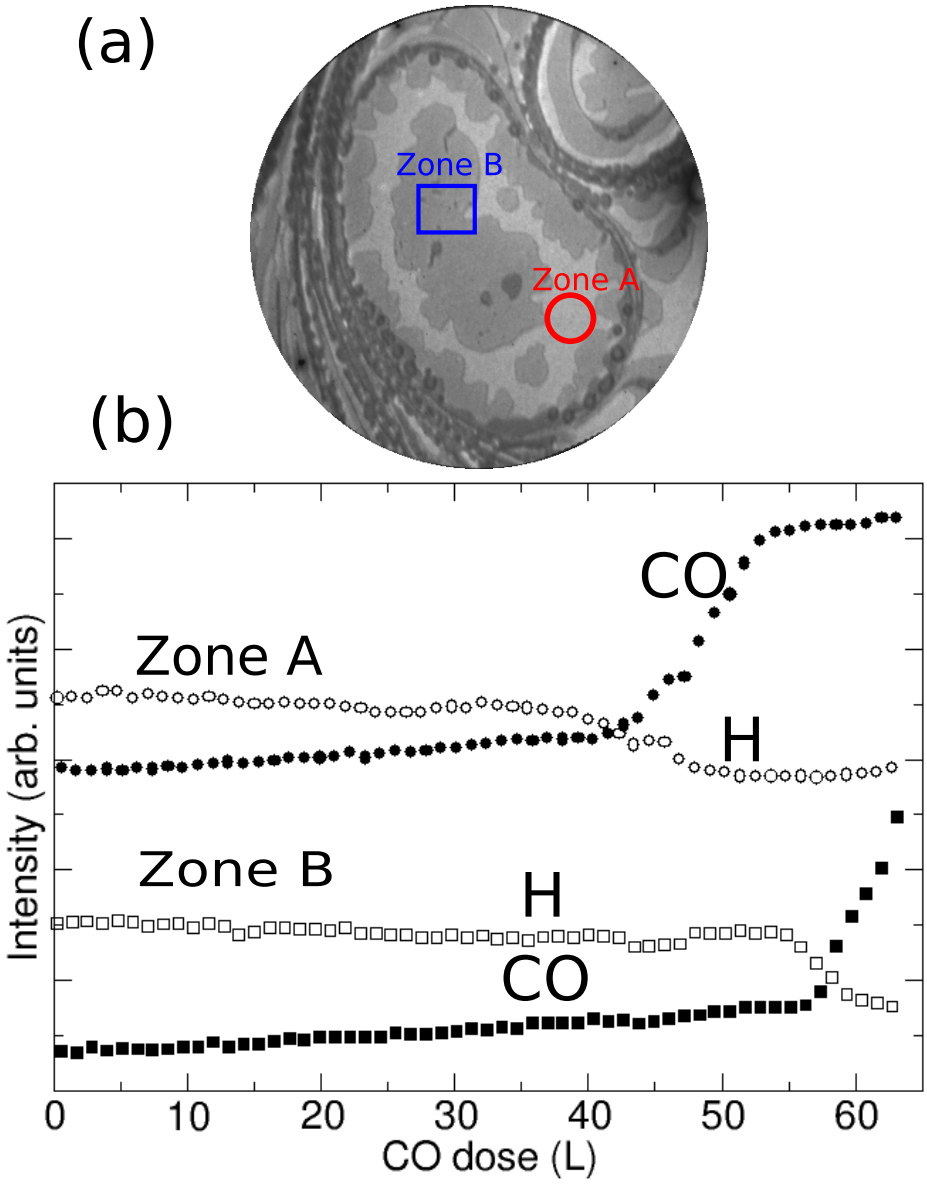

Figure 4.9 (a) LEEM image of a 6 ML Pd film on Ru(0001). The field of view is 9.3 μm. The circle and square mark the regions where the reflected intensities in (b) were measured. (b) Reflectivity at 10 eV (empty symbols) and 16 eV (filled symbols) during CO dosing. Circles are from "zone A", and squares are from "zone B".

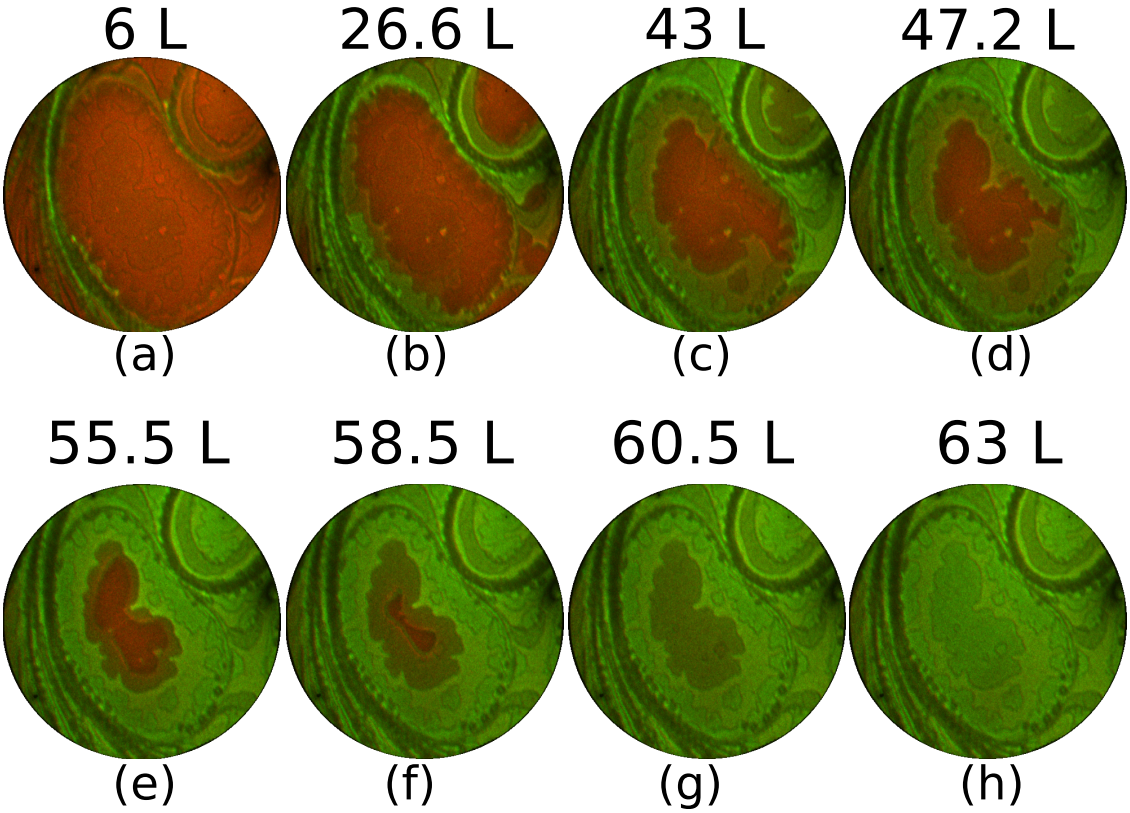

Figure 4.10 Snapshots from the sequence of images acquired while scanning electron energy and dosing CO. Each frame is a composite image from combining the LEEM images acquired at 10 eV (red, H) and 16 eV (green, CO). CO dose is indicated in each frame

after 63 L of CO. The spots of the Pd are indicated in red circles and the green circles show a c(4x2) pattern. This is the same pattern obtained when CO was dosed on clean Pd (see figure 4.6) indicating the presence of CO on the surface. The best-fits to the multiple-scattering simulations give an interlayer spacing for the last two Pd layers of 2.31±0.05 Å essentially the same result as directly dosing CO on clean Pd.

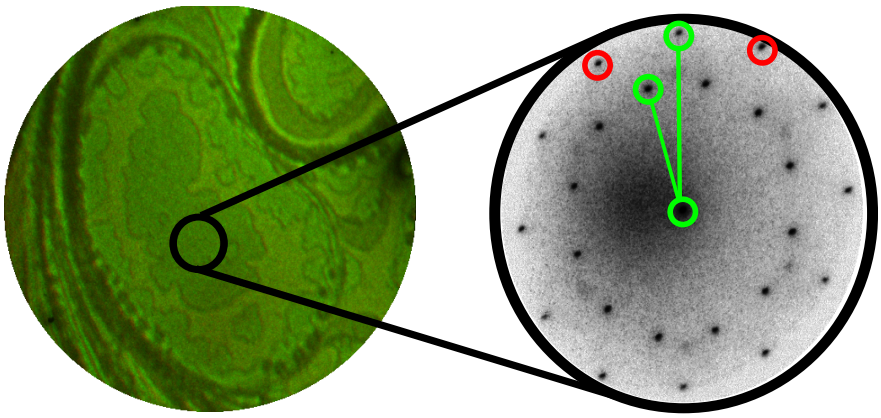

Figure 4.11 Composite image from the hydrogen and CO energy. LEED pattern at 32 eV after the CO dose

4.4.3 Co-dosing atomic hydrogen and CO

Our final approach at incorporating H into the Pd films at 170 K used larger doses of atomic H, 49 KL_H. After the dose, a weak arc-like is observed in LEED pattern, as shown in figure 4.12 (c) for the Pd films. The arc-pattern is the same as detected when having a CO coverage in the range 0.55–0.66 ML, see figure 4.6(d). Thus, the dose of 49 kL_H of atomic hydrogen is accompanied by a simultaneous dose of 0.6–0.7 L_{CO}. To quantify the amount of CO deposited, the atomic hydrogen cracker was used on the clean Ru substrate at high temperature. After 9 minutes, graphene islands [172] appeared and grew. We estimate the CO dose from the fractional coverage of graphene islands. For 10^4 L_H of atomic hydrogen, our estimation is that the hydrogen cracker gives a dose of 0.5 L_{CO}. In good agreement with the amount of graphene formed on a hot Ru surface.

The low-energy electron reflectivity data confirmed that the large atomic H doses led to CO adsorption. As in the case of CO dosed onto the Pd films, the Bragg peak at 22 eV first decreases, and eventually the feature at 16 eV appears as shown in figure 4.12, following the same evolution in the surface exposed to CO (figures 4.7 and 4.8). The intensity in the 8–11 eV range increases at first, but after the appearance of the 16 eV peak, it is removed.

At the end of the atomic H dose, LEED-IV data was acquired. The multiple-scattering best-fit of the Pd slab (i.e., without adsorbed CO or H) found much larger expansions between the top two Pd layers than in the case of adsorbed H or CO. For all but the thinnest film, 2 ML, the layer separations were at least 2.35 ± 0.03 Å. In contrast, the separations are 2.27 Å for the clean films and 2.30 Å after H- or CO-adsorption. In figure4.13(b) we show the best LEED-IV fit for the case of 6 ML of Pd, and the model used for the theoretical calculations.Table 4.2 summarizes the structural results for pseudomorphic films 2 to 6 ML thick. A similar relative expansion was detected in the 20 ML thick films. The Pendry factors are slightly higher than before, although they still show well-defined minima as a function of the structural parameters and the errors in the distances are similar to the previous experiments. Although the error bars in the interlayer spacings are, as expected, larger for deeper layers, all the multiple-scattering best-fits rule out similar expansions deeper in the Pd films. Also, no additional LEED spots or changes in the spatially resolved electron reflectivity are detected, suggesting no changes in the in-plane lattice spacing of the films. For example, a crumpling of the film relative to the substrate would be easily detected by the formation of a moiré pattern with a periodicity corresponding to the difference in lattice spacings between films and substrate. These results suggest the incorporation of sub-surface H into the films but only between the last two Pd layers.

To confirm that the last layer Pd expansion can be attributed to hydrogen in sub-surface positions, we have performed ab-initio calculations (performed with the ab-initio code SIESTA [178, 178], which is based on density, functional theory (DFT)) of a slab of the proper number

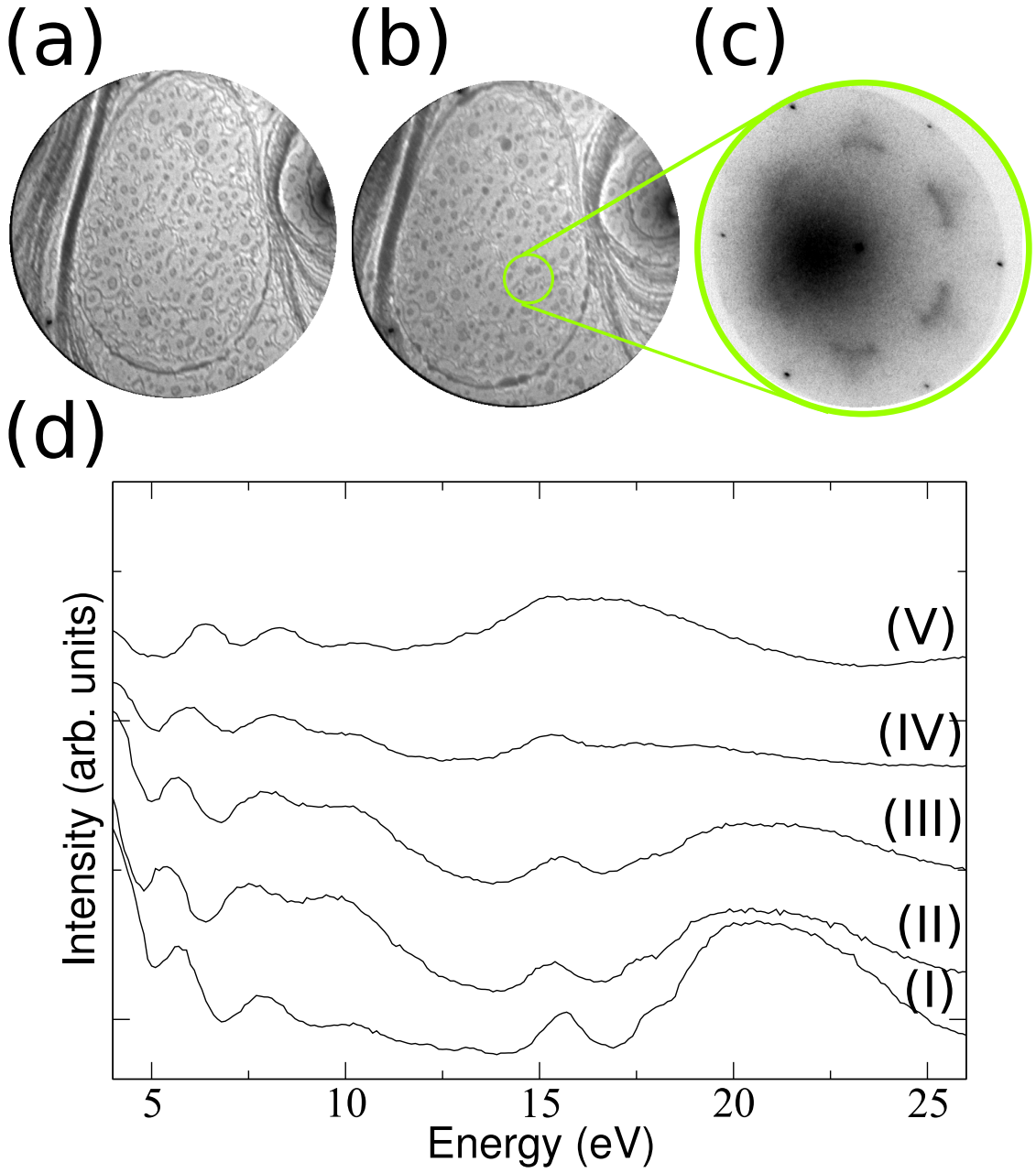

Figure 4.12 (a)Low-energy reflectivity data from a 6 ML Pd/Ru(0001) film at 6.1 eV the field of view is 9.3 μm, (b) same area after 6 KL_H at 6.1 eV. (I) Bare film at 170 K. (II) reflectivity after dose of 5.8 KL_H of atomic hydrogen, (III) after 5.8 KL_H of atomic hydrogen and 7.8 KL_H of molecular hydrogen, (IV) and (V) after doses of 47.6, 49.5 kL_H, respectively. The data sets are offset for clarity.

	2 ML	3 ML	4 ML	5 ML	6 ML
	ABac	ABacb	ABacba	ABacbac	ABacbacb
Pd_1Pd_2	2.32±0.06	2.38±0.08	2.35±0.06	2.35±0.07	2.35±0.03
Pd_2Pd_3	2.21±0.06	2.28±0.08	2.27±0.06	2.25±0.08	2.24±0.05
Pd_3Pd_4		2.20±0.09	2.29±0.04	2.27±0.09	2.28±0.07
R_p	0.18±0.05	0.35±0.09	0.25±0.06	0.35±0.07	0.27±0.06

Table 4.2 LEED-IV results for Interlayer spacing after the hydrogen dose for different thickness cases. Distances are in Ångstroms.

	4 ML Pd/Ru
Stacking	BA/bcaγbγ
Pd_1Pd_2	2.36
Pd_2Pd_3	2.29
Pd_3Pd_4	2.27
Pd_4Pd_5	2.19
Ru_1Ru_2	2.09

Table 4.3 Interlayer spacing from DFT calculations for 4 ML of Pd.

of Pd layers pseudomorphic with the Ru substrate with a 1/3 ML of hydrogen between the two last Pd layers and 1/3 of ML of CO on the surface. All the first-principle calculations give an expansion only in the topmost Pd layer. The calculated expansion is in all cases close to 2.36 Å, in agreement with the expansions experimentally detected by LEED-IV fits showed in table4.2. Table4.3 shows the result for the case of 4 ML of Pd. Ab-initio calculations confirmed that the expansion is due to the population of sub-surface position with hydrogen.

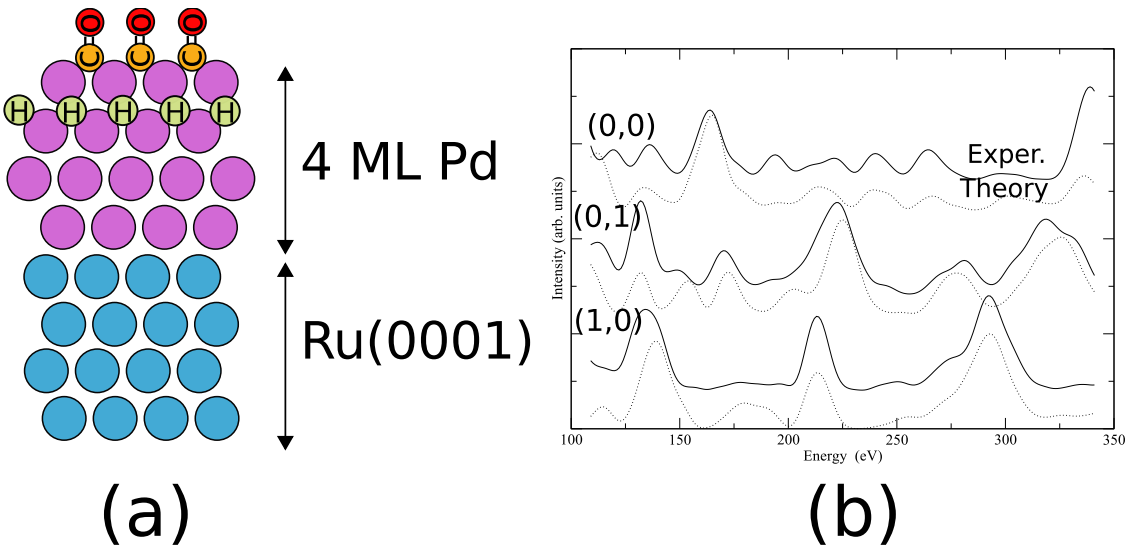

Figure 4.13 (a) Schematic of the system employed for the LDA calculations of last Pd layers separation. (b)LEED-IV fit for 6 ML of Pd on Ru(0001) after large atomic H dose at 170 K.

4.5 Discussion

Dosing ultrathin Pd films with molecular hydrogen at 170 K causes a small expansion, below 1.4%, in the separation of the topmost two Pd layers (d_{12}=∼2.30 Å) [166], [116], [164]. Deeper layers are not expanded. The expansion is consistent with DFT simulations of adsorbed hydrogen without significant concentrations of subsurface hydrogen, in agreement with the literature of bulk Pd. We found no evidence for subsurface H in the structural data for doses of molecular hydrogen of up to 10 KL_{H_2} at pressures of 10^{-6} Torr. To exclude the possibility that subsurface H was only stable when a background of H_2 was present, we collected LEED-IV data at 170 K in 5x10^{-6} Torr of molecular hydrogen and again found the same small expansion between the topmost two layers. Adsorbed hydrogen causes a large increase in electron reflectivity between 8–11 eV, giving LEEM the ability to quantitatively image the local hydrogen concentration [179]. We observe no spatial dependence on the adsorption process, consistent with a non-activated process and high surface mobility.

Our thinnest films, 2-6 ML thick, are pseudomorphic with the Ru(0001) substrate [166]. That is, they are strained to the Ru(0001) lattice parameter in plane. In contrast, thicker (20 ML) films on Ru(0001) and W(110) are relaxed in-plane to the bulk Pd lattice parameter [166]. Exposure of all these films to molecular hydrogen at 170 K only leads to adsorbed hydrogen, as evidenced by the same, small increased separation between the top two Pd layers (d_{12}=$\sim$2.30 Å). The 20 ML films are effectively decoupled from the substrate by a network of interfacial dislocations [166].

Since atomic hydrogen has been used to increase hydrogen absorption into bulk Pd(111) [180], we also examined the effect of atomic hydrogen on the structure of the ultrathin films. Doses of over 3 kL_H at 170 K revealed adsorbed H in the electron reflectivity (fig. 4) but only the same small expansion between the topmost two layers. The lack of subsurface H at 170 K is consistent with its instability at this temperature, as measured by temperature programmed desorption [180], [139].

We only find evidence for subsurface hydrogen for conditions that led to CO adsorption. That is, large doses of atomic hydrogen led to the characteristic LEED patterns in figure 4.12 and the electron reflectivity "fingerprints" figure 4.7 of adsorbed CO. The structural data from LEED-IV of films co-dosed with CO and atomic hydrogen show significant expansion (3.1%) of the outer two Pd layers but not of the deeper layers. Previous LEED-IV work in the literature [115, 176, 177] and our own structural analysis and DFT calculations show CO adsorption alone cannot induce this amount of top-layer expansion. Instead, our DFT calculations are consistent with a CO-covered surface and a significant concentration of hydrogen between the topmost two Pd layers as shown in figure 4.13.

We next discuss how CO adsorption leads to H between the topmost two Pd layers. At our exposure temperature, CO is known to compress and ultimately displace adsorbed H from the surface. Figure 4.10 shows the displacement in real space. The literature also claims that some of hydrogen is displaced into the Pd interior [159, 160, 181]. In addition, the CO prevents desorption of sorbed hydrogen to above room temperature. These effects lead to two ways that CO may cause

the subsurface population with hydrogen. First, CO drives the hydrogen in. Second, CO prevents subsurface hydrogen from desorbing.

Insight into the first scenario comes from the experiment used to image CO displacing hydrogen, where a H-saturated surface was converted to a CO-covered surface after 63 L CO. After the hydrogen displacement, the LEED-IV data gives a top-layer separation identical (2.31 Å) to a CO-covered surface (see section 1. Effects of CO). Thus, the displacement of a saturated surface does not introduce sufficient subsurface H to be measured structurally. This observation suggests that additional hydrogen from the gas-phase must be injected into the subsurface.

Another experiment was performed to test this proposal. A 6 ML Pd film on Ru(0001) was saturated with 5 L CO at 170 K and then exposed to about 3 kL atomic hydrogen. CO remained on the surface giving the same diffuse arcs obtained in figure 4.6 (d). After this treatment, which produced a d_{12}=2.33 Å. consistent with significant H between the topmost two Pd layers. These observations show that atomic H does not displace CO, like molecular hydrogen, and some of the atomic hydrogen enters the subsurface.

A consistent interpretation is that CO adsorption prevents the loss of subsurface H, allowing its accumulation between the first and second Pd layers. The question then is why does hydrogen not build up between the deeper layers, as hydrogen should ready diffuse through the entire film thickness at 170 K [145]. An explanation is that hydrogen between the first two Pd layers is more stable than deeper hydrogen, as theory and experiment suggest. Support for this interpretation comes from an additional experiment. Starting from a 3 ML film on Ru(0001), we deposited about three additional Pd layers at 170 K during exposure to atomic H at $5\text{x}10^{-6}$ Torr. This lead to a CO-covered surface and significant expansion of the topmost Pd layers to 2.35Å. without any expansion of the deeper layers. That is, hydrogen resides between the first two Pd layers but not deeper. In the procedure, new Pd layers overgrew Pd layers that already had hydrogen between them. This could have given a pathway to build-up a hydride layer-by-layer. Instead, we only find significant

concentrations of hydrogen between the top two Pd layers. These results are consistent with the deeper hydrogen being unstable at significant concentrations at 170 K, even in the presence of adsorbed CO.

Such expansion is in agreement with the expansion predicted by first-principle calculations with a occupation of sub-surface positions by hydrogen and CO on the surface.

4.6 Conclusions

We have studied the location of hydrogen on ultrathin films of Pd on Ru(0001) by LEEM. Figure 4.14 summarizes all the experiments performed. Changes in the low-energy electron reflectivity provide a local determination of the presence of hydrogen and carbon monoxide on the films surface. Measurement of the topmost Pd layers interlayer distances by selected-area LEED-IVs allows for the determination of sub-surface hydrogen.

Hydrogen is adsorbed on the surface of the films at 170 K, using either molecular or atomic hydrogen. When removing the incoming flux of hydrogen, the adsorbed hydrogen remains on the films up to a temperature of 270 K. There is no significant sub-surface or near surface hydrogen as determined by LEED-IVs, albeit this method is unlike to determine concentrations below 10%. The lack of sub-surface hydrogen occurs also when a molecular hydrogen background is maintained in the system.

If carbon monoxide at coverages above 0.3 ML is deposited on the surface -generated by the hydrogen cracker or purposefully leaked- then an expansion of the last two palladium layers, according with ab-initio calculations, signals sub-surface hydrogen. Hydrogen is located only between the last two layers. In particular, in bilayer films the Ru-Pd interface is not expanded, indicating the lack of hydrogen incorporation at the film-substrate interface.

Dosing CO on hydrogen-precovered films allows for the real-space observation of the displace-

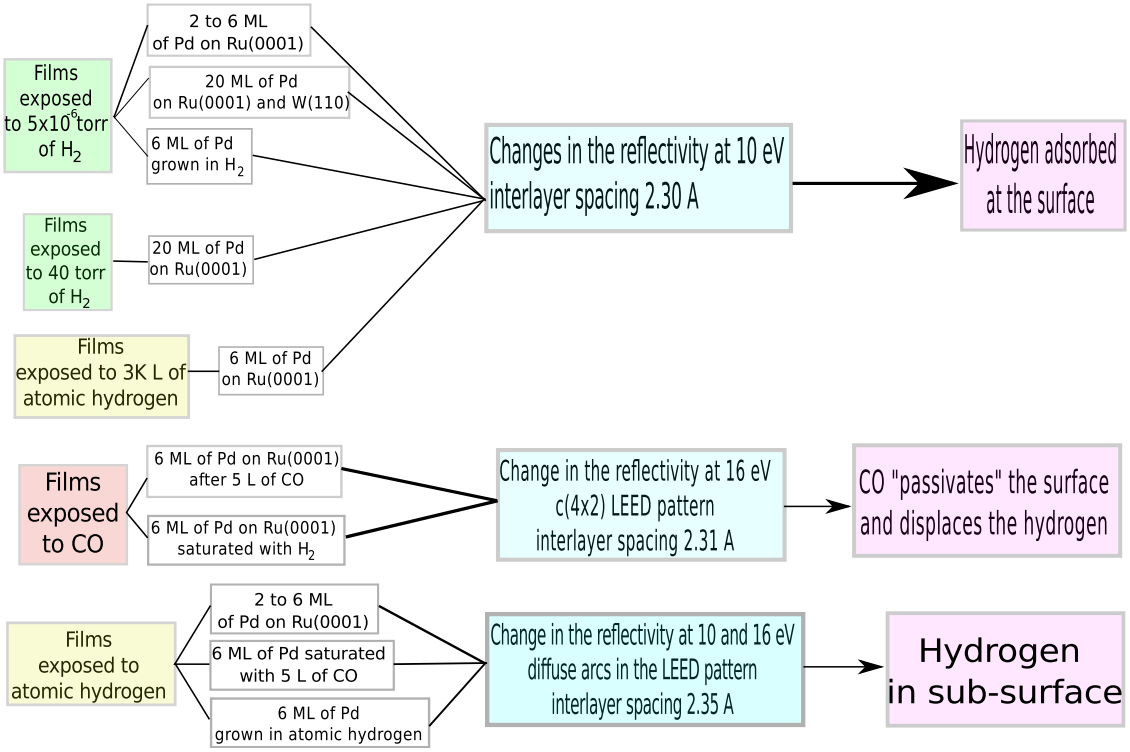

Figure 4.14 Summary of the experiments performed, with the changed observed in each case

ment of hydrogen by CO. This starts at the step edges of the film, and proceeds in layer-by-layer steps.

Chapter 5

Growth and Structure of Mg films

5.1 Introduction

Magnesium is a commonly available non-toxic metal. From a technology point of view, its hydride MgH_2 has been proposed as a lightweight hydrogen carrier, despite its if kinetic and thermodynamic limitations. From a fundamental point of view, Mg, together with Be and Al, have been studied as part of the so-called free-electron-like metals with quite ideal metallic bonding. In particular, Mg has an ideal hexagonal close-packed lattice with a simple electronic structure. Its low sublimation temperature limits the preparation of high quality single crystals in ultra-high vacuum (UHV). Mg is known to grow as highly perfect thin films on many substrates. On some of them, the interface with the substrate is very sharp. With the appropriate substrate, quantization of the Mg sp-bands has been observed up to a thickness of several nanometers [182].

There are only a limited number of studies on the growth of Mg on refractory metals, most of them on W(110) [182, 183]. On W(110), a real-space study by low-energy electron microscopy [183] found a very high quality layer-by-layer growth. The quality of such thin films is so good that is has been used to study how the bulk electronic structure develops as a function of thickness [182]

and influences chemical reactivity [184].

Over et al. [185] characterized the epitaxial growth of Mg over Ru(0001) using LEED, work function changes and temperature programmed desorption (TPD). They reported that magnesium grows over Ru(0001) in an incommensurate manner, i.e., keeping its own in-plane spacing. This was understood to be due to the large mismatch between the respective in-plane lattice spacings (around 18%). The result is an overlayer film without significant strain. A moiré was observed in the LEED pattern, starting at coverages as low as 0.05 magnesium monolayers. From θ=0.05-0.65 ML Mg the LEED indicated a (5x5) periodicity with a Mg-Mg distance of 3.35 Å (4% expansion with respect to the Mg bulk value). When the coverage was increased to 0.65-0.75 ML Mg, a compression of the Mg overlayer was observed, with the LEED pattern changing gradually to a (7x7) periodicity with a final Mg-Mg distance of 3.13 Å (slightly compressed with respect to the bulk distance of 3.21 Å). When θ=0.75 ML Mg there were no further changes in the LEED patterns and the authors considered that the first layer of Mg/Ru completely covered the substrate. From TPD measurements, the authors described several peaks that shifted to higher temperatures when the coverage increased. On Mg multilayers, there were three main TPD peaks: α at 750 K corresponding with the first Mg layer; β at 580 K, corresponding with the second and γ at 500 K for the third and subsequent layers. From these results it can be deduced that the first Mg layer interacts more strongly with the support than the second and subsequent layers. The same group published later [186] a LEED-IV fit providing a crystallographic structure of the first 3 ML_{Ru} of Mg over Ru(0001). They used the (5x5) symmetry for the analysis of the first Mg overlayer. The second and third overlayers were treated within a mirror approximation, giving the films a $7/6x7/6$ structure.

A few works have described STM imaging of epitaxial Mg grown (up to 2 ML) at room temperature. Pezzegara et al. [187] described recently the growth of continuous Mg films over a semiconductor, GaN(0001), using STM and RHEED. The in-plane lattice mismatch with Mg is

only 0.3%. In agreement with this small mismatch, they did not observe a moiré pattern on the Mg surface. They reported hexagonal-shaped Mg islands with a height of 2.80 Å (slightly larger than the interlayer spacing of close-packed planes in bulk Mg, 2.60 Å). When the coverage was lower than 0.4 ML, the islands displayed atoll-like shapes. Increasing the Mg coverage changed the shape of the islands, making them more compact. The appearance of the islands depended also on the STM imaging bias. With 4 V the islands looked flat. However, if the bias was lowered to 0.5 V there was a detectable corrugation at their surface of 0.06 Å. The submonolayer grow of Mg over Si(001) was characterized by Hutchinson et al. [188] at room temperatures using STM. Deposited magnesium formed rows that are roughly perpendicular to the substrate dimer rows.

In this chapter[1] we present a real-space STM and LEEM study of the growth of Mg on Ru(0001).

5.2 Growth in LEEM

The low-energy electron microscopy view of the first stages of Mg growth on Ru(0001) is shown in figure 5.1 (a)–(f). The LEEM snapshots are selected from a sequence acquired while continuously imaging the surface during magnesium deposition. Growth of first-layer islands cannot be imaged directly by LEEM [figure 5.1 (a)]. At first, only a uniform decrease of the electron reflected intensity is detected and the substrate steps become less visible. At the same time, in the real-space images, the substrate steps are suddenly visible again [figure 5.1 (b)]. Nevertheless the Mg-covered substrate terraces are not imaged like the bare Ru substrate. The fine-scale contrast in figure 5.1 (b) suggests that there are structures in the monolayer whose size is close to the resolution limit of the LEEM, which for our instrument is about 10 nm. The same observation (lack of first monolayer LEEM island contrast, with the substrate steps clearly visible at close to the compact monolayer)

[1] Most of the information of this chapter has been published in T. Herranz, B. Santos, K.F. McCarty and J. de la Figuera, *Surf. Sci.* **605** (2011) 903, from where it has been reused with permission.

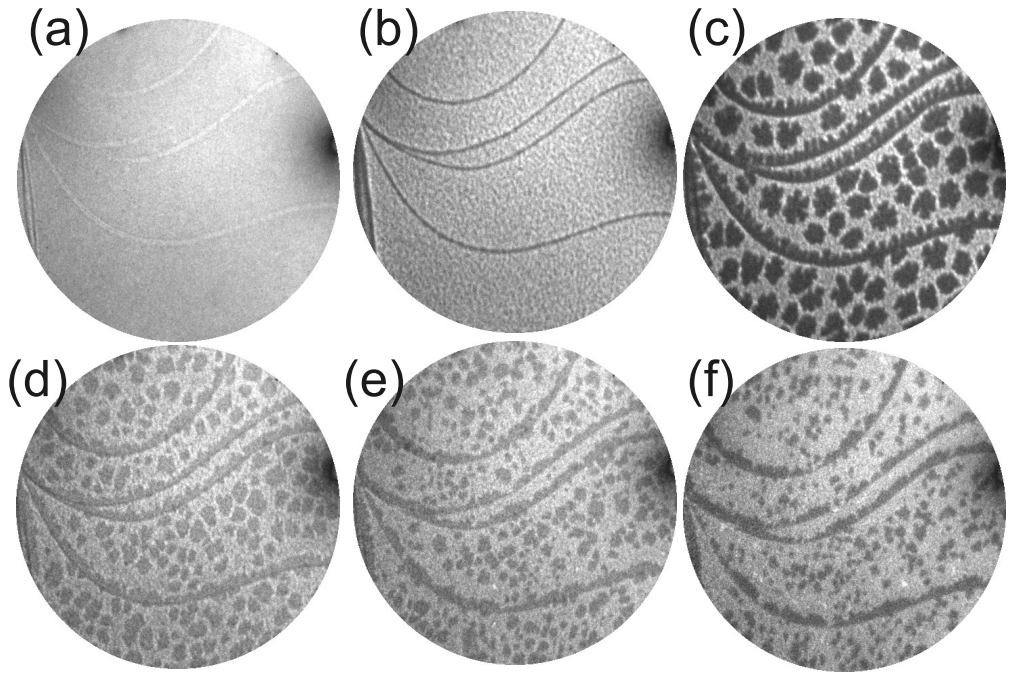

Figure 5.1 (a)–(f) LEEM snapshots from a sequence acquired while growing Mg on Ru(0001) at 373 K. The FOV is 7 μm, and the electron energy is 5 eV. (a) shows the bare substrate. (b) corresponds with the substrate just before the appearance of the 2 ML islands. (c)–(e) and (f) show islands 2, 3, 4, 5 ML thick respectively. The first ML islands cannot be distinguished in LEEM [b)], but the surface looks rough when compared with the Ru substrate [a)].

has been reported for Mg/W(110) [183] and ascribed to the formation of small islands.

The nucleation of the second layer, by contrast, is clearly observed, and proceeds through well-defined island growth[figure 5.1 (c)–(f)]. The nucleation density increases slightly for the next layers. At the electron energy of 5 eV, no clear oscillations of the reflected intensity are detected beyond the monolayer. The islands are roughly round in shape, as expected for a three fold structure on the three fold symmetric Ru(0001) substrate (in contrast, there is a strong uniaxial island growth in Mg/W(110) due to the anisotropy induced by the W(110) substrate [183]).

In figure 5.2, a sequence is shown up to a thickness close to 10 ML. The electron energy was varied to achieve optimum interlayer contrast for the different thickness. The growth is completely layer by layer, with no more than 3 different thicknesses exposed at a given time except at step bunches, where a more three-dimensional growth is observed. All together, the quality of the growth is very high, improving with thickness.

In figure 5.3 (a)-(c), the growth of the second layer is followed at a slightly higher temperature of 408 K. The islands have now a dendritic shape, very different from the compact shapes observed at lower temperatures. Dendritic islands have been observed for many metal/metal growth systems. In particular, wide-arm dendritic islands have been explained as resulting either from alloy formation changing surface diffusion [113], or to instabilities in the diffusion field around growing islands, as, for example, diffusion limited aggregation (DLA) of Au/Ru(0001) [189, 190]. In our case, it is striking that the islands are compact at a lower temperature, and dendritic at a higher temperature. This might indicate alloy formation. But the temperature is still extremely low for ruthenium to alloy with Mg [191], and the observed islands correspond to the nucleation of the second layer over a single continuous monolayer film. If alloying would happen, it would be expected to occur at the monolayer islands. Furthermore if the deposition is stopped, the dendritic islands slowly disappear, as show in the figure 5.3 (d)-(f) and summarized in the island size evolution plotted in figure 5.3 (g) (similar observation was reported for Mg on W(110) [183]). The

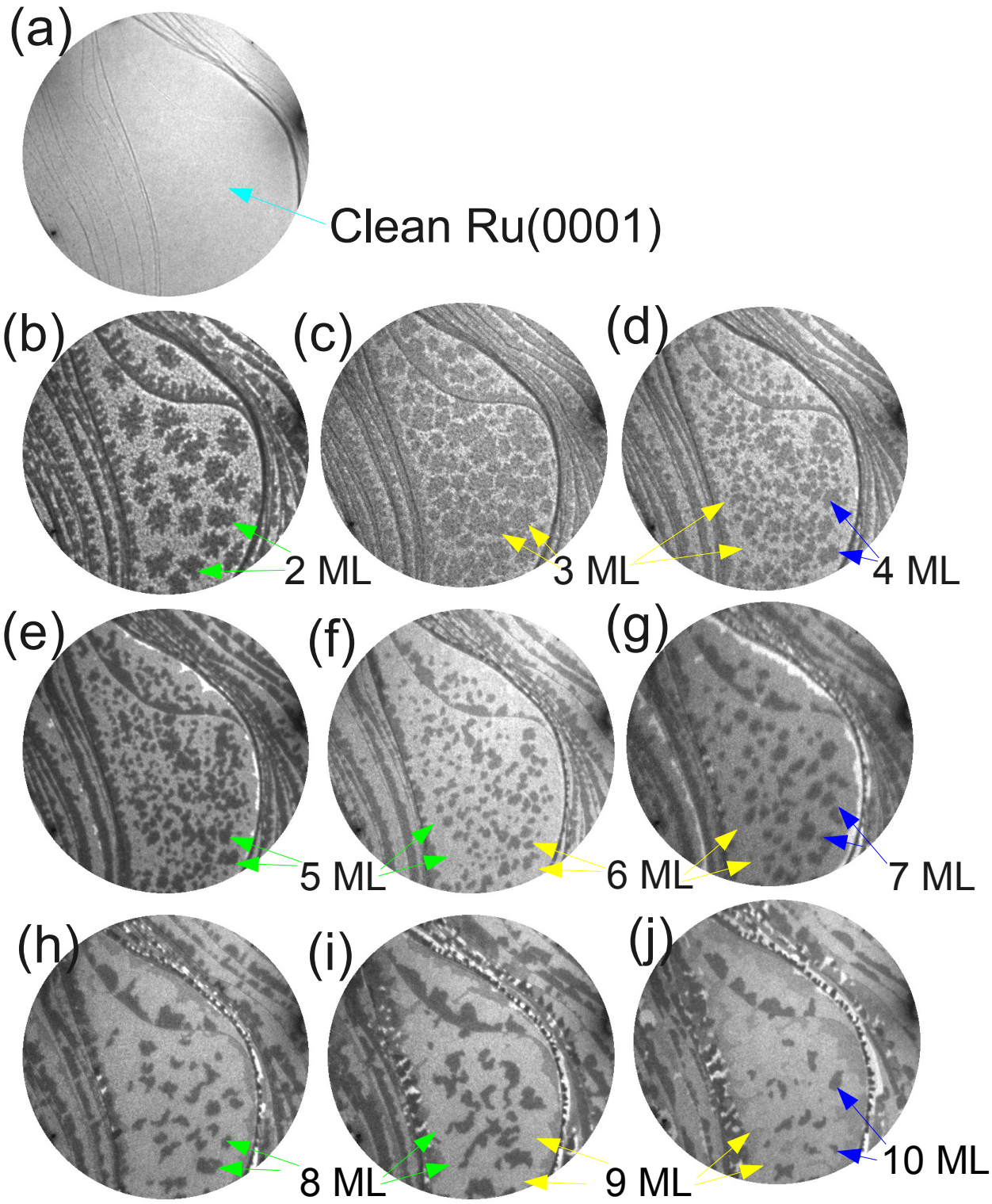

Figure 5.2 (a)-(j) Sequence of LEEM images showing the growth of Mg on Ru(0001) up to a thickness of 10 ML. The field of view is 7 μm. The electron energy has been varied between 3–7 eV to maximize contrast between consecutive layers. The growth temperature is 383 K. Thicknesses of newly nucleated Mg islands are labeled.

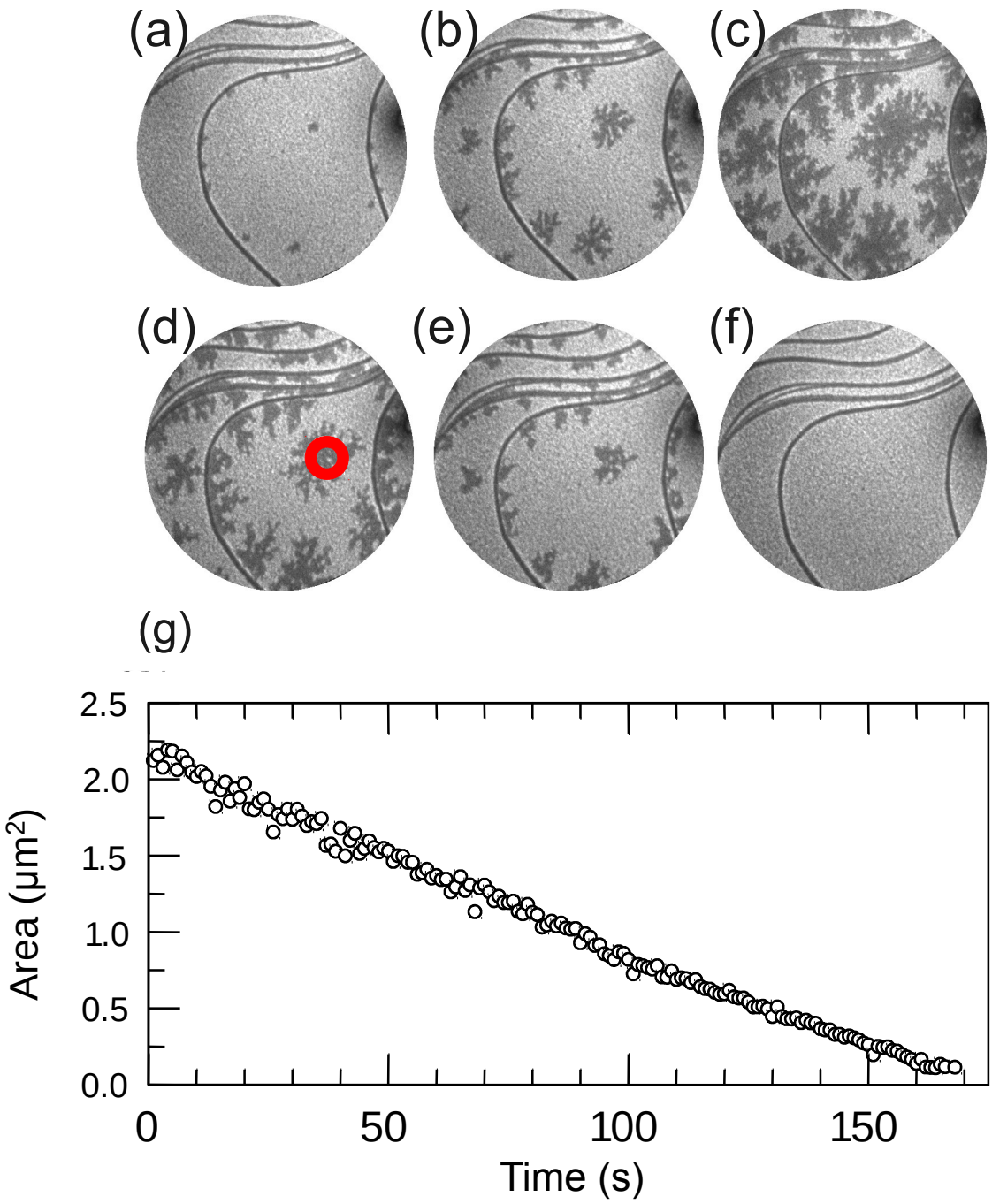

Figure 5.3 Growth and sublimation of Mg at a sample temperature of 408 K. Images (a)-(c) correspond to the deposition of Mg at a rate of 1 ML/minute. After frame (c), the Mg flux was stopped. Frames (d), (e) and (f) were acquired 99, 172 and 233 sec after frame (c). The field of view is 7μm, and the electron energy is 5 eV. (g) Plot of the area of the island marked in (d) with a white circle as a function time.

2 ML islands disappearance is due to alloying is also highly unlike. Reported work by TDS of multilayer Mg films on Ru [185] indicates that the third Mg layer is bound less strongly than the second. In agreement with this observation, we have been unable to nucleate any third layer island at the conditions of the experiment shown in figure 5.3 (a).

We thus propose that the observed dendritic island growth is due to a combination of energetics that includes significant sublimation. Actually, even while the islands are disappearing at the measurement temperature, there is hardly any change in the islands shape, suggesting a larger edge-diffusion energy barrier, compared to the desorption energy barrier. That is, the edge adatoms of the second monolayer islands desorb from the surface before they have a chance of moving around the island, in marked contrast with most metal/metal system.

5.2.1 LEED

In figure 5.4, the LEED pattern acquired from a 2 μm diameter-area of the sample is presented for the Ru(0001) substrate (figure 5.4 (a)), the initial pattern observed when there is a coverage below 0.65 (figure 5.4 (b)), and the pattern observed when the 2 layer starts to nucleate (figure 5.4 (c)). The images are snapshots from a sequence of LEED patterns acquired while growing Mg at a slower rate than the previous films, with the substrate kept at 357 K. The LEED patterns present six-fold symmetry because they were acquired from several substrate terraces. As the LEED pattern from adjacent terraces present rotated three-fold symmetric patterns, they average to the observed six-fold pattern [124]. Initially only the Ru LEED is detected, with the unreconstructed 1x1 periodicity of the hcp(0001) bare surface. At a coverage of 0.6 ML, additional spots start to appear, forming a superstructure of a periodicity close to (5x5) where only the first superstructure order spots are detected. The most straightforward interpretation of the LEED pattern is a coincidence pattern between the Mg film and the underlying Ru substrate [185]. By calibrating the Mg spot separations using the Ru spots, we estimate the initial Mg in-plane lattice spacing

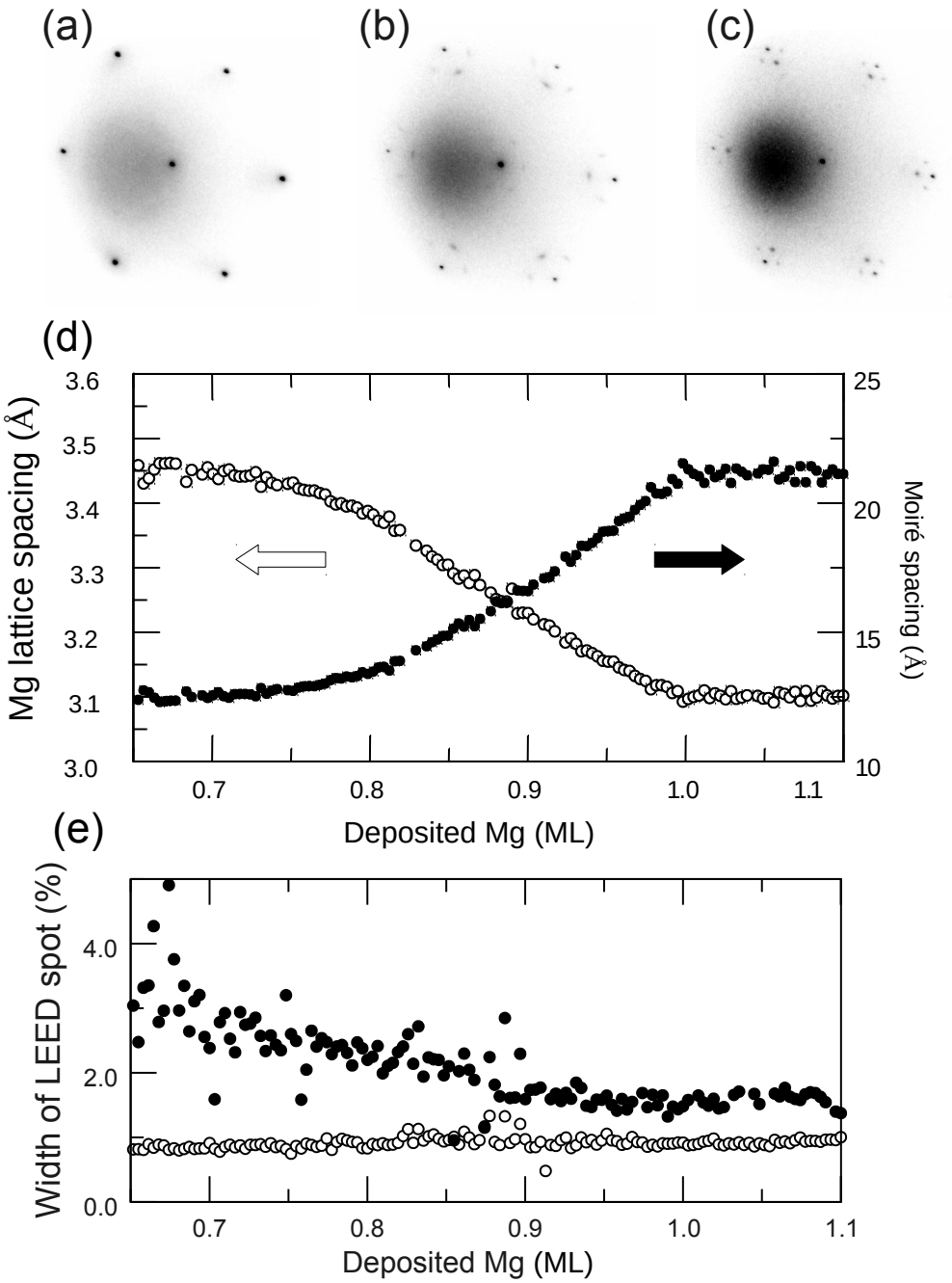

Figure 5.4 (a)–(c) LEED snapshots at an electron energy of 42 eV from a sequence acquired while growing 2 ML of Mg on Ru(0001). The substrate temperature is 357 K. (a) Bare Ru. (b) Initial pattern showing a periodicity close to 5x5 (coverage between 0.50 and 0.65). (c) Final pattern with a periodicity of 7x7. Thicker coverages show the same pattern with weaker Ru spots until only the Mg spots can be seen. (d) Evolution, measured from the sequence of LEED patterns of the real-space in-plane lattice spacing of the Mg beams (empty circles) and the distance in real space between the Mg and Ru beams (filled circles), i.e., the distance corresponding to the moiré periodicity. (e) Evolution of the spot width of the Mg (filled circles) and the Ru (empty circles) first order beams, normalized by the distance of each spot (Mg or Ru respectively) to the specular beam.

to be 3.45±0.07 Å. The 2% error arises from distortions in the imaging lenses of our LEEM, as estimated from comparing the distances measured using different, equivalent spots. The lattice spacing initially stays roughly constant before gradually decreasing to 3.10±0.06 Å, as show in figure 5.4 (d). This periodicity is close to a 7x7 pattern. With more Mg deposition, the intensities of the Ru spots decrease until only a 1x1 pattern of Mg first-order beams remains. The lattice spacing decrease shown in figure 5.4 (d) occurs when the surface is already covered with a layer of magnesium. Further magnesium deposition densifies the already complete monolayer. Only when the first layer is completely dense do second-layer islands nucleate. Our LEED/LEEM in-plane distance measurements are in agreement with the LEED results obtained with the standard LEED diffractometer used in Ref. [185]. In addition, in figure 4 (e),the evolution of the spot width with coverage in the same coverage range is presented. The spot width of a LEED beam can be related to the average domain or island size of the surface. In our case, the spot width of the Ru beams is quite constant (close to 1% of the spot distance to the specular beam). This width can be considered the error limit of our measurements (the LEED data was acquired on a single Ru substrate terrace, so there is no influence of substrate steps). On the other hand, the Mg spot starts with a larger size, and decreases with coverage from 3.5% to 1.7% even before the change in lattice spacing starts. This implies that the domain size increases during the transition. Using the estimate hs/a* ∼a/d (where hs/a* is the half- width of the Mg spot with respect to the Mg spot separation with the specular beam, a is the atomic spacing f the Mg film, and d is the domain size) the domain size increases from close to 100 Å before the compression begins to about 180 Å when the 7x7 pattern is reached. It is clear from the spot evolution that there is no coexistence of 7x7 and 5x5, but rather a continuous compression of the Mg layer.

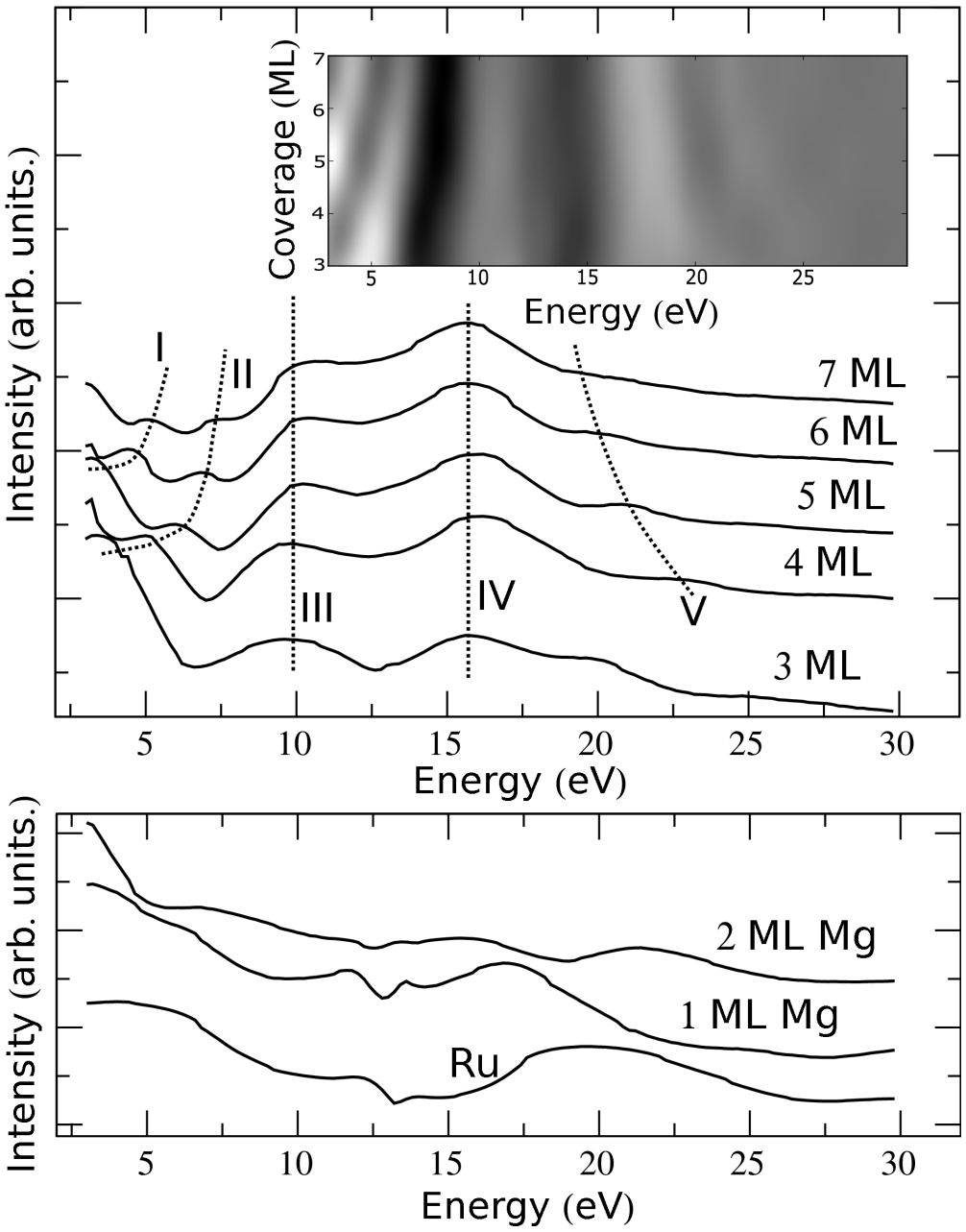

Figure 5.5 Electron reflectivity of Mg/Ru(0001), shown as a function of energy and coverage. Lower graph: reflectivity for Ru, 1 ML Mg and 2 ML of Mg/Ru(0001). Upper graph: reflectivity for 3–7 ML Mg/Ru(0001). The inset is a bidimensional image showing the change of reflected intensity as a function of both coverage and energy. The data has been differentiated to enhance the contrast. The substrate temperature was 358 K. The dotted lines show the maxima of the reflected intensities as a guide to the eye.

5.2.2 Reflectivity

In figure 5.5 we show how the energy-dependent electron reflectivity evolves with Mg thickness. A sequence of LEEM images was acquired at a low deposition rate of 0.12 ML/min while, at the same time, scanning the electron energy between 3 and 30 eV at a rate of 68 seconds per energy scan. The reflected intensity is extracted by averaging the image intensity within a box several micrometers in size. Both reflectivity curves of uniformly thick layers (see individual plots in figure5.5) as well as the intermediate thicknesses (see inset of figure 5.5).

In the plots of figure 5.5 we have separated the reflectivity of the thinner films (bottom panel) and the thicker one (top panel). The first scan shown corresponds to the bare Ru substrate, with a broad peak at the (0002) bulk Bragg reflection near 20 eV. As Mg is deposited, the electron reflectivity changes, and eventually reaches the reflectivity of a Mg bulk-like surface. Although from a structural point of view even the first compact Mg layer is very close to a bulk-Mg surface, the electron reflectivity is very different from bulk Mg due to the interaction with the Ru substrate. Only from the third layer onwards, the reflectivity lacks features that might be attributed to the Ru substrate. For the thicker films (upper panel of figure 5.5) the largest peaks in the reflectivity (peaks marked III and IV, at 10 and 16 eV respectively) do not change their energy with coverage anymore. On the other hand, other smaller peaks clearly change energy when changing the coverage. These latter peaks actually shift in energy in different ways depending on their energy range. Peaks below 10 eV (I and II) shift to higher energy with increasing coverage. The peak above 16 eV (peak V) shifts instead to lower energy. Although maxima (minima) of the reflectivity are related to a low (high) unoccupied density of states, to properly interpret the electron reflectivity data requires not only knowledge of the unoccupied band structure but a multiple scattering calculation. Regular LEED codes are not generally appropriate for the energy range discussed here [169], although in some cases they have been successfully applied [192]. We thus refrain from discussing in more detail the initial stages of the Mg reflectivity. For thicker films, the band structure should

correspond closely to the bulk-Mg band structure. We suggest that the broad peaks (III and IV) that do not shift in energy with coverage correspond to gaps in the Mg band structure. The additional oscillations in the reflectivity (I, II, and V) are attributed to quantum interference peaks [163] arising from a Fabry-Perot interference effect between electron reflection at the substrate/film and at the film/vacuum interfaces [193]. The presence of the vacuum barrier and the interface with the substrate in a thin film of Mg collapse the unoccupied energy bands of bulk Mg into a discrete set of allowed energy values. Unlike for occupied states where quantum well states might appear, for unoccupied states we have quantum well resonances: they form a discrete set of energies at which electrons can be injected into the Mg film which forms the resonator [194] giving rise to quantum interference peaks. When the number of layers of the film is increased, more allowed quantum well resonances appear. To accommodate more energy states in a given bulk band as the thickness is increased, the allowed energy levels shift towards the nearest band edge [194]. The shift in energy in the quantum interference peaks as the coverage is increased marked in the top graph of figure 5.5 is then naturally explained: for the quantum interference peaks marked I and II, the bulk band approaches the nearest band edge at 10 eV. For the quantum interference peaks marked with IV, the corresponding bulk band presumably approaches the band edge at 16 eV. We note that the presence of these quantum interference peaks indicate that the Mg/Ru interface is sharp and devoid of alloying.

5.2.3 Stacking faults

The stacking sequence of Mg/Ru has been reported as an ...ABAB hexagonal close packed sequence since the beginning of the film growth [186]. (This naming scheme describes the stacking sequence by labelling each possible hexagonal layer in a close packed sequence as A, B or C, with the topmost layer as the rightmost letter.) Nevertheless, there is the possibility of a significant fraction of stacking faults within the films which might arise from the interface or appear later during

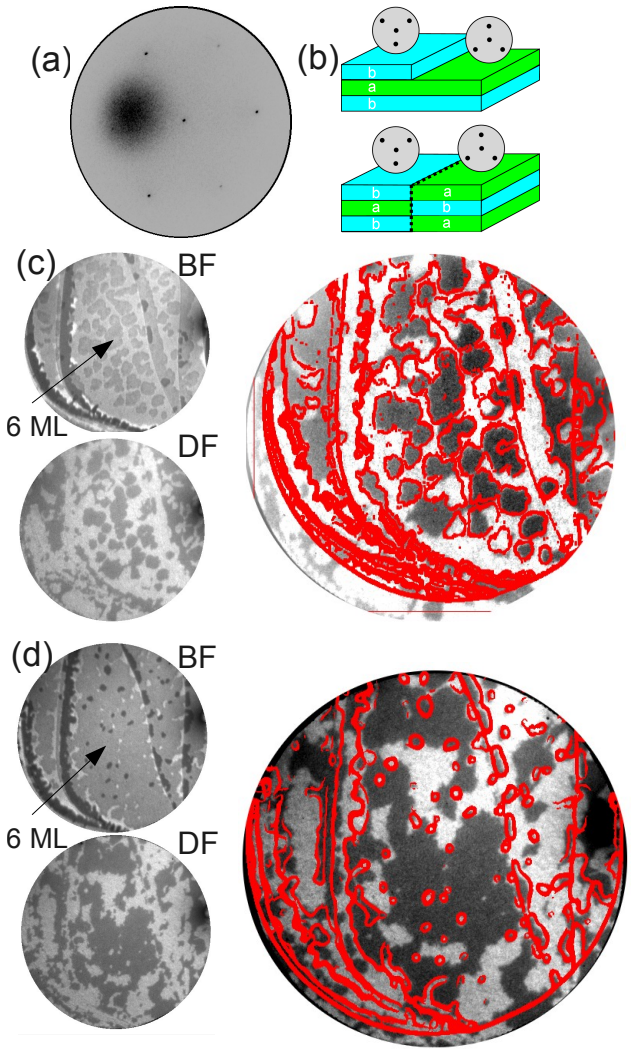

Figure 5.6 (a) Selected-area diffraction pattern of a 6 ML thick Mg film on Ru(0001) acquired from a region of uniform stacking and thickness. (b) Schematic showing how the diffraction patterns should change because consecutive thicknesses have different surface terminations (top) or because layers of the same thickness have different initial stacking (bottom). (c) LEEM images of a mostly 5 ML film with 6 ML thick islands. The field of view is 7 μm. Top: bright field image, bottom: dark field image, reflecting the stacking termination, right: composite image showing the Mg step edges from the bright field image (in red) superimposed on the dark-field image. Electron energies for the bright and dark field images are 3 and 30 eV respectively. (d) Same combination of images acquired on a different film (albeit grown on the same substrate terrace) with a nearly complete 6 ML layer. Electron energies for the bright and dark field images are 4.3 and 30 eV respectively.

the film growth. To check for the presence of different surface terminations, dark-field images were acquired in addition to the regular bright-field images. While the latter are created from the specular beam, the dark-field images were formed from one of the first-order diffraction beams (i.e., a (01)-type beam) of the Mg film. As discussed elsewhere [111, 124, 128], the three-fold symmetry of the LEED pattern [see in figure 5.6 (a) the pattern acquired in a film area of uniform thickness and stacking] reflects the symmetry of a given hcp stacking-sequence termination. When changing the stacking termination from ...ABAB to ...BABA, the diffraction pattern rotates by 180° [124]. This can happen when moving across monoatomic steps of the film (we note that the unit cell of an hcp crystal is composed of two hexagonal layers, so consecutive terraces are not crystallographically equivalent), as shown in the top schematic of figure 5.6 (b). Thus, the dark-field image should shown reversed contrast on different surface terminations [124]. This effect is easily observed in a film with intermediate coverage between full layers, such as the film shown in figure 5.6 (c). An image from the film using the specular beam, i.e., a bright field image, is shown as the first image of figure 5.6 (c) (marked BF), showing the topography of the film surface, with the different thicknesses presenting different contrast due to the quantum size effect on the reflectivity, as seen in figures 5.1 and 5.2. Selecting one of the first-order diffracted beams by means of an aperture, a dark-field image is shown in figure 5.6 (c) (marked with DF). As can be seen more clearly in the composite image (with the island outlines marked in red) at most island boundaries, where the film changes by one layer in thickness, there is a bright-dark contrast change in the dark-field image indicating the change in surface termination. Nevertheless, there are some islands that do not show the expected change. The simplest explanation is that the stacking sequence is changed in those islands. In order to check this effect more clearly, a nearly complete-layer film was grown in the same substrate terrace in figure 5.6 (d). Again the bright field image (marked BF) shows the film topography. The dark field image, as before, reflects the different surface terminations. It is clear from the composite image that even at the same level there are bright and dark areas, which we

interpret along the bottom schematic of figure 5.6 (b). Thus, we find substantial areas with stacking faults in the film. The stacking faults might be present from the Mg/Ru interlayer, or they might arise later in the film growth. Further work will be required to determine their location.

5.3 Growth in STM

In addition to using LEEM to study the Mg/Ru growth, we have also employed STM to characterize the growth at room temperature (RT).

5.3.1 Initial stages

A first goal was to determine any possible special features of the growth for the first monolayer, where LEEM shows a continuous decrease in reflected intensity up to 0.3 ML, with no clear monolayer island growth detected. This effect was attributed to the growth of Mg islands smaller than the LEEM spatial resolution (see figure 5.7). The STM image in figure 5.7 (a), 4000 Å wide, shows a Mg coverage of less than a complete monolayer, where approximately half of the surface is covered by ramified islands. The gray inset shows an image with the same size from the LEEM (i.e.,4000 Å wide, where the two wide stripes correspond to the substrate terraces). As expected, the ramified monolayer islands are below the resolution of our LEEM instrument, and could well be the origin of the "rough" LEEM images of the Mg monolayer.The height of the monolayer islands changes strongly with the tunneling bias. Such effect is clearly seen in the comparison of the STM image acquired with positive and negative bias in figure 5.7(a) (we note that in the STM image the substrate has double steps, 4.2 Å high).

A more detailed image of the Mg film is shown in figure 5.7(b). The Mg islands have an arrangement of hexagonal protrusions on top of them, up to 0.7 Å high. We interpret these protrusions as reflecting the coincidence pattern between the Mg and the underlying Ru substrate, giving

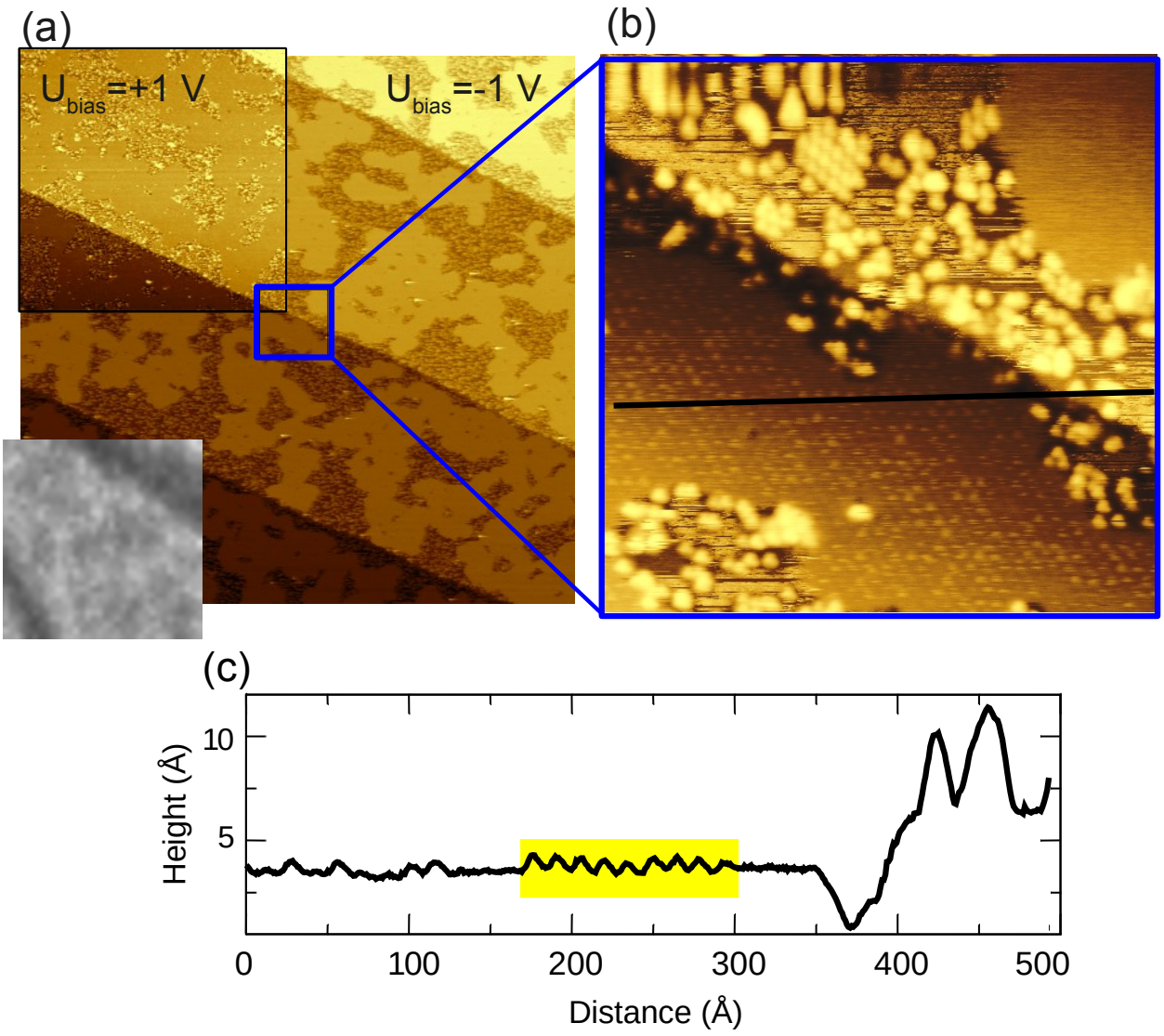

Figure 5.7 (a) STM image of the first Mg ML evaporated at room temperature over Ru(0001). The image is 4000 Å wide, and the tunneling parameters are I=1.27 nA and U=-1.06 V. The gray inset shows a section of a LEEM image of the same width (400 nm), with two diagonal substrate steps after growing nearly one complete Mg layer. On the upper top-left corner the same surface is imaged with the opposite bias (U=+1.06 V). (b) Image 500 Å wide of the same area showing both the hexagonal pattern on the flat islands as well as the features on the uncovered Ru substrate. A double-height substrate step runs diagonally across the image. (c) Profile along the line marked in image (b). The ordered protrusions on the film are highlighted in yellow.

rise to a moiré in real space and to the observed satellites in the LEED pattern. If so, one question is why the pattern is detected only in some parts of the islands (see figure 5.7 (c)). Actually, the pattern can be detected also in the areas of the islands that at first appear flat, albeit with a much smaller corrugation, at the resolution limit of our STM electronics. We propose that they actually correspond to molecules on the surface adsorbed at specific positions of the moiré pattern. In any case, the moiré spacing itself is 14 Å . This in-plane periodicity is close to 6 Ru atoms and would correspond to slightly over 5 Mg atoms if their lattice spacing was 3.10 Å . Presumably, this is the origin of the pseudo(5x5) periodicity measured in LEED when the deposited magnesium did not cover the entire Ru surface (see figure 5.4).

There seems to be material deposited on the Ru in between the flat Mg islands. An image of these islands with higher resolution shows grain-like structure with a mean size of the grains of around 12 Å (see figure 5.7(b)), albeit with a different orientation than the protrusions on the extended Mg islands. While we do not have an unambiguous explanation, we suggest that these grains are small islands of magnesium surrounded by adsorbed molecules of CO that inhibit further growth. To try to avoid preadsorbed molecules on the surface, the substrate was flashed just before dosing magnesium. Still, the time delay between flashing and dosing would allow the adsorption of a fraction of a monolayer of CO or H_2O (a few minutes at $5x10^{-10}$ mbar), which would be enough to decorate the observed islands. The first islands would then trap the impurities on the surface, and eventually, new magnesium islands would encounter a clean surface and would grow to give rise to the large flat areas. The observed effect is also probably at work in the LEEM images, where the first layers appear more "rough" than later ones.

Dosing more Mg eventually nucleates the second Mg layer. Figure 5.8 shows a typical image of the substrate totally covered by a monolayer of magnesium and several islands on a second level. In the underlying first layer there are several holes extending down to the substrate. These holes are more frequent in the terrace edges and display an irregular shape. The 2^{nd} ML islands

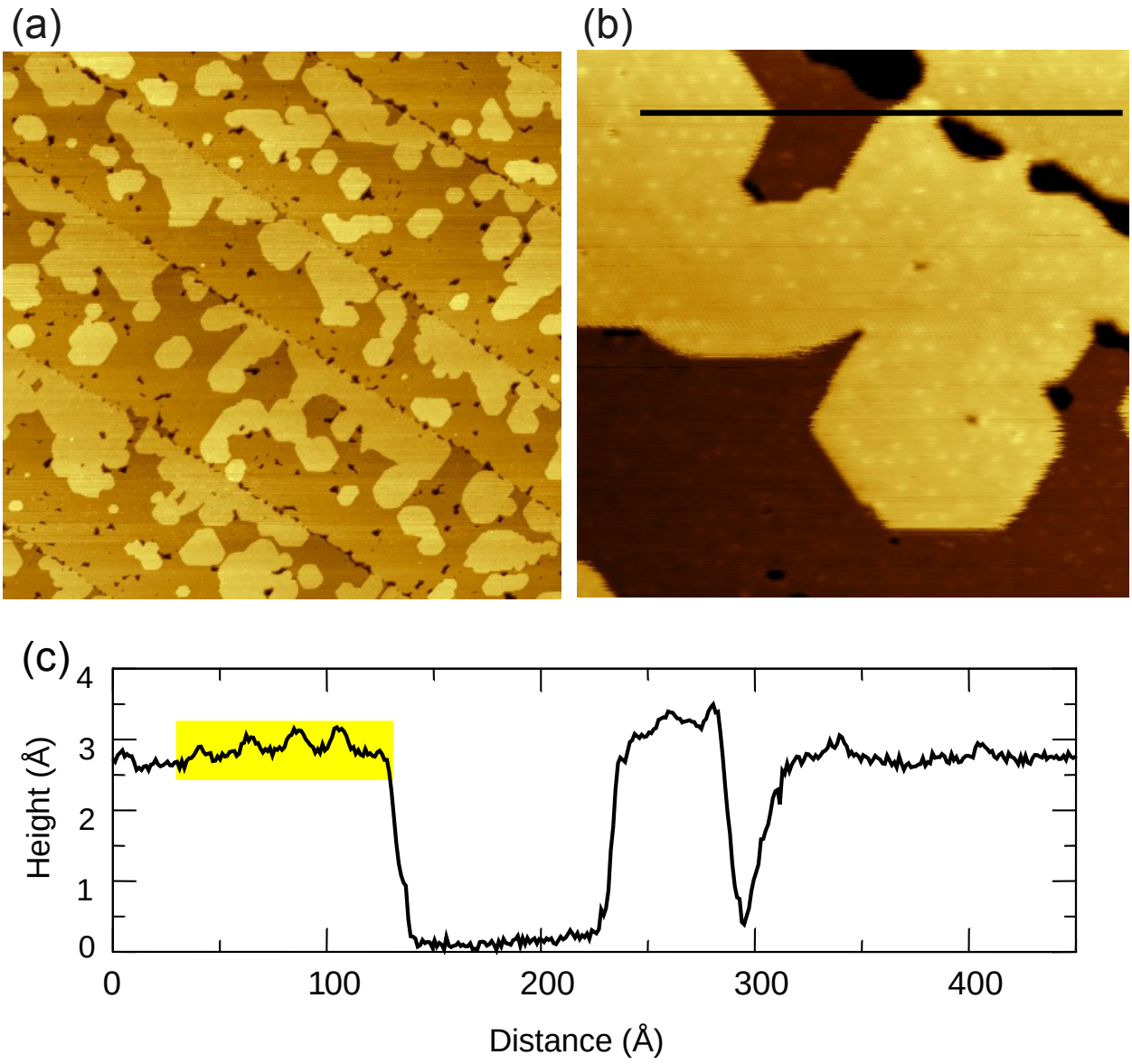

Figure 5.8 (a) Film with 2 ML islands and a nearly complete first layer. The image is 4000 Å wide. (b) Detail of the islands (the image is 500 Å wide). (c) Profile along the line marked in image (b). The ordered protrusions on the film are highlighted in yellow.

nucleate preferentially at the lower edge of the substrate steps, as detected also in LEEM images (see figures 5.1 and 5.2). The islands show compact edges along the compact directions of the substrate. The LEEM images also detected the preferential nucleation at the step edges (see figures 5.1 and figure 5.2). But this technique does not directly distinguish which side of the step has the lower or higher terrace, unlike STM.

The height of bulk-Ru and bulk-Mg steps are, respectively, 2.11 and 2.60 Å. The values experimentally determined by LEED are, for 9 ML thick film 2.64$\pm$0.02 Å [185], while for the monolayer and second layer they are 2.33$\pm$0.04 Å and 2.73$\pm$0.03 Å respectively [186]. The height we obtain relative to the Ru substrate for the submonolayer islands depends strongly on the tunneling bias, with a $\times$2 difference (from 2Å to 4Å), indicating that is it dominated by electronic effects. On the other hand, the step height for the second monolayer is not strongly bias dependent, and is close to the reported value, 2.6 Å, as show in the profile of figure 5.8 (c). Furthermore, the same profile shows that the step difference between a 2 ML Mg island and a 1 ML Mg region sitting on the adjacent (lower) substrate terrace is 0.5 Å. This corresponds to the difference in step height between Ru and Mg.

As in the submonolayer islands, there are protrusions arranged in an hexagonal pattern on the Mg islands. Their height is 0.4 Å. Their in-plane spacing is 2.2 nm (shown in the profile presented in figure 5.8 (c), nearly double the spacing of the protrusions for the sub-monolayer Mg islands. The same periodicity is observed on top of the 1 ML and the 2 ML Mg areas. Again, in addition to the clearly defined protrusions we detect a weak corrugation with the same periodicity in otherwise empty areas. We thus assume that the protrusions arise from molecules adsorbed on a moiré pattern. The periodicity of the pattern, 2.2 nm, agrees with the LEED measurements of the 7x7 compact layer, 21.2$\pm$0.5 Å(see figure 5.4 (d). After the Ru surface is completely covered with magnesium, additional Mg densifies the layer, and the in-plane spacing contracts from 3.45 Å to 3.10 Å and the moiré increases smoothly from 1.2 to 2.2 nm. The second Mg layer islands

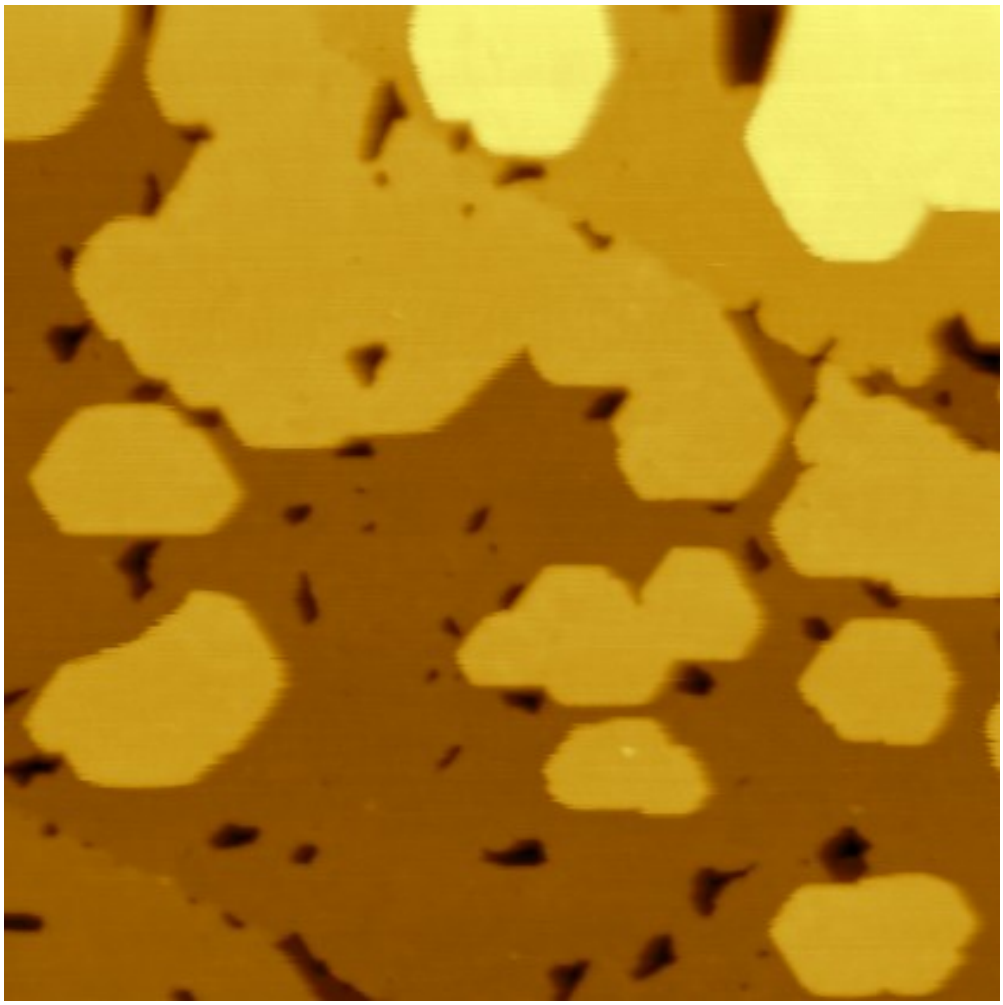

Figure 5.9 STM image of 2 ML of Mg with 3 ML islands over Ru(0001). The image is 1500 Å wide.

start to nucleate only when the latter value is reached. Mg is a system where the moiré periodicity can be continuously tuned between 10 and 20 Å , similar to a few metal/metal systems such as Pd/W(100). This behavior might be used to produce ordered arrays of molecules with a tunable separation. The next layers grow in the same way as the second layer, as shown in figure 5.8: the islands nucleate again preferentially at the terrace edges, adjacent to ascending Ru steps. Smaller islands (width of around 200 Å) display sharp edges and hexagonal shapes. We observed no signs of a moiré pattern on Mg thicker than two layers.

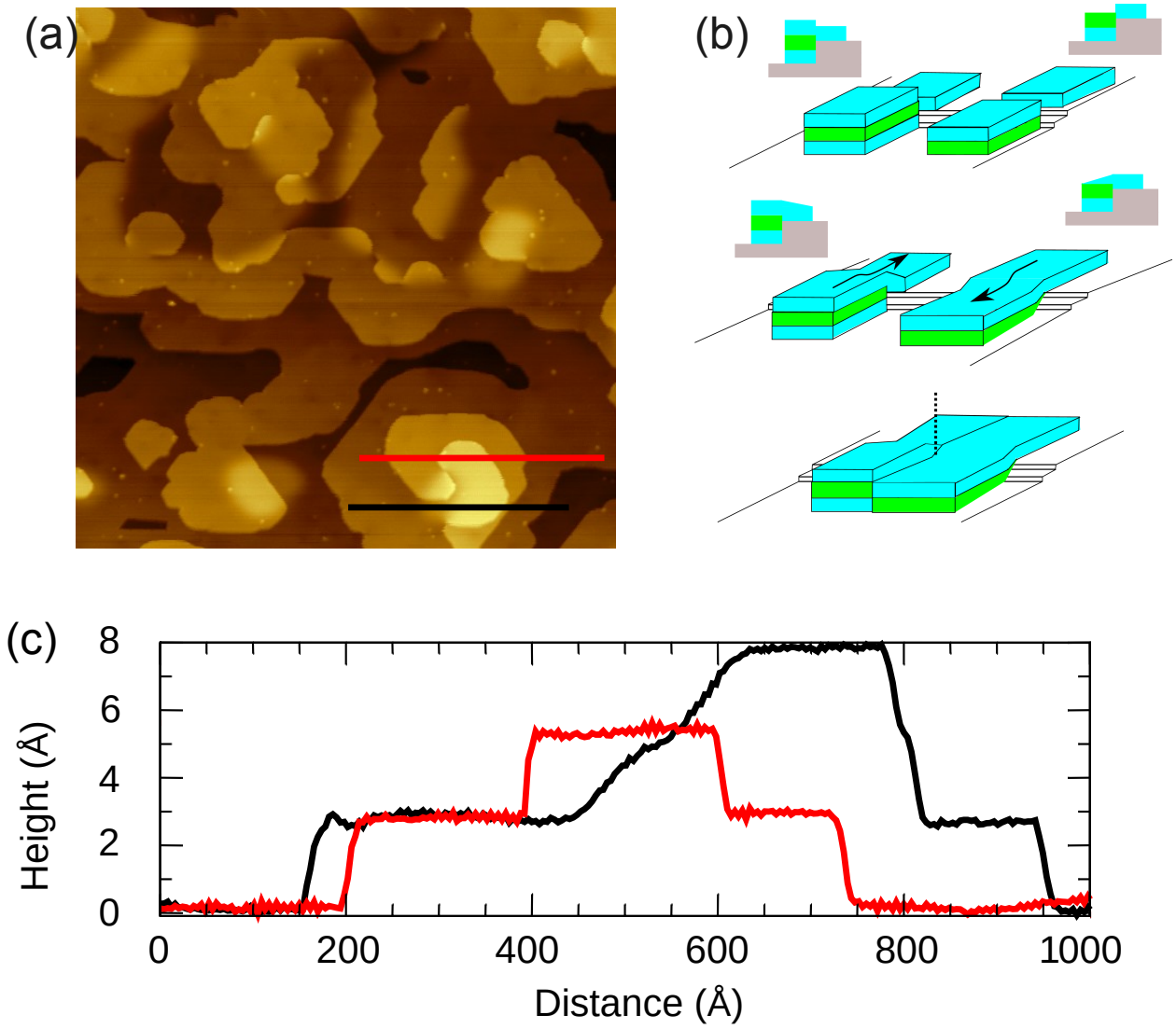

Figure 5.10 (a) STM image of 5 ML of Mg over Ru(0001). The image size is 2070 Å wide. (b) Schematic of a suggested origin of the screw dislocations in the film. On the left, two islands with the same stacking connect across a substrate double step. On the right, the two islands across the Ru double step have different stacking. When the two different connected islands coalesce, they originate a screw dislocation. (c) Line profile along the red and black lines in image (a).

5.3.2 Thicker films

Thicker films contain a high density of points where one or more Mg steps originate, as shown in figure 5.10 (a). These points are where dislocations, with a component of their Burgers vector perpendicular to the surface, emerge at the film's surface. At the origin of the dislocations we find the same type of sharp steps observed in thinner films and also smooth steps where the height change takes place along a much larger in-plane distance, up to 10 nm (see the profile presented in figure 5.10 (c).Since such screw dislocations can grow new layers without having to nucleate additional layers [195], regions with dislocations grow faster. As we do not observe spiral growth in large flat terraces of the substrate, like those followed by LEEM in figure 5.2, substrate steps seem to be required to generate the dislocations,together with a minimum film thickness.

Similar observations have been reported in other hcp epitaxial systems, such as Dy films on W(110) [196] or ice on Pt(111) [197]. The same behavior is also described in misoriented nanocrystals [198]. While in the latter case the meeting point of three nanocrystals is the proposed origin of the screw dislocations, in thin films the presumed explanation lies in the coalescence of a minimum of three islands. Two islands are on the same substrate terrace. One of them has a stacking fault. The third island is on an adjacent substrate terrace. We propose, following [197] that a crucial point in the ultra-thin film case is the presence of stacking faults in the film and substrate steps that differ in height from film steps. (Both can be understood to provide the small misorientation of the nanocrystal case). This kind of interface defect has been much discussed under the general name of a "disconnection" [199]. In the ruthenium substrate, double steps are often observed (see figure 5.7 (a)). A Ru double step has a height of 4.2 Å . On the other hand, two Mg (bulk-like) steps are 5.2 Å high. That implies that to connect between them, the Mg layers on both sides of such substrate step are offset by 1.0 Å if they connect islands with the same stacking (see left side islands of the schematics of figure 5.10 (b)), or by 2.6–1.0 = 1.6 Å for islands of different stacking where the first island is one layer thicker (see right side islands of the same schematic).

If both types of regions then coalesce, the meeting point will have a screw dislocation, with an abrupt step on one side and a smooth step on the other side of the screw dislocation. These steps initially follow the location of the substrate step. (The order in which the islands connect in figure 5.10 has been chosen for clarity.) We believe that this mechanism, or related ones, can explain the presence of screw dislocations in Mg films grown on stepped areas of the Ru substrate as well as their absence in large flat terraces.

5.4 Conclusions

By means of low energy electron microscopy and scanning tunneling microscopy we have characterized in real-space the growth of Mg films on Ru(0001), from less than one layer to 10 ML. The multilayer films, grown at temperatures between room temperature and 390 K, present a strict layer-by-layer growth mode with at most three different levels exposed. The submonolayer islands of Mg on Ru present a moiré pattern with a periodicity of 1.2 nm corresponding to a pseudo-5x5 LEED pattern and consistent with a Mg in-plane lattice spacing of 3.45 ± 0.07 Å. When the monolayer is completed at the start of second layer growth, the layer is compacted reaching a lattice spacing of 3.10 ± 0.06 Å reflected in a real-space moiré pattern of 2.2 nm and a 7x7 LEED pattern. The moiré pattern is only detected by STM up to the second monolayer of Mg. Thicker films have stacking faults as detected by dark-field LEEM and, on stepped areas, present screw dislocations. The latter arise due to the mismatch in Mg and Ru step heights on stepped areas. Electron reflectivity shows quantum size effects in the unoccupied bands, indicating an abrupt Mg-Ru interface for the thicker films.

Chapter 6

Hydrogen on Mg films

6.1 Introduction

Among the potential hydrides for H storage [200], magnesium hydride (MgH_2) has been singled out due to magnesium's low cost, availability and lack of toxicity. Furthermore, large amounts of H, up to 7.6 Wt %, can be stored as MgH_2 [201]. Well-known limitations are the thermodynamics requirements (up to 600 K for H release) and slow kinetics. Possible solutions to address these problems are the use of small nanoparticles [202], the alloying with transition metals [83] or a combination of both approaches [203]. Surface-science studies, under ultra-high-vacuum (UHV) conditions, of well-controlled Mg surfaces interacting with H hold the promise to understand the limiting steps in magnesium hydridring/dehydriding. But such studies are scarce [204]. To avoid the problems involved in the use of Mg single crystals, thin films can be grown on several substrates with high perfection [134, 205]. By this method, Chorkendorff et al. have performed hydriding studies of Mg(0001) films on Mo(111) [206]. The characterization techniques employed were thermal desorption (TD) and x-ray photoelectron spectroscopy (XPS). The main findings confirm several ideas that had been put forward in less-controlled experiments, such as the lack of reactivity

to molecular hydrogen [206], the deleterious effect of magnesium oxide on the hydride formation [207] and the possibility of using transition metals such as Pd [208] to dissociate H_2 and provide a source of atomic H. But to the best of our knowledge, no study has resolved the formation and decomposition of MgH_2 in real space.

In this chapter[1], we study the growth and decomposition of thin layers of Mg and magnesium hydride on Ru(0001) using LEEM.

6.2 Mg layers upon hydrogen exposure

The growth and structure of Mg films has been described in the previous chapter. Exposure to molecular hydrogen with a total dose of over 200 L produces no detectable changes in the Mg films (as reported before [206]). Figure 6.1 shows selected frames during molecular hydrogen exposure. In contrast, figure 6.2 shows selected frames during exposure to the same dose of atomic hydrogen. Just after turning on the H_2 cracker (figure 6.2), black islands start to nucleate and grow, the signature of a first-order phase transition.

With increased exposure time, there is little further nucleation. Instead, the initially nucleated islands grow. This implies that nucleation is a rare event that requires a large supersaturation of H atoms on the Mg film, a supersaturation that is removed by the nucleation and growth of the hydride. The lateral growth of the islands is initially fast but slows down markedly with time. Eventually they cover most of the field of view. The growth of black islands does not modify the distribution of the Mg islands (the brightest regions in figure 6.2), indicating that there is not significant Mg diffusion under atomic hydrogen exposure. The dark islands are stable in UHV at temperatures below 460 K.

[1] Most of the information of this chapter has been published in T. Herranz, K. F. McCarty, B. Santos, M. Monti, and J. de la Figuera, *Chem. Mat.* **22** (2010) 1291, from where it has been reused with permission.

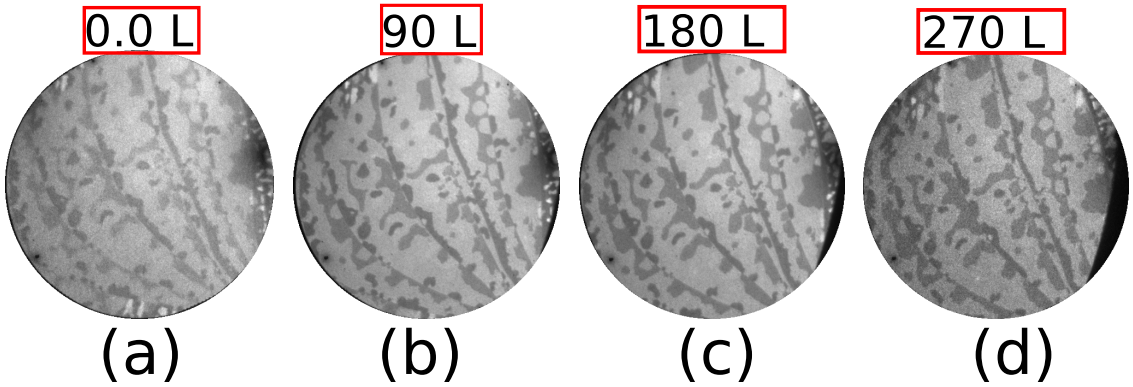

Figure 6.1 LEEM images of a 10 ML Mg/Ru film exposed to molecular hydrogen at 305 K. The FOV is 7 μm and the electron beam energy 3.14 eV. Hydrogen dose is: a) 0.0 L b) 90 L c) 180 L d) 270 L

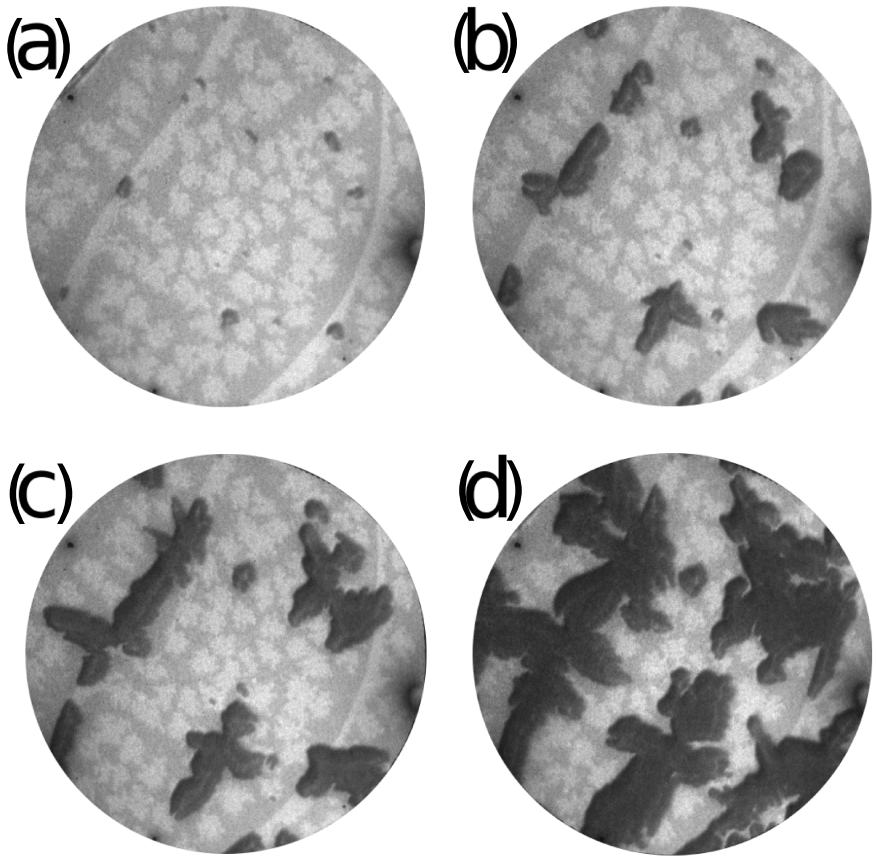

Figure 6.2 LEEM images of a 10 monolayers Mg/Ru film exposed to atomic H at 305 K. The FOV is 15 μm and the electron beam energy 1.25 eV. H dose: a) 90 L b) 250 L c) 850 L d) 1200 L

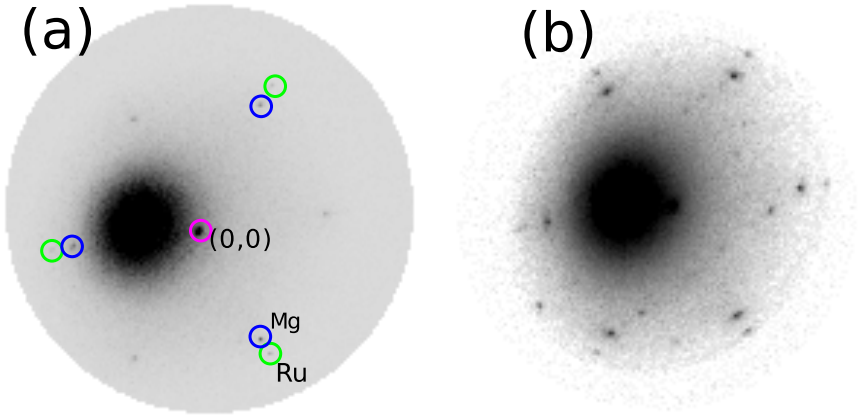

Figure 6.3 (a) LEED pattern from a 4 layers Mg film acquired at 150 eV (b) LEED pattern obtained from a black island attributed to MgH_2 acquired at 15 eV

6.2.1 LEED

The LEED patterns of the 4 ML thick Mg films in Figure 6.3 (a) shows two sets of 6-fold diffraction spots, one set from the film and the other from the substrate. Attempts to obtain diffraction patterns from the black islands were frustrated because of the strong beam damage caused by electrons with kinetic energy higher than a few eV. So the LEED pattern of Figure 6.3 (b) was taken at 15 eV and exposing the area to the electron beam for less than 1 second. The LEED patterns from black islands have sharp diffraction spots distinct from those of Ru(0001) and Mg(0001), showing that the black islands are crystalline. Different patterns were obtained from different islands, suggesting that they can have different orientations. LEEM images of the black islands during growth and decomposition were acquired using electrons of sufficiently low energy (0.6-1.3 eV) that they only interact weakly with the surface (so-called mirror-mode microscopy) [61].

6.2.2 Thermal desorption spectroscopy

After exposing to hydrogen (either molecular or atomic), the films were heated in UHV and the surface was simultaneously imaged by LEEM and gas generation monitored by TD. The desorption

of Mg exposed to molecular hydrogen is observed to take place layer by layer from 450 K. At 460 K, only the first layer of Mg remains on the Ru(0001) surface. This layer is more strongly bound to the substrate than to the Mg layers above and it desorbs at much higher temperatures, as reported by Over et al. [205]. The evolution of the m/e=2 signal after molecular hydrogen exposure is a smooth function of temperature (see bottom curve in Figure 3). The very broad peaks are attributed to H desorption from the manipulator due to the non-ideal TD setup, and correlate well with the m/e=28 signal (CO). The behavior of the films exposed to atomic hydrogen, where the growth of black islands was observed, is markedly different. In the LEEM images, there is no change up to temperatures around 450 K, where desorption of the Mg layers starts. At the heating speed used, the Mg islands do not exhibit Ostwald ripening [209] prior to desorption. Only when the temperature reaches 463 K in a film originally composed of 8 Mg ML with some 9 ML islands, do the dark islands start to disappear. By 479 K the islands are gone, leaving only a shadow of where they were.

Correlated with the disappearance of the black islands, there is a sudden spike in the m/e=2 TD signal, as seen in the upper curve in Figure 6.4. No spikes were detected in any other signal (m/e of 18, 24, 28 and 32 amu were monitored). This implies that the hydrogen release and the decomposition of the black islands produced during exposure to H are linked. Consequently we identify the black islands as magnesium hydride. The temperature at which the spike in the m/e=2 signal appears is in agreement with the one observed by Chorkendorff et al. for the decomposition of Mg hydride thin films (less than 10 ML) [206]. In agreement with the relative stability of magnesium and its hydride, the decomposition temperature of the hydride is by about 10 K higher than the sublimation temperature of Mg itself [206].

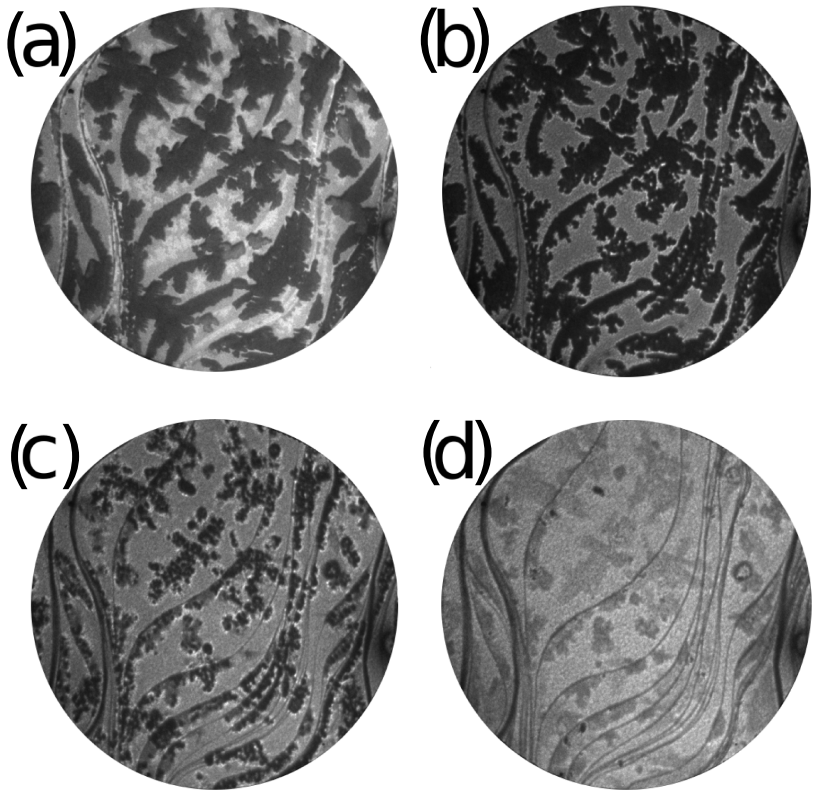

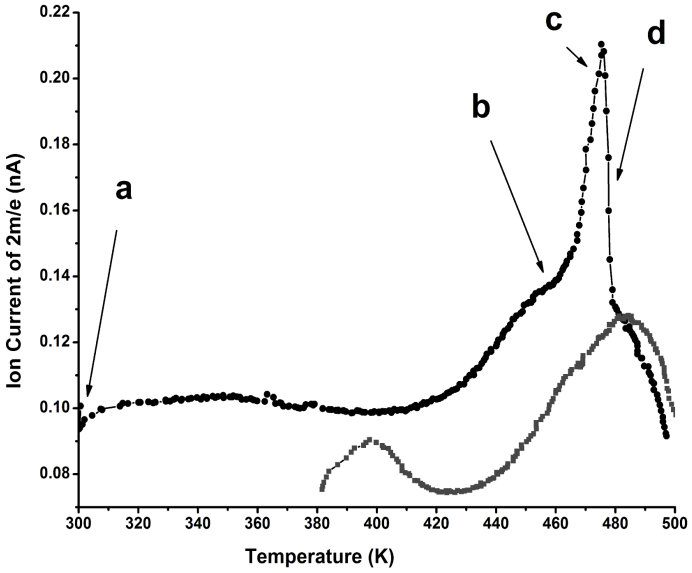

Figure 6.4 Upper: LEEM images during thermal decomposition of hydride. The FOV is 15 μm. Plot: TD signal of m/e=2. The lower curve corresponds a 9 ML Mg/Ru film exposed to H_2; the upper curve to a similar film exposed to H. Labeled temp.correspond to the images a-d.

6.3 Discussion

We have explored the dependence of the magnesium hydride islands as a function of initial Mg thickness and H dose. As shown in figure 6.5, the decomposition temperature is reduced by $\sim$10 K when the Mg film decreases from 9 to 4 ML thick layers. An obvious question is why the starting thickness of the Mg layers should have any influence on the MgH_2 stability. This is specially puzzling because by the time the hydride starts to decompose there is hardly any magnesium left on the Ru(0001) substrate, except for the initial Mg layer. A likely explanation is that the film thickness influences the thickness of the hydride grown on top: thicker films can accommodate thicker hydride islands. The depth of the hydride islands cannot be determined from the LEEM images. However, the slowdown of the lateral growth under atomic H exposure could imply that the growth of the hydride continues into the Mg film forming 3D islands. The decomposition temperature of hydride islands grown for a film with the same thickness, but with a dose of 100 L ($\sim$1/10 of the dose employed in Figure 6.5) is strongly reduced by 20 K, as detected by LEEM. This result can be reconciled with the data shown in Figure 6.5 if we assume that the hydride islands grew during the initial stages mostly in-plane (bi-dimensional shape), and only later (if the film is thick enough) three-dimensionally.

6.4 Conclusions

In summary, we have followed by means of simultaneous LEEM and TP the growth and thermal desorption of Mg and magnesium hydride on Ru(0001). The disappearance of the hydride is simultaneous with a spike in the m/e=2 amu signal in the background pressure of the experimental system. We have studied the effect of temperature, hydrogen dose and Mg film thickness on the growth kinetics and on the thermal desorption of the hydride. Magnesium sublimates at lower temperatures than the thicker hydride formed. An increase in the decomposition temperature of the

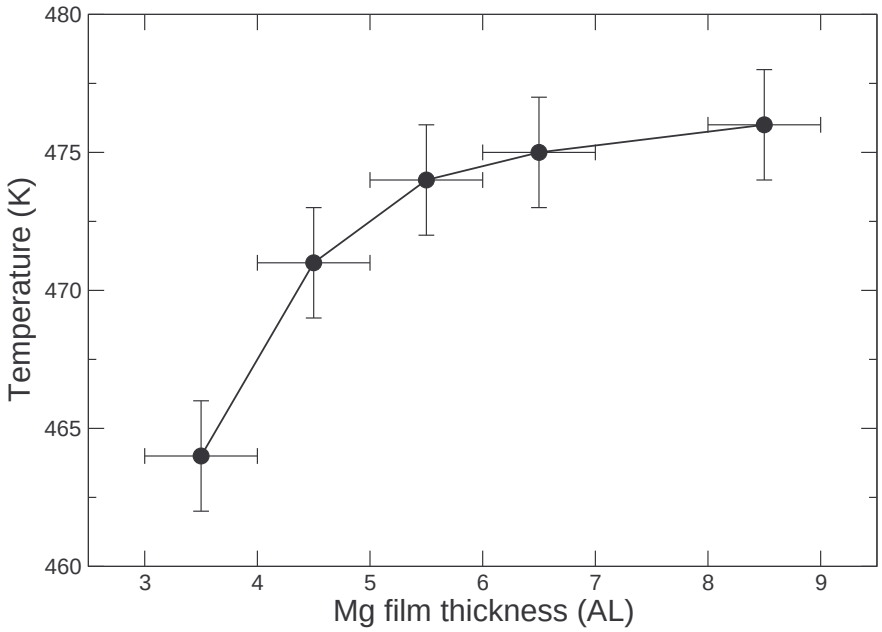

Figure 6.5 Dependence of the peak of the 2 amu signal as a function of the Mg film thickness before exposing to H. Horizontal error bars: presence of islands with$\pm$1 AL in the film. Vertical error bars: $\pm$2 K (variance in the temp of the spike in H_2 evolution observed in control experiments).

hydride is observed the thicker the original film used to growth the hydride. This is attributed to the more three-dimensional character of the hydride grown. This real-space nanometric study provides a way to explore the kinetic limitations on magnesium hydride formation and decomposition.

Chapter 7

Growth and Magnetic Domains on Co films

7.1 Introduction

Magnetic thin films often present different properties that bulk materials [210]. For example thin films can present larger magnetic anisotropies (up to one order of magnitude larger [42, 211]) than the bulk. These differences arise from the increasing importance of the surface contribution to the magnetic anisotropy when the thickness of a film is reduced. This surface term does not depend of the number of layers, but only on the topological and crystallographic structure of the interface between the substrate and the ferromagnetic film grown on it. This fact implies that a good characterization for a proper understanding of the magnetic properties of the films is very important. For example, the discrepancies regarding the magnetization easy-axis in Co/Au(111) reported by Allenspach [212] and Pommier [213] were attributed to differences in the growth mode of the films. Other example is the Curie temperature of Co monolayers, reported to be the same as for bulk, while later work attributed the result to a coverage determination problem [214].

In this chapter we study the micromagnetic structure of large, 3 ML thick, Co islands grown on Ru(0001) at 550 K and the relationship existing between their structure and magnetization patterns.

For completion, we also have studied the growth and the magnetization easy-axis orientation of thin Co films grown on Ru(0001) at RT. Although the structure and orientation of the magnetization easy-axis of Co/Ru films have been already studied in our group [73, 128], we have considered necessary to repeat some of those experiments in order to favor the understanding of the new results on this system that we will be presenting along chapter 7 and 8 of this thesis.

7.2 Large Co islands on Ru

We first grew Co films up to 3 ML at elevated temperature, typically 550 K. We selected this temperature because:

- We wanted 3 ML Co islands with lateral dimensions as large as possible and
- it is not enough as to produce alloying of Co with the substrate.

As it will be presented later in this chapter, Co islands grown at RT have a typical size of 9 nm, and they are too small to be observed by LEEM. To increase the island size, the growth parameters can be changed. Decreasing the flux of incoming Co atoms during dosing, or increasing the temperature of the substrate during growth decreases the density of nucleated islands, as the Co atoms being deposited on the surface have a higher chance of reaching preexisting Co islands before encountering another atom. As temperature has an exponential effect on islands size, it has a much more pronounced effect than the change in flux. But a higher temperature means also a higher probability of interdiffusion with the substrate atoms. We have found that a growth temperature of $\sim$550 K together with an atom flux of $\sim$ 0.3 ML/min provide islands as large as a micrometer and does not give place to Co-Ru alloying.

7.2.1 Growth

The growth of thin Co films up to 3 ML at 550 K was followed in real time by LEEM. Figure 7.1 shows selected frames from a LEEM image sequence acquired during growth. We can see that Co grows at 550 K in a layer-by-layer mode on large terraces of Ru(0001) despite the 8% misfit between the Co and Ru bulk in-plane lattice parameters [27]. Figure 7.1 (a)-(f) shows the nucleation and growth of the first and second layers of Co. The Co islands present a triangular shape[1], and all the islands have the same orientation in the same substrate terrace. In adjacent terraces, the islands change their orientation by 180°. The nucleation of the second layer is not detected until the first layer is completed. The second layer nucleates also as triangular islands, with the islands rotated by 180° respect to the first layer islands. The third layer of cobalt grows as triangular islands too [figure 7.1 (g)-(h)]. But in this case the islands present two orientations on the same substrate terrace.

El Gabaly et al. [27] discussed the triangular shape of the islands, a finding which had already been reported previously [215, 216]. They suggested that the triangular shape of Co islands was given by kinematic limitations. To explain the triangular shape of the islands, we consider a bi-dimensional hexagonal-shaped island on a hexagonal substrate [figure 7.1 (i)]. An hexagonal island would present two types of step edges [figure 7.1 (i)]. The first type of step would present square facets (with the local geometry of a (100) facet, named type A), while the other type of step would present triangular facets (with the local geometry of a (111) facet, named type B) [190]. When an adatom reaches the surface of the substrate, it will diffuse on the surface until it is trapped by an island (or a substrate step). At the growth temperature, the energy of the adatom is not enough to overcome the trapping barrier, making the attachment to the islands irreversible. However, the

[1] This is more easily observed on the 2 ML islands because they are larger (and less dense) than the first layer. This trend continues in the 3 ML islands which are also larger and less dense than 2 ML islands. The measured island density for films grown at 550 K is shown in table 7.2.

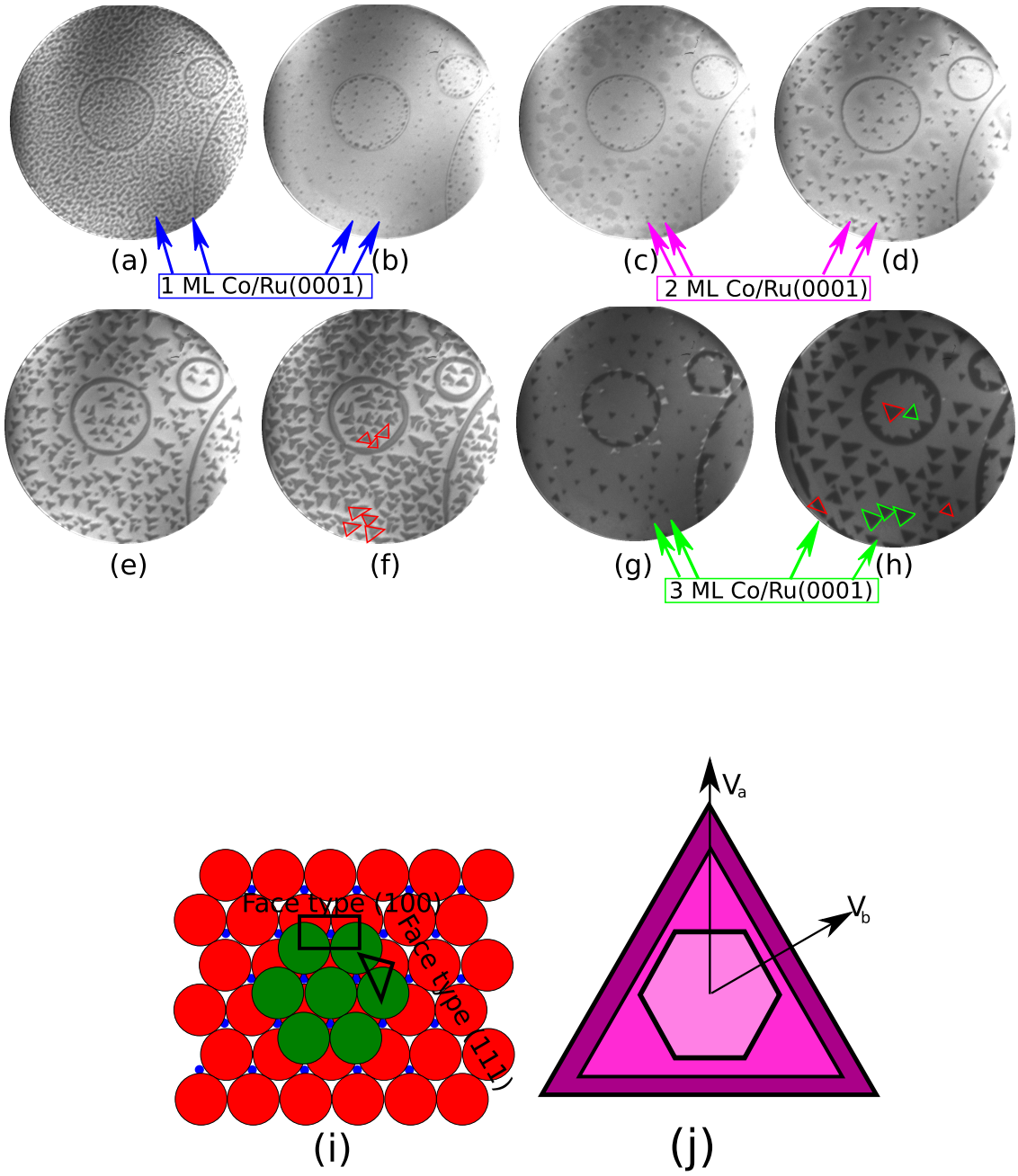

Figure 7.1 LEEM images acquired during the growth of Co on Ru(0001) at 550 K. (a)-(b) The growth of the first layer. (c)-(f) Completion of the first layer and nucleation of the second layer. (g)-(h) Nucleation and growth of the third Co layer. The field of view is 8μm and the energy of the beam is 7.2 eV. (i) Bi-dimensional island with an fcc stacking sequence on a hexagonal substrate. The island presents two different types of steps. (j) Starting from a hexagonal island, if the growth of one step edge is faster than the other the island will adopt a triangular shape.

Co coverage	$a_{\parallel}$	d_1	d_2
1 ML Co hcp	2.70	2.05±0.05	2.10±0.02
2 ML Co hcp	2.56±0.08	1.94±0.06	2.14±0.08
3 ML Co hcp	2.52±0.06	1.97±0.04	1.99±0.06
3 ML Co fcc	2.54±0.08	1.94±0.06	2.06±0.08

Table 7.1 Structural parameters obtained by El Gabaly et al. from the fits of LEED-IV curves recorder from different Co/Ru thick films. $a_{\parallel}$ is the in-plane lattice parameter, d_1 and d_2 are the interlayer spacing, for the first and the second layer, respectively.

adatom is able to overcome the smaller edge diffusion barrier and diffuse around the step edge of the island [190, 217]. An adatom trapped in a type-A step edge has a different environment than a adatom trapped in a step edge type-B so the diffusivity of the adatom will be different depending of the step edge. Thus the step edge where the diffusion is slower will grow faster than the other one [figure 7.1 (j)], giving rise to the observed triangular shape.

Islands with a different stacking present the same type of step edges but with different orientation, which by the same argument leads to a triangular shape with a different orientation. The conclusion is that if triangular islands with two orientations are found on the same substrate terrace, like in 3 ML Co/Ru, they should have a different stacking sequence. Islands with two orientations have been reported in several systems [217–220]. In Co/Ru, El Gabaly et al. [27, 73] confirmed by LEED-IV data the correspondence between the island orientation and the fcc/hcp stacking sequence in the 3 ML thick Co islands.

The change in island orientation between consecutive levels on the same substrate terraces is due to the film having an hcp stacking sequence. Labelling the two possible hexagonal planes of an hcp structure as A and B gives the sequence ABABABA for a substrate terrace. If Co grows keeping the same hcp stacking sequence, then the first Co layer will be b, having a sequence BABAb and the second will have BABAba. Both terminations Ab and Aba are rotated by 180 °,

and, in consequence, the triangular islands will also rotate by 180 ° to expose the same type of step edge. The same mechanism explains that the islands change orientation between one substrate terrace and the next one.

El Gabaly et al. also noted that films 2 ML, and thicker, present a moiré pattern [73] arising from a difference between the in-plane lattice parameter of the Co film and the substrate. In the 2 ML case they determined the lateral spacing to be a||=2.56 Å consistent with a unit cell of 14x14 Co atoms. The optimized structural parameters from the LEED-IV fit by El Gabaly et al. are shown in table 7.1.

Summarizing, the first and the second layer of Co on Ru(0001) grow keeping an hcp stacking sequence. The third layer presents islands with hcp and fcc stacking sequence on the same terrace.

7.2.2 Magnetization of 2 and 3 ML thick Co islands

The appearance and changes of magnetic domains while the Co film is growing were observed in real-space by SPLEEM for several films. We show a typical one in figure 7.2, where both selected LEEM (left) and SPLEEM (right) images (the electron-beam spin-polarization direction is in-plane) are presented. The LEEM images reflect the same sequence that was presented in the previous section: the growth of mostly triangular islands whose orientation reflects their stacking sequence. Unlike the previous sequence shown, the substrate terraces are smaller, and there is a substantial growth at the substrate steps. There are two multilevel pits on the substrate surface shown (that they are pits and not mesas is easily detected because the Co decoration grows only on the lower side of the substrate steps). In fact, the bottom of both pits is a round terrace. These features of the surface can be used to grow circular islands by filling them with the deposited material [221]. During the growth of islands one and two layers thick, no magnetic contrast (in the in-plane direction) was observed [figure 7.2 (e,f)]. Although the first layer of Co/Ru(0001) should present an in-plane easy axis of magnetization [222], its Curie temperature is below the growth

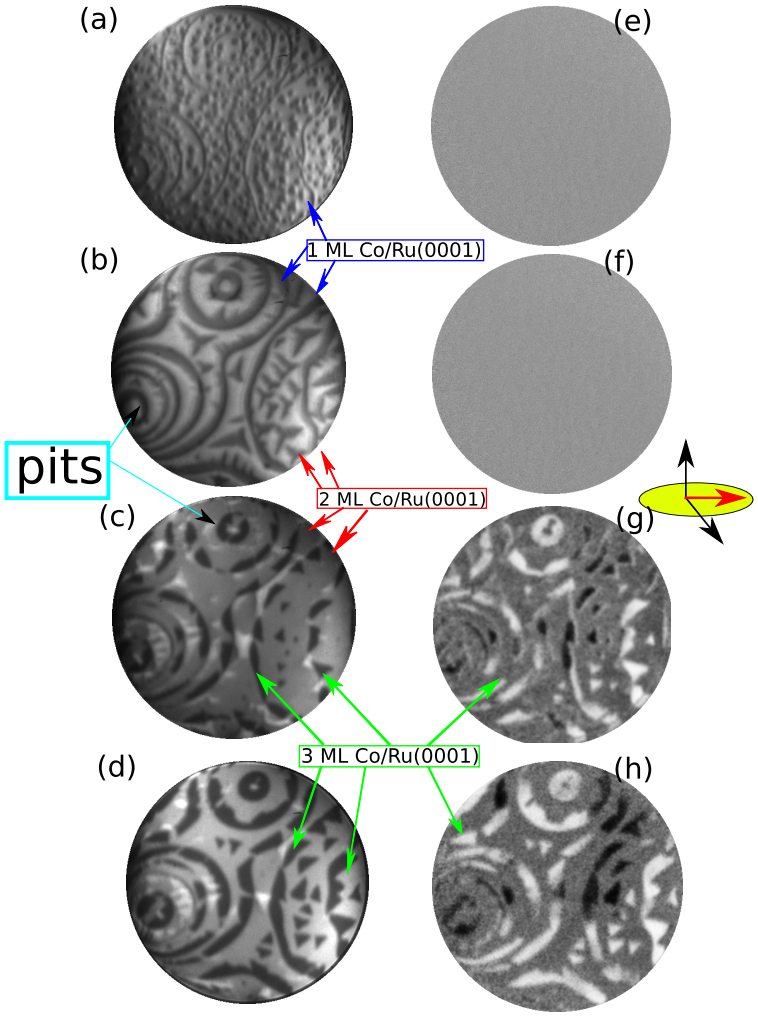

Figure 7.2 (a)-(d) LEEM and (e)-(f) SPLEEM images acquired during the growth of over 2 ML of Co on Ru(0001) at 550 K. The electron-beam spin-polarization direction was in-plane. Only the third layer presents magnetic contrast at 550K. The FOV is 8 μm and the beam energy is 7 eV.

temperature so the lack of contrast is to be expected. The 2 ML thick islands [figure 7.2(b,f)] also lack in-plane magnetic contrast. This is consistent with their previously reported out-of-plane magnetization. When the third layer appears, it shows in-plane magnetic domains [figure 7.2 (c)-(g)]. In some of the islands the magnetization direction changes during growth, as can be detected comparing figures 7.2 (g) and (h).

After the growth was stopped, the Co films were cooled to RT for further SPLEEM characterization. Figure 7.3 shows a LEEM image with SPLEEM images for three orthogonal directions of the electron beam spin polarization. The LEEM image [figure 7.3 (a)] shows 3 ML thick islands, which appear dark at the electron beam energy used (7.2 eV) on a continuous film 2 ML thick. The islands in the middle of the substrate terraces are triangular with two orientations. The triangular shape is less defined in the 3 ML thick Co areas adjacent to the substrate steps, although triangular edges are also detected. As discussed in the growth section, the triangular orientation of the islands reflects their stacking sequence. Figure 7.3 (b) presents the SPLEEM image with out-of-plane magnetization contrast. The 2 ML thick areas are the only ones than present black or white domains, that correspond to domains where the magnetization locally points out of the film (black) or into the film (white). The areas of the film which correspond to 3 ML appear gray in the same image, indicating that their out-of-plane magnetization component is zero. The domain walls of the 2 ML areas seem to be locked at the 3 ML thick islands, and they appear quite abrupt, with a domain wall size of 0.20 μm. The domains have an irregular shape, and can be as large as 6 μm. The last two SPLEEM images show the local magnetization along two in-plane orthogonal directions. Now the 2 ML areas present zero magnetization component in-plane, while the 3 ML areas present non-zero magnetization in both in-plane directions (their total magnetization is the vectorial sum of the magnetization along the two directions of the SPLEEM images [figure 7.3 (c,d)]. Most of the 3 ML thick islands do not present a uniform magnetization, showing changes in either in-plane component or both.

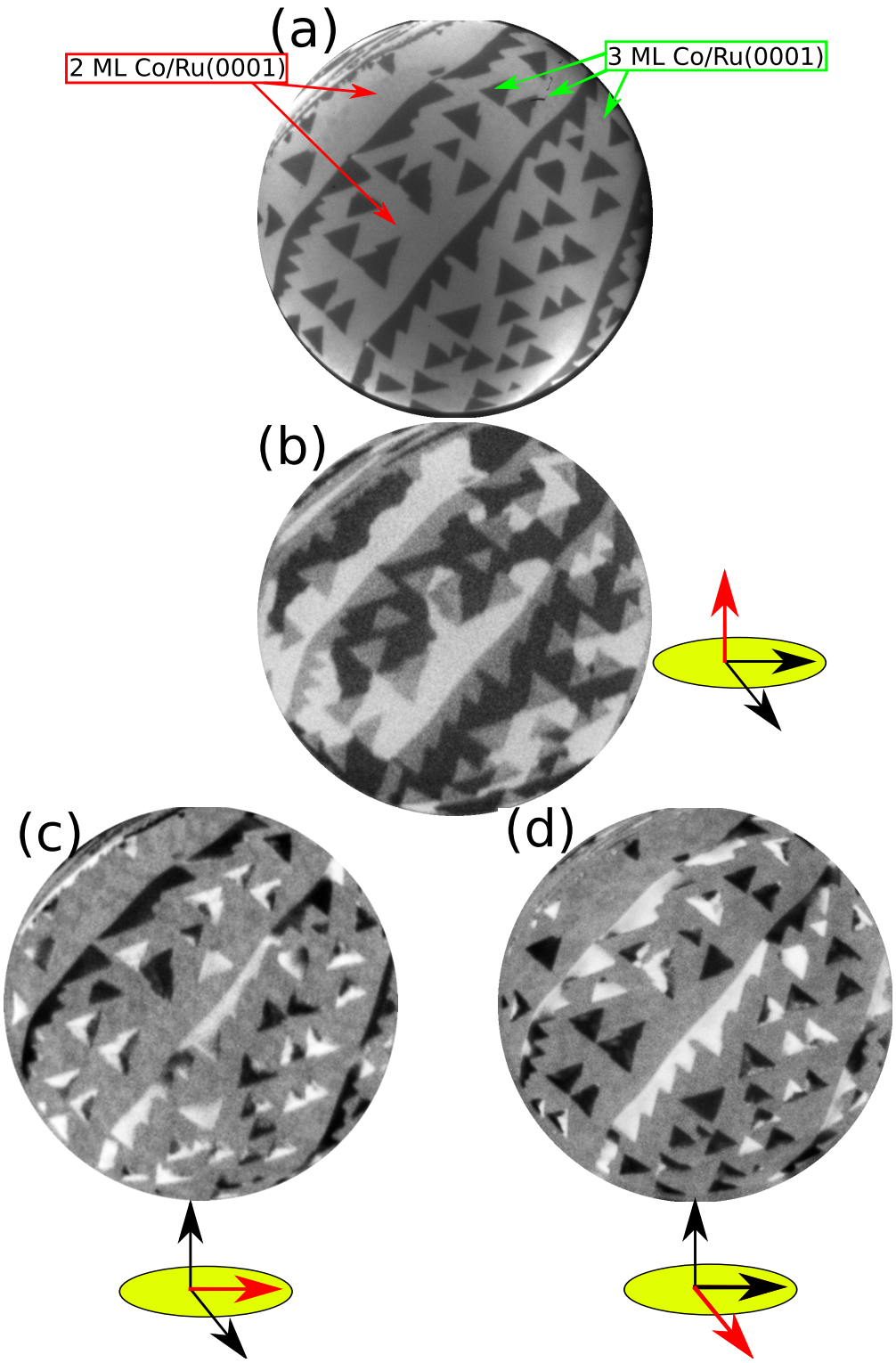

Figure 7.3 (a) LEEM image acquired after cooling down the sample to RT. (b) SPLEEM with the electron-beam spin-polarization direction out-of-the plane. Magnetic contrast is observed only from the 2 ML thick areas. (c)-(d) Magnetic signal with the beam polarization along two orthogonal in-plane directions. The FOV is 8 μm and the beam energy is 7.2 eV.

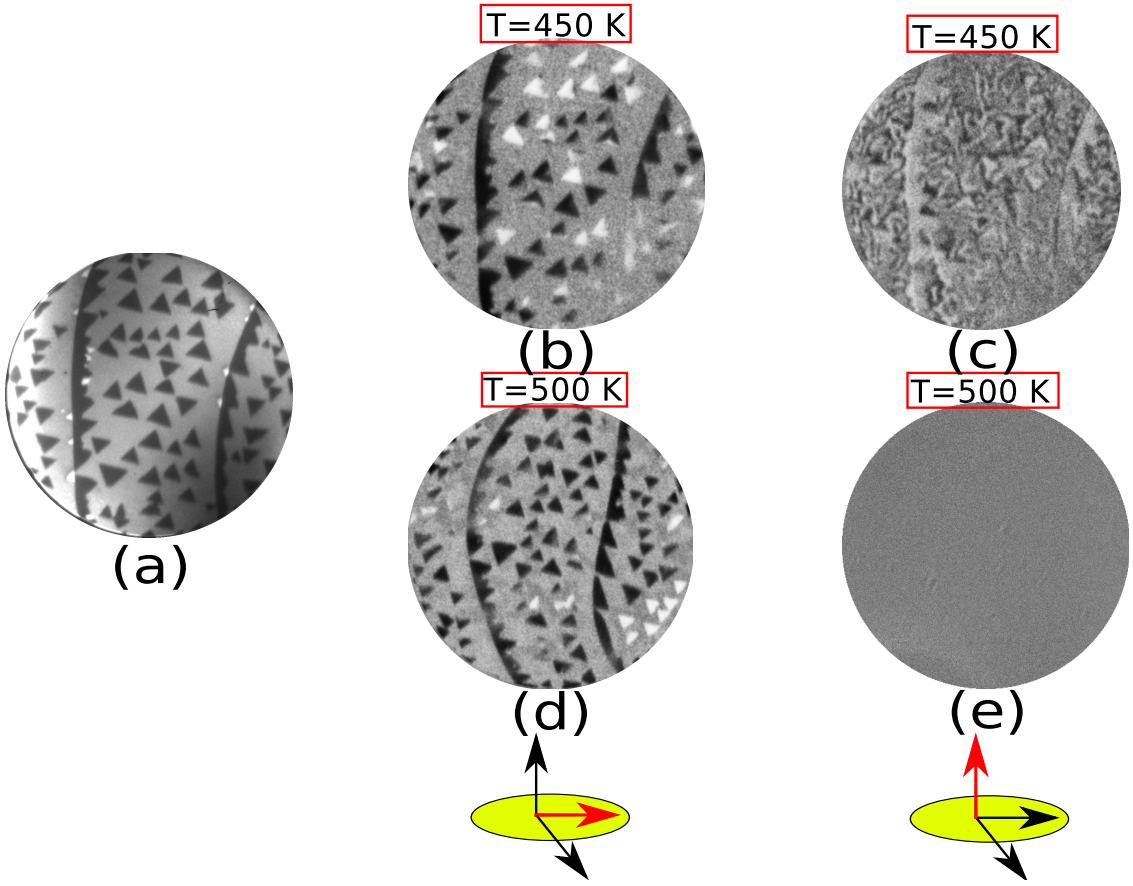

Figure 7.4 (a) LEEM image of 2.3 ML of Co/Ru(0001) acquired at 450 K (b)-(c) SPLEEM images acquired at 450 K. (d)-(e) SPLEEM images acquired at 500 K. The electron-beam spin-polarization is out-of-plane in (c)-(e). The electron-beam spin-polarization out-of-plane in (b)-(d). The FOV is 8 μm and the beam energy is 6.2 eV.

The Curie temperature is strongly thickness dependent. The SPLEEM images shown in [figure 7.4] were recorded from a Co film in consecutive temperature scans between the growth temperature of 550 K and RT, first with the electron-beam spin-polarization direction in-plane, and then out-of-the plane. While the 3 ML islands are always magnetized (although the magnetization of individual islands changed direction within the plane), the 2 ML areas only shown domain patterns below 450 K, and at first, with small sized domains. In consequence, we consider the Curie temperature of 2 ML Co to be 450 K.

The non-uniform magnetization of 3 ML islands can be observed in more detail in a film with larger islands, shown in figure 7.5. As before, 3 ML thick Co islands in the LEEM image the appear darker than the 2 ML areas. The two orientations of the 3 ML islands are marked in figure 7.5 (a), and as discussed previously, they correspond to islands that have an hcp stacking sequence (red triangle, islands pointing up) and an fcc stacking sequence (green triangle, islands pointing down), respectively. The identification of each sequence is done by comparing their orientation with the orientation of the islands of the previous layers during the film growth (not shown). In figure 7.5 (b) the SPLEEM image with in-plane magnetic contrast shows that the magnetic domain pattern present on each island seems to be related to the island stacking. In the figure, islands with an hcp stacking sequence (red triangle) present either single domains or two different domains separated by wide domains walls. In contrast, fcc islands (green triangle) present a more complex multidomain magnetic pattern. In these type of islands we can distinguish at least 3 different magnetic domains separated by sharp domain walls (sharp when compared with the wide domains of the hcp islands). In figure 7.5 (c) we present contrast profiles (which are related to the local magnetization) acquired across the two type of islands in the SPLEEM image. The average domain wall width in the hcp islands is $0.70\pm0.05\mu$m. In the case of fcc islands the domain wall width is $0.35\pm0.05\mu$m.

At RT the 2 ML thick areas surrounding the 3 ML thick Co islands are magnetized out-of-plane.

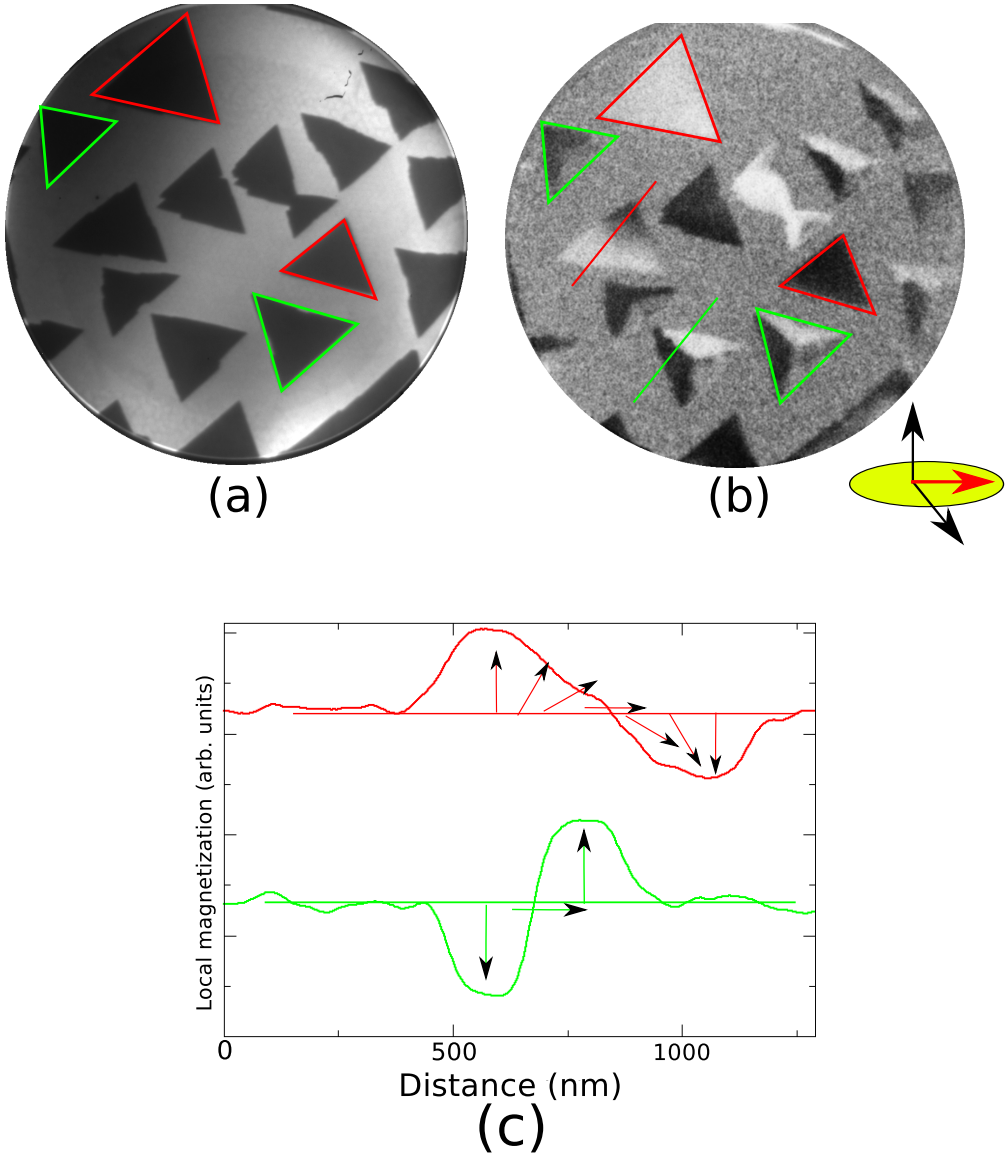

Figure 7.5 (a) LEEM image from 2.4 ML of Co on Ru(0001). (b) SPLEEM image of the same area. Islands with different orientation present different domain patterns. The electron beam spin polarization direction is in-plane. The FOV is 10 μm and the beam energy is 7.2 eV. c) Profiles acquired on both fcc (green) and hcp (red) 3 ML thick Co islands. The height on each profiles represents the local magnetization in each magnetic domain.

One open question is the possible influence of the 2 ML areas on the 3 ML magnetization. The 2 ML areas might couple the magnetization between different 3 ML islands, and the magnetization of the 3 ML islands might be some kind of closure domain from the 2 ML areas. To check for this possible effect, the temperature of the film was raised above the Curie temperature of the 2 ML film, and the patterns on the 3 ML thick islands were compared in figure 7.6. The first two images show a film with in-plane and out-of-plane magnetic contrast at 500 K. In the in-plane image, the 3 ML thick islands present either three domains in the typical pattern present on fcc islands, while the hcp islands are nearly single domain. There are also two circular pits of the substrate filled with 3 ML islands. Although the stacking of these islands cannot be detected from their shape (they are circular), they are probably hcp (at higher temperatures most of the growth from substrate step edges is hcp, and they present wide domain walls). As a consequence of the film temperature being above the Curie temperature of the second layer, no magnetic contrast is detected out-of-plane [figure 7.6 (b)]. When the film is cooled down below the Curie temperature of the second layer, the exposed 2 ML thick Co areas show magnetization with an magnetization easy-axis perpendicular to the film. Meanwhile, 3 ML thick Co islands mostly keep their magnetic domain patterns. Although there are some changes, the fcc islands retain their black-white-gray clockwise magnetization patterns[2]. This result indicate that the magnetic domain patterns observed in the 3 ML thick islands is not directly due to the coupling with the surrounding 2 ML areas.

In summary, 2 ML thick areas have an out-of-plane magnetization easy axis. The domains are quite large at RT, and the Curie temperature is estimated to be 445$\pm$10 K. The 3 ML thick Co areas are magnetized in-plane. The stacking sequence of the 3 ML islands influences their (in-plane) magnetic domain pattern. While fcc islands have sharper domain walls, and they present a peculiar three-domain pattern. The hcp islands show larger domain wall widths, and are often

[2]The difference in the morphology of the islands in figure 7.6 (c) and figure 7.6 (a) is due to a dewetting process that takes place slowly at temperatures above at 500 K.

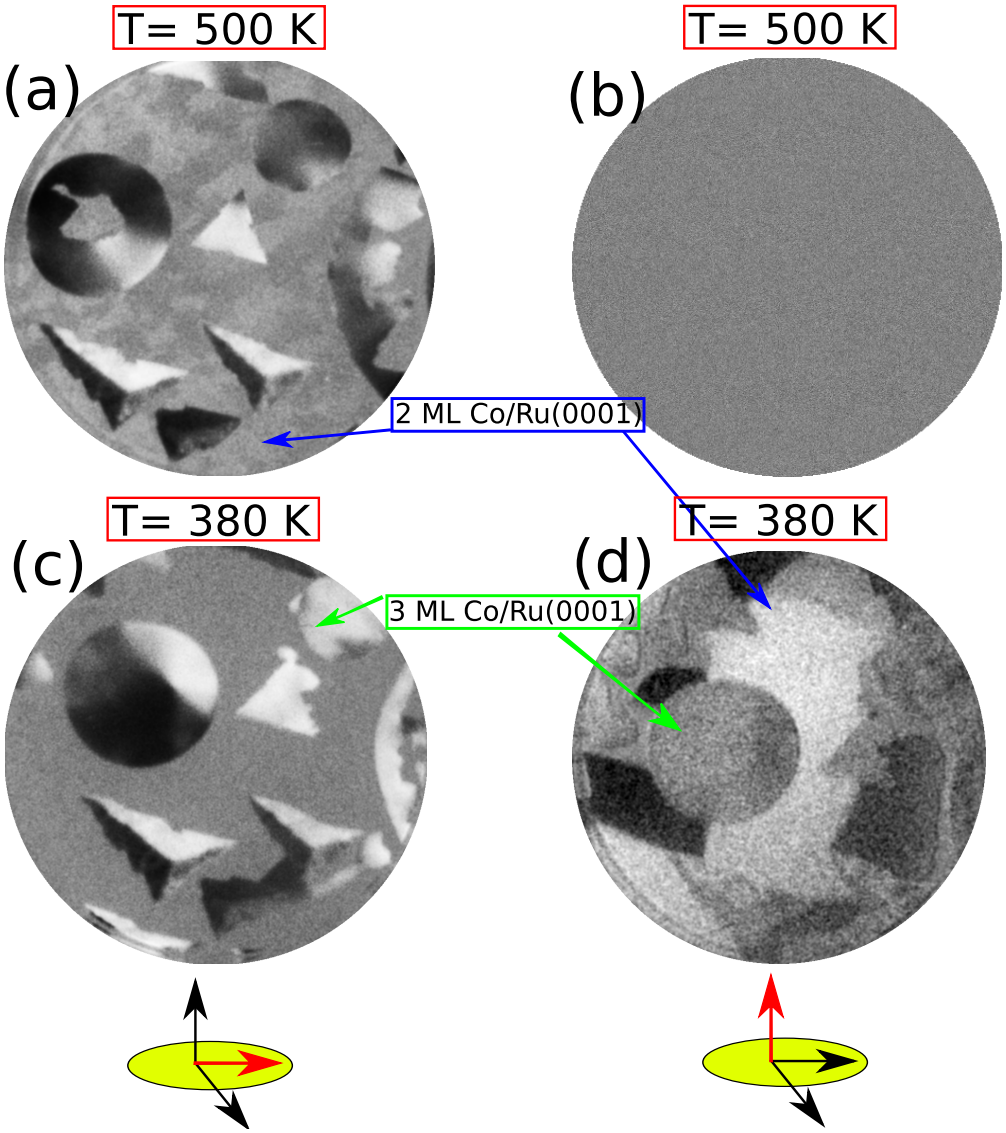

Figure 7.6 SPLEEM images acquired from 2.5 ML Co/Ru(0001) at two different temperatures. (a),(c) The electron beam spin polarization direction is in-plane. (b),(d) The electron beam spin polarization direction is out-of-plane. Beam energy was 7.2 eV and the FOV is 8 μm in both cases

single domain. The latter islands domain patterns are similar in triangular and round islands. The Curie temperature of the 3 ML islands is higher than 550 K.

7.2.3 Discussion

The origin of the magnetization easy-axis reorientation when going from 2 to 3 ML in thickness has been addressed theoretically in Ref. [222]. We focuss here in the magnetic domain patterns observed in 3 ML thick Co islands. The relationship between domain wall width and stacking sequence is intriguing. The observed domain wall widths are not very far from those found in other Co systems such as Co/Ru/Co trilayers [223] where the domains wall width is $\sim$0.2 μm or the 0.1–0.5 μm found in fcc Co disks [224]. However, they are much larger than than the 0.01 μm domain wall width found in ultrathin Fe/W(110) [225, 226], or in bulk Fe (0.02 μm [227]).

The domain wall in an ultra-thin film with in-plane magnetization is expected to be a Néel wall: due to the magnetic anisotropy energy, the magnetization rotates in-plane from one domain to another. This agrees with the lack of out-of-plane contrast along the domain wall that would be expected for a Bloch wall. The Néel wall width w is determined by the competition between the exchange energy (via the exchange stiffness[3]) and the in-plane magnetic anisotropy energy $K_{inplane}$. A larger exchange energy favors wider domain walls while a larger anisotropy energy favors thin walls. Clearly there is some difference in either the exchange stiffness or the in-plane magnetic anisotropy between fcc and hcp islands:

$$\begin{aligned} w_{hcp} &\sim \sqrt{\frac{A_{hcp}}{K_{hcp}}} \\ w_{fcc} &\sim \sqrt{\frac{A_{fcc}}{K_{fcc}}} \\ w_{hcp} &\approx 2 \times w_{fcc} \end{aligned} \tag{7.1}$$

Changes in domain wall widths due to changes in the film structure have been reported for

[3]The exchange stiffness is defined as JS^2/a where a is the lattice parameter, J is the is the exchange integral, and S is the spin moment [52, 228]

Fe [225, 226] and FeCo alloys [229]. In the case of Fe/W(001), Bodea et al. [226] suggested that the reduction of the domain wall width was due to a reduction in the exchange stiffness, caused by the strain of the pseudomorphic Fe films as the exchange stiffness A varies approximately with the interatomic distance d as d^{-5}. In their case, the strain found in pseudomorphic Fe films on W(110) could reduce the exchange stiffness by $\sim$40%. The fcc and hcp islands might be strained by different amounts. In fact, Co in hcp islands have been reported [27] to be more relaxed (less strain) towards the Co bulk in-plane lattice parameter [27] than hcp ones. But this difference in the lattice parameter between hcp and fcc Co is very small, so it would only reduce the exchange stiffness by $\sim$4%. The exchange energy might be somewhat different due to the stacking sequence, but it is not expected to differ widely. There are no obvious indications that fcc and hcp islands present large differences in the exchange stiffness. For example, their Curie temperatures are at least not widely different [figure 7.6][4]. First principle theoretical calculations [231] confirm similar values for the exchange constant for Co^{fcc} (0.16 meV) and Co^{hcp}(0.13 meV).

The other source of different wall widths might be the magnetic anisotropy energy. Higher values in the anisotropy of fcc vs hcp Co would explain the differences found between them. The problem is that we have not found in-plane anisotropy values for different stacking sequences. But the total magnetic anisotropy energy between in-plane and out-of-plane actually depends on the stacking sequence. The main contribution to the volume contribution K_v is the shape anisotropy, which does not depend on the stacking (in the case of bulk Co it has a value of -1.27 MJ/m^3 (9.3x10^{-5} eV/atom). The magnetocrystalline anisotropy energy, however, is negligible for buk fcc Co, but it is equal to -0.54 MJ/m^3 (3.9x10^{-5}eV/atom) for bulk hcp Co [211]. So in principle, large differences in the magnetic anisotropy are possible. Although this numbers are for bulk Co, also ab-initio calculations [232] have found that for films 3 ML thick of Co, the magnetic

[4] In mean-field theory the Curie temperature T_c depends linearly on the exchange energy J, $T_c = 2J/k_B$, where k_B is the Boltzmann constant [230]. No changes of the Curie temperature in both fcc and hcp 3 ML thick Co films were observed heating the sample up to 650 K.

anisotropy energy depends on the stacking sequence even to the point of changing its sign[5] . So it is expected that the observed changes arise from the magnetic anisotropy energy dependence on the stacking sequence of the 3 ML islands. Further theoretical studies will be required to confirm this hypothesis.

Another interesting result is the observation of particular magnetic patterns frequently observed on the fcc islands [figure 7.5 (b)]. The patterns consist of a periodic sequence of dark-gray-white domains when moving clockwise[6]. In figure 7.7 (a) we present one of the experimental images. Taking into account that the experimental image shows only the magnetization component along one in-plane direction, we can interpret the sequence of gray-levels as corresponding to the magnetization presented in figure 7.7 (b): the magnetization of each domain is aligned to each island side, curling around the central point.

The lowest energy magnetic configuration of a flat island has been calculated theoretically by micromagnetic calculations. For very small islands, smaller than the domain wall width, the lowest energy configuration is a single-domain state. Larger islands break up into a multidomain pattern. Before the multidomain pattern, a vortex state is found, where the magnetization curls continuously around a central point, but at the central core it either points up or down. The vortex core size is typically 10 nm wide [234, 235]. The presence of a vortex core depends on the aspect ratio of the nanostructure and the magnetic hardness of the material[7]. For a fixed magnetic hardness the presence of a vortex is given by the thickness of the magnetic material. Goll et al. [236] calculated that the critical thickness to obtain a vortex configuration in a Co platelet of similar dimensions to our triangles (1μmx1μm) is 20 nm. Similar results were found by different groups [237, 238],

[5]the calculated vales of the anisotropy (excluding the shape anisotropy energy) for 3 ML thick Co films on Ru(0001) are K_{Co}^{hcp}=0.184 meV, K_{Co}^{fcc}=-0.087 meV [232]

[6]The same patterns were observed in fcc Co islands on Ru by Mascaraque et al. [233] by x-ray magnetic circular dichroism with photoemision microscopy (XMCD-PEEM).

[7]The magnetic hardness is defined as $Q=2\mu_0 K/J^2$, where K is the magnetic anisotropy and J is the exchange energy

reporting that no out-of-plane magnetic signal is obtained in thin Co films or Co nanostructures with thicknesses below ∼22 nm. Experimentally, Oepen et al. [239,240] reported that as-grown Co films on Cu(100) present a single domain state. A similar result was found in other ferromagnetic thin films such as Fe/Ag(100) [241], but that state could be broken into multiple in-plane domains by applying a magnetic field. Similar effects have been reported in Co films after applying short magnetic pulses [242].

We suggest that as the Co islands grow, they are initially single domain. We note that during growth the heating filament used to keep the sample at the growth temperature generates an applied magnetic field of a few Gauss[8]. For the hcp islands, the domain walls are so wide that the islands remain mostly single domain while they grow until their final size. On the other hand, the fcc islands reach the limit size for the single domain state at smaller sizes, and they form several domains when reaching a micrometer size. The fact that the multidomain pattern has a definite chirality (the sequence is black-white-gray clockwise) is related to the shape of the island and the externally applied field during growth.

To understand the interplay of applied field direction and island orientation some tests were performed with the micromagnetic simulation package OOMMF [244]. We remark that the parameters for the OOMMF simulation do not correspond to the correct aspect ratio of our islands (0.6 nm thick and 1 μm wide) and that they are only intended as a first check on the origin of the domain pattern. More realistic simulations are being performed by Dr. Lucas Pérez at the UCM and the preliminary results seem to confirm the results presented here. To generate the simulated pattern, a magnetic field was applied until the Co island was uniformly magnetized. The field was then removed by small steps and the configuration energy minimized for each step. The grey contrast on the simulation corresponds to the component of the magnetization along the upper-right

[8]This heating filament is made of a W wire with a spiral shape and placed behind the sample. To keep the sample temperature at 550 K, a 2.5 A current is applied through the wire that creates a magnetic field estimated to be 1–2 Gauss [243] within the film plane.

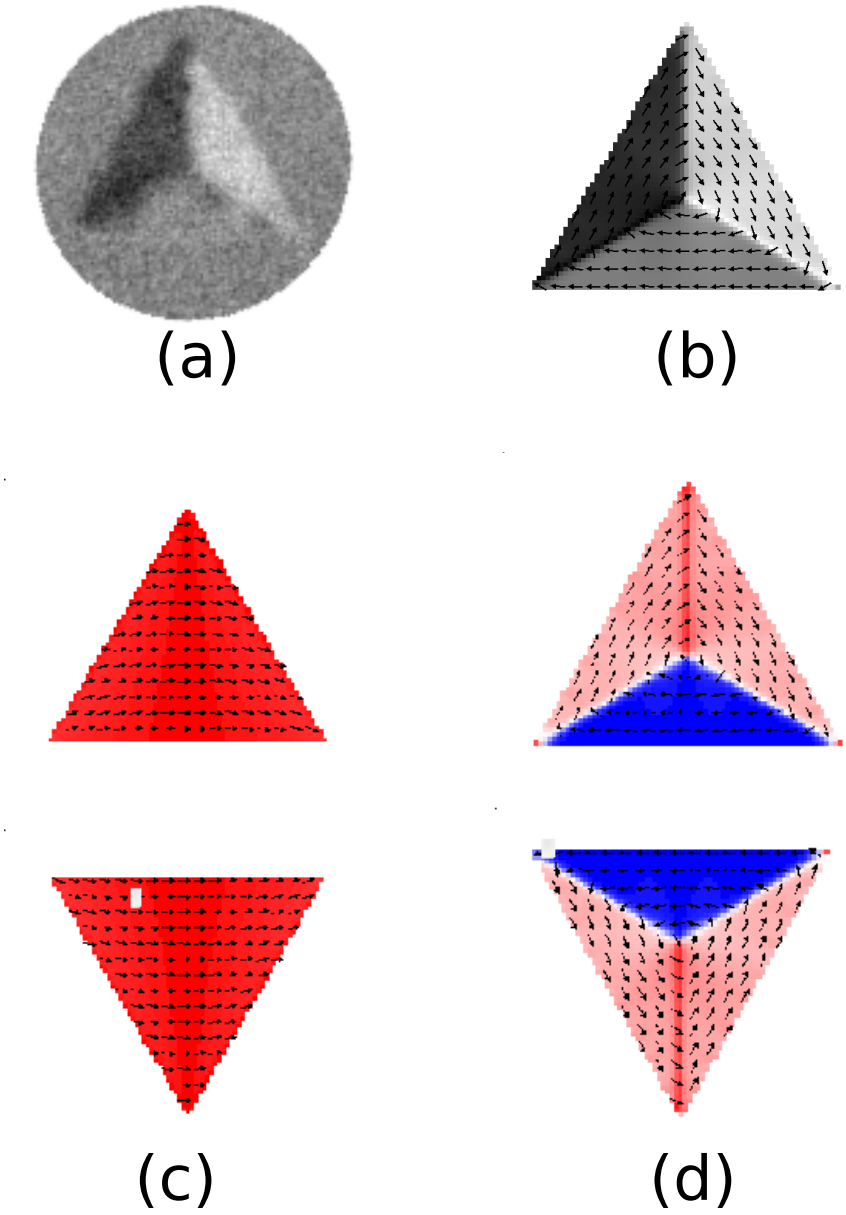

Figure 7.7 (a) SPLEEM image acquired of a 3 ML fcc Co islands. (b) Micromagnetic simulation of a configuration that reproduces the experimental picture. The grey level corresponds to the component of the magnetization along the upper-right islands edge. The arrows indicate the magnetization vector. (c) Single state triangular islands with two orientations. (d) Relaxed configuration after removing the field where the chirality of the pattern depends on the relative orientation of the island and the applied magnetic field.

side of the triangular island [figure 7.7(a)-(b)]. The simulation reproduces nicely the experimentally observed pattern. Following the micromagnetic simulations for different orientations of the islands relative to the applied magnetic field clarifies the origin of the domain pattern. The local magnetization on the island tends to align with the edges of the triangular island as the external field is removed. This effect is the two-dimensional equivalent to the demagnetizing effect that gives rise to the shape anisotropy in a thin film [28]: the magnetization aligns itself with the long edges of the island to reduce the total magnetostatic energy. If the island is misaligned with the external magnetic field by less than 30°, we obtain the same final pattern. When the island is rotated by a larger angle, the pattern changes to the opposite chirality, as shown in figure 7.7(c)-(d).

Similar in-plane magnetic domain patterns were observed in Ni and Fe nanostructures [235, 245–248] with different shapes such as triangles [245, 247] (were the magnetic domain structure found is very similar to the magnetic pattern observed in 3 ML Co thick islands), squares [246,249] or parallelepipeds [234]. In these structures, the magnetic domain structure and the number of magnetic domains were determined by the geometry of the system: the shape of magnetic domains was explained by the decrease of the magnetostatic energy of the system by aligning the local magnetization along the nearest edges of the structure, creating a flux closure configuration. One difference between the Co triangles and the mentioned works is the presence of an out-of-plane vortex core in the center of the structure. In our case a vortex state is unlike to be stable due to the thickness of the islands, but in any case it is probably beyond the resolution limit of the SPLEEM.

In summary, the stacking sequence in 3 ML thick Co islands influence their magnetic properties: the domain wall width is different in the two types of islands. In the hcp islands, the domain patterns are often single domain, while most of the fcc islands have a distinctive three-domain pattern with a given chirality. The pattern is explained by the lowering of the magnetostatic energy by alinging the magnetization with each side of the triangle. The chirality can be explained by the relative orientation of an external magnetic field and the island shape. The differences in domain

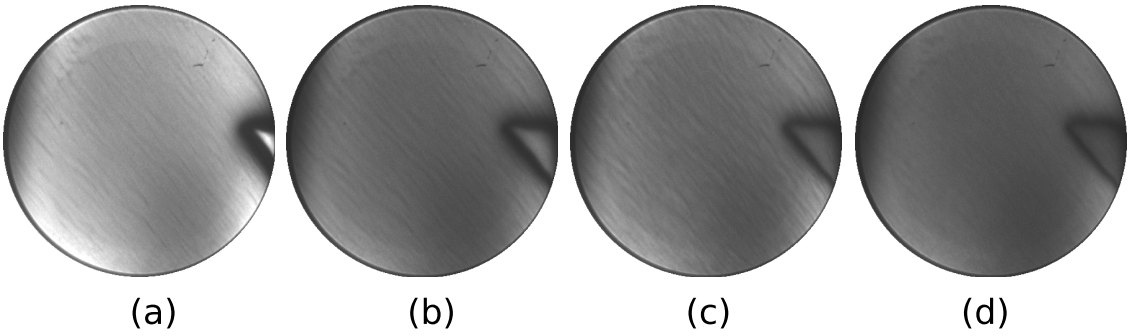

Figure 7.8 LEEM images acquired during the growth of Co on Ru(0001) at room temperature. (a) LEEM image of the clean Ru(0001) where the atomic steps of the substrate can be observed. (b) LEEM image acquired on 0.5 ML Co/Ru(0001). (c) LEEM image at the completion of the first layer of cobalt. (d) Image corresponding at 2 ML of Co/Ru(0001). The FOV is 8μm, beam energy was 6.2eV

patterns and domain wall widths between fcc and hcp islands are probably due to differences in their in-plane magnetic anisotropy energy.

7.3 Small Co islands on Ru

The study of Co/Ru(0001) was completed by characterizing the growth and magnetic easy-axis of Co films grown at RT. A sequence of LEEM images acquired during RT-growth is shown in figure 7.8(a)-(d). The amount of material deposited was calibrated by growing the films at higher temperature where the completion of each layer is easily followed. As it can be seen in the images, the deposition of Co at RT produces a uniform change in the reflected intensity, with no islands being detected. This can be explained if the size of the growing islands is smaller than the 10 nm resolution attainable by LEEM. To characterize the growth we then resort to STM.

7.3.1 Growth

STM images acquired from Co RT-grown films, 0.65, 1.6 and 3 ML thick respectively, are shown in figure 7.9. In the first film, Co islands have nucleated on the terraces of the Ru substrate, and

also decorate the atomic steps of the substrate. The Co islands present a triangular shape, similar to that shown by Co islands grown at 550 K but much smaller in size (9 nm) before they coalesce. Islands in the same terrace present the same orientation. Between islands on adjacent substrate terraces, the Co islands are rotated 180°, as for Co films grown at 550 K reflecting the hcp stacking sequence of Ru(0001). The height of the islands relative to the Ru surface is 0.21 nm. This result agrees well with the values obtained in Co islands grown at 550 K (0.20±0.05 nm [27]). The few 2^{nd} layer islands are 0.20 nm high, again in good agreement with the distance 0.19±0.06 nm obtained by LEED-IV in large Co islands. Some second layer islands do not have a well defined shape, but others present a nice triangular shape. The latter suggest that the 2 ML islands grow at RT following the hcp stacking sequence. The same behavior is observed on the next film, 1.65 ML thick [figure 7.9 (b)]. Second level Co islands decorate the substrate steps and nucleate on the terraces. The Co islands present a triangular shape. All the islands in the same terrace are oriented in the same direction and are rotated by 180° in consecutive substrate terraces.

A film with 3 ML thick islands is presented in figure 7.9 (c). The 3 ML Co islands present a triangular shape. Unlike the first and the second layers islands, three layers-thick islands showed two opposite orientations on the same substrate terrace, although the number of triangles pointing in the minority direction (downwards) was only 10%. As for larger islands grown at 550 K we can conclude that the third layer islands have two possible stacking sequences, hcp and fcc. Co growth cannot be followed layer-by-layer in STM, but due to the similitudes observed between Co growth at RT and Co growth at 550 K, we suggest that the majority orientation in 3 ML Co islands grown at RT is the same that those observed on Co growth at 550 K i.e. the majority orientation is opposite to the 2 ML. This implies that most of the islands are hcp with the minority orientation being fcc. The height of the third layer is 0.19 nm (in agreement with the LEED fits [27]). The density of islands [shown in table 7.2] is constant for the first and second Co layer, and 3 orders of magnitude larger than the density of islands obtained when the films were grown at 550 K.

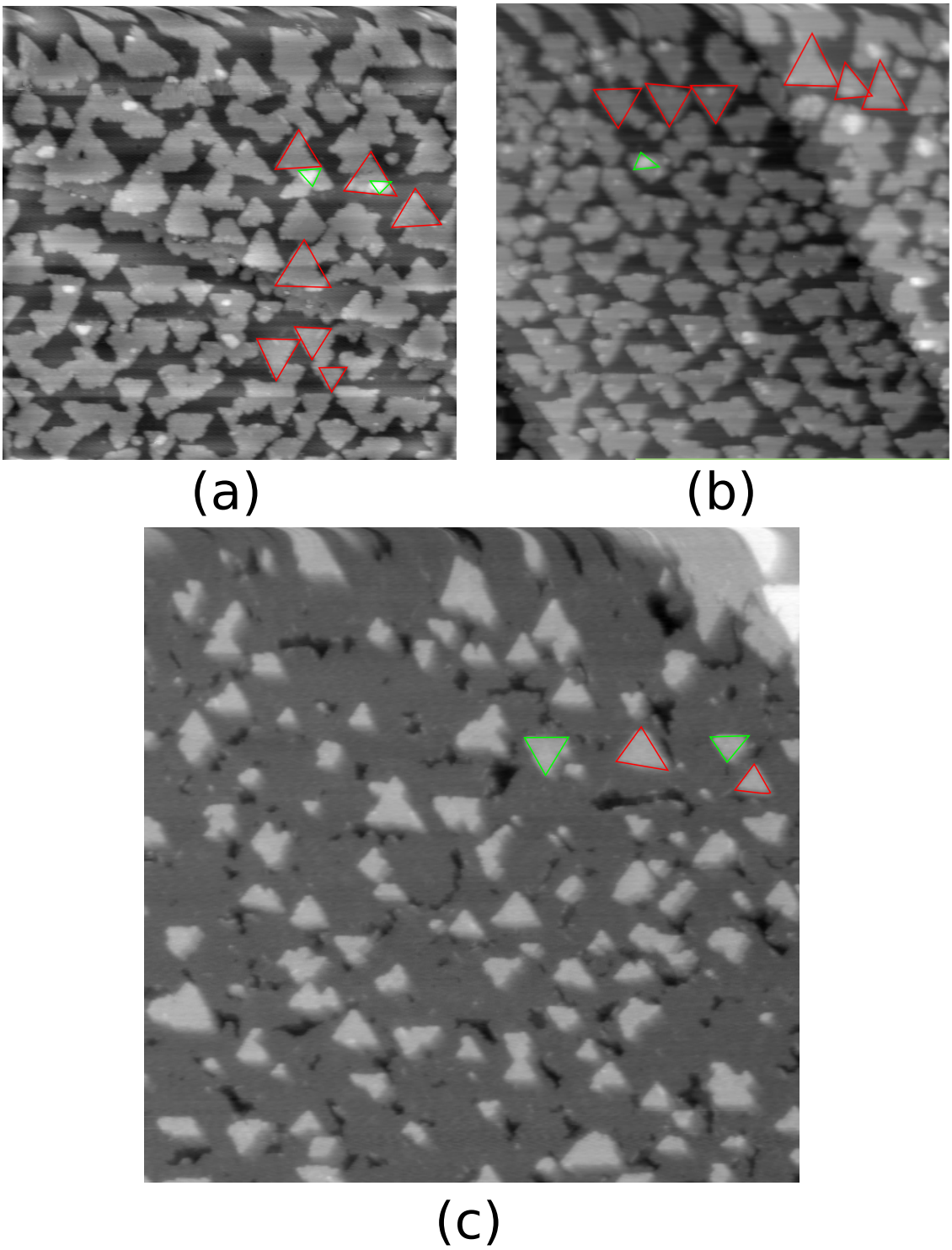

Figure 7.9 (a) 70 nm×70 nm STM image of 0.65 ML of cobalt grown on Ru(0001) at RT. (b) 70 nm×70 nm STM image acquired on 1.6 ML of Co grown on Ru(0001) at RT. (c) 100 nm×100 nm STM image of acquired on 3 ML thick Co islands grown on Ru(0001) at RT.

	Films grown at 550 K	Films grown at RT
1 ML Co	1.4×10^{10}	3.6×10^{13}
2 ML Co	8.9×10^{9}	3.2×10^{13}
3 ML Co	6.0×10^{9}	7.9×10^{11}

Table 7.2 Measured density (number of islands per cm^2) for each layer.

However, we observe that the density of islands decreases for the third layer of Co grown at RT.

In conclusion, we have shown that Co grows in a layer by layer mode on Ru(0001) at RT up to 3 ML. This is in agreement with previous works [250, 251], but in disagreement with the 3D-growth mode reported by Bader et al. [252] by studying the Ru and Co Auger peak-to-peak intensity versus deposition time. Similar contradictory results were found in the case of Co growth on different substrates. In the case of Co growth on Pt(111) an "imperfect layer-by-layer growth" was observed [253,254]. We suggest a different the density of steps in samples studied by different groups might account for the different results.

7.3.2 Magnetism of small Co islands

By means of SPLEEM we have studied the magnetic domain structure of Co films grown at RT on Ru(0001) up to 4 ML. Figure 7.10 presents a sequence of SPLEEM images acquired while the Co film was grown, which correspond to the LEEM images presented in figure 7.8. During the deposition of a total coverage equivalent to 1 ML [figure 7.10 (a)], no magnetic contrast is detected. This was already seen in the growth at 550 K, and is expected because the Curie temperature of 1 ML Co was reported to be below RT [222]. The deposition of a total coverage of 2 ML [figure 7.10 (b)] also fails to show any magnetic contrast. At elevated temperature, the lack of in-plane magnetic contrast is expected, as 2 ML islands have PMA. Only total Co coverages of 3 ML or thicker [figure 7.10 (c)–(d)] show in-plane magnetic contrast. The magnetic domains for 2.5 ML

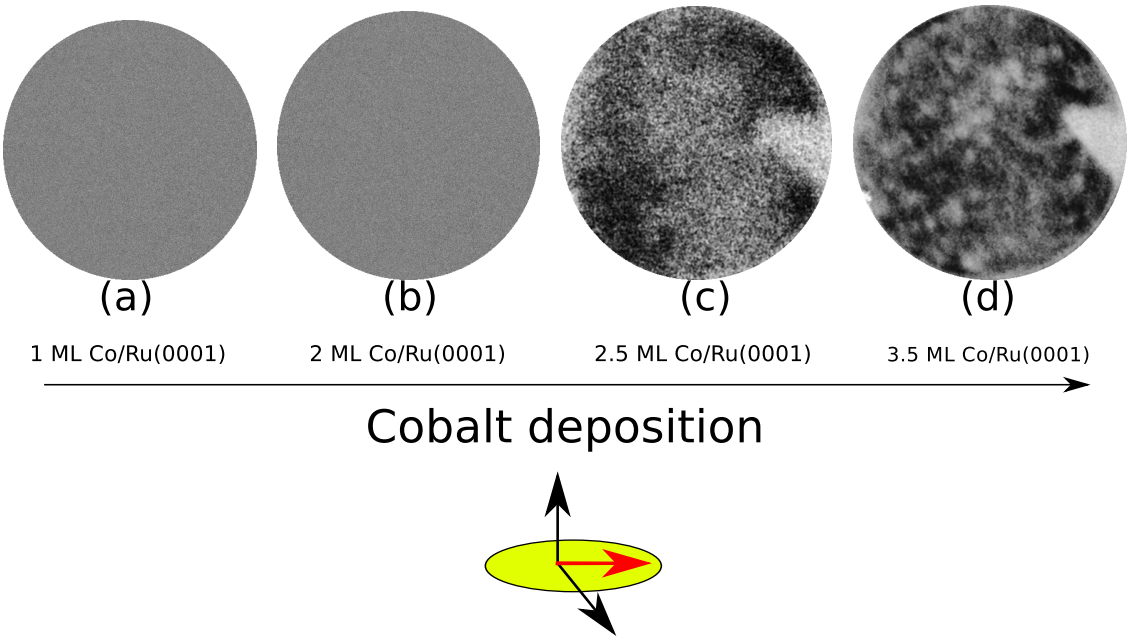

Figure 7.10 SPLEEM images recorder in Co films grown at RT on Ru(0001) with the electron beam spin-polarization direction in the plane of the film. Only films with 2.5 ML Co or thicker present magnetic contrast. The FOV is 8μm. The beam energy is 6.2 eV.

that would correspond to the presence of small 3 ML Co islands, present an irregular shape. They become better defined as the thickness of the film is increased to 3.5 ML.

In films with an average of 2 ML Co, in-plane magnetic contrast was sought. Surprisingly, no magnetic contrast was detected (not shown). This lack of out-of-plane magnetic contrast is puzzling, and contrasts with the out-of-plane magnetization of large 2 ML thick Co islands. Our interpretation is that the small 2 ML islands (9 nm) also present a PMA, but due to the typical island size, the magnetic domains are below the resolution of SPLEEM (20 nm). That this is not the case for the, similar equally small, 3 ML islands (12 nm) is probably due to larger domain size in the latter.

7.4 Conclusions

By means of LEEM and STM we have studied the growth and the morphology of thin Co films grown at RT on Ru(0001). The growth of the films is a layer-by-layer mode up to the maximum coverage studied of 3 ML. The third layer presents islands of hcp or fcc stacking sequence on the same substrate terrace, both at RT and at 550 K.

By means of SPLEEM we have studied the easy-axis of magnetization, and the magnetic domains patterns in thin Co films grown at 550 K and at RT on Ru(0001). We have confirmed that three-layers thick Co films grown at 550 K present in-plane magnetization. The magnetic domains of 3 ML thick Co islands depend on the stacking sequence of the islands. Hcp islands present mono-domains or magnetic domains separated by wide domain walls. Fcc islands present usually a more complex magnetic domain pattern, with at least 3 magnetic domains separated by thinner domain walls. The difference between domain walls width is assigned to different values in the in-plane magnetic anisotropy energy for fcc and hcp islands. The domain patterns observed in fcc Co islands correspond to the magnetization aligning with the sides of the triangular islands, and the chirality of the pattern is proposed to arise from the interaction with the external field generated during growth by the heating filament. We also have determined that films two layers thick present perpendicular magnetization with a Curie temperature of 450 K. By means of SPLEEM we also have studied the magnetization direction of Co films grown at RT on Ru(0001). Only three or more layers present in-plane magnetization. No perpendicular magnetic contrast was obtained in any case.

Chapter 8

Hydrogen on Co films

8.1 Introduction

Adsorption of gases can modify the structure and interlayer spacings [117] of metallic thin films or surfaces. It should not come as a surprise, then, that it can also significantly affect their magnetic properties if the films themselves are magnetic. Although the bulk of adsorption studies have been focused on catalysis applications [255–259], there is a growing number of works on the interplay of magnetism and gas adsorption. The field was started more than forty years ago when changes in the magnetization of ferromagnetic materials produced by the chemisorption of hydrogen were reported [260]. The most straighforward changes involve the modification of the magnetic moment of the topmost atoms of the metal film upon gas adsorption, which is expected if there is any charge transfer between the adsorbates and the metal atoms. It is common to observe [261–265] a decrease in the magnetic moment of the topmost atoms of a ferromagnetic film. More unusual is the enhancement of the magnetic moment of the magnetic layer upon gas adsorption, which was predicted [266] and later confirmed [267] for oxygen on iron. Obviously, large effects are expected if the adsorbate reacts with the surface atoms producing some magnetic compound, as for oxygen

on ferromagnetic $3d$ metals [268, 269].

Changes in the magnetic anisotropy of a thin film upon gas adsorption are more unpredictable, in line with the smallness of the magnetic anisotropy energy that arises from a delicate balance of competing contributions. In particular, hydrogen has been observed to induce an spin-reorientation transition on Ni/Cu films through strain effects [25]. Hydrogen is also the main suspect on the SRT of Fe/W(110) observed by spin-polarized STM upon residual gas absorption [270, 271]. A problem with hydrogen is that it is largely unobservable when using position-sensitive experimental techniques such as LEED or STM but in a few special cases [272, 273]. To date no real-space study of an adsorbate induced spin-reorientation transition has been reported.

In this chapter we present our discovery of an hydrogen-induced spin-reorientation transition on a cobalt bilayer on Ru, grown both at 550 K and at RT. By means of SPLEEM, we image in real-space the evolution of the magnetic domains while the SRT takes place. LEED and reflectivity data will add information about the possible origin of the SRT. After describing the experimental results, we will proceed to discuss the reasons for the observed domain pattern evolution. In the case of RT-grown cobalt films, STM was also used to study possible structural changes after hydrogen adsorption.

8.2 Hydrogen adsorption on a flat Co bilayer

8.2.1 Experimental results

To study possible effects of hydrogen adsorption on Co/Ru(0001), a cobalt film with 3 ML Co islands on a nearly continuous 2 ML Co film on Ru(0001) was grown. As in the previous chapter, the film was grown at a 550 K substrate temperature so the Co islands are quite large possible while preventing significant interdifussion with the substrate. Figure 8.1 (a) shows a LEEM image acquired at RT after the growth of such a film. As discussed in the previous chapter, all the out-

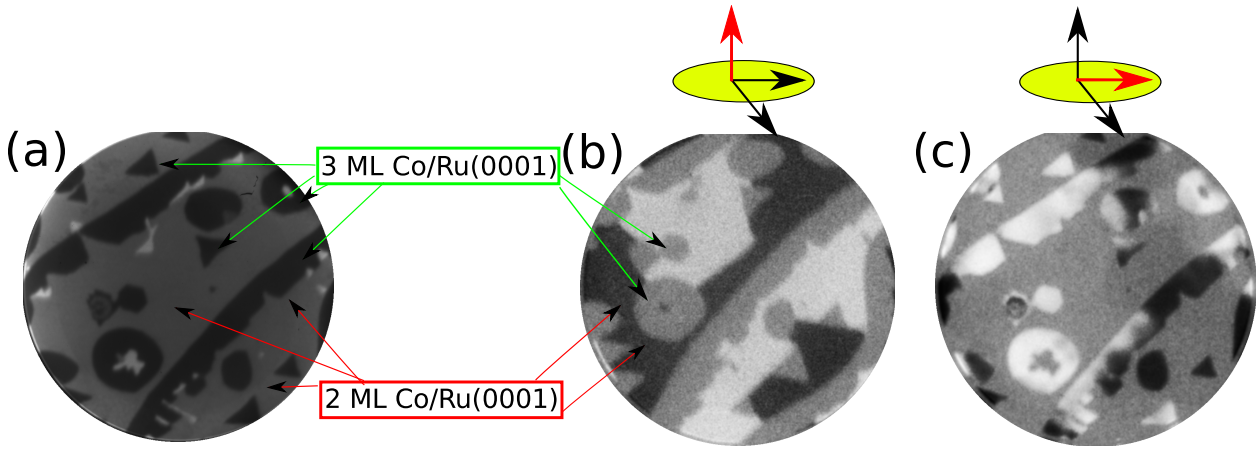

Figure 8.1 (a) LEEM image acquired at RT of a film with 3 ML Co thick islands on a 2 ML continuous films on Ru(0001), grown at 550 K. The 3 ML Co thick areas of the film appear dark gray at the electron beam energy of 5.2 eV. While most of the 3 ML islands are triangular, there are a few round islands which correspond to round pits of the Ru subtrate. Some minor areas light gray, and correspond to uncovered 1 ML Co thick regions. (b) SPLEEM image with the electron beam spin polarization out-of-plane. Only the 2 ML thick Co areas present contrast, i.e., perpendicular magnetic anisotropy (PMA) (c) SPLEEM image with in-plane electron beam spin direction, where all the magnetic contrast arises from the 3 ML Co thick areas of the film. The FOV of the images is 4 μm. The 1 ML thick areas do not present any magnetic contrast, as they have a Curie temperature below RT.

of-plane magnetic contrast [see figure 8.1 (b)] arises from 2 ML thick areas, while the in-plane magnetic contrast only appears on the 3 ML thick islands [see Figure 8.1 (c)]: the 2 ML one have an out-of-plane magnetic easy axis, while the 3 ML islands have an in-plane easy axis, showing the well documented SRT [222] of Co/Ru as a function of thickness.

A sequence of SPLEEM images with the electron-beam spin-polarization direction out-of-plane was acquired at RT while exposing the cobalt film to molecular hydrogen (by filling the chamber to 8×10^{-10} Torr of H_2). Figure 8.2 shows selected frames extracted from the image sequence. There is an initial induction period were no changes were observed in the out-of-plane magnetic domain pattern of the 2 ML thick Co areas of the film [figure 8.2 (a)-(b)]. But as the hydrogen dose was increased above 0.12 L_{H_2}, the domain pattern changed in two stages. At first,

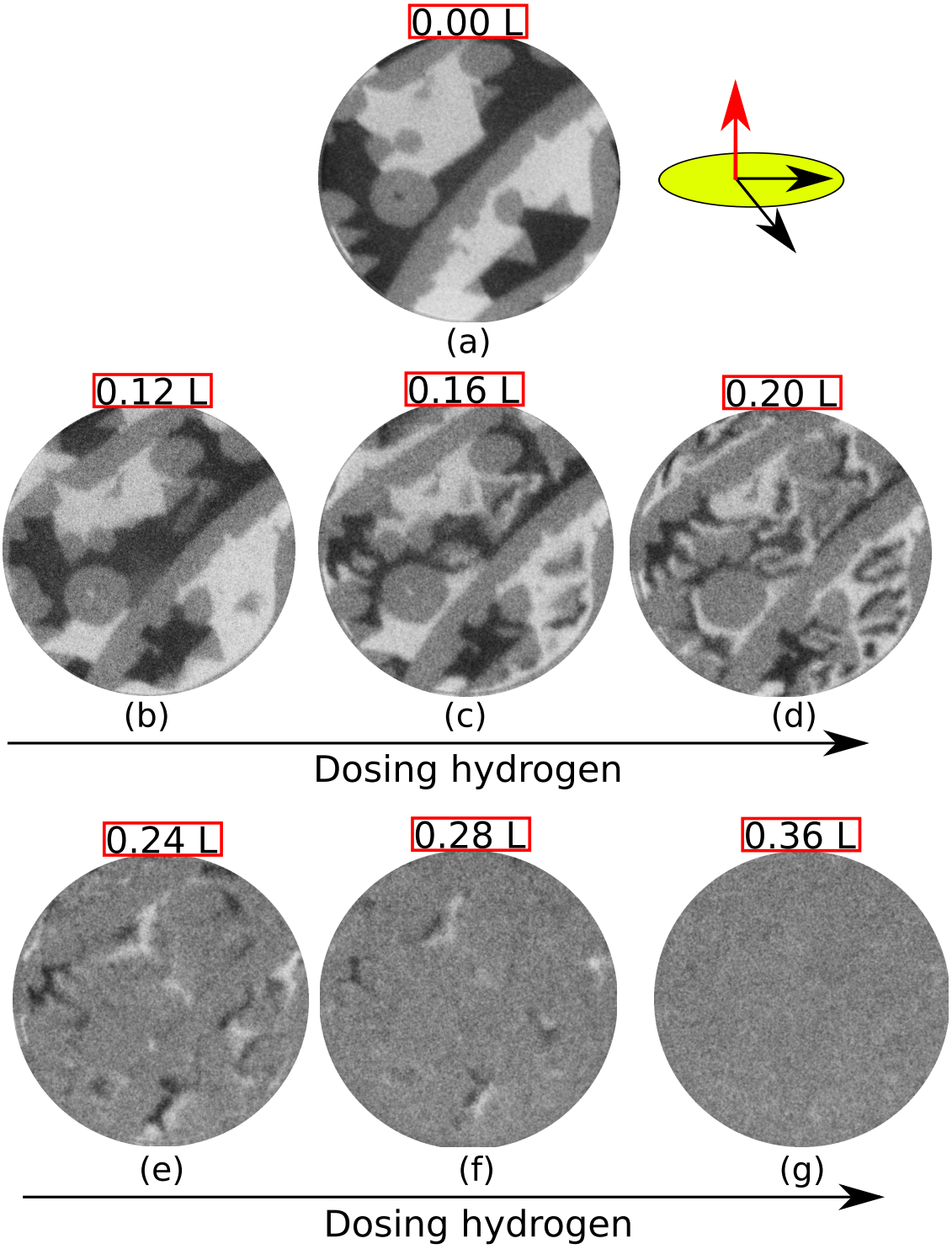

Figure 8.2 Out-of-plane magnetic contrast SPLEEM images of the film shown in figure 8.1 acquired while hydrogen was dosed on the film. The hydrogen dose is indicated in each image. The FOV is 4 μm, beam energy is 5.2eV

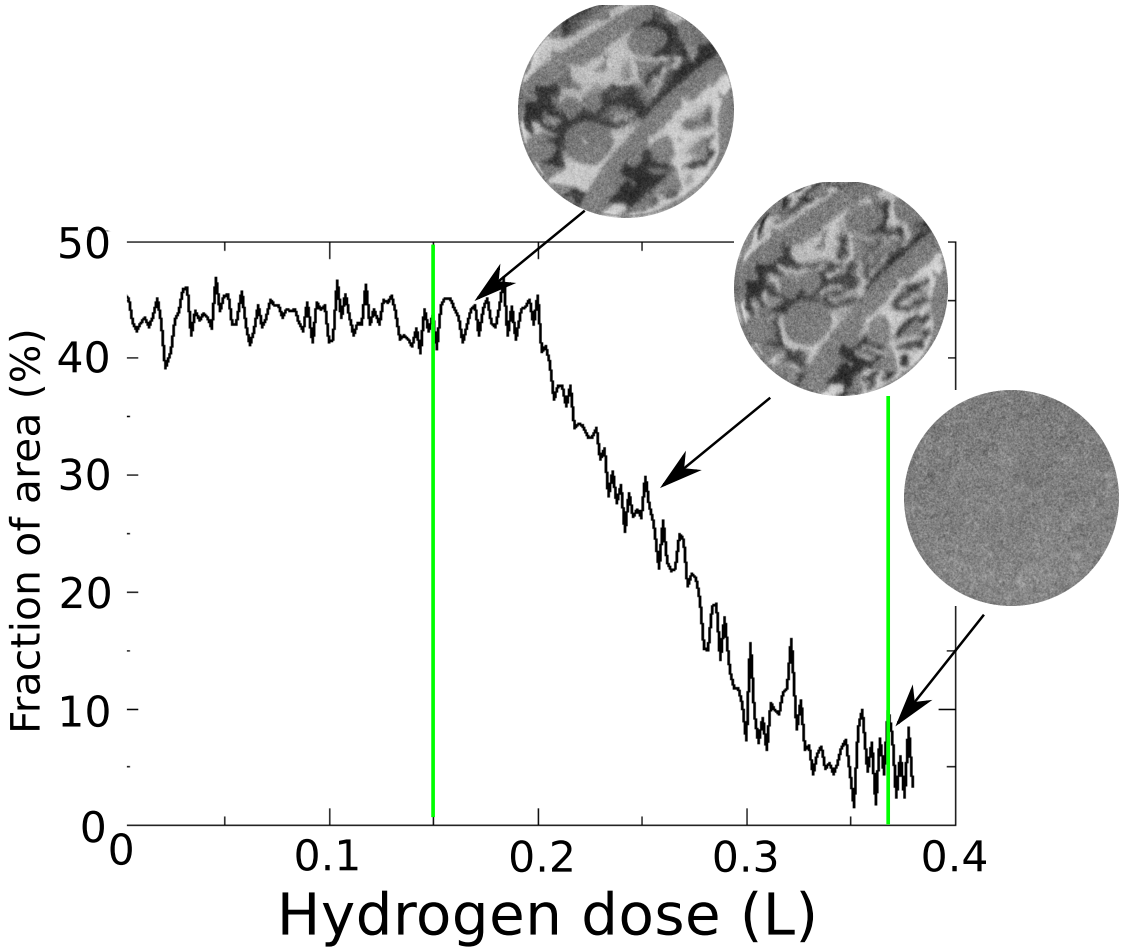

Figure 8.3 Image area covered with up (white) out-of-plane domains in the previous figure versus the hydrogen dose.

the magnetic domains broke up into smaller ones forming a kind of disordered stripe pattern, as shown in figure 8.2 (c)-(d). At a second stage with doses higher than 0.20 L_{H_2}, the total area with up-and-down domains decreased until all the out-of-plane magnetic contrast disappeared, as shown in figure 8.2 (e)-(g). The decrease can be followed by integrating the total image area covered with white domains as a function of the hydrogen dose, shown in figure 8.3. The decrease of the white domains is nearly linear with the hydrogen dose. During all the dosing no change was detected in the LEEM (topography) images themselves.

To understand the effect of hydrogen on the cobalt bilayer, several further experiments were performed to:

- check that the change in the domain patterns is due to adsorbed hydrogen,
- quantify the amount of hydrogen required for this effect,
- check if this change in the magnetic contrast corresponds to an spin reorientation transition,
- and determine whether the effect is due to structural modifications of the film upon hydrogen adsorption

We will then discuss the observed domain pattern evolution with hydrogen dose.

Reversing the transition

We cannot directly detect the presence of hydrogen on the surface of Co (below we describe the attempt to measure changes in the Co film structure). An indirect proof linking the effect on the magnetic domains of the Co bilayer with the presence of hydrogen on top of the film is to heat a hydrogen-exposed film up to the desorption temperature of hydrogen on Co(0001). Hydrogen desorbs from Co at a temperature of 370 K [274]. As this temperature is still below the Curie temperature of Co bilayers (see chapter 4), an experiment can be performed looking for the out-of-plane magnetic contrast while annealing the film to the H/Co desorption temperature.

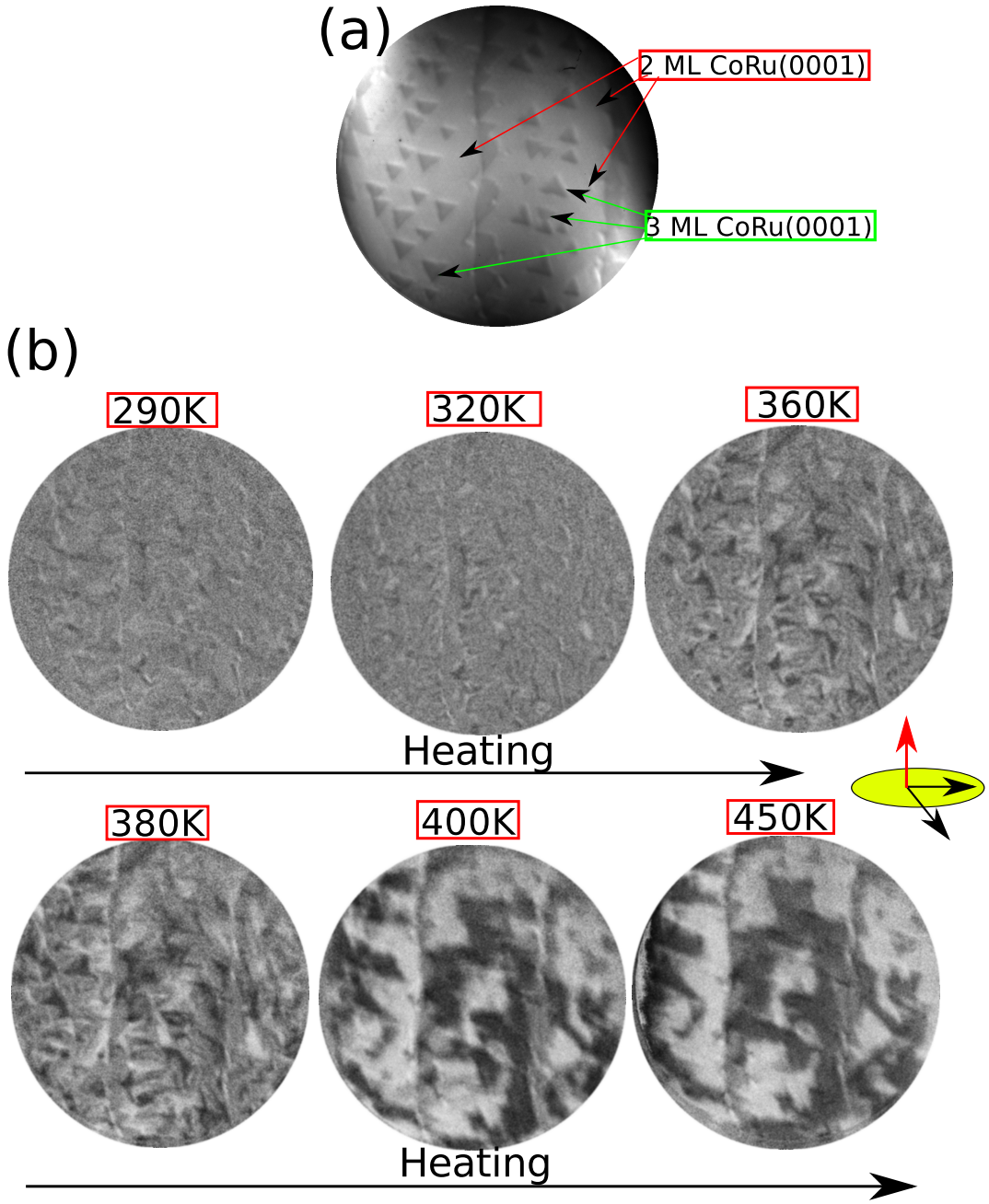

Figure 8.4 PONER TOPOGRAFIA. SPLEEM images acquired while heating the sample after dosing hydrogen. The temperature of the sample is shown in each image. The FOV is 8μm. Beam energy is 5.2 eV

To such end, a film with 3 ML thick Co islands on top of a 2 ML film was grown on Ru(0001). After cooling down to RT the film was exposed to 0.4 L_{H_2}. Then, the film out-of-plane magnetization was monitored while the sample temperature was slowly[1] increased to 400 K. In figure 8.4, selected frames from a sequence of images acquired while increasing the temperature are presented. In agreement with the previous observations, there is no out-of-plane magnetic contrast in the initial frame, which corresponds to the film, after hydrogen exposure, at 290 K. The faint contrast observed is attributed to some minor misalignment in the out-of-plane spin-polarization direction of the illuminating electron beam. As the sample temperature reaches 360 K some areas start to shown out-of-plane magnetic contrast. The areas with magnetic contrast (white or black) increase in size until the sample temperature is 400 K, when the magnetic contrast typical of the 2 ML thick Co areas is restored. The temperature at which the magnetic contrast is restored agrees with the desorption temperature of hydrogen [274] or deuterium [275] from Co(0001) and is lower than the desorption temperature of other adsorbates on Co such as CO ($\sim$430 K [274,275]). After annealing to 400 K, the out-of-plane magnetic contrast is conserved when cooling the film down to RT. Thus, the hydrogen induced dissapareance of the out-of-plane magnetic contrast is reversible upon heating the film above the desorption temperature of hydrogen on Co. This result strongly supports that adsorbed hydrogen is responsible for the observed change in the magnetic domain patterns.

Hydrogen coverage

To obtain the total hydrogen dose, the pressure of the UHV chamber (measured by an ionization gauge and corrected by a factor of 0.46 for hydrogen [102]) was attributed to hydrogen (the background pressure before the H_2 leak valve was opened was below 7×10^{-11} Torr so the error is less

[1] SPLEEM images require the heating rate to be small, as otherwise drift between the images gives rise to spurious signals when subtracting LEEM images to provide the SPLEEM ones.

than 10%). Integrating the hydrogen dose through the experiment presented in figures 8.2 (and subsequent experiments, see figure 8.5) gave a total hydrogen dose for the out-of-plane magnetic contrast removal of 0.38 ± 0.02 L_{H_2}.

But that only provides the dose, not the hydrogen adsorbed on the surface of the film. Hydrogen adsorption on Co has been studied previously [1, 274, 275]. At RT, hydrogen adsorbs as atomic hydrogen on Co, and the absorption is supposed to be non-activated. To check for a possible role of activation in hydrogen absorption in our experiments, they were repeated with the ionization gauge of the system turned off, to prevent it from dissociating the molecular hydrogen. The dose required to make the out-of-plane magnetic contrast to vanish was still the same, confirming that the cobalt surface dissociates molecular hydrogen.

The required dose of 0.38 L_{H_2} was achieved by filling the chamber with 8×10^{-10} Torr of molecular hydrogen. A total dose of 0.38 L_{H_2} at most can give a coverage of Θ_{max}=0.38×2 ML=0.74 ML, assuming a constant sticking coefficient of 1. It might be much lower if the sticking coefficient were lower, or if substantial desorption of hydrogen took place at RT. The desorption energy of H/Co has been measured by several methods, giving numbers in the range of 0.85–1.0 eV/atom [1]. These numbers imply that the residence time of hydrogen adatoms is in the minutes–hours range, ruling out significant desorption during the thermal desorption spectroscopy [1, 276]. Another check on desorption of hydrogen during the experiments was done by changing the pressure of hydrogen used to reach the $\sim$0.4 L_{H_2} dose, again with negative results. The sticking coefficient has been reported to be 0.5 up to coverages of 0.5 ML. In consequence, we believe that a coverage of Θ=0.3–0.4 is a reasonable assumption in the absence of more information.

Spin reorientation transition

So far, we have shown that the out-of-plane magnetic contrast, i.e. the domains magnetized up and down on the Co bilayer, change and then disappear when exposed to $\sim$0.4 L_{H_2}. There are

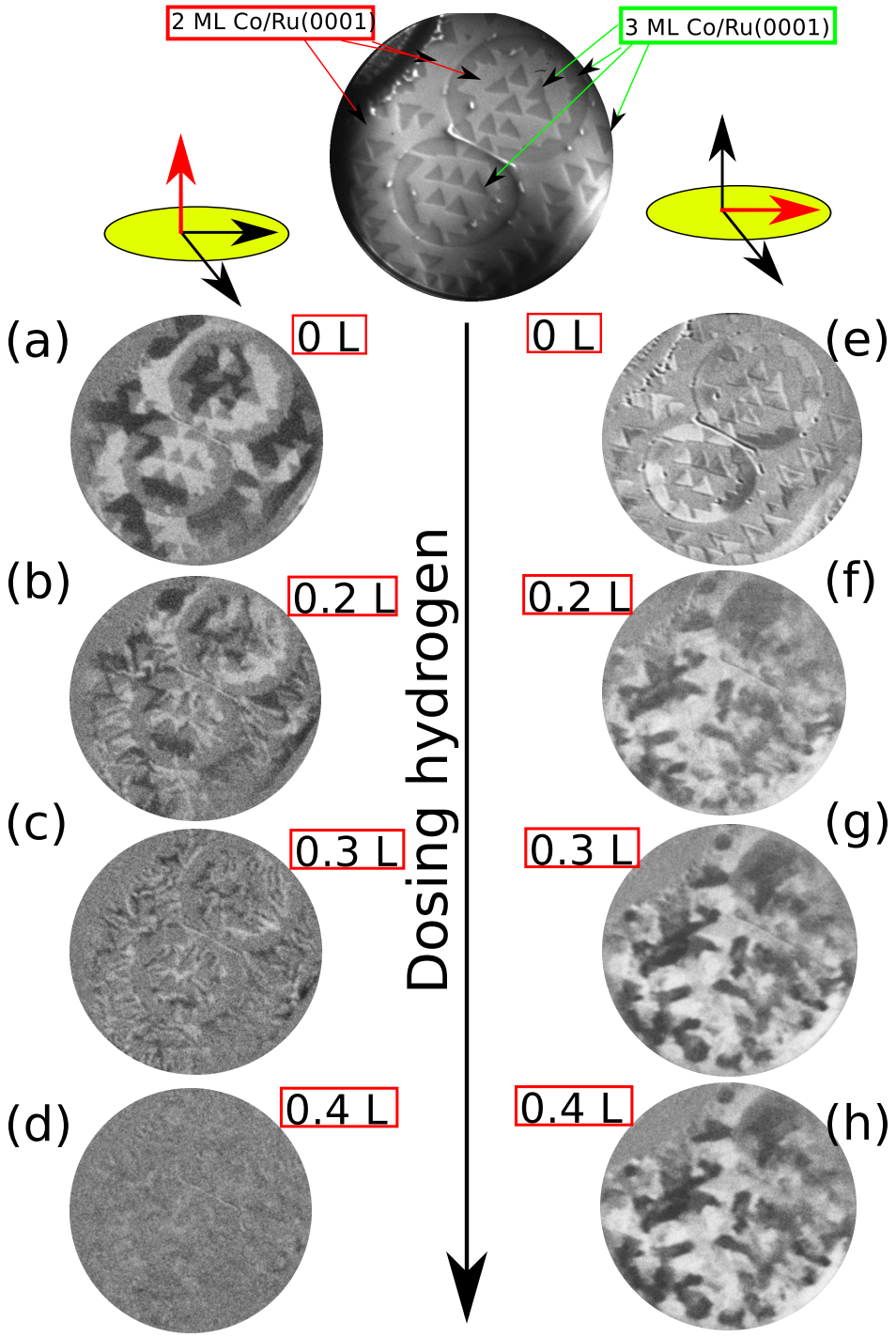

Figure 8.5 Top: LEEM image of a film with 3 ML Co islands (dark gray) on a nearly continuous 2 ML Co film. Two pits of the substrate can be observed, with 3 ML Co islands decorating the lower step. Some light gray areas correspond to exposed 1 ML Co. Left column(a)–(c) SPLEEM images from a sequence acquired while molecular hydrogen was dosed while the electron-beam spin-direction is out-of-plane. After it the sample was heated up and cooled to RT to repeat the hydrogen dose and acquire a new SPLEEM (e)–(f) image sequence with the electron-beam spin-direction in-plane. The FOV was 8 μm, beam energy was 5.2 eV

several reasons why the out-of-plane magnetic contrast might disappear. The most likely one is that the easy-axis of magnetization has changed, becoming in-plane, i.e. hydrogen induces a spin-reorientation transition (SRT). To confirm this, the hydrogen exposure was repeated on a Co film but observing first the out-of-plane magnetic contrast (as before) and then the in-plane magnetic contrast[2]. In Figure 8.5 the experiment performed with out-of-plane contrast [figure 8.5 (a)-(d)] is compared with the consecutive experiment [figure 8.5 (e)-(h)] with in-plane contrast in the same area of the Co film. Between the experiments, the film was annealed to 420 K to remove the hydrogen adsorbed during the first experiment. The LEEM image shows a film with several 3 ML triangular islands (light gray) and some 3 ML islands decorating the lower steps of two pits of the substrate. Before hydrogen exposure in both experiments, the out-of-plane magnetic contrast is observed only in the 2 ML areas, while the 3 ML islands have only in-plane magnetization [compare figure 8.5 (a) and (e)]. As the film was exposed to hydrogen, the sequence sensitive to out-of-plane magnetization shows the same breakup of domains followed with a disappearance of the magnetic contrast that was observed with higher resolution in figure 8.2. At the same hydrogen dose that the out-of-plane magnetic contrast disappears, magnetic contrast appeared in the SPLEEM sequence sensitive to in-plane magnetization in the 2 ML Co thick areas of the film. At the end of the experiment, all the film was completely magnetized within the film plane: hydrogen adsorption changed the easy axis magnetization of the 2 ML thick areas from an out-of-plane orientation to an in-plane direction. Thus, hydrogen induced a spin-reorientation transition on the 2 ML Co thick areas of the film, reversible upon hydrogen removal. No changes were observed in the 3 ML areas.

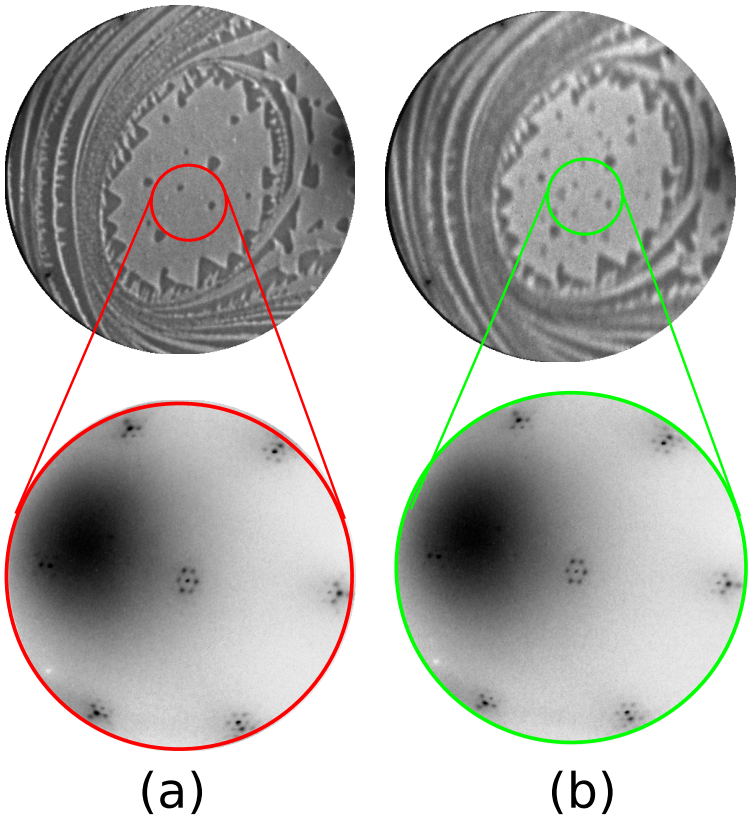

Figure 8.6 (a)LEEM image and LEED pattern taken on mostly 2 ML thick Co film on Ru(0001). The LEED pattern was acquired from the central area of the LEEM image. (b) LEEM and LEED pattern acquired after dosing 20 L of molecular hydrogen. The beam energy in LEEM images was 3 eV and the FOV is 7μm. The LEED patterns were taken at 72 eV.

Structure changes, or lack of

In the H-induced SRT of Ni/Cu, the effect was attributed to a change in the strain of the Ni film upon hydrogen adsorption. So we searched for possible structural effects of the adsorption of hydrogen on the Co films. The presence of adsorbed hydrogen itself cannot be resolved using diffraction techniques as LEED due to the low scattering power of hydrogen as we have seen in previous chapters. To complicate the problem, the mobility of hydrogen on the Co surface is expected to be high even at moderate temperatures [1]. Although some authors reported the formation of a faint LEED pattern when hydrogen was adsorbed on Co(0001) [274,275], they also indicated that it was difficult to reproduce those LEED patterns, a problem they associated with electron beam damage.

To detect possible changes in the structure of Co/Ru films upon molecular hydrogen adsorption, LEED and reflectivity data were acquired in a 2 ML thick Co film. To avoid a possible beam damage, the LEED patterns were acquired in a hydrogen background of 4×10^{-8} Torr. As the base pressure of the Sandia LEEM during the present experiments was 2×10^{-10} Torr, it was possible to involuntary dose hydrogen from the chamber residual gas. To prevent this from ocurring, the bare Co data was acquired while the substrate temperature was 400 K, above the desorption temperature of H on Co. LEEM images and LEED patterns recorded before and after hydrogen exposure are shown in figure 8.6. No changes were observed in the LEED pattern.

LEED-IV curves were also acquired [figure 8.7 (a)]. The plotted curves corresponds to the spot intensity of the specular beam together with its satellite spots [label Beam(0,0)], and the integer beams also adding the intensity of the corresponding satellite spots [Beam(0,1), Beam(1,0)]. The LEED IV curves before and after hydrogen exposure are basically identical: the mean Pendry's R-factor for the three beams was 0.04, although we caution that the energy range is relatively small,

[2]For technical reasons, it is simpler to perform first a full sequence of images with one magnetic-contrast direction and then the other than to switch the spin-polarization direction between each frame.

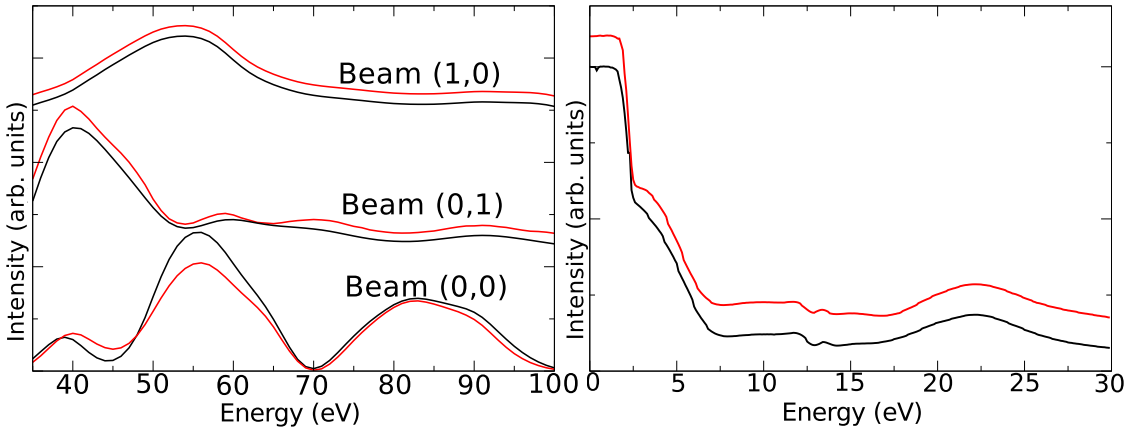

Figure 8.7 (a) LEED IV curves acquired from 2 ML Co on Ru(0001) before (black curves) and after(red curve) hydrogen exposure. (b) Low energy reflectivity curves taken before (black curve) and after (red curve) the hydrogen exposure. Curves are offset for clarity

and the integration of the main diffracted spots together with the satellite beams might wash out some fine details.

The electron reflectivity in the 0–30 eV range acquired from the same area as the LEED-IV data is shown in figure 8.7 (b). For comparison, the substrate Ru reflectivity in the same range is presented in figure 8.8 (page 180) (we note that the energy scale between the two spectra is shifted, because the data has been acquired with different instruments that have a different zero calibration of the energy scale). After a high reflectivity at very low electron energies (for energies below 2 eV, below the vacuum level of the sample where all the electrons from the illuminating beam are reflected back from the sample), the reflected intensity decays until reaching a plateau at 7 eV. In this 2–7 eV range, the adsorption of hydrogen on either Ru (figure 8.8) or Pd (figure 4.1) is detected as an increase of the reflected intensity. As shown in figure 8.7, this is not the case for Co. The abrupt changes in the Co films reflectivity around 12 eV are probably related to gaps arising from band crossings; they do not show any change upon hydrogen adsorption. Finally, the broad peak

at 22 eV is related in bulk-terminated samples with the gap associated with the first Bragg peak. Presumably a change in energy in its position might indicate a change in the Co lattice spacing (for example, a similar peak appears at a lower energy corresponding to larger spacing in real space-in the Ru spectra in figure 8.8), although as shown in Chapter 4, adsorbates can invalidate this simple picture.

Despite the obvious effect of hydrogen adsorbed on the Co magnetization, there is no however sign of it in the electron reflectivity of the Co films, nor in the LEED patterns or LEED-IV data in the energy range 30–100 eV. This is in stark contrast with the case of the Pd films studied in the chapter 4 (or in the Ru surface to be presented in the next section 8.3).

8.2.2 Discussion

We have discovered an spin reorientation transition on the Co 2 ML thick islands or films upon a hydrogen dose of 0.4 L_{H_2}. The SRT is reversible upon heating up to a sample temperature of 400 K. No clear structural changes have been detected in the Co films after the hydrogen dose, ruling out a change in the strain state of the films. Before the magnetization easy axis direction changes from out-of-plane to in-plane, the domain pattern changes for exposures between 0.2–0.4 L_{H_2}. In that range the large, micrometer sized, up and down magnetic domains break up into much smaller elongated domains, that in the smaller dimensions reach a size of 0.31 $\pm 0.03 \mu$m. Eventually, the out-of-plane contrast disappears in a non-homogeneous manner.

We first discuss the origin of the striped pattern of out-of-plane magnetic domains with decreasing size that is observed observed with a hydrogen dose of 0.2–0.4 L_{H_2}. It is reminiscent of other striped patterns observed in surfaces, such as polymers [277], submonolayer islands [278], ferroelectric films [279] or ferromagnetic materials [280–285]. Landau and Lifshitz [286, 287] were the first to propose a formalism to decribe the energetics of stripe domain formation, they proposed that the origin of the stripes lies in the interplay between short- and long-range forces.

The stripe domain patterns observed in different systems lead to a reduction of the total energy of the system, although the particular interactions depend on each physical system. In the case of thin ferromagnetic films with perpendicular magnetic anisotropy, the stripe pattern arises from the competition between the exchange interaction J, the dipolar interaction Ω and the magnetocrystalline anisotropy K_{mca} [54, 288, 289]. While the long range dipolar interaction promotes the creation of domains, the domain walls themselves have an energy cost that depends on the effective magnetic anisotropy K_e and the exchange interaction J (The balance between the two interactions gives rise to a preferred domain wall width as discussed in the previous chapter). As the magnetic anisotropy energy decreases, the cost of creating a domain wall also decreases, and domain walls multiply in the film. In consequence, the observed decrease in the domain size reflects the underlying decrease of the magnetic anisotropy energy caused by the hydrogen adsorption on the Co film.

The model gives predictions for the stripe periodicity. Won et al. [54, 288, 289] used it to explained the stripe pattern observed in ultrathin Fe/Ni/Cu(001) films near a SRT. For a 2D Heisenberg square lattice, they proposed that the hamiltonian can be expressed as:

$$H = -J\sum_{ij}\vec{S}_i\vec{S}_j - K\sum_i S_{ij}^2 - \frac{\Omega}{4\pi}\sum_{i,j}\frac{\vec{S}_i\vec{S}_j - 3(\vec{S}_i r_{ij})(\vec{S}_j r_{ij})}{[(n_i-n_j)^2(n_i-n_j)^2]^{3/2}} \tag{8.1}$$

where J is the exchange interaction, K is the uniaxial magnetic anisotropy (excluding the shape anisotropy), $\vec{S}_i$ is the spin at site i and Ω is the dipolar interaction strength. By minimizing the energy, the width of a stripe pattern (given in units of lattice constant) was found to be [54]:

$$L_{min} = \frac{5J\pi^2\exp(\sqrt{J\pi^4K_e/\Omega_L^2+1})}{6\Omega\sqrt{J\pi^4K_e/\Omega_L^2+1}} \tag{8.2}$$

where $K_e = K - \Omega$ is the effective magnetic anisotropy. In the case of ultrathin films, the values of J, K and Ω must be normalized by the film thickness. If the system is composed of d atomic layers, the d spins in the vertical direction can be considered to be rigidly connected. Thus, the exchange interaction J in the 2D lattice system should be multiplied by a factor d. The volume

anisotropy K scales linearly with d and the surface anisotropy is unchanged. The dipolar energy must be split into a short-range part, Ω_s (that corresponds to the conventional shape anisotropy), and a long-range part Ω_l that arises from the dipolar interaction between two blocks of d spins at a distance greater than the film thickness. At the SRT point, the effective anisotropy is K_e=0 and the stripe width in equation 8.2 reaches a minimum value of:

$$L_{min} = \frac{2.27\pi^2 J}{\Omega_l} \tag{8.3}$$

In fact, this minimum value represents a static spin-density wave due to the dipolar interaction as it was reported by Bruno et al. [290]. Far from the SRT point ($K_e \neq 0$), the stripe pattern width increases exponential with the anisotropy, which can be written in the alternative form:

$$L = \frac{5J\pi^2 L_{dip} exp(\pi^2 L_{dip}/L_{ani} + 1)}{6\pi^2 L_{dip}/L_{ani} + 1} \tag{8.4}$$

where $L_{ani} = \sqrt{J/K_e}$ is the anisotropy length and $L_{dip} = \frac{J}{\Omega_l}$ is the dipole length. The uniaxial magnetic anisotropy favors a single domain state, while the dipolar interaction favors a stripe domain phase. The exponential dependence of the stripe width with the anisotropy arises from a crossover from a regime where its stripe pattern is dominated by the dipolar interaction ($L_{dip} \ll L_{ani}$) to a regime where the stripe pattern dominated by the anisotropy regime ($L_{ani} \ll L_{dip}$). Equation 8.4 also represents the transition from a stripe phase where L$\sim$L$_{dip}$ to a single in-plane domain where L$\sim \infty$.

Regrettably, our experiments do not have a resolution good enough to determine the stripe periodicity evolution with the hydrogen dose, and check whether it is exponential as predicted by equation 8.2. But we can still estimate the L_{min} in our system at the SRT, given by equation 8.3. For bulk Co, the values for J, and Ω_l are[3]:

- $J = J_{Co} \times d_{Co}$. Values of J_{Co} range from 14 meV (from ferromagnetic resonance, [291,292]) to 12 meV, obtained from first principles [231].

[3]We give the formulas in the S.I. system. In [54, 288, 289] there is a mixture of cgs and S.I.

- Ω_l=$\frac{\mu_0(d_{Co}\mu_{Co})^2}{a_{\|}^3}$. The magnetic moment of cobalt μ_{Co} is 1.7 μ_B [293–295], while the experimental in-plane lattice parameter $a_{\|}$ is 2.56 Å [128], while μ_0 being the vacuum permeability

The result is

$$L_{min}^{Co\ bulk} \sim 0.64\mu\mathrm{m} \tag{8.5}$$

This value is larger that the experimental one by about a factor of $\times 2$. Of course, the magnetic moment and the exchange constant for a Co bilayer on Ru might differ from the bulk values. Silvia Gallego has calculated the former and it is nearly unchanged for either a bilayer or a H-covered bilayer [294]. Curiously enough, she predicts that for intermediate coverage the magnetic moment can be larger. To estimate the latter, we scale it taking into account that the mean-field theory indicates that the Curie temperature is proportional to the exchange constant $T_c = 2/3J$. As the Curie temperature for Co bulk obtained from experimental measurements is $T_c^{Cobulk} \sim 1400$ [296, 297] while the Curie temperature of 2 ML is T_c^{2ML}=450 K (as we shown in chapter 7). We obtain the next relation:

$$\frac{T_c^{Co\ bulk}}{T_c^{2\ ML}} \sim 3 \Rightarrow J^{Co\ bulk} \sim 3J^{2\ ML} \tag{8.6}$$

where J^{2ML} is the exchange for 2 ML Co films. Applying this result in equation 8.3 we obtain that the stripe domain width for our system is one third of the stripe width of Co bulk,

$$L_{min}^{2\ ML} \sim 0.21\mu m \tag{8.7}$$

This result in much better agreement with the experimental value of 0.31 ± 0.03 μm. We note also that the predictions of Won et al. are based on a square lattice, while obviously Co/Ru has a hexagonal lattice.

The stripe domain period obtained is also in reasonably agreement with the stripe domain width observed experimentally(0.1–0.5 μm [212, 238, 287, 298, 299]) in Co films with perpendicular

stripe pattern, indicating the reliability of equation 8.2 to calculate the period of magnetic stripe patterns.

So the stripe width changes can be understood by the decrease of the magnetic anisotropy upon hydrogen exposure, and the stripe minimum periodicity is in reasonable agreement with the dipolar length of the bilayer. Now we propose a model for the observed behavior of the magnetic domains upon hydrogen exposure. The basic assumption is that the magnetic anisotropy energy (MAE) depends locally on the adsorbed hydrogen concentration, and changes sign for a given concentration. The adsorption of hydrogen on the Co surface probably occurs in the same stages as other gases, or as hydrogen on other metal films. First, molecular hydrogen dissociates upon arriving to the surface into individual hydrogen atoms. No differences were observed when using molecular or atomic hydrogen, so the adsorption process is likely to be non-activated, as reported previously [1]. The dissociation of hydrogen, nevertheless, might be more favorable at substrate steps, positions that are usually more reactive due to their uncoordinated character. The hydrogen adatoms remain on the film surface, without going into subsurface positions as evidenced by the lack of expansion of the last interlayer distance that would be obvious in LEED or electron reflectivity. The hydrogen adatoms are expected to diffuse rapidly around the surface, giving rise to an averaged constant density of hydrogen. A range of surface concentrations should be possible on the surface, with the hydrogen behaving as a increasingly dense two-dimensional adatom gas. In this range, changes on the out-of-plane domain size take place at the same time all over the 2 ML thick Co film, and following the previously discussed theories of striped patterns in magnetic films, the observed decrease in domain size reflects the gradual reduction in the magnetic anisotropy energy. Upon increasing the hydrogen dose, a critical concentration is reached when a phase transition occurs and the hydrogen separates into a condensed phase in coexistence with the 2D atom gas. A further increase on the hydrogen dose would only make the condensed phase grow and the adatom gas shrink, while the latter density stayed constant (at a given temperature). This split of the hydrogen

covered surface into two regions with different hydrogen densities would explain the latter stage of the SRT, where the magnetic contrast is found to disappear from some regions that grow from steps around the 3 ML thick Co islands, while it survives until higher doses in other regions (with small out-of-plane magnetic domains): the regions with a H-condensed phase would correspond to places where the SRT already has taken place (no out-of-plane contrast), while the others regions with a 2D-adatom gas would have small sized out-of-plane domains. The magnetization changes in the Co films upon hydrogen exposure would then be an useful way of following the fate of adsorbed hydrogen on the surface, which is very difficult to detect otherwise.

The presence of condensed phases of hydrogen in coexistence with 2D hydrogen adatom gas has been reported for several metal surfaces. The typical coverages at which ordered phases appear are $\Theta \sim 0.3$–1.0, and the critical temperatures are in the range of 30–290 K, with the highest critical temperatures found for the H/Co($10\bar{1}0$) case [1]. As we mentioned before, the amount of adsorbed hydrogen on the Co films has not been directly measured although we estimated it to be a fraction of a monolayer, and the experiments were performed at RT. Both conditions are reasonably close to some of the reported H/metal phases. It is in any case a promising venue for future work.

The origin of the anisotropy change due to the hydrogen adsorption should be an electron hybridization effect, as no structural changes have been detected in the films that would imply a strain effect. To check this explanation, we are in collaboration with S. Gallego at the ICMM-CSIC in Madrid. Preliminary results confirm the electronic origin of SRT.

8.3 Magnetization easy-axis changes on Co films grown at RT on H/Ru

The growth mode of thin films on metallic substrates is influenced by, among other factors, differences in the surface energy between the film and the substrate. This surface energy can be

modified by the presence of predeposited surfactants[4] on the substrate giving as a result changes in the growth mode or in the structure of the films [300, 301]. Cobalt growth on surfaces with different surfactants has been studied by several groups [302–305]. An example is the Co/Cu/Co coupling, which is greatly affected by the perfection of the layers and where the growth mode has been optimized through the use of Pb as a surfactant [306–311].

In this section we will study the magnetic easy axis of Co films grown at RT on H-terminated Ru(0001). The surface of the substrate was characterized by low-energy electron reflectivity. Cobalt films were characterized by STM and the magnetization direction was determined by SPLEEM. In the previous chapter we found that RT-grown Co films present a typical island size below the resolution limit of LEEM. They only presented a detectable magnetization for an average thickness of 3 ML or thicker. In particular, no magnetic out-of-plane nor in-plane magnetic signal was detected for an average thickness of 2 ML, in contrast to the observation of perpendicular magnetic anisotropy in large Co islands 2 ML thick grown at 550 K.

Experimental results

We first briefly characterize the Ru(0001) surface by means of low-energy electron reflectivity. Figure 8.8 (black curve) presents the reflectivity of the bare Ru surface. We observe that the electron reflectivity is constant until 5 ev, as the beam energy increases, the reflectivity of the surface decreases until 15 eV, where a sharp feature related with a band crossing is observed. Then, the reflectivity increases until 21 eV where a broad peak associated with the first Bragg reflection is observed. Upon hydrogen adsorption, different changes in the electron reflectivity stand out [figure 8.8 (red curve)]. The first change is a shift of 0.16 eV between the two curves in the 2-4.5 eV range. This shift reflects a change in the work function of the surface upon hydrogen adsorption [1], and it has also been observed in other metallic films [61]. Other changes after

[4]defined as a substance that reduces the surface energy

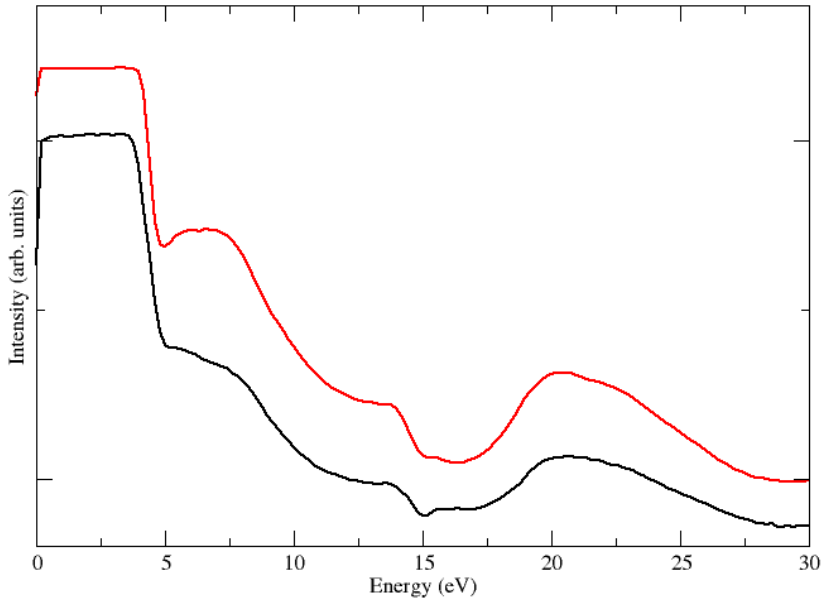

Figure 8.8 Electron reflectivity data acquired on Ru (black curve) and on H/Ru (red curve, offset for clarity). The data has been acquired at RT.

hydrogen adsorption are the presence of a broad peak at 6.5 eV, associated to hydrogen adsorption on the Ru surface. finally, in figure 8.8 we observe that after hydrogen adsorption the sharp feature at 15 eV changed and now at this energy the electron reflectivity shows a shoulder, this change in the reflectivity at 15 eV is due to a reduction of the density of unoccupied surface states upon hydrogen adsorption [169, 170].

We then followed in SPLEEM [figure 8.9] the RT-growth of the cobalt films on H/Ru. No magnetic contrast in-plane or perpendicular to the plane was found during the deposition of an average of 1 ML of Co [figure 8.9 (a)]. This result is not surprising taking into account that the Curie temperature of 1 ML thick Co film is below RT. Films with a total deposited coverage of 2–4 ML presented in-plane magnetic contrast [figure 8.9 (b)–(c)]. Unlike for RT-grown films of Co/Ru where no magnetic contrast was detected, the films grown at RT on H/Ru present an in-plane

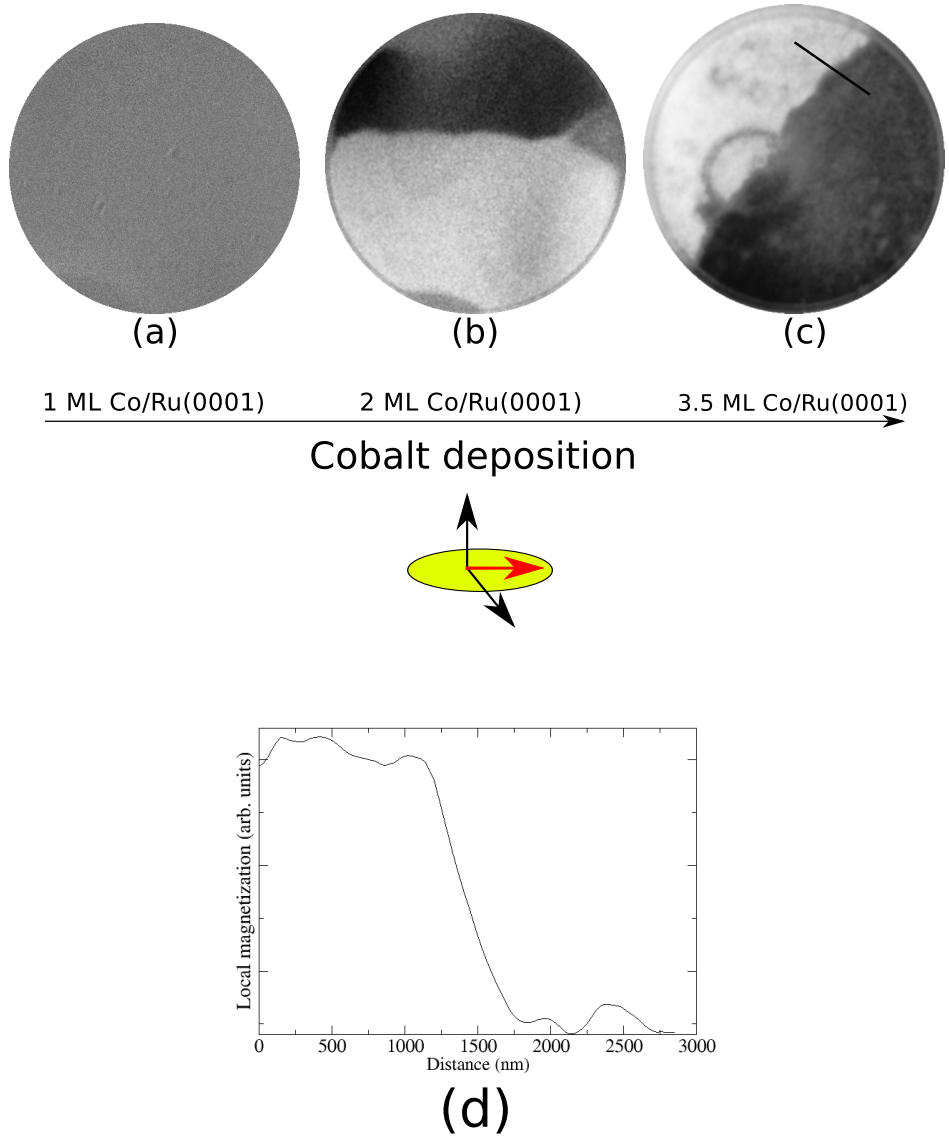

Figure 8.9 SPLEEM images acquired during the growth of Co on H-terminated Ru(0001), only second and successive layers present in-plane magnetization. The FOV is 11 μm. Beam energy was 6.2eV. (d) Profile acquired along the line marked in (c). The height represents the local magnetization in each domain.

magnetization easy-axis for an average thickness of 2 ML (contrast is also observed for thicker films). Another difference with the films grown at RT on Ru is the size of the magnetic domains.

The in-plane magnetic domains for Co coverages of 2 and 3 ML [figure 8.9 (b)–(c)] reach 15 μm in width. These domains are 10–20 times larger than the in-plane magnetic domains observed in the case of 3 ML of Co grown at RT on Ru. The domain wall width is also different [figure 8.9 (d)]. In the case of the films grown at RT on H/Ru(0001) the domain walls have a width of $0.65\pm0.05\mu$m, to be compared with $0.35\pm0.05\mu$m for the films grown on bare Ru [figure 7.10]. This reduction in the domain wall width must be due to a decrease in the magnetic anisotropy, similar to the the reduction of the anisotropy observed at the SRT point discussed in previous section.

Co films were grown in the STM chamber following the same steps as in the SPLEEM system, albeit with a larger background pressure of 2×10^{-10} Torr. In addition, we have also performed another experiment where 1 ML of Co at RT was grown in a 2×10^{-9} Torr of hydrogen. Figure 8.10 (a) and (b) shows STM images acquired after the growth of 0.9 and 2 ML of Co, respectively. In the image we can observe that cobalt decorates the atomic steps of the substrate and nucleates also as triangular islands in the substrate terraces. The Co islands have a size of $\sim$9 nm. All the islands are oriented in the same direction within the same substrate terrace, and are rotated 180° at consecutive terraces of the substrate. The number of islands is similar to that of Co grown at RT on bare Ru (see table 8.1), as is the height of the Co islands (0.20 nm). The growth and morphology of 1 ML thick Co films is thus similar when Co is deposited on either bare Ru(0001) or H/Ru(0001). Finally a 0.4 ML thick Co film was grown in a hydrogen background ($8\text{x}10^{-9}$ Torr)[8.10 (c)], again without significant differences with the previous cases.

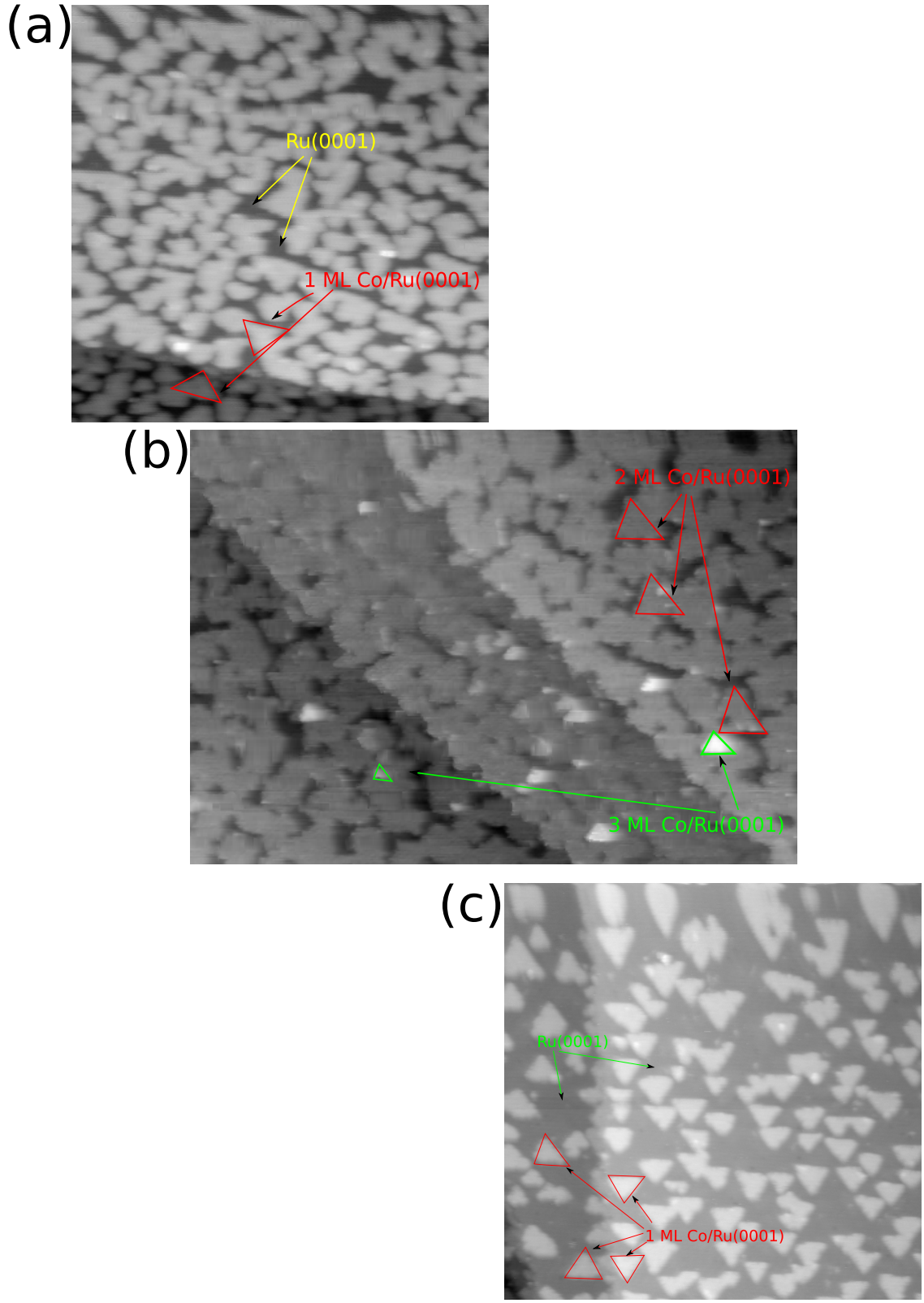

Figure 8.10 STM images of Co grown on H/Ru. (a) 0.9 ML (70 nm×70 nm), (b) 2 ML (100 nm×70 nm), and (c) 0.4 ML (70 nm×70 nm) grown on hydrogen atmosphere.

	Films grown Ru on bare	Films grown at RT then exposed to hydrogen	Films grown in H background
1 ML Co	$3.6x10^{13}$	$7.3x10^{13}$	$3.9x10^{13}$

Table 8.1 Density of islands (given in number of islands/cm^2) for Co film grown on bare Ru(0001), hydrogen terminated Ru and films grown in a hydrogen background.

Discussion

The most interesting result from the RT-grown Co films on H/Ru(0001) is the in-plane magnetic contrast in films with an average of 2 ML Co. This result resembles the hydrogen induced spin reorientation transition observed on flat bilayer films grown at 500 K. In both cases, no structural changes were detected when comparing the case with or without hydrogen, and in both cases the magnetization easy-axis of the second layer was in-plane when hydrogen was present in the system. We suggest that the same hydrogen-induced effect on the magnetic anisotropy occurs on the RT- grown films. A natural assumption is that the layer of hydrogen diffuses to the Co surface when Co atoms arrive to the Ru surface. After the growth, part of the hydrogen is then located at the surface of the Co film, a similar situation to that observed when the films were grown at 550 K and hydrogen was adsorbed on the surface of the films [figure 8.11 (a)].

8.4 A novel gas sensor

We have proposed to use the sensibility to hydrogen exposure of the cobalt magnetization easy-axis as a gas sensor, for which we were granted the patent PCT/US2010/032990. The motivation for such a sensor is that hydrogen is used in many industrial applications such as chemical industries, petroleum refining, or power plants. In these environments, safety is important because a hydrogen/oxygen mixture only needs 0.02 mJ [312] to be ignited (10 times lower than a propane/oxygen

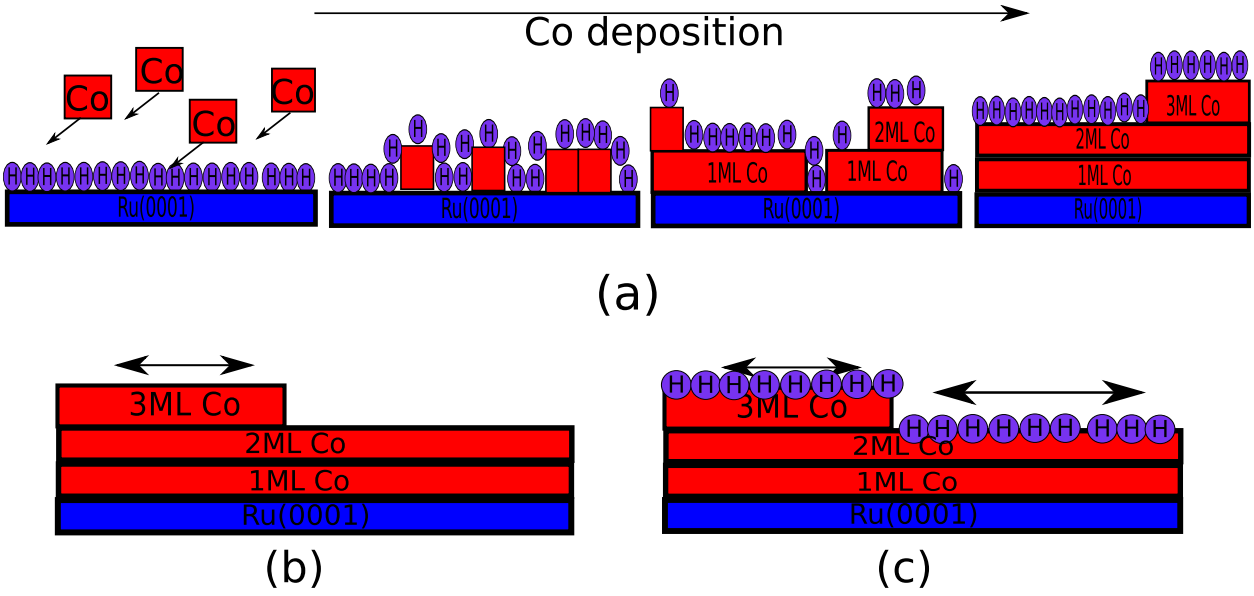

Figure 8.11 (a) Model representation to explain the change in the anisotropy of the second layer.(b)-(c)Schematics of the anisotropies of the different layers of cobalt grown on Ru(0001) at RT. (b) Co growth on clean Ru(0001). (c) Co layers grown on pre-saturated Ru(0001).

mixture): a small electrical discharge is enough to start the combustion [313]. Furthermore it is known that hydrogen absorption into the iron of containment vessels can produce mechanical failures in steel [314–316] producing hydrogen leaks. In consequence, the detection of hydrogen is a problem that has received much attention. It is possible to detect very small quantities of hydrogen with a high sensitivity in laboratories equipped with bulky and very expensive devices and detectors. However commercial detectors [317–320] present disadvantages such as a high concentration threshold or the possibility of interference with other gases present in the environment. For all these reasons, there is a need for hydrogen sensors that are simpler, cheaper to produce, more compact, and consume less energy.

8.4.1 Description of the sensor

Our proposed gas detector works as follows: a sensor is made of a stack of ferromagnetic layers separated by Ru layers. This multilayer stack structure should exhibit a giant magneto resistive effect [43, 321, 322]. The electrical resistance of the multilayer structure can then change from low to high values when the direction of the magnetization of the upper and the lower magnetic layers are parallel or anti-parallel, respectively. The sensor requires that the magnetization of the lower ferromagnetic film remains in the same direction, while the upper ferromagnetic layer is made of a ferromagnetic layer that can flip its magnetization easy-axis in the presence of hydrogen. All this multilayered stack would be mounted on a heater chip to desorb hydrogen when needed. Figure 8.12 shows a schematic representation of the device.

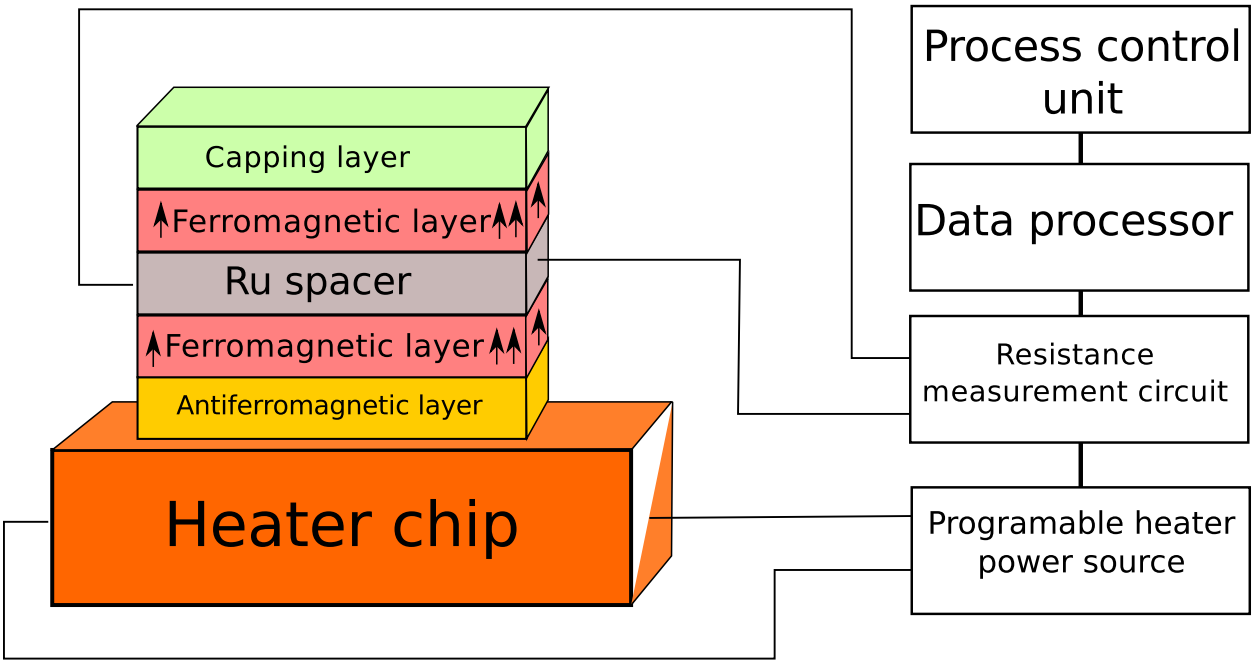

Figure 8.12 Schematic of the gas sensor.

The stack would be mounted on a circuit board that reads the resistance of the stack. The resistance would change as a function of whether or not the easy axis of the exposed layer of epitaxial cobalt film is in-plane or out-of-plane. The circuit board might include a programmable

heater power source and a process control unit which could be used to both calculate amounts and concentrations of the detected gases as well as, in combination with the programmable heater power source, identify the gas detected. By thermally desorbing gases which have been adsorbed onto the surface of the detector, it could be reset to the original orientation of the magnetization of the upper ferromagnetic layer.

Some of the advantages of our detector would be:

- Size: it should be possible to build a multilayered stack with nanometer dimensions.
- Hight selectivity: the capping layer might be designed and used as a filter for an specific gas.
- Response time: due to the small dose needed to obtain the change in the magnetization, the response of the system can be below one second for partial pressures of 10^{-6} Torr.
- Low energy use: the simplicity of the mounted circuit boards would make the energy requirements of the detector very low.

In order to use the sensor in real atmospheres and protect the Co films from oxidation, the stack would have to include a protective capping layer. The capping layer of a multilayered system could be used to functionalize the sensor for a variety of different gases.

8.5 Conclusions

By means of SPLEEM we have discovered a hydrogen-induced spin reorientation transition on large 2 ML thick Co islands or films (grown at 550 K), from the initial out-of-plane easy-axis orientation to an in-plane one, we have characterized first time in real space such a gas-induced SRT. The H_{H_2} dose required to achieve that SRT is $\sim$0.4 L_{H_2}. This SRT is reversed by heating the films to 400 K, presumably by desorbing the hydrogen from the film. No structural changes were detected in the films after hydrogen adsorption. Before the magnetization easy-axis direction

changes from out-of-plane to in-plane, the domain pattern changes for exposures between 0.2–0.4 L_{H_2}. In that range the large, micrometer sized, up and down magnetic domains break up into much smaller elongated domains, that in the smaller dimensions, reach a size of $0.20 \pm 0.02 \mu$m. This periodicity is in reasonable agreement with the predictions of a model incorporating the competition of exchange, anisotropy and dipolar interactions at the SRT. Eventually, the out-of-plane contrast disappears in a non-homogeneous manner. We propose that the changes are related to the local density of hydrogen on the surface of the Co film, with the non-homogeneous character of the SRT reflecting a non-homogenous hydrogen density due to hydrogen separating into a two phase system above a critical concentration.

We also have studied the magnetization easy-axis of Co films grown at RT on H/Ru(0001). For an average coverage of 2 ML, unlike for films grown on Ru, the films are magnetized in-plane. No structural differences where found when comparing the films grown on bare Ru and on H/Ru. We presume the same SRT occurs on RT grown Co films as found on large Co islands grown at 550 K, and, additionally, that hydrogen floats to the surface of the film during Co growth.

Finally, we have proposed a gas sensor based on the hydrogen-induced spin reorientation transition. By integrating the cobalt film into a spin-valve structure, the change in the anisotropy of the film would be detected as a change in the electrical resistance of the spin-valve. We suggest that metal capping layers might be useful for functionalizing the sensor to other gases.

Chapter 9

Pd capping of Co deposited on Ru

9.1 Introduction

Ultra thin magnetic films with perpendicular magnetization [323–326] have been studied due to their technological applications in the magnetic recording industry [327–331]. With its large magnetic perpendicular anisotropy and large Kerr rotation at low photon wavelengths, Pd/Co multilayers are a popular system. The magnetization easy-axis in Pd/Co multilayers can be tuned by selecting the Pd or the Co layers thickness. But the detailed influence of other parameters such as the growth conditions is still under discussion. While Dorantes et at. [332] attributed the change in the direction of the magnetization to the role that Pd atoms play in the spin-orbit interactions, Nakagawa et al. [333] indicated that the magnetic properties in Co/Pd mulilayers are related with the surface and interface morphology of the films.

It has been reported that hydrogen adsorption induces changes in the magnetic moment of the Pd/Co combination or changes in its magnetization easy-axis [23, 334, 335]. In all cases a low hydrogen adsorption gave an enhancement of the PMA, while a higher hydrogen amount of adsorbed hydrogen induced a decrease of the PMA, although the origin of the detected changes is

not well understood yet.

These results suggest the need to study the growth and the magnetization of Pd on Co. In this chapter we present our results on the growth of Pd on Co/Ru, and on the magnetic easy axis of the Pd/Co/Ru films. Then possible changes in the magnetization easy-axis will be sought by hydrogen adsorption.

9.2 Pd capping of Co/Ru

We have grown Pd on regions 2–5 ML thick of Co/Ru(0001). To such end we have used two Co films. The first is a film with 3 ML thick Co islands on a mostly 2 ML film [figure 9.1 (a)], while the second is a film with 5 ML islands on a mostly 4 ML thick Co film [figure 9.2 (a)–(e)]. In both cases, the Co films were grown at 550 K.

Growth

In the first Co film, the 3 ML thick Co areas appeared dark-gray at the beam energy of 7 eV [figure 9.1 (a)]. The 2 ML areas appear medium-gray, and some light-gray areas corresponded to 1 ML Co. Frames from the sequence of LEEM images acquired during the Co film growth have been shown in a previous chapter (figure 7.1). There are several substrate steps where the 3 ML Co thick areas formed a continuous ribbon, with additional 3 ML triangular islands with two orientations (indicating the presence of hcp and fcc stacking sequences in the Co film). Pd is deposited while the substrate is kept at 550 K. The Pd islands appear as light-gray triangles on both the 2 ML and 3 ML areas of the Co film [figure 9.1 (b)–(d)].

The Pd triangular islands nucleated on top of the triangular 3 ML Co islands have the same orientation as the underlying Co island. That only one orientation of the triangular islands is detected on each triangular Co island (and on the 2 ML Co areas) implies that Pd does not present

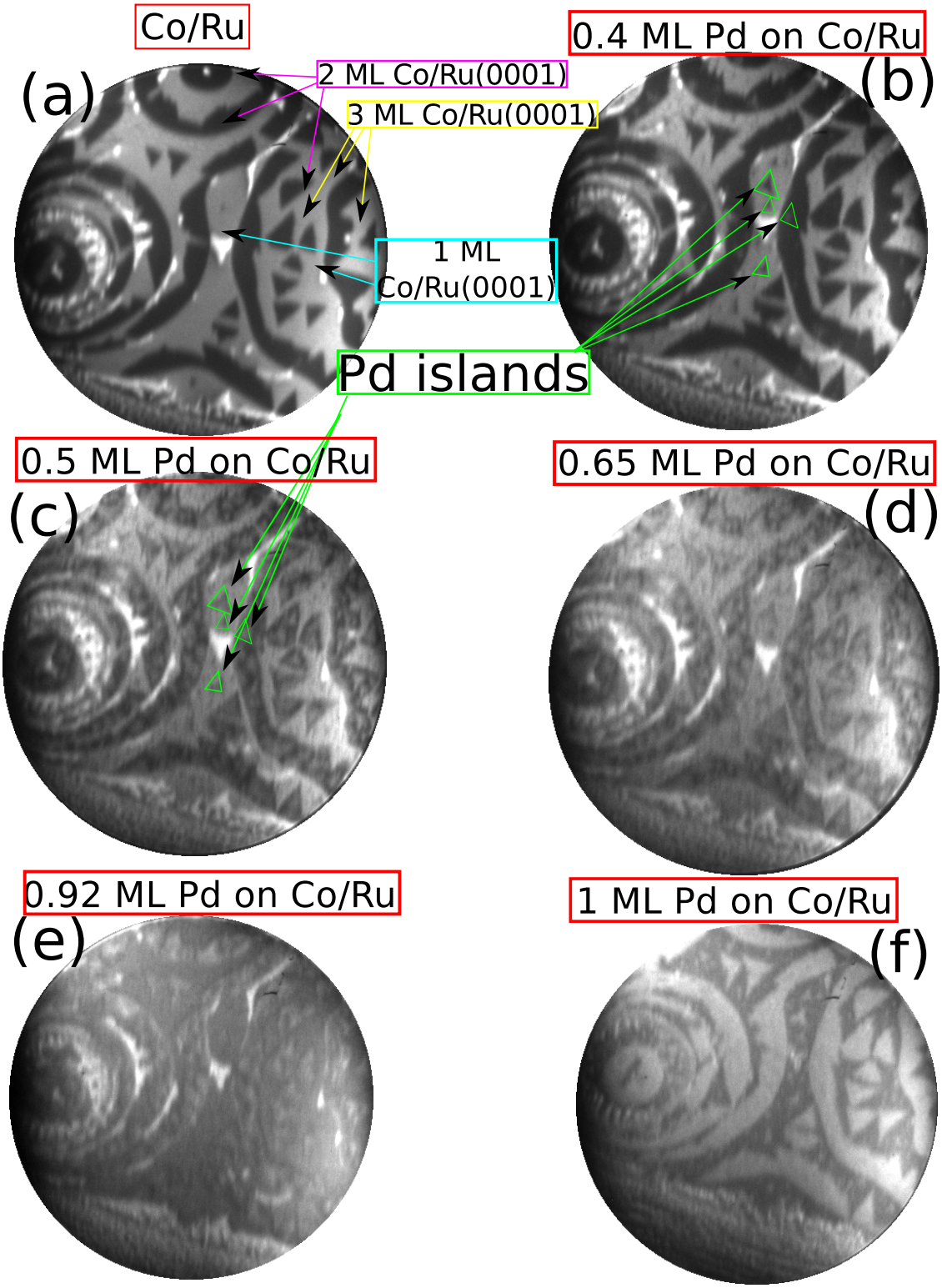

Figure 9.1 (a)–(f) Image sequence acquired in LEEM during the growth of 1ML of Pd on a Co film with 1,2 and 3 ML areas exposed (the growth of the film is presented in figure 7.1). The FOV is 8μm and the beam energy is 7 eV. The growing Pd appears as light grey on the Co film.

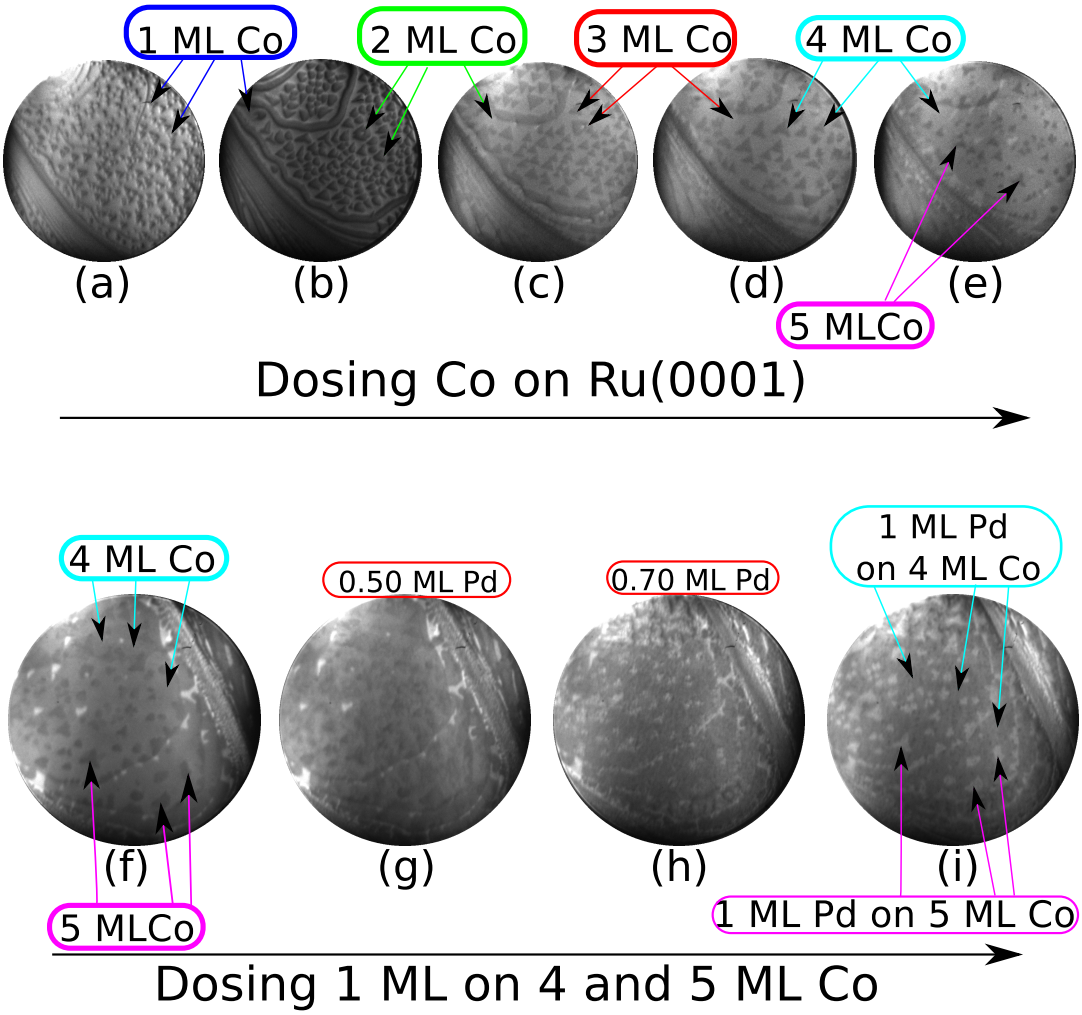

Figure 9.2 (a)–(e) Image sequence acquired in LEEM during the growth of 5 ML Co/Ru(0001) at 550 K. After it, we grew 1ML of Pd on a 5 ML thick Co islands and 4 ML tick areas exposed. (e)–(i) show the image sequence acquired in LEEM during the growth of the Pd layer. The FOV is 8μm and the beam energy was 5.2 eV. The growing Pd appears as light grey on the Co film.

stacking faults when grown on Co. After completing 1 ML Pd [figure 9.1(f)] the contrast of the Co layers is reversed when compared with the situation of the bare Co film: Pd on 2 ML Co areas appear darker than Pd on 3 ML Co areas. Further Pd growth produced a uniform change in the electron reflectivity, but no further nucleation of islands was observed in LEEM.

Pd growth on the thicker Co film is presented in figure 9.2. The top images in figure 9.2 (a)–(e) show the growth of a film up to a coverage over 4 ML Co. The initial steps [figure 9.2 (a)–(c)] are similar to previous films described in chapter 7 which correspond to films with 3 ML islands on 2 ML films. Image 9.2 (d) shows that an additional ML of Co gives rise to a film with 4 ML thick triangular islands, which have different orientations. This is to be expected, as already the 3 ML islands had two different stacking sequences (fcc and hcp) that are the same for the underlying 2 ML, while they can be considered to have a stacking fault at the last layer. This can also happen at the 4 ML level, giving rise to 4 different stacking sequences in the 4 ML Co islands. With the deposition of an additional layer, the 5 ML islands do not have a well-defined triangular shape although the island density is not too different from the previous level. In any case, in figure 9.2 (e) we can observe that 5 ML thick Co islands appear dark-gray on 4 ML thick exposed areas which appear light-gray. In figure 9.2 (g)–(i) we present frames from a sequence of LEEM images acquired during the growth of 1 ML Pd (the temperature of the sample was 550 K). The nucleation of individual Pd islands is not detected and only a uniform change in the electron reflectivity is observed during the Pd deposition. After the completion of the Pd layer, the contrast of the 5 and 4 ML thick Co areas is reversed: the Pd capped 5 ML islands appear darker than the Pd capped 4 ML areas.

Low-energy electron reflectivity curves in the range of 0–30 eV were acquired on 1 ML Pd/2 ML Co/Ru and on 1 ML Pd/3 ML Co/Ru [curves (III) and (IV) in figure 9.3]. For comparison, in figure 9.3 we also present low-energy reflectivity curves acquired on 2 ML Co on Ru [curve (I)] and 3 ML Co/Ru [curve (II)]. The reflectivity of 2 ML and 3 ML Co/Ru films presents a broad

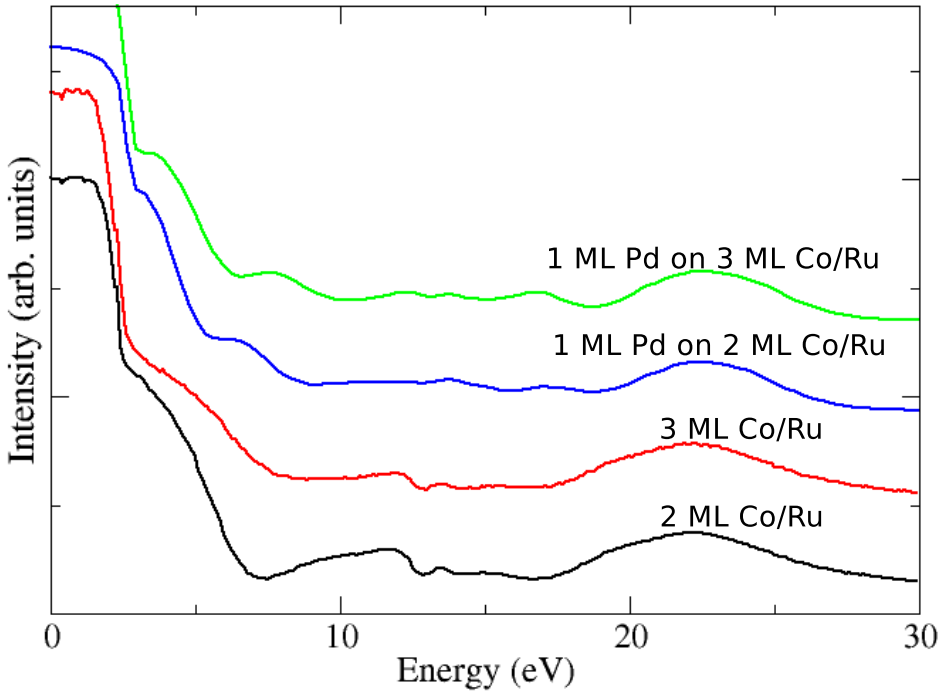

Figure 9.3 Low-energy reflectivity curves acquired on (I) 2 ML Co/Ru,(II) 3 ML Co/Ru, (III) 1 ML Pd/2 ML Co/Ru, and (IV) 1 ML Pd/3 ML Co/Ru, respectively. Data have been offset for clarity

peak near 21 eV and a sharp feature at 13 eV (which correspond to a Bragg reflexion and a band crossing, respectively [121]). The data acquired on the Pd capped layers show that the broad peak is now located at 22 eV. This is same energy at which the broad peak was found on a Pd film (see chapter 3). The sharp feature at 13 eV in the bare Co films vanishes. The additional oscillations in the 7–15 eV energy range in 1 ML Pd/3 ML Co/Ru are attributed to quantum interference peaks.

Spin-reorientation upon Pd capping

In addition to the LEEM images, SPLEEM data were acquired simultaneously during Pd deposition on the 2+3 ML Co film. In figure 9.4 (a) we present the surface topography [it corresponds to figure 9.1 (a)] of the Co film. The corresponding SPLEEM image with an in-plane electron-beam spin-polarization shows magnetic contrast only on the 3 ML areas of the Co film. As Pd is deposited [figure 9.4 (c–f)] the magnetic in-plane contrast of 3 ML Co islands dissapears from the Pd covered areas, until no in-plane magnetic contrast remains at the completion of the Pd capping layer [figure 9.4 (g)]. After the Pd deposition, the sample was cooled down to RT and further SPLEEM images were acquired, this time with the beam spin-polarization out-of-plane (figure 9.5). In the SPLEEM out-of-plane image both the 2 ML and the 3 ML Co areas present out-of-plane magnetic contrast: the Pd capping layer has switched the magnetization easy-axis of 3 ML thick Co islands from in-plane to out-the-plane, while no change is observed in the magnetization easy-axis of the 2 ML areas [see the schematic in figure 9.5 (c)].

We have repeated the Pd capping on the thicker 4+5 ML Co film [Figure 9.6 (i)]. Figure 9.6 (a) shows the LEEM image acquired after the growth of the complete Pd monolayer. Before the Pd deposition, all the film presented in-plane magnetization (not shown), as expected for Co films thicker that 2 ML [128]. Figure 9.6 (b)–(c) shows the SPLEEM image of the same area with the electron-beam spin-polarization direction in-plane and out-of-plane, respectively. While the Pd capping layer reoriented the magnetization easy-axis of 4 ML Co from in-plane to out-of-plane,

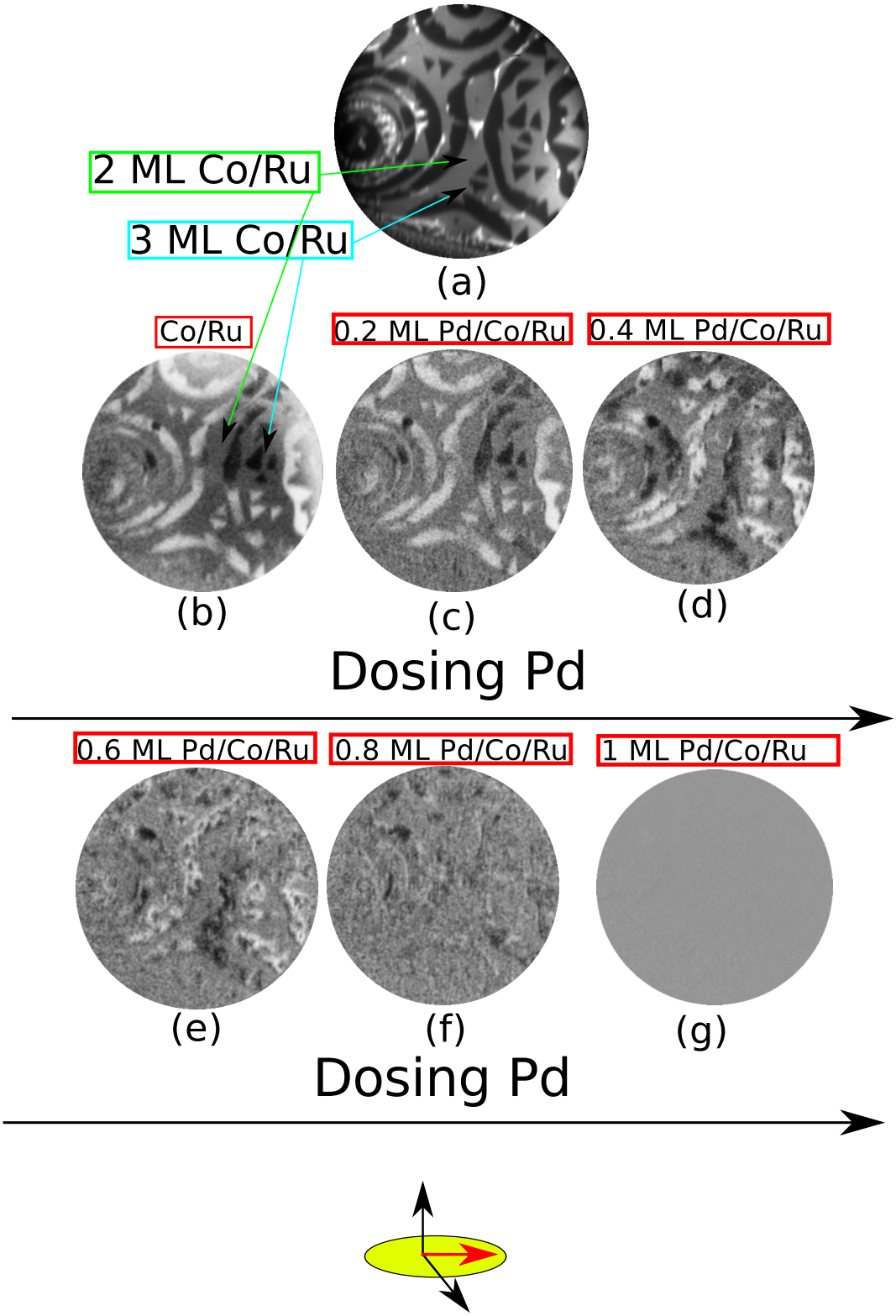

Figure 9.4 (a)LEEM image acquired on 2 and 3 ML thick Co areas (b)–(g)SPLEEM image sequence acquired during Pd deposition, the electron-beam spin-polarization direction is in-plane. During the Pd dose, the in-plane magnetic contrast vanishes. The FOV is 8μm and the beam energy was 7 eV in both LEEM and SPLEEM images.

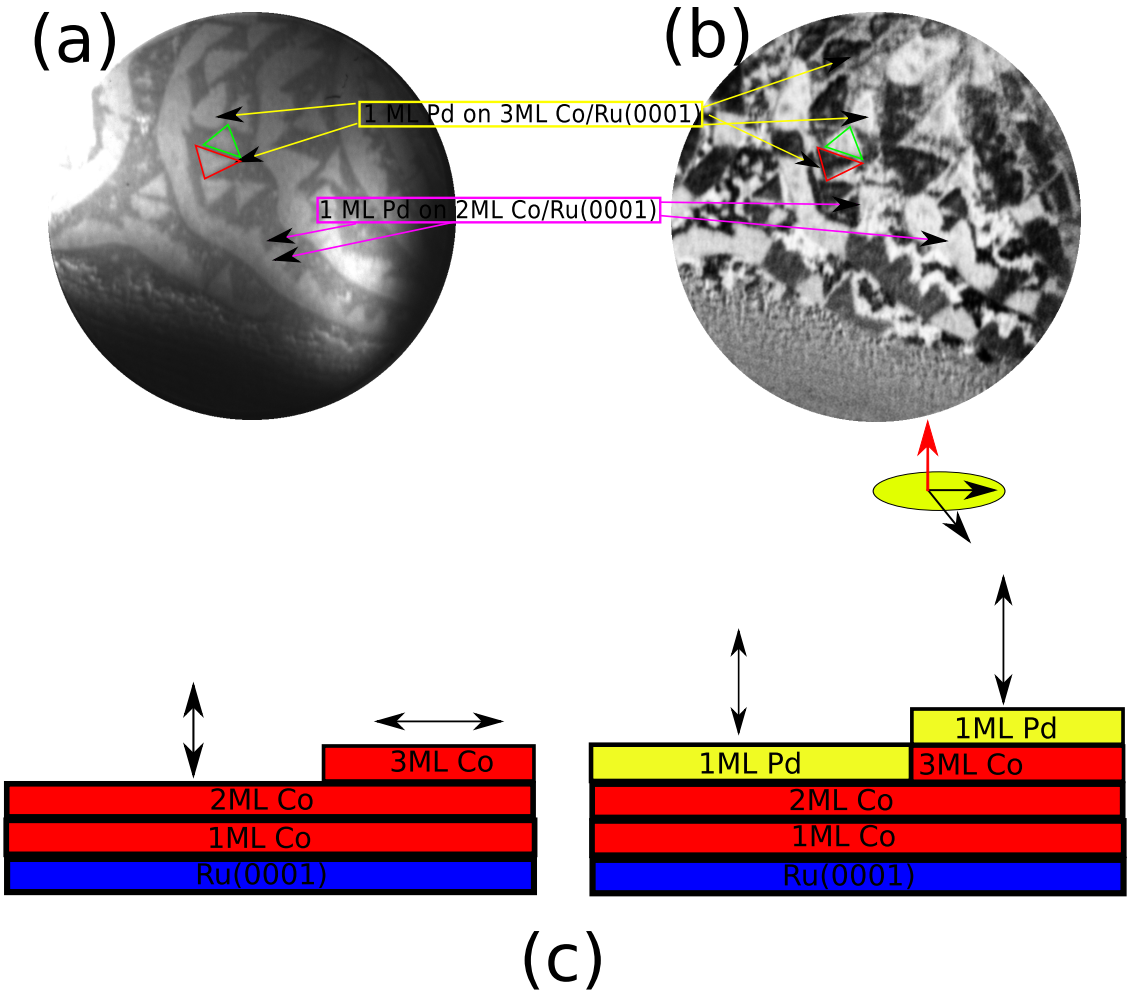

Figure 9.5 (a,b) LEEM and SPLEEM images, respectively, acquired at RT on the Pd-capped Co film presented in figure 9.1. The FOV is 8 μm and the beam energy was 7 eV. The electron-beam spin-polarization direction was out-of-plane. (c) Schematic representation showing the magnetization easy-axis before and after depositing the Pd capping. Both 2 ML and 3 ML Co areas now present an out-of-plane easy axis when covered with Pd.

the magnetization easy-axis of 5 ML Co stayed in-plane. The magnetic domains of 1 ML Pd/4 ML Co/Ru had sizes between 0.40–1.10 μm. This value is smaller that the domains presented by 1 ML Pd/2,3 ML Co/Ru areas (which are 0.84–2.25μm wide) from the first film (figure 9.5).

Discussion

Capping ultrathin ferromagnetic films with non-magnetic metals often affects the films magnetization easy-axis. Cu or Au increase the out-of-plane magnetic anisotropy on Co films on W(110) [336], and the deposition of any of the coinage metals on Co films on Ru(0001) actually reorients the easy axis of magnetization to an out-of-plane direction for selected combinations of the thickness of the capping layer and the Co film [337]. So far, the effect of Pd is similar to that of Cu and Au: while Pd extends the PMA in Co films up to the 4 ML, Cu extends it to 4 ML, and Ag extends it to 3 ML. We note that the out-of-plane domain sizes are smaller for 1 ML Pd/4ML than for 1 ML Pd/3ML Co or 1 ML Pd/2ML Co. Actually the domain sizes observed ($\geq$0.4 μm) are close to the stripe domain width size predicted for a PMA cobalt film using the bulk Co exchange constant and magnetic moment discussed in the previous chapter, 0.4 μm for a d_{Co}=4 ML film. This would imply that the effective magnetic anisotropy in 1 ML Pd/4ML Co is very close to zero. This is compatible with the observation that for 1 ML Pd/5ML Co the MAE already changed sign giving an in-plane magnetization easy-axis.

9.3 Pd/Co/Ru upon gas exposure

In this section, we study the possible effect of hydrogen on Pd-capped Co films. During gas dosing, the magnetic domains of the Co film were monitored by SPLEEM in real time. To monitor the adsorption of the different gases, low-energy reflectivity curves were acquired at the end of each dose and compared with the reference curves taken on the bare Pd/Co/Ru films.

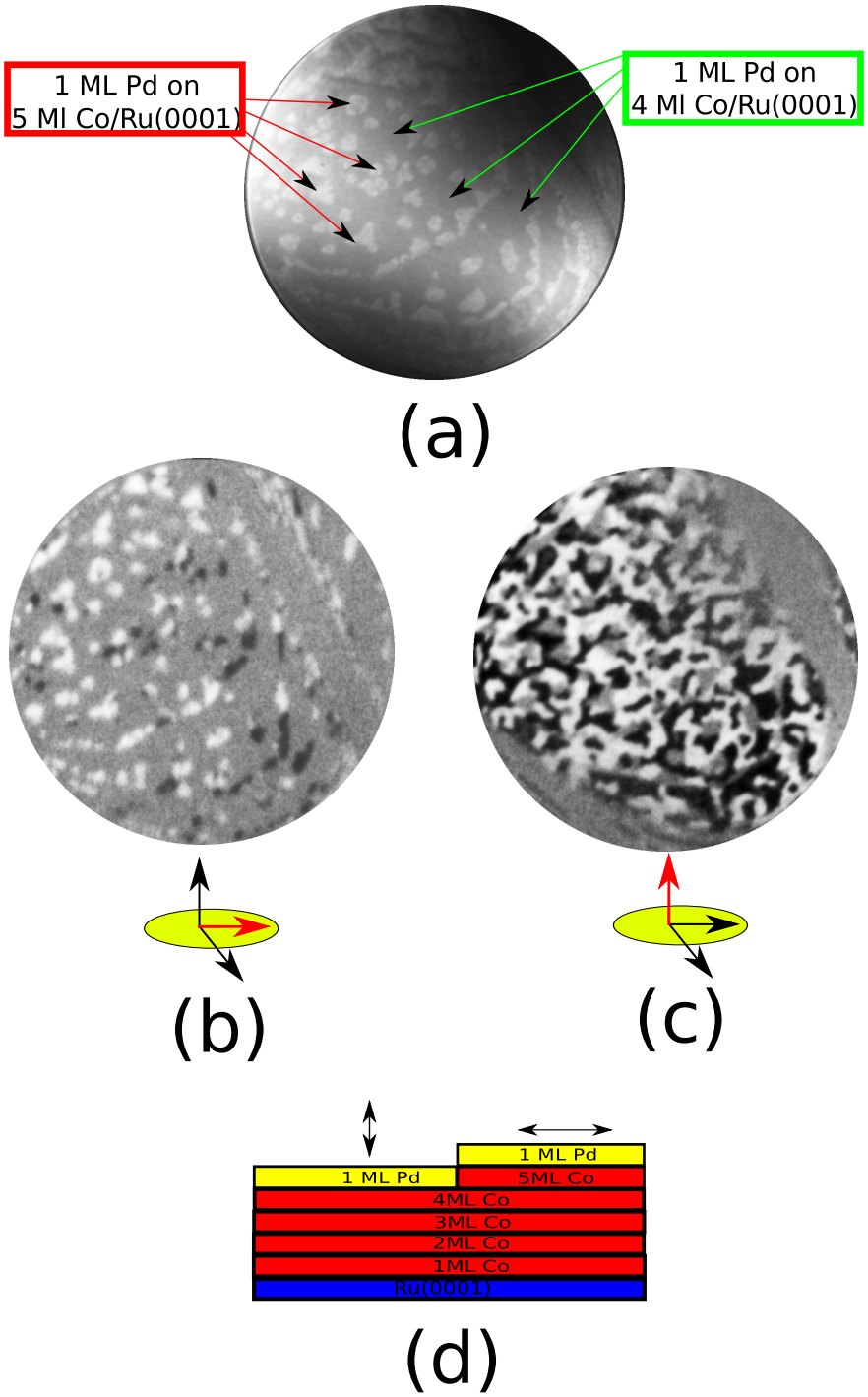

Figure 9.6 (a) LEEM recorded after growing 1 ML of Pd on areas covered with 4 and 5 ML of Co/Ru(0001). (b) SPLEEM image acquired with the electron beam spin polarization direction out-of-plane. (c) SPLEEM image acquired with the electron beam spin polarization direction in-plane. The FOV is 8 μm. The beam energy is 5.2 eV. (d) Schematic representation of the magnetization direction for each thickness of the film shown in (a).

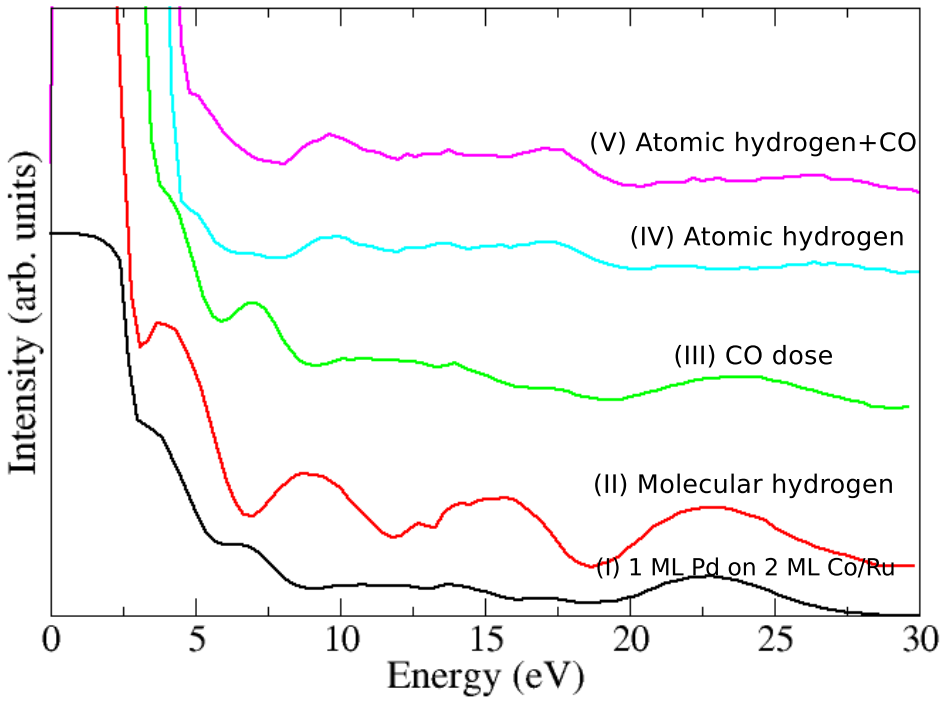

Figure 9.7 Low-energy electron reflectivity curves acquired on 1 ML Pd/2 ML Co/Ru after dosing different gases [(I) initial Pd/Co/Ru film], (II) 2 L_{H_2}, (III) 3 L_{CO}, (IV) 90 L_H, and (V) 60 L_{H+CO}. The data have been offset for clarity.

Molecular hydrogen

In the study of hydrogen exposure to Pd films presented in chapter 4, adsorbed hydrogen was detected in the electron reflectivity of the Pd films. In particular, the regions between 5–10 eV presented a higher reflectivity when hydrogen was present on the film surface. The same effect has been observed also on the Ru(0001) substrate (chapter 8, page 180). However, the presence of hydrogen on the Co films, which was evident in the change of the magnetic easy-axis, was not accompanied by any increase in the reflected intensity in the 5–10 eV range. In figure 9.7 we present the electron reflectivity of the Pd-capped 2 ML Co/Ru film [curve (I)], and of the film after

exposure of 2 L_{H_2} [curve (II)]. After the hydrogen dose, we observe that the reflectivity of the sample in the range of 7–18 eV is increased while the broad peak at 22 eV did not change position. As in the case of Pd films, we suggest that this enhancement in the reflectivity is due to hydrogen adsorbed on the surface of the film. In figure 9.8(b) and (c) we shown the SPLEEM out-of-plane image of the Pd-capped 2 ML Co film before and after exposure to H_2, respectively. No change in the magnetization easy-axis was observed after 2 L_{H_2}.

Effects of CO

CO adsorption on Pd films was studied in chapter 4 by low-energy electron reflectivity and LEED-IV. Upon CO adsorption, the peak located at 22 eV in the electron reflectivity curve became wider and decreased its intensity until it finally vanished, and a new peak appeared at lower energy (16 eV). LEED-IV data suggested that CO was adsorbed on the surface of the films. We also discussed CO adsorption on Pd pre-saturated with hydrogen. During the CO exposure, we observed that the peak at 10 eV (due to hydrogen adsorption) vanished, at same time the broad peak at 22 eV decrease its intensity and a new peak at 16 eV was detected i.e. adsorbed CO displaced hydrogen from the Pd surface [see figure 4.8 pag. 85]. Figure 9.7 curve (III) (green) shows the low-energy electron reflectivity acquired on Pd/Co/Ru after dosing 3 L_{CO}. Comparing the electron reflectivity of the CO-exposed Pd/Co/Ru film with the one from the bare Pd/Co/Ru film, the peak at 22 eV has became wider and its height decreased, while the peaks at 7–18 eV has decreased its intensity. We also observe an increase of the electron reflectivity at 7 eV not observed in chapter 4 when CO was adsorbed on Pd, (in this case we cannot explain the origin of this peak at 7 eV). The behavior of the reflectivity after CO doses, is similar to the one observed when hydrogen and CO were dosed on Pd [see figure 4.8 pag.85], suggesting that CO ends up adsorbed on the surface of the Pd/Co/Ru film. Figure 9.8 shows the LEEM and SPLEEM images acquired before the CO dose [figure 9.8 (d)–(e)] and after exposing the surface to 3 L_{CO} [Figure 9.8 (f)]. We can see that CO did not change

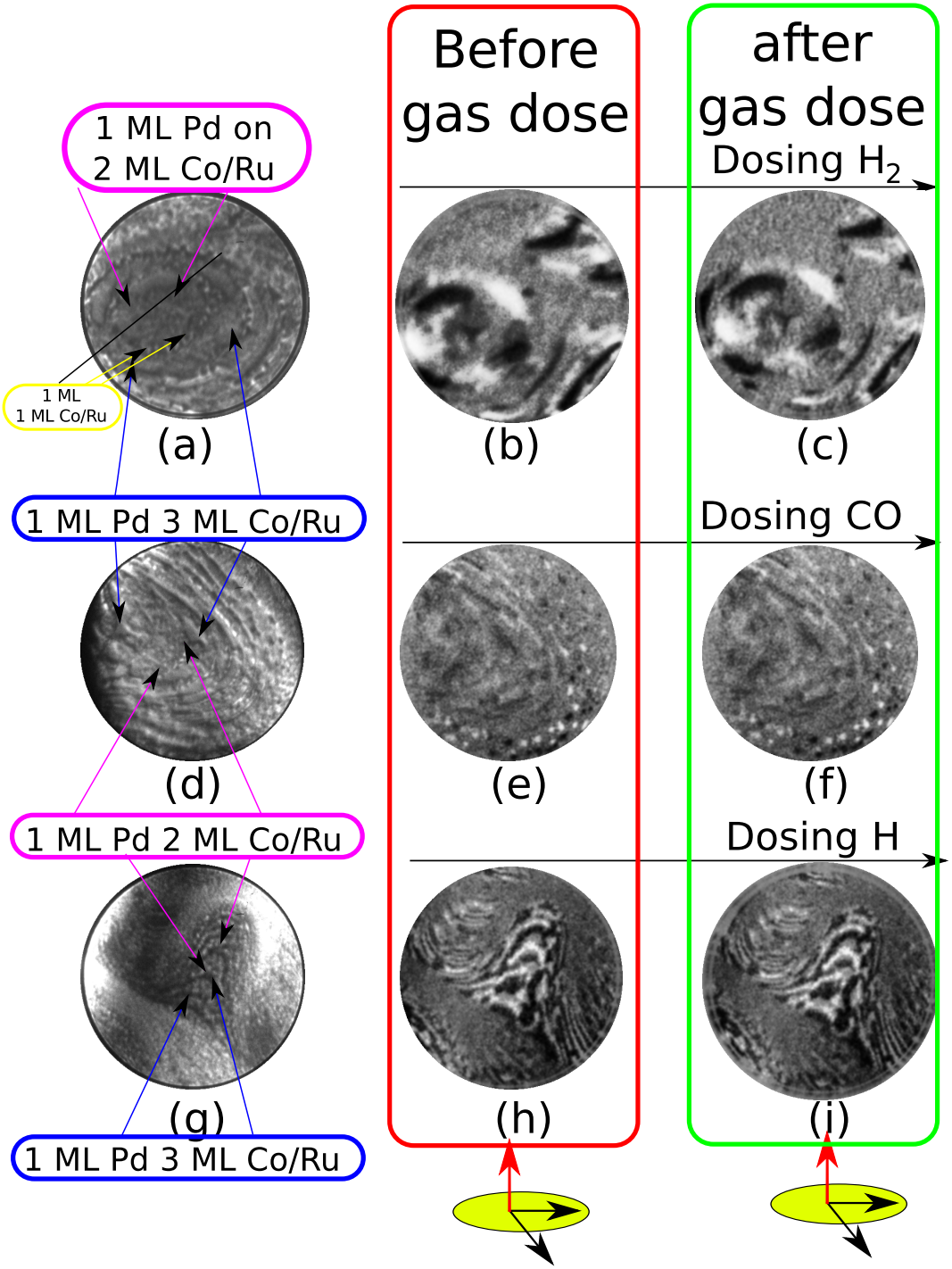

Figure 9.8 LEEM and SPLEEM images acquired before and after exposing the films to different gases. (a)-(b) LEEM and SPLEEM image respectively acquired before molecular hydrogen exposure, (c) SPLEEM image acquired after 2 L_{H_2}, (d)–(e) LEEM and SPLEEM images respectively acquired before CO exposure (f) SPLEEM image after exposing the films to 3 L of CO (g)–(h) LEEM and SPLEEM image respectively acquired before exposing the films to atomic hydrogen, (i) SPLEEM image acquired after exposing the films to 90 L_H. The bean energy is 6.1 eV in both LEEM and SPLEEM images. FOV is 10μm

the magnetization easy-axis.

Effects of atomic hydrogen

Atomic hydrogen is a more effective way of introducing hydrogen in a metal subsurface positions [11, 338] (see also chapter 4). In figure 9.7 the electron reflectivity acquired on Pd/Co/Ru after 90 L_H [curve (IV)] is shown. In this experiment we used an hydrogen cracker of the same design as the one built in Madrid and described in chapter 2. The SPLEEM electron source (see chapter 2) becomes contaminated by hydrogen in the LEEM chamber, preventing a continuous monitoring in SPLEEM of the magnetic easy-axis for exposures larger than 90 L_H. Upon exposing to such a dose, the broad peak at 22 eV in the electron reflectivity of the Pd/Co/Ru film vanished, and a small peak in the energy range of 7–10 eV appeared together with another peak at 17 eV. These changes in the electron reflectivity are similar to those of atomic hydrogen dosed on Pd films (see chapter 4). Thus, they can be explained using the same type of reasoning. The increase of the electron reflectivity in the range of 7–10 eV suggests the presence of a small amount of hydrogen on the surface, while the peak at 17 eV and the lack of a broad peak at 22 eV suggests the presence of CO (generated by the hydrogen cracker) adsorbed on the surface of Pd/Co/Ru film. After 90 L_H, no changes in the magnetization easy-axis were detected in SPLEEM as shown in figure 9.8 (i) to be compared with the SPLEEM image acquired previously to the atomic hydrogen exposure figure 9.8 (h).

In chapter 4, when dosing the Pd film with atomic hydrogen together with some CO, hydrogen populated the sub-surface positions. The presence of CO was necessary to prevent hydrogen desorption from Pd. The changes observed in the electron reflectivity of Pd/Co/Ru films upon atomic hydrogen suggest that hydrogen is incorporated into the Pd/Co interface, but if so, it did not change the magnetization easy-axis.

One possible explanation is that the amount of CO present on the surface is not enough to

prevent hydrogen desorption from Pd. To check this possibility, a final experiment was performed to force hydrogen into the Pd/Co sub-surface positions by co-dosing CO and atomic hydrogen, increasing in this way the amount of CO on the Pd surface. Typical partial pressures used were 3×10^{-8} Torr of atomic hydrogen and 2×10^{-8} Torr for CO, giving a total pressure of 5×10^{-8} Torr. Curve (V) (magenta) in figure 9.7 shows the electron reflectivity of the surface after 60 L_{CO+H}. The curve is identical to that obtained when only atomic hydrogen was dosed: a small peak in the electron reflectivity at 10 eV indicates that hydrogen is adsorbed on the surface, and a peak at 17 eV together with the lack of a peak at 22 eV indicates the presence of CO on the Pd surface. After the combined CO+atomic hydrogen dose no changes in the magnetization easy-axis were detected in SPLEEM. After this experiment the electron source was regenerated and an additional 36 L_{CO+H} were dosed. Again, no changes in the magnetization easy-axis of the sample were observed.

Discussion

Motivated by the results obtained in chapter 8, where a SRT was observed upon hydrogen exposure, we have studied if the same phenomenology occurred on Pd/Co/Ru films. For this goal, we have tried to populate the Pd/Co interface with hydrogen to induce a change in the magnetization easy-axis from out-of-plane to in-plane. After individual dosing of molecular hydrogen, CO or atomic hydrogen no changes in the magnetization easy-axis were detected by SPLEEM [see figure 9.8] even if the reflectivity data acquired on Pd/Co/Ru after gas exposure suggested hydrogen incorporation in the Pd/Co interface (when comparing with the results of Chapter 4 on Pd films).

Different factors may explain the lack of change in the magnetization easy-axis. The first reason is the system chosen. Pd induces a strong perpendicular magnetic easy-axis. It might be easier to turn the magnetization easy-axis with hydrogen exposure by selecting a Pd and Co thickness combination where the perpendicular anisotropy energy is smaller. A way to do this is by increasing the thickness of the Co layer to 4 ML. As it was shown in figure 9.6 with 1 ML Pd

capping, the Co films have their magnetization easy-axis out-of-plane until they are 4 ML thick (the easy-axis in the fifth layer is already in-plane), i.e. the effect of the Pd layer is to overcome the shape anisotropy of $\sim$2 Co layers. From the results obtained in this section and taking into account the results presented in chapter 4, if seems that it should be easier to turn the magnetization easy-axis upon hydrogen exposure in a stack made of 1 ML of Pd on 4 ML Co/Ru.

Other factor is the hydrogen pressure. Different works have reported that hydrogen can be absorbed by Pd in systems composed of ferromagnetic films capped with Pd layers. For example in Pd/Co/Pd it was reported [335] that upon hydrogen exposure, hydrogen was detected in the Pd films and the magnetization easy-axis of the Co underneath changed. Other works [334] reported that hydrogen could be absorbed by Pd capping layers and it could diffuse through 3–4 ML Pd layers inducing changes in the interlayer spacing of the films, and producing an increase of the in-plane magnetic signal of the ferromagnetic film. The main difference between these experiments and our experiments is the hydrogen pressure used. The works cited were performed at hydrogen pressures around 1 atm (760 Torr), ten orders of magnitude higher than the pressures used in our UHV conditions. Although hydrogen absorption by Pd has been reported at high hydrogen pressures, the data shown in this chapter and chapter 4 [11, 339] indicate that under UHV conditions it is not possible to obtain a significant hydrogen absorption through Pd layers even when using atomic hydrogen. This can explain the lack of change in the magnetization easy-axis in the Pd/Co system. Using a higher hydrogen pressure it might be possible to switch the Co magnetization easy-axis. A related problem is the limited hydrogen doses employed. Due to the limitations in the SPLEEM electron source, the maximum continuous dose was 90 L_H. In chapter 4 we discussed that in order to populate the subsurface position doses above 10 kL were needed.

9.4 Conclusions

By means of LEEM and SPLEEM we have studied the growth of 1 ML of Pd on 2–5 ML of Co/Ru(0001). A monolayer Pd capping turns the magnetization to an out-of-plane easy-axis orientation for Co films 3 and 4 ML thick.

The adsorption of molecular and atomic hydrogen was studied by SPLEEM and low-energy electron reflectivity. Atomic hydrogen produced changes in the electron reflectivity of Pd/Co/Ru similar to those observed on Pd/Ru films, suggesting that hydrogen incorporated at the Pd/Co interface. But changes in the magnetization easy axis of Pd-capped 2 and 3 ML thick Co films were not detected.

Chapter 10

Summary and conclusions

10.1 Final conclusions

We have studied the structure and, for Co films the magnetic domains, of ultrathin films of Pd, Mg and Co on Ru(0001) by LEEM, SPLEEM and STM. Then, the effect of exposure to various amounts of hydrogen on each film was characterized.

Pd films were characterized by LEEM and LEED-IV. With LEED-IV, the interlayer spacing of the topmost Pd layers was determined for film regions with exactly 2, 3, 4, 5 and 6 ML of Pd, and showing an fcc stacking sequence. Pd fcc twins grew on consecutive Ru terraces, and some additional stacking faults were detected on the films by dark-field imaging. Thicker Pd films on Ru(0001) and W(110) were also characterized, with the same distribution of twins in the Ru substrate, while on W(110) twins were not related to the substrate terraces. This study proves that LEEM is not only a useful technique to characterize the growth of thin films but, when combined with LEED-IV it becomes a powerful tool to solve the crystal structure of the grown films. This assertion might be evident. However it has not been realized in the published literature.

Then, the effect of exposing the Pd films to hydrogen was studied. By means of LEEM and

LEED we have been able to deduce the location of hydrogen on the Pd even if hydrogen itself could not be detected. When dosing large doses of atomic H, we have observed that, because of our particular experimental condition, it was unavoidable to co-dose some CO. At selected electron energies, hydrogen and CO present characteristic features in the electron reflectivity data that could be used as a fingerprint of the presence of each adsorbate on the film surface, to such extent that the real time dynamics of the displacement of hydrogen by CO could be followed. By means of LEED-IV fits, an expansion of the last Pd layer was detected, a signal that hydrogen was populating sub-surface positions in the Pd films. We have not been able to form an ordered hydride in the Pd film. Only by exposing to large doses of atomic hydrogen and some CO, the sub-surface positions could be populated. We confirmed that CO prevents hydrogen desorption from the sub-surface positions.

The next ultra-thin metal system studied was Mg on Ru(0001). The growth and the morphology of the Mg films up to 10 ML were studied by LEEM and STM. By observing the LEED pattern, the change of in-plane lattice spacing of the first Mg monolayer could be followed in real-time. LEEM shows a perfect layer-by-layer growth for tens of ML. Due to the limitations in lateral resolution of LEEM, we have used STM to characterize the morphology of the Mg/Ru surface down to the atomic level, showing in real space changes in the moiré pattern of the first monolayer. Thick Mg films present stacking faults, and screw dislocations in stepped areas, probably due to the mismatch between Ru and Mg step heights. We have shown that the combination of STM and LEEM allows to characterize in a wide lateral scale, extending from atomic distances to tens of microns the film morphology and structure.

Exposing Mg to molecular hydrogen did not produce any change in the morphology of the films. However, exposure to atomic hydrogen resulted in the nucleation and growth of a magnesium hydride as observed by LEEM and TDS (electron beam damage prevented a LEED characterization of the hydride). TDS measurements showed that the Mg hydride decomposed under

heating when heating it and the decomposition temperature depended on the thickness of the Mg film. This effect was attributed to a 3D growth mode of the hydride on the Mg film. To the best of our knowledge this is the first time that the formation and decomposition of an hydride has been followed in real space and real time at the nanometer scale.

Finally we have studied the properties of thin Co films grown on Ru(0001) up to 3 ML thick by LEEM and SPLEEM. Confirming previous studies, these Co films present an hcp stacking sequence up to the second layer while 3 ML already presented both fcc and hcp stacking sequences. SPLEEM provided a real-space view of the magnetic domains in the Co films. The magnetic domain patterns of 3 ML thick islands depended on their stacking sequence, probably through differences in the magnetic anisotropy energy.

Exposure to hydrogen (of the Co films) produced a spin-reorientation transition in bilayer-thick Co areas. The transition was reversible by heating to the desorption temperature of hydrogen on Co. No structural changes were detected in the films after hydrogen adsorption. Before the magnetization easy-axis direction changed from out-of-plane to in-plane, the large, micrometer sized, up and down magnetic domains broke up into smaller elongated domains, reflecting the decrease in the effective magnetic anisotropy. Eventually, the out-of-plane contrast disappeared in a non-homogeneous manner. We also characterized the growth and easy-axis changes of a Pd capping layer on the Co Films, although no SRT was observed upon hydrogen exposure.

Our results open the way to study the detailed behavior of hydrogen on Co films through the changes in the Co bilayer magnetization.

10.2 Conclusiones finales

En esta tesis hemos estudiado por medio de LEEM, SPLEEM y STM, la estructura, (y en su caso la imanación), de películas metálicas ultra delgadas de Pd, Mg y Co. Posteriormente, hemos

caracterizado los efectos de la exposición a hidrógeno en cada una de estas películas.

Las películas de Pd fueron caracterizadas mediante LEEM y LEED-IV. El interespaciado entre las capas superiores de Pd y su secuencia de apilamiento fueron determinados mediante ajustes de LEED-IV tanto para películas con espesores de 2 a 6 monocapas como para películas de Pd de mayor espesor crecidas sobre Ru(0001) y W(110). Mediante imágenes de campo oscuro hemos detectado la presencia de maclas de Pd en terrazas consecutivas de Ru, y sobre cada terraza de W(110). Nuestros resultados prueban que el LEEM no es sólo una técnica útil para caracterizar el crecimiento de películas delgadas, sino que también es una herramienta muy versátil a la hora de resolver la estructura cristalina de las películas cuando éste se combina con LEED-IV adquirido en el mismo instrumento. Sin embargo, no hay apenas trabajos publicados que se aprovechen de esta combinación de LEEM y LEED.

Después de la caracterización estructural de las películas de Pd, se analizaron los efectos de la exposición de hidrógeno en dichas películas. Por medio de LEEM y LEED, hemos sido capaces de deducir la posición del hidrógeno en las películas de Pd incluso si el hidrógeno no fue detectado directamente. Hemos observado que al exponer a grandes dosis de H atómico en nuestras condiciones es inevitable co-depositar algo de CO. El hidrógeno y el CO presentan una señal característica en la reflectividad de electrones que puede ser usada como una huella dactilar de la presencia de dichos adsorbatos en la superficie de la película y ello nos ha permitido seguir en espacio real el desplazamiento de hidrógeno por el CO. Sin embargo, no hemos sido capaces de crear hidruros en Pd y sólamente cuando las películas de Pd fueron expuestas a grandes dosis de hidrógeno atómico con CO, las posiciones sub-superficiales pudieron ser pobladas con hidrógeno, poblamiento que se detectó gracias a la expansión producida en las últimas capas de Pd (mediante LEED-IV). Hemos comprobado también que la presencia de CO en la superficie bloquea la desorción del H absorbido.

El siguiente sistema estudiado fue Mg sobre Ru(0001). El crecimiento y la morfología de las películas de Mg fueron estudiados mediante LEEM y STM. Estudiando el patrón de LEED en

tiempo real pudimos seguir el cambio de las distancias a primeros vecinos de la primera capa de Mg. En las imágenes de LEEM hemos podido observar un crecimiento capa a capa para un total de 10 capas atómicas. Las películas de Mg más gruesas presentan defectos de apilamiento y dislocaciones de tornillo en áreas con escalones, posiblemente debido a la diferencia de altura entre los escalones de Ru y Mg. Con estos experimentos hemos demostrado que la combinación de STM y LEEM permite la caracterización de películas delgadas en un gran rango de escalas laterales que va desde distancias atómicas hasta decenas de micrómetros.

La exposición de las películas de Mg a hidrógeno molecular no produjo ningún cambio en ellas. Sin embargo al utilizar hidrógeno atómico se pudo observar en LEEM la nucleación y el crecimiento de un hidruro. El daño producido por el haz de electrones impidió la caracterización del hidruro mediante LEED. Sin embargo, se observó que al calentar el hidruro aumentaba la presión parcial de hidrógeno en el sistema experimental a la vez que se observaba que las islas de hidruro se descomponían. La temperatura de descomposición del hidruro dependía del espesor de las películas de Mg, efecto atribuido a un crecimiento 3D de dicho hidruro sobre la película de Mg. Que nosotros sepamos, esta ha sido la primera vez que se ha observado la formación y la descomposición de un hidruro a tiempo y espacio real y a escala nanométrica.

Finalmente, por medio de LEEM y SPLEEM hemos estudiado las propiedades de películas delgadas de Co hasta un espesor de 3 ML. Hemos confirmado estudios anteriores donde se indicaba que las películas de Co en Ru(0001) crecían con una secuencia de apilamiento hcp hasta la segunda capa, pero que tres capas de Co presentaban secuencias hcp y fcc en distintas islas. El SPLEEM nos permitió obtener imágenes en el espacio real de los dominios magnéticos de las películas de Co. Los dominios magnéticos de las películas de cobalto de 3 capas de espesor dependían de su secuencia de apilamiento, posiblemente debido a diferencias en la energía de anisotropía magnética.

La exposición de las películas de Co a hidrógeno produjo una reorientación de espín en las bica-

pas de Co. Esta transición era reversible calentando las películas hasta la temperatura de desorción del hidrógeno en Co. No se han detectaron cambios estructurales en las películas de Co después de la adsorción de hidrógeno. Durante la exposición a hidrógeno, los dominios magnéticos orientados fuera del plano se rompieron en dominios mas pequeños con forma elongada, reflejando la reducción de la anisotropía magnética efectiva. Finalmente, el contraste magnético fuera del plano desapareció de manera inhomogénea. También hemos caracterizado el crecimiento y los cambios en la imanación de las películas de Co recubiertas con Pd, aunque no hemos observado una reorientación de espín después de exponer las películas a hidrógeno.

Nuestros resultados indican que el comportamiento del hidrógeno sobre películas de Co puede ser determinado estudiando los cambios que se producen en las propiedades magnéticas de las bicapas de Co.

Appendix A

List of publications and patents

A.1 List of publications

- "Structure and magnetism of ultrathin Cr layers on W(110)" B. Santos, Juan M. Puerta, Jorge I. Cerda, Roland Stumpf, Kirsten von Bergmann, Roland Wiesendanger, Matthias Bode, Kevin F. McCarty, Juan de la Figuera. New J. Phys. **10** 013005 (2008)

- "Crystallographic structure and surface composition of NbN_x thin films grown by RF magnetron sputtering" J. E. Alfonso, J. Buitrago, J. Torres, B. Santos, J. F. Marco, Microelec. J. **39**, 1327– 1328 (2008)

- "Structure and magnetism in ultra thin iron oxides by low energy electron microscopy" B. Santos, Elena Loginova, Arantzazu Mascaraque, Andreas K. Schmid, Kevin F. McCarty, Juan de la Figuera. J. Phys. cond. mat. **21** (2009) 314011

- "Real space observations of magnesium hydride formation and decomposition" T. Herranz, K. F. McCarty, B. Santos, M. Monti and J. de la Figuera, Chem. Mater. **22**, 1291–1293 (2010)

- "Structure of ultrathin Pd films determined by low-energy electron microscopy and diffraction", B. Santos, J. M. Puerta, J. I. Cerda, T. Herranz, K. F. McCarty and J. de la Figuera, New J. Phys. **12** , 023023, (2010)

- "Influence of fabrication parameters on crystalization, microstructure and surface composition of NbN thin films deposited by RF magnetron sputtering" J. E. Alfonso, J. Buitrago, J. Torres, J. F. Marco, B. Santos. J. Mater. Science. **45**, 20, (2010)

- "Synthesis and characterization of $La_{1+x}Sr_{2-x}CoMnO_{7-\delta}$ (x=0,0.2; δ=0,1)" H. El Shinawi, A. Bertha, J. Hadermann, T. Herranz, B. Santos, J. F. Marco, F. J. Berry. J. Sol. Stat. Chem., **183** (6), 2261–2269, (2010),

- "The ionic conductivity and local environment of cations in Bi9ReO17" M. Thompson, T. Herranz, B. Santos, J. F. Marco, F. J. Berry, C. Graves. J. Sol. Stat. Chem. **183**, 1985–1991 (2010)

- "Real-space study of the growth of magnesium on ruthenium" T. Herranz, B. Santos, K. F. McCarty, J. de la Figuera, Surface science (2011), Surf. Sci., **605**, 903–911, (2011)

- "How thin can magnetite still be magnetic?" Matteo Monti, Benito Santos, Arantzazu Mascaraque, Oscar Rodríguez de la Fuente, Miguel Angel Niño, Tevik Onur Mentes, Andrea Locatelli, Kevin F. McCarty, José F. Marco and Juan de la Figuera, in press (2011)

- "The role of CO in hydrogen adsorption into ultra-thin Pd Films" B. Santos et al. (2011) in preparation

- "Hydrogen induced spin-reoritation transition in a cobalt bilayer" B.Santos et al. (2011) in preparation

- "Magnetic domain patterns on trilayer Co islands" B. Santos et al. (2011) in preparation

A.2 Other

- "Patent PCT/US2010/032990" Gas sensor.

Appendix B

Agradecimientos

En primer lugar quiero dar mi más sincera gratitud y agradecimiento a mi director de tesis Juan de la Figuera por haberme dado la gran oportunidad de realizar esta tesis, por su valiosa ayuda, por todo lo aprendido y por la gran paciencia que ha tenido para conmigo en todo el proceso, especialmente en las correcciones. También quiero agradecer de forma muy especial la ayuda y la confianza depositada en mi por Pepe Marco durante estos años. A Kevin y Ellen por abrirme las puertas de su casa durante mis estancias en USA. A Andreas K. Schmid por su agradable acogida en Berkely. A Karsten y Bogdan por hacer tan agradable mi estancia en New Hampshire. A Jorge y Juanma por explicarme una y otra vez como correr programas en linux y los buenos momentos del café. A la gente del ICMM Silvia, M. Carmen y J. Méndez por su ayuda. A la gente de la UCM, Óscar, Juan Rojo, Miguel Ángel y Arantzazu por las interesantes reuniones de grupo. A la gente de la UAM en en especial a Enrique G. Michel, Julio Camarero, J. Emilio Prieto por todos los saberes adquiridos de ellos. A J. J. Hinarejos por todo lo que me ha enseñado. A todos los del Roca"MaTTeo, Lucía, Roberto, Tirma, Mercedes, Ramón, Carlos, Ángel, Claudio y María. A Cristina Murga, por informarme de que Juan buscaba a alguien para hacer la tesis. A la gente del taller de la UAM y del Roca. A Lucía Alvarez por usurparle su sitio en el despacho de Juanma y los buenos momentos en los congresos. A Erika Jimenez por los momento de café en la UAM y

los momentos de compras en Boston. A la gente que me ha ayudado o se ha interesado por mis andanzas por el mundo de la ciencia a Nuria (6), Marta Towers y al comandante J. G. Lezcano.

Y por supuesto a toda mi familia, a mi madre y hermano, tios/as, primos/as en especial a Raquel, también a Bawy y Shishu.

Y en general a todo aquel que me haya ayudado a *perpetrar* esta tesis.

Bibliography

[1] K. Christmann, "Interaction of hydrogen with solid surfaces," Surf. Sci. Reports **9,** 1–163 (1988).

[2] J. A. Dean, *Lange's Handbook of Chemistry*, 15 ed. (McGraw-Hill Professional, 1998).

[3] J. Rifkin, *The Hydrogen Economy*, 1 ed. (Tarcher, 2003).

[4] M. Pozzo and D. Alfè, "Hydrogen dissociation and diffusion on transition metal (= Ti, Zr, V, Fe, Ru, Co, Rh, Ni, Pd, Cu, Ag)-doped Mg(0001) surfaces," Int. J. Hydrogen Energ. **34,** 1922–1930 (2009).

[5] B. Dam, R. Gremaud, C. Broedersz, and R. Griessen, "Combinatorial thin film methods for the search of new lightweight metal hydrides," Scripta Mater. **56,** 853–858 (2007).

[6] G. Sandrock and R. C. Bowman, "Gas-based hydride applications: recent progress and future needs," J. Alloy. Comp. **356-357,** 794–799 (2003).

[7] F. Yang, G. Wang, Z. Zhang, X. Meng, and V. Rudolph, "Design of the metal hydride reactors - A review on the key technical issues," Int. J. Hydrogen Energ. **35,** 3832–3840 (2010).

[8] B. Sakintuna, F. Lamari-Darkrim, and M. Hirscher, "Metal hydride materials for solid hydrogen storage: A review," Int. J. Hydrogen Energ. **32,** 1121–1140 (2007).

[9] Y. Wang, K. S. Chen, J. Mishler, S. C. Cho, and X. C. Adroher, "A review of polymer electrolyte membrane fuel cells: Technology, applications, and needs on fundamental research," Applied Energ. **88,** 981–1007 (2011).

[10] K. Papathanassopoulos and H. Wenzl, "Pressure-composition isotherms of hydrogen and deuterium in vanadium films measured with a vibrating quartz microbalance," J. Phys. F. Met. Phys. **12,** 1369–1381 (1982).

[11] S. T. Ceyer, "The Unique Chemistry of Hydrogen beneath the Surface: Catalytic Hydrogenation of Hydrocarbons," Accounts. Chem. Res. **34,** 737–744 (2001).

[12] I. Yarovsky and A. Goldberg, "DFT - study of hydrogen adsorption on Al13 clusters," Mol. Simulat. **31,** 475 (2005).

[13] J. B. Gaither, Ph.D. thesis, 2011.

[14] W. J. Nellis, A. C. Mitchell, P. C. McCandless, D. J. Erskine, and S. T. Weir, "Electronic energy gap of molecular hydrogen from electrical conductivity measurements at high shock pressures," Phys. Rev. Lett. **68,** 2937 (1992).

[15] L. Hornekaer, A. Baurichter, V. V. Petrunin, D. Field, and A. C. Luntz, "Importance of Surface Morphology in Interstellar H2 Formation," Science **302,** 1943 –1946 (2003).

[16] "Energy (science),", http://en.citizendium.org/wiki/.

[17] A. Balakrishnan, V. Smith, and B. P. Stoicheff, "Dissociation energy of the hydrogen molecule," Phys. Rev. Lett. **68,** 2149 (1992).

[18] S. J. . E. Blanksby and G. B. Blanksby, S. J.; Ellison, "Bond Dissociation Energies of Organic Molecules," Acc. Chem. Res. **36,** 255–263 (2003).

[19] J. Norskov and F. Besenbacher, "Theory of hydrogen interaction with metals," J. Less-Common. Met. **130,** 475–490 (1987).

[20] W. Moritz, R. Imbihl, R. J. Behm, G. Ertl, and T. Matsushima, "Adsorption geometry of hydrogen on Fe(110)," J. Chem. Phys. **83,** 1959 (1985).

[21] C. Lebouin, Y. Soldo-Olivier, E. Sibert, M. D. Santis, F. Maillard, and R. Faure, "Evidence of the Substrate Effect in Hydrogen Electroinsertion into Palladium Atomic Layers by Means of in Situ Surface X-ray Diffraction," Langmuir **25,** 4251–4255 (2009).

[22] F. Greuter, I. Strathy, E. W. Plummer, and W. Eberhardt, "Photoemission from H adsorbed on Ni(111) and Pd(111) surfaces," Phys. Rev. B. **33,** 736 (1986).

[23] D. Lederman, Y. Wang, E. H. Morales, R. J. Matelon, G. B. Cabrera, U. G. Volkmann, and A. L. Cabrera, "Magnetooptic properties of Fe/Pd and Co/Pd bilayers under hydrogen absorption," Appl. Phys. Lett. **85,** 615 (2004).

[24] D. Labergerie, K. Westerholt, H. Zabel, and B. Hjörvarsson, "Hydrogen induced change of the atomic magnetic moments in Fe/V-superlattices," J. Magn. Magn. Matter. **225,** 373–380 (2001).

[25] D. Sander, W. Pan, S. Ouazi, J. Kirschner, W. Meyer, M. Krause, S. Müller, L. Hammer, and K. Heinz, "Reversible H-Induced Switching of the Magnetic Easy Axis in Ni/Cu(001) Thin Films," Phys. Rev. Lett. **93,** 247203 (2004).

[26] U. Gradmann, "Magnetism of surfaces and interfaces," J. Magn. Magn. Matter. **6,** 173–182 .

[27] F. E. Gabaly, J. M. Puerta, C. Klein, A. Saa, A. K. Schmid, K. F. McCarty, J. I. Cerda, and J. de la Figuera, "Structure and morphology of ultrathinCo/Ru(0001) films," New J. Phys. **9,** 80–80 (2007).

[28] J. Stöhr and H. C. Siegmann, *Magnetism: From Fundamentals to Nanoscale Dynamics*, illustrated edition ed. (Springer, 2006).

[29] R. M. White, *Quantum theory of magnetism: magnetic properties of materials* (Springer, 2007).

[30] N. Majlis, *The quantum theory of magnetism* (World Scientific, 2007).

[31] R. I. Masel, *Principles of Adsorption and Reaction on Solid Surfaces*, 1 ed. (Wiley-Interscience, 1996).

[32] G. A. Somorjai and Y. Li, *Introduction to Surface Chemistry and Catalysis* (John Wiley and Sons, 2010).

[33] K. W. Kolasinski, *Surf. Sci.: Foundations of Catalysis and Nanoscience*, 2 ed. (Wiley, 2008).

[34] D. Farias, Ph.D. thesis, Institut for experimental physics, 1996.

[35] R. Baetzold, "Calculated model for metal cluster catalysis: H2 dissociation," Surf. Sci. **51,** 1–13 (1975).

[36] A. Gross, "Hydrogen dissociation on metal surfaces - a model system for reactions on surfaces," Appl. Phys. A **67,** 627–635 (1998).

[37] D. hayward, *Chemisorption*, 2nd ed ed. (Butterworths, 1964).

[38] D. Bird, L. Clarke, M. Payne, and I. Stich, "Dissociation of H2 on Mg(0001)," Chem. Phys. Lett. **212,** 518–524 (1993).

[39] J. K. Norskov, A. Houmoller, P. K. Johansson, and B. I. Lundqvist, "Adsorption and Dissociation of H2 on Mg Surfaces," Phys. Rev. Lett. **46,** 257 (1981).

[40] M. Pozzo and D. Alfe, "Hydrogen dissociation on Mg(0001) studied via quantum Monte Carlo calculations," Phys. Rev. B. **78,** 245313 (2008).

[41] Y. Li, Y. Yang, B. Sun, Y. Wei, and P. Zhang, "Dissociation of hydrogen molecules on the clean and hydrogen-preadsorbed Be(0001) surface," Phys. Lett. A **375,** 2430–2436 (2011).

[42] D. Sander, "The magnetic anisotropy and spin reorientation of nanostructures and nanoscale films," J. Phys-condens. Mat. **16,** R603–R636 (2004).

[43] P. Grünberg, R. Schreiber, Y. Pang, M. B. Brodsky, and H. Sowers, "Layered Magnetic Structures: Evidence for Antiferromagnetic Coupling of Fe Layers across Cr Interlayers," Phys. Rev. Lett. **57,** 2442 (1986).

[44] A. Ney, C. Pampuch, R. Koch, and K. H. Ploog, "Programmable computing with a single magnetoresistive element," Nature **425,** 485–487 (2003).

[45] S. S. P. Parkin *et al.*, "Exchange-biased magnetic tunnel junctions and application to non-volatile magnetic random access memory (invited)," J. Appl. Phys. **85,** 5828 (1999).

[46] O. Hjortstam, K. Baberschke, J. M. Wills, B. Johansson, and O. Eriksson, "Magnetic anisotropy and magnetostriction in tetragonal and cubic Ni," Phys. Rev. B. **55,** 15026 (1997).

[47] U. Gradmann, "Ferromagnetism near surfaces and in thin films," Appl. Phys. **3,** 161–178 (1974).

[48] "La variation du ferromagnetisme du temperature," Comptes Rendus 143 .

[49] R. Ramchal, Ph.D. thesis, 2004.

[50] A. Hubert and R. Schäfer, *Magnetic Domains: The Analysis of Magnetic Microstructures*, corrected ed. (Springer, 2008).

[51] A. Hubert and R. Schafer, *Magnetic domains: the analysis of magnetic microstructures* (Springer, 1998).

[52] J. Stöhr and H. C. Siegmann, *Magnetism: From Fundamentals to Nanoscale Dynamics*, illustrated edition ed. (Springer, 2006).

[53] J. Lohau, A. Moser, C. T. Rettner, M. E. Best, and B. D. Terris, "Writing and reading perpendicular magnetic recording media patterned by a focused ion beam," Appl. Phys. Lett. **78,** 990 (2001).

[54] Y. Z. Wu, C. Won, A. Scholl, A. Doran, H. W. Zhao, X. F. Jin, and Z. Q. Qiu, "Magnetic Stripe Domains in Coupled Magnetic Sandwiches," Phys. Rev. Lett. **93,** 117205 (2004).

[55] H. Kwon, S. Hong, J. Seok, K. Bu, Y. Wu, Z. Qiu, and C. Won, "A study of the stripe domain phase at the spin reorientation transition of two-dimensional magnetic system," J. Magn. Magn. Matter. **322,** 2742–2748 (2010).

[56] H. J. Choi, W. L. Ling, A. Scholl, J. H. Wolfe, U. Bovensiepen, F. Toyama, and Z. Q. Qiu, "Spin reorientation transition of Fe films in magnetically coupled Fe/Cu/Ni/Cu(001)," Phys. Rev. B. **66,** 014409 (2002).

[57] A. Kashuba and V. L. Pokrovsky, "Stripe domain structures in a thin ferromagnetic film," Phys. Rev. Lett. **70,** 3155 (1993).

[58] A. Vindigni, N. Saratz, O. Portmann, D. Pescia, and P. Politi, "Stripe width and nonlocal domain walls in the two-dimensional dipolar frustrated Ising ferromagnet," Phys. Rev. B. **77,** 092414 (2008).

[59] M. Biskup, L. Chayes, and S. A. Kivelson, "On the Absence of Ferromagnetism in Typical 2D Ferromagnets," Commun. Math. Phys. **274,** 217–231 (2007).

[60] B. Diaconescu, G. Nenchev, J. de la Figuera, and K. Pohl, "An ultrahigh vacuum fast-scanning and variable temperature scanning tunneling microscope for large scale imaging," Rev. Sci. Instr. **78,** 103701 (2007).

[61] E. Bauer, "Low energy electron microscopy," Rep. Progr. Phys. **57,** 895–938 (1994).

[62] C. Kittel, *Introduction to Solid State Physics*, 8 ed. (Wiley, 2004).

[63] N. W. Ashcroft, *Solid State Physics* (Thomson Press (India) Ltd, 2003).

[64] "http://www.physicsarchives.com/index.php/courses/872," .

[65] P. Champness, *Electron Diffraction in the Transmission Electron Microscope*, 1 ed. (Garland Science, 2001).

[66] S. J. Pennycook and P. D. Nellist, *Scanning Transmission Electron Microscopy: Imaging and Analysis*, 1st edition. ed. (Springer, 2011).

[67] D. B. Williams and C. B. Carter, *Transmission Electron Microscopy: A Textbook for Materials Science*, 2nd ed. (Springer, 2009).

[68] "National center for electron microscopy (NCEM),", http://ncem.lbl.gov/frames/spleem.html.

[69] A.-M. Abdullah, Ph.D. thesis, .

[70] N. Rougemaille and A. K. Schmid, "Magnetic imaging with spin-polarized low-energy electron microscopy," Eur. Phys. J-Appl. Phys. **50,** 20101 (2010).

[71] "Elmitec,".

[72] D. T. Pierce, F. Meier, and P. Zürcher, "Negative electron affinity GaAs: A new source of spin-polarized electrons," Appl. Phys. Lett. **26,** 670 (1975).

[73] F. E. Gabaly, Ph.D. thesis, Universidad Autónoma de Madrid, 2006.

[74] J. C. Grobli, D. Oberli, F. Meier, A. Dommann, Y. Mamaev, A. Subashiev, and Y. Yashin, "Polarization Resonances of Optically Spin-Oriented Photoelectrons Emitted from Strained Semiconductor Photocathodes," Phys. Rev. B. **74,** 2106 (1995).

[75] "patent genius,", http://www.patentgenius.com/patent/5877510.html.

[76] B. Reihl, M. Erbudak, and D. M. Campbell, "Production of spin-polarized electrons by photoemission from GaAs(110)," Phys. Rev. B. **19,** 6358 (1979).

[77] T. Duden and E. Bauer, "A compact electron-spin-polarization manipulator," Rev. Sci. Instrum. **66,** 2861 (1995).

[78] M. A. V. Hove, W. H. Weinberg, and C. M. Chan, *Low-Energy Electron Diffraction: Experiment, Theory and Surface Structure Determination* (Springer, 1986).

[79] J. Pendry, *Low Energy Electron Diffraction: The Theory and Its Application to Determination of Surface Structure* (Academic Press Inc.,U.S., 1974).

[80] M. Van Hove and S. Tong, *Surface Crystallography by LEED* (Springer-Verlag, Berlin, 1979).

[81] J. I. Cerdá, Ph.D. thesis, Universidad Autónoma de Madrid, 1995.

[82] H. Huang, S. Tong, W. E. Packard, and M. B. Webb, "atomic geometry of Si(111) 7x7 by dynamucal low-energy electron-diffraction," Phys. Lett. A **130,** 166 (1988).

[83] A. Baraldi, J. Cerdá, J. Martin-Gago, G. Comelli, S. Lizzit, G. Paolucci, and R. Rosei, "Oxygen induced reconstruction of the Rh(100) surface: general tendency towards threefold oxygen adsorption site on Rh surfaces," Phys. Rev. Lett. **82,** 4874–4877 (1999).

[84] J. B. Pendry, "Reliability factors for LEED calculations," J. Phys. C: Sol. Stat. Phys. **13,** 937–944 (1980).

[85] I. Prigogine, *Advances in chemical physics* (John Wiley and Sons, 1971).

[86] A. U. MacRae, "Low-Energy Electron Diffraction," Science **139,** 379 –388 (1963).

[87] G. Binnig, "Tunneling through a controllable vacuum gap," Appl. Phys. Lett. **40,** 178 (1982).

[88] G. Binnig, H. Rohrer, C. Gerber, and E. Weibel, "Surface Studies by Scanning Tunneling Microscopy," Phys. Rev. Lett. **49,** 57 (1982).

[89] G. Binnig, H. Rohrer, C. Gerber, and E. Weibel, "7 x 7 Reconstruction on Si(111) Resolved in Real Space," Phys. Rev. Lett. **50,** 120 (1983).

[90] J. Tersoff and D. R. Hamann, "Theory of the scanning tunneling microscope," Phys. Rev. B. **31,** 805 (1985).

[91] J. Bardeen, "Tunnelling from a Many-Particle Point of View," Phys. Rev. Lett. **6,** 57 (1961).

[92] A. L. V. de Parga, Ph.D. thesis, Universidad Autónoma de Madrid, .

[93] "nobelprize.org," in *The Nobel Prize in Physics 1920*

[94] "Nickel Magazine," in *Nickel & Its Uses* (Nickel Institute, 2005).

[95] "Loctite,".

[96] "Epotek technology,".

[97] "EBL electronics precision,".

[98] G. Thayer, Ph.D. thesis, University of California, Davis & Sandia Livermore, .

[99] P. Zahl, M. Bierkandt, S. Schröder, and A. Klust, "The flexible and modern open source scanning probe microscopy software package GXSM," Rev. Sci. Instr. **74,** 1222 (2003).

[100] P. Zahl, T. Wagner, R. Moller, and A. Klust, "Open source scanning probe microscopy control software package GXSM," In *J. Vac. Sci. Technol. B*, **28,** C4E39–C4E47 (AVS, 2010).

[101] P. Klapetek, D. Necas, and C. Anderson, "Gwyddion user guide,", http://gwyddion.net/, 2004–2009.

[102] "http://www.mksinst.com/docs/ur/GaugeGasCorrection.aspx," .

[103] "Createc, engeneering science,", http://www.createc.de/.

[104] U. Bischler, "Simple source of atomic hydrogen for ultrahigh vacuum applications," J. Vac. Sci. Technol. **11,** 458 (1993).

[105] "goodfellow," .

[106] C. Eibl, "Quantitative characterization of a highly effective atomic hydrogen doser," J. Vac. Sci. Technol. **16,** 2979 (1998).

[107] D. Jollie, "Platinum 2009," Review of supply and demand of platinum group metals, Johnson Matthey (2009) .

[108] B. Sampedro, P. Crespo, A. Hernando, R. Litrán, J. C. S. López, C. L. Cartes, A. Fernandez, J. Ramírez, J. G. Calbet, and M. Vallet, "Ferromagnetism in fcc Twinned 2.4 nm Size Pd Nanoparticles," Phys. Rev. Lett. **91,** 237203 (2003).

[109] T. Shinohara, T. Sato, and T. Taniyama, "Surface ferromagnetism of Pd fine particles," Phys. Rev. Lett. 91 (2003).

[110] S. Alexandre, E. Anglada, J. Soler, and F. Yndurain, "Magnetism of two-dimensional defects in Pd: Stacking faults, twin boundaries, and surfaces," Phys. Rev. B **74,** 054405 (2006).

[111] B. Santos, J. M. Puerta, J. I. Cerda, T. Herranz, K. F. McCarty, and J. de la Figuera, "Structure of ultrathin Pd films determined by low-energy electron microscopy and diffraction," New J. Phys. **12,** 023023 (2010).

[112] H. Hartmann, T. Diemant, A. Bergbreiter, J. Bansmann, H. Hoster, and R. Behm, "Surface alloy formation, short-range order, and deuterium adsorption properties of monolayer PdRu/Ru(0 0 0 1) surface alloys," Surf. Sci. **603,** 1439–1455 (2009).

[113] N. Rougemaille, F. E. Gabaly, R. Stumpf, A. K. Schmid, K. Thurmer, N. C. Bartelt, and J. de la Figuera, "Labyrinthine Island Growth during Pd/Ru(0001) Heteroepitaxy," Phys. Rev. Lett. **99,** 106101–4 (2007).

[114] A. de Siervo, E. D. Biasi, F. Garcia, R. Landers, M. D. Martins, and W. A. A. Macedo, "Surface structure determination of Pd ultrathin films on Ru(0001): Possible magnetic behavior," Phys. Rev. B. **76,** 075432 (2007).

[115] H. Ohtani, M. V. Hove, and G. Somorjai, "Leed intensity analysis of the surface structures of Pd(111) and of CO adsorbed on Pd(111) in a $\sqrt{3} \times \sqrt{3}$R30° arrangement," Surf. Sci. **187,** 372–386 (1987).

[116] T. E. Felter, E. C. Sowa, and M. A. V. Hove, "Location of hydrogen adsorbed on palladium (111) studied by low-energy electron diffraction," Phys. Rev. B **40,** 891 (1989).

[117] P. Feibelman, "Disagreement between experimental and theoretical metal surface relaxations," Surf. Sci. **360,** 297–301 (1996).

[118] "webelements,".

[119] W. L. Ling, T. Giessel, K. Thurmer, R. Q. Hwang, N. C. Bartelt, and K. F. McCarty, "Crucial role of substrate steps in de-wetting of crystalline thin films," Surf. Sci. **570,** L297–L303 (2004).

[120] K. McCarty *et al.*, "How metal films de-wet substrates-identifying the kinetic pathways and energetic driving forces," New J. Phys. 11 (2009).

[121] R. C. Jaklevic and L. C. Davis, "Band signatures in the low-energy-electron reflectance spectra of fcc metals," Phys. Rev. B **26,** 5391 (1982).

[122] M. N. Read, "Tamm surface resonances in very low-energy electron scattering from clean metal surfaces," Phys. Rev. B **75,** 193403–4 (2007).

[123] I. Bartos, M. A. V. Hove, and M. S. Altman, "Cu(111) electron band structure and channeling by VLEED," Surf. Sci. **352-354,** 660–664 (1996).

[124] J. de la Figuera, J. Puerta, J. Cerda, F. E. Gabaly, and K. McCarty, "Determining the structure of Ru(0001) from low-energy electron diffraction of a single terrace," Surf. Sci. **600,** L105–L109 (2006).

[125] B. Santos, T. Herranz, J. I. Cerda, J. de la Figuera, and K. F. McCarty, in preparation (unpublished).

[126] M. Morkel, G. Rupprechter, and H.-J. Freund, "Ultrahigh vacuum and high-pressure coadsorption of CO and H_2 on Pd(111): A combined SFG, TDS, and LEED study," J. Chem. Phys. **119,** 10853–10866 (2003).

[127] S. Walter, V. Blum, I. Hammer, S. Muller, K. Heinz, and M. Giesen, "The role of an energy-dependent inner potential in quantitative low-energy electron diffraction," Surf. Sci. **458,** 155–161 (2000).

[128] F. E. Gabaly, J. M. Puerta, C. Klein, A. Saa, A. K. Schmid, K. F. McCarty, J. I. Cerda, and J. de la Figuera, "Structure and morphology of ultrathin Co/Ru(0001) Films," New. J. Phys. **8,** 80 (2007).

[129] J. de la Figuera, A. K. Schmid, N. C. Bartelt, K. Pohl, and R. Q. Hwang, "Determination of buried dislocation structures by scanning tunneling microscopy," Phys. Rev. B **63,** 165431 (2001).

[130] W. L. Ling, J. de la Figuera, N. C. Bartelt, R. Q. Hwang, A. K. Schmid, G. E. Thayer, and J. C. Hamilton, "Strain Relief through Heterophase Interface Reconstruction: Ag(111)/Ru(0001)," Phys. Rev. Lett. **92,** 116102 (2004).

[131] I. V. Markov, *Crystal Growth for Beginners: Fundamentals of Nucleation, Crystal Growth, and Epitaxy*, 2 ed. (World Scientific Publishing Company, 2004).

[132] W. Schlenk and E. Bauer, "Properties of ultrathin layers of palladium on a tungsten 110 surface," Surf. Sci. Lett. **93,** A87 (1980).

[133] H. Knoppe and E. Bauer, "Growth, electronic structure and chemisorption behaviour of ultrathin Pd layers on W(110)," Z. Phys. Chemie-Int. J. Res. Phys. Chem. Chem. Phys. **202,** 45–57 (1997).

[134] L. Aballe, A. Barinov, A. Locatelli, S. Heun, S. Cherifi, and M. Kiskinova, "Spectromicroscopy of ultrathin Pd films on W(110): interplay of morphology and electronic structure," App. Surf. Sci. **238,** 138–142 (2004).

[135] L. B. Bautista, Ph.D. thesis, Universität Hamburg, 2006.

[136] K. Christmann, G. Ertl, and O. Schober, "LEED intensities from clean and hydrogen covered Ni(100) and Pd(111) surfaces," Surf. Sci. **40,** 61–70 (1973).

[137] T. Engel and H. Kuipers, "A molecular-beam investigation of the scattering, adsorption and absorption of H2 and D2 from/on/in Pd(111)," Surf. Sci. **90,** 162–180 (1979).

[138] T. Mitsu, M. Rose, E. Fomin, D. Ogletree, and M. Salmeron, "Dissociative hydrogen adsorption on palladium requires aggregates of three or more vacancies," Nature **422,** 705–707 (2003).

[139] G. Gdowski, T. Felter, and R. Stulen, "Effect of surface temperature on the sorption of hydrogen by Pd(111)," Surf. Sci. 181 (1987).

[140] T. Felter, S. Foiles, M. Daw, and R. Stulen, "Order-disorder transitions and subsurface occupation for hydrogen on Pd(111)," Surf. Sci. Letters **171,** L379–L386 (1986).

[141] Y. Fukai, *The Metal-hydrogen System: Basic Bulk Properties*, 2nd rev. and updated ed. ed. (Springer, 2003).

[142] P. A. Bennett and J. C. Fuggle, "Electronic structure and surface kinetics of palladium hydride studied with x-ray photoelectron spectroscopy and electron-energy-loss spectroscopy," Phys. Rev. B **26,** 6030 (1982).

[143] M. Shirai, Y. Pu, M. Arai, and Y. Nishiyama, "Reactivity of permeating hydrogen with thiophene on a palladium membrane," Appl. Surf. Sci. **126,** 99–106 (1998).

[144] D. Teschner, J. Borsodi, A. Wootsch, Z. Revay, M. Hävecker, A. Knop-Gericke, S. Jackson, and R. Schlögl, "The roles of subsurface carbon and hydrogen in palladium-catalyzed alkyne hydrogenation," Science **320,** 86–89 (2008).

[145] M. Wilde, M. Matsumoto, K. Fukutani, and T. Aruga, "Depth-resolved analysis of subsurface hydrogen absorbed by Pd(1 0 0)," Surf. Sci. **482-485,** 346–352 (2001).

[146] O. M. Lovvik and R. A. Olsen, "Adsorption energies and ordered structures of hydrogen on Pd(111) from density-functional periodic calculations," Phys. Rev. B. **58,** 10890 (1998).

[147] S. Hong and T. S. Rahman, "Adsorption and diffusion of hydrogen on Pd(211) and Pd(111): Results from first-principles electronic structure calculations," Phys. Rev. B. **75,** 155405 (2007).

[148] N. Ozawa, T. A. Roman, H. Nakanishi, H. Kasai, N. B. Arboleda, and W. A. D. no, "Potential energy of hydrogen atom motion on Pd(111) surface and in subsurface: A first principles calculation," J. Appl. Phys. **101,** 123530 (2007).

[149] H. Okuyama, T. Nakagawa, W. Siga, N. Takagi, M. Nishijima, and T. Aruga, "Subsurface Hydrogen at Pd(100) Induced by Gas-Phase Atomic Hydrogen," J: of Phys. Chem. B **103,** 7876–7881 (1999).

[150] M. Johansson, E. Skúlason, G. Nielsen, S. Murphy, R. Nielsen, and I. Chorkendorff, "Hydrogen adsorption on palladium and palladium hydride at 1 bar," Surf. Sci. **604,** 718–729 (2010).

[151] J. Eastman, L. Thompson, and B. Kestel, "Narrowing of the palladium-hydrogen miscibility gap in nanocrystalline palladium," Phys. Rev. B **48,** 84–92 (1993).

[152] P. Vermeulen, A. Ledovskikh, D. Danilov, and P. H. L. Notten, "The Impact of the Layer Thickness on the Thermodynamic Properties of Pd Hydride Thin Film Electrodes," J: of Phys. Chem. B **110,** 20350–20353 (2006).

[153] B. Stritzker and W. Buckel, "Superconductivity in the palladium-hydrogen and the palladium-deuterium systems," Zeit. Phys. **257,** 1–8 (1972).

[154] A. Doyle, S. Shaikhutdinov, S. Jackson, and H.-J. Freund, "Hydrogenation on Metal Surfaces: Why are Nanoparticles More Active than Single Crystals?," Ange. Chemie Int. Ed. **42,** 5240–5243 (2003).

[155] A. Casanovas, J. Llorca, N. Homs, J. Fierro, and P. R. de la Piscina, "Ethanol reforming processes over ZnO-supported palladium catalysts: Effect of alloy formation," J. Mol. Cat. A **250,** 44–49 (2006).

[156] T. Nowitzki, H. Borchert, B. Jürgens, T. Risse, V. Zielasek, and M. Bäumer, "UHV studies of methanol decomposition on mono- and bimetallic CoPd nanoparticles supported on thin alumina films," Chem. Phys. Chem. **9,** 729–739 (2008).

[157] I. Ratajczykowa, "The influence of CO on hydrogen sorption by Pd(111) single crystals," Surf. Sci. **172,** 691–714 (1986).

[158] N. López, B. Bridier, and J. Pérez-Ramírez, "Discriminating Reasons for Selectivity Enhancement of CO in Alkyne Hydrogenation on Palladium," J. Phys. Chem. C **112,** 9346–9350 (2008).

[159] M. Eriksson and L. G. Ekedahl, "Real time measurements of hydrogen desorption and absorption during CO exposures of Pd: hydrogen sticking and dissolution," Appl. Surf. Sci. **133,** 89–97 (1998).

[160] I. Ratajczykowa, "The influence of CO on hydrogen sorption by Pd(111) single crystals," Surf. Sci. **172,** 691–714 (1986).

[161] P. Berlowitz and D. Goodman, "Chemisorption of ultrathin Pd layers on W(110) and W(100): Adsorption of H2 and CO," Langmuir **4,** 1091–1095 (1988).

[162] M. Kiskinova and G. Bliznakov, "Adsorption and coadsorption of carbon monoxide and hydrogen on Pd(111)," Surf. Sci. **123,** 61–76 (1982).

[163] M. S. Altman, "Trends in low energy electron microscopy," J. Phys.: Cond. Matt. **22,** 084017 (2010).

[164] M. Gsell and D. Menzel, "The geometries of coadsorbate layers of O and H on Ru(0 0 1): How well can quantitative LEED see hydrogen atoms?," Surf. Sci. **603,** 1397–1404 (2009).

[165] M. S. Altman, W. F. Chung, Z. Q. He, H. C. Poon, and S. Y. Tong, "Quantum size effect in low energy electron diffraction of thin films," App. Surf. Sci. **169-170,** 82–87 (2001).

[166] B. Santos, J. M. Puerta, J. I. Cerda, T. Herranz, K. F. McCarty, and J. de la Figuera, "Structure of ultrathin Pd films determined by low-energy electron microscopy and diffraction," New J. Phys. **12,** 023023 (2010).

[167] R. C. Jaklevic and L. C. Davis, "Band signatures in the low-energy-electron reflectance spectra of fcc metals," Phys. Rev. B. **26,** 5391 (1982).

[168] E. R. Cohen *et al.*, *Quantities, Units and Symbols in Physical Chemistry*, 3rd ed. (Royal Society of Chemistry, 2007).

[169] M. Lindroos, H. Pfnür, and D. Menzel, "Theoretical and experimental study of the unoccupied electronic band structure of Ru(001) by electron reflection," Phys. Rev. B **33,** 6684 (1986).

[170] M. Lindroos, H. Pfnür, P. Feulner, and D. Menzel, "A study of the adsorption sites of hydrogen on Ru(001) at saturation coverage by electron reflection," Surf. Sci. **180,** 237–251 (1987).

[171] A. K. Schmid, W. Swiech, C. S. Rastomjee, B. Rausenberger, W. Engel, E. Zeitler, and A. M. Bradshaw, "The chemistry of reaction-diffusion fronts investigated by microscopic LEED I-V fingerprinting," Surf. Sci. **331-333,** 225–230 (1995).

[172] E. Loginova, N. C. Bartelt, P. J. Feibelman, and K. F. McCarty, "Factors influencing graphene growth on metal surfaces," New J. Phys. **11,** 063046 (2009).

[173] E. Fermi, *Thermodynamics* (Dover Publications, 1956).

[174] M. Morkel, H. Unterhalt, M. Salmeron, G. Rupprechter, and H. Freund, "SFG spectroscopy from 10^{-8} to 1000 mbar: less-ordered CO structures and coadsorption on Pd(1 1 1)," Surf. Sci. pp. 103–107 (2003).

[175] W. Kuhn, J. Szanyi, and D. Goodman, "CO adsorption on Pd(111): the effects of temperature and pressure," Surf. Sci. **274,** L611–L618 (1992).

[176] H. Conrad, G. Ertl, and E. E. Latta, "Coadsorption of hydrogen and carbon monoxide on a Pd (110) surface," J. Catal. **35,** 363–368 (1974).

[177] R. Behm, K. Christmann, G. Ertl, M. V. Hove, P. Thiel, and W. Weinberg, "The structure of CO adsorbed on Pd(100): A leed and hreels analysis," Surf. Sci. **88,** L59–L66 (1979).

[178] J. M. Soler, E. Artacho, J. D. Gale, A. Garcia, J. Junquera, P. Ordejón, and D. Sanchez-Portal, "The SIESTA method for ab initio order-N materials simulation," J. Phys. Cond. Matt. **14,** 2745–2779 (2002).

[179] E. Bauer, "LEEM basics," Surf. Rev. Lett. 5 .

[180] G. Pauer and A. Winkler, "Water formation on Pd(111) by reaction of oxygen with atomic and molecular hydrogen," J. Chem. Phys. **120,** 3864 (2004).

[181] P. Berlowitz and D. Goodman, "Chemisorption of ultrathin Pd layers on W(110) and W(100): Adsorption of H2 and CO," Langmuir **4,** 1091–1095 (1988).

[182] F. Schiller, M. Heber, V. D. P. Servedio, and C. Laubschat, "Electronic structure of Mg : From monolayers to bulk," Phys. Rev. B **70,** 125106 (2004).

[183] L. Aballe, A. Barinov, A. Locatelli, T. Mentes, and M. Kiskinova, "Initial stages of heteroepitaxial Mg growth on W(110): Early condensation, anisotropic strain, and self-organized patterns," Phys. Rev B 75 (2007).

[184] L. Aballe, A. Barinov, A. Locatelli, S. Heun, and M. Kiskinova, "Tuning Surface Reactivity via Electron Quantum Confinement," Phys. Rev. Lett. **93,** 196103 (2004).

[185] H. Over, T. Hertel, H. Bludau, S. Pflanz, and G. Ertl, "EPITAXIAL-GROWTH OF MAGNESIUM ON Ru(0001)," Phys. Rev. B **48,** 5572–5578 (1993).

[186] S. Schwegmann, H. Over, M. Gierer, and G. Ertl, "Initial growth of Mg films on Ru(0001): An efficient approximation scheme for the LEED analysis of incommensurate structures," Phys. Rev. B **53,** 11164 (1996).

[187] S. Pezzagna, S. Vézian, J. Brault, and J. Massies, "Layer-by-layer epitaxial growth of Mg on GaN(0001)," App. Phys. Lett. **92,** 233111 (2008).

[188] J. N. P. Hutchinson, M.M.R. Evans, "Initial stages of Mggrowth on the Si(001) surface studied by STM," Surf. Sci. **411,** 99–110 (1998).

[189] R. Q. Hwang, J. Schröder, C. Guñther, and R. J. Behm, "Fractal growth of two-dimensional islands: Au on Ru(0001)," Phys. Rev. Lett. **67,** 3279 (1991).

[190] T. Michely and J. Krug, *Islands, Mounds, and Atoms: Patterns and Processes in Crystal Growth Far from Equilibrium*, 1 ed. (Springer, 2003).

[191] H. Over, T. Hertel, H. Bludau, S. Pflanz, and G. Ertl, "Epitaxial growth of magnesium on Ru(0001)," Phys. Rev. B. **48,** 5572 (1993).

[192] J. Sun, J. B. Hannon, G. L. Kellogg, and K. Pohl, "Local structural and compositional determination via electron scattering: Heterogeneous Cu(001)-Pd surface alloy," Phys. Rev. B. **76,** 205414 (2007).

[193] L. Aballe, C. Rogero, and K. Horn, "Quantum size effects in ultrathin epitaxial Mg films on Si(111)," Phys. Rev. B **65,** 125319 (2002).

[194] S. Egger, C. H. Back, J. Krewer, and D. Pescia, "A Spin Selective Electron Interferometer," Phys. Rev. Lett. **83,** 2833 (1999).

[195] W. K. Burton, N. Cabrera, and F. C. Frank, "The Growth of Crystals and the Equilibrium Structure of their Surfaces," Philos. T. R. Soc. A **243,** 299 –358 (1951).

[196] L. Berbil-Bautista, Ph.D. thesis, University of Hamburg, 2006.

[197] K. Thürmer and N. C. Bartelt, "Growth of multilayer ice films and the formation of cubic ice imaged with STM," Phys. Rev. B. **77,** 195425 (2008).

[198] R. L. Penn, "Imperfect Oriented Attachment: Dislocation Generation in Defect-Free Nanocrystals," Science **281,** 969–971 (1998).

[199] J. P. Hirth and R. C. Pond, "Steps, dislocations and disconnections as interface defects relating to structure and phase transformations," Acta Mater **44,** 4749–4763 (1996).

[200] W. Grochala and P. P. Edwards, "Thermal Decomposition of the Non-Interstitial Hydrides for the Storage and Production of Hydrogen," Chem. Rev. **104,** 1283–1316 (2004).

[201] G. Thomas and G. Sandrock, "DOE/SNL Hydride database,", http://hydpark.ca.sandia.gov.

[202] K. Aguey-Zinsou and J. Ares-Fernández, "Synthesis of Colloidal Magnesium: A Near Room Temperature Store for Hydrogen," Chem. Mater. **20,** 376–378 (2008).

[203] G. Liang, J. Huot, S. Boily, A. V. Neste, and R. Schulz, "Catalytic effect of transition metals on hydrogen sorption in nanocrystalline ball milled MgH2-Tm (Tm=Ti, V, Mn, Fe and Ni) systems," J. Alloys Comp. **292,** 247–252 (1999).

[204] P. Sprunger and E. Plummer, "An experimental-study of the interaction of hydrogen with the Mg(0001) surface," Chem. Phys. Lett. **187,** 559–564 (1991).

[205] H. Over, T. Hertel, H. Bludau, S. Pflanz, and G. Ertl, "EPITAXIAL-GROWTH OF MAGNESIUM ON RU(0001)," Phys. Rev. B **48,** 5572–5578 (1993).

[206] C. W. Ostenfeld, J. C. Davies, T. Vegge, and I. Chorkendorff, "Growth and hydrogenation of ultra-thin Mg films on Mo(1 1 1)," Surf. Sci. **584,** 17–26 (2005).

[207] C. W. Ostenfeld and I. Chorkendorff, "Effect of oxygen on the hydrogenation properties of magnesium films," Surf. Sci. **600,** 1363–1368 (2006).

[208] M. Johansson, C. W. Ostenfeld, and I. Chorkendorff, "Adsorption of hydrogen on clean and modified magnesium films," Phys. Rev. B **74,** 193408–4 (2006).

[209] L. Ratke and P. W. Voorhees, *Growth and coarsening: Ostwald ripening in material processing* (Springer, 2002).

[210] F. Huang, M. T. Kief, G. J. Mankey, and R. F. Willis, "Magnetism in the few-monolayers limit: A surface magneto-optic Kerr-effect study of the magnetic behavior of ultrathin films of Co, Ni, and Co-Ni alloys on Cu(100) and Cu(111)," Phys. Rev. B. **49,** 3962 (1994).

[211] M. T. Johnson, P. J. H. Bloemen, F. J. A. den Broeder, and J. J. de Vries, "Magnetic anisotropy in metallic multilayers," Rep. Prog. Phys. **59,** 1409–1458 (1996).

[212] R. Allenspach, M. Stampanoni, and A. Bischof, "Magnetic domains in thin epitaxial Co/Au(111) films," Phys. Rev. Lett. **65,** 3344 (1990).

[213] J. Pommier, P. Meyer, G. Pénissard, J. Ferré, P. Bruno, and D. Renard, "Magnetization reversal in ultrathin ferromagnetic films with perpendicular anistropy: Domain observations," Phys. Rev. Lett. **65,** 2054 (1990).

[214] C. M. Schneider, P. Bressler, P. Schuster, J. Kirschner, J. J. de Miguel, and R. Miranda, "Curie temperature of ultrathin films of fcc-cobalt epitaxially grown on atomically flat Cu(100) surfaces," Phys. Rev. Lett. **64,** 1059 (1990).

[215] R. Q. Hwang, "Nucleation and growth of thin metal films on clean and modified metal substrates studied by scanning tunneling microscopy," J. Vac. Sci. Technol. **10,** 1970 (1992).

[216] C. Günther, S. Günther, E. Kopatzki, R. Q. Hwang, J. Schröder, J. Vrijmoeth, and R. J. Behm, "Microscopic Aspects of Thin Metal Film Epitaxial Growth on Metallic Substrates," Berichte der Bunsengesellschaft für physikalische Chemie **97,** 522–537 (1993).

[217] J. de la Figuera, Ph.D. thesis, Universidad Autónoma de Madrid, 1995.

[218] D. W. Pashley, M. J. Stowell, M. H. Jacobs, and T. J. Law, "The growth and structure of gold and silver deposits formed by evaporation inside an electron microscope," Philosophical Magazine **10,** 127 (1964).

[219] H. Oka, P. A. Ignatiev, S. Wedekind, G. Rodary, L. Niebergall, V. S. Stepanyuk, D. Sander, and J. Kirschner, "Spin-Dependent Quantum Interference Within a Single Magnetic Nanostructure," Science **327,** 843 –846 (2010).

[220] O. Pietzsch, S. Okatov, A. Kubetzka, M. Bode, S. Heinze, A. Lichtenstein, and R. Wiesendanger, "Spin-Resolved Electronic Structure of Nanoscale Cobalt Islands on Cu(111)," Phys. Rev. Lett. **96,** 237203 (2006).

[221] K. F. McCarty, "Deterministic Positioning of Three-Dimensional Structures on a Substrate by Film Growth," Nano Lett. **6,** 858–861 (2006).

[222] F. E. Gabaly, S. Gallego, C. M. noz, L. Szunyogh, P. Weinberger, C. Klein, A. K. Schmid, K. F. McCarty, and J. de la Figuera, "Imaging Spin-Reorientation Transitions in Consecutive Atomic Co Layers on Ru(0001)," Phys. Rev. Lett. **96,** 147202 (2006).

[223] Z. Li, R. Skomski, S. Liou, S. Michalski, M. Chipara, and R. D. Kirby, "Magnetization precession and domain-wall structure in cobalt-ruthenium-cobalt trilayers," J. Appl. Phys. **109,** 07C113 (2011).

[224] C. A. F. Vaz, L. Lopez-Diaz, M. Kläui, J. A. C. Bland, T. L. Monchesky, J. Unguris, and Z. Cui, "Observation of a geometrically constrained domain wall in epitaxial FCC Co small disks," J. Magn. Magn. Matter. **272-276,** 1674–1675 (2004).

[225] D. Sander, R. Skomski, C. Schmidthals, A. Enders, and J. Kirschner, "Film Stress and Domain Wall Pinning in Sesquilayer Iron Films on W(110)," Phys. Rev. Lett. **77,** 2566 (1996).

[226] S. Bodea, W. Wulfhekel, and J. Kirschner, "Influence of step edges and strain on the domain wall width," Phys. Rev. B. **72,** 100403 (2005).

[227] H. P. Oepen and J. Kirschner, "Magnetization Distribution of 180° Domain Walls at Fe(100) Single-Crystal Surfaces," Phys. Rev. Lett. **62,** 819 (1989).

[228] C. Antoniak, J. Lindner, K. Fauth, J. Thiele, J. Minár, S. Mankovsky, H. Ebert, H. Wende, and M. Farle, "Composition dependence of exchange stiffness in Fex Pt1-x alloys," Phys. Rev. B. **82,** 064403 (2010).

[229] R. H. Yu, S. Basu, Y. Zhang, A. Parvizi-Majidi, and J. Q. Xiao, "Pinning effect of the grain boundaries on magnetic domain wall in FeCo-based magnetic alloys," J. Appl. Phys. **85,** 6655 (1999).

[230] A. Hernando and J. Rojo, *Fiscia De Los Materiales Magneticos* (Sintesis, 2001).

[231] M. van Schilfgaarde and V. P. Antropov, "First-principles exchange interactions in Fe, Ni, and Co," J. Appl. Phys. **85,** 4827 (1999).

[232] S. Gallego, "Private communication," (unpublished) .

[233] A. Mascaraque, L. Aballe, J. F. Marco, T. O. Mentescedil, F. E. Gabaly, C. Klein, A. K. Schmid, K. F. McCarty, A. Locatelli, and J. de la Figuera, "Measuring the magnetization of three monolayer thick Co islands and films by x-ray dichroism," Phys. Rev. B. **80,** 172401 (2009).

[234] A. Wachowiak, "Direct Observation of Internal Spin Structure of Magnetic Vortex Cores," Science **298,** 577–580 (2002).

[235] F. Garcia *et al.*, "Tailoring magnetic vortices in nanostructures," Appl. Phys. Lett. **97,** 022501 (2010).

[236] D. Goll, G. Schütz, and H. Kronmüller, "Critical thickness for high-remanent single-domain configurations in square ferromagnetic thin platelets," Phys. Rev. B. **67,** 094414 (2003).

[237] M. Kisielewski, A. Maziewski, and V. Zablotskii, "High cobalt layer thickness spin-reorientation phase transition," J. Magn. Magn. Matter. **316,** 277–280 (2007).

[238] M. Hehn, S. Padovani, K. Ounadjela, and J. P. Bucher, "Nanoscale magnetic domain structures in epitaxial cobalt films," Phys. Rev. B. **54,** 3428 (1996).

[239] H. Oepen, M. Benning, H. Ibach, C. Schneider, and J. Kirschner, "Magnetic domain structure in ultrathin cobalt films," J. Magn. Magn. Matter. **86,** L137–L142 (1990).

[240] H. Oepen, "Magnetic domain structure in ultrathin cobalt films," J. Magn. Magn. Matter. **93,** 116–122 (1991).

[241] J. L. Robins, R. J. Celotta, J. Unguris, D. T. Pierce, B. T. Jonker, and G. A. Prinz, "Domain images of ultrathin Fe films on Ag(100)," Appl. Phys. Lett. **52,** 1918 (1988).

[242] F. Romanens, J. Vogel, W. Kuch, K. Fukumoto, J. Camarero, S. Pizzini, M. Bonfim, and F. Petroff, "Influence of topography and Co domain walls on the magnetization reversal of the FeNi layer in FeNi/Al_2O_3/Co magnetic tunnel junctions," Phys. Rev. B. **74,** 184419 (2006).

[243] A. Quesada, "private communucation," .

[244] M. Donahue and D. Porter, "OOMMF User's Guide, Version 1.0," Interagency Report NISTIR 6376 (1999).

[245] M. Jaafar, R. Yanes, A. Asenjo, O. Chubykalo-Fesenko, M. Vázquez, E. M. González, and J. L. Vicent, "Field induced vortex dynamics in magnetic Ni nanotriangles," Nanotechnology **19,** 285717 (2008).

[246] J. M. Garcia, A. Thiaville, J. Miltat, K. J. Kirk, J. N. Chapman, and F. Alouges, "Quantitative interpretation of magnetic force microscopy images from soft patterned elements," Appl. Phys. Lett. **79,** 656 (2001).

[247] C. S. Lin, H. S. Lim, C. C. Wang, A. O. Adeyeye, Z. K. Wang, S. C. Ng, and M. H. Kuok, "Spin wave localization in a triangular nanomagnet," J. Appl. Phys. **108,** 114305 (2010).

[248] M. Jaafar, R. Yanes, D. P. de Lara, O. Chubykalo-Fesenko, A. Asenjo, E. M. Gonzalez, J. V. Anguita, M. Vazquez, and J. L. Vicent, "Control of the chirality and polarity of magnetic vortices in triangular nanodots," Phys. Rev. B. **81,** 054439 (2010).

[249] A. Asenjo, M. Jaafar, E. González, J. Martin, M. Vázquez, and J. Vicent, "Imaging magnetic domains in Ni nanostructures," J. Magn. Magn. Matter. **310,** e936–e938 (2007).

[250] K. Ounadjela, D. Muller, A. Dinia, A. Arbaoui, P. Panissod, and G. Suran, "Perpendicular anisotropy and antiferromagnetic coupling in Co/Ru strained superlattices," Phys. Rev. B. **45,** 7768 (1992).

[251] P. J. Godowski, J. Onsgaard, M. Trzebiatowska-Gusowska, K. Pater, and Z. S. Li, "Photoemission Study of the Initial Growth of Co on Ru(0001),", 2007.

[252] C. Liu and S. Bader, "Magnetism and growth of ultrathin Co films grown epitaxially on Ru(0001)," J. Magn. Magn. Matter. **119,** 81–86 (1993).

[253] E. Lundgren, G. Leonardelli, M. Schmid, and P. Varga, "A misfit structure in the Co/Pt(1 1 1) system studied by scanning tunnelling microscopy and embedded atom method calculations," Surf. Sci. **498,** 257–265 (2002).

[254] R. Kalousek, M. Schmid, A. Hammerschmid, E. Lundgren, and P. Varga, "Slowing down adatom diffusion by an adsorbate: Co on Pt(111) with and without preadsorbed CO," Phys. Rev. B. **68,** 233401 (2003).

[255] J. Heidberg, H. Weiß, and P. Wissmann, "Chapter 6: Vibrational Spectroscopy of Adsorbates on Thin Metal Films," in *Thin Metal Films and Gas Chemisorption* (Elsevier, 1987), Vol. Volume 32, pp. 196–279.

[256] H. Poppa, "Model studies in catalysis with uhv-deposited metal particles and clusters," Vacuum **34,** 1081–1095 (1984).

[257] W. Sachtler and P. V. D. Plank, "The role of individual surface atoms in chemisorption and catalysis by nickel-copper alloys," Surf. Sci. **18,** 62–79 (1969).

[258] M. Primet, J. M. Basset, M. V. Mathieu, and M. Prettre, "Infrared study of CO adsorbed on Pt/Al2O3. A method for determining metal-adsorbate interactions," J. Catal. **29,** 213–223 (1973).

[259] H. Busse, M. R. Voss, D. Jerdev, B. E. Koel, and M. T. Paffett, "Adsorption and reaction of gaseous H(D) atoms with D(H) adatoms on Pt(1 1 1) and Sn/Pt(1 1 1) surface alloys," Surf. Sci. **490,** 133–143 (2001).

[260] C. R. Abeledo and P. W. Selwood, "Chemisorption of Hydrogen on Cobalt," J. Chem. Phys. **37,** 2709 (1962).

[261] R. L. Fink, G. A. Mulhollan, A. B. Andrews, J. L. Erskine, and G. K. Walters, "Spin- and angle-resolved photoemission study of chemisorbed p(1 x 1) O on epitaxial ultrathin Fe/W(001) films," Phys. Rev. B. **45,** 9824 (1992).

[262] N. B. Brookes, A. Clarke, and P. D. Johnson, "Interaction of carbon monoxide with Fe(001)," Phys. Rev. Lett. **63,** 2764 (1989).

[263] M. Getzlaff, J. Bansmann, and G. Schönhense, "Spin-resolved photoemission from physisorbed xenon on ferromagnetic surfaces: Evidence for magnetic interactions," Phys. Rev. Lett. **71,** 793 (1993).

[264] S. Pick and H. Dreyssé, "On the gas adsorption effect upon electronic structure of ferromagnetic Co(0 0 0 1)," Surf. Sci. **540,** 389–394 (2003).

[265] S. Gallego, N. Sanchez, S. Martin, C. M. noz, and L. Szunyogh, "Formation of a stable H overlayer on ultrathin Co films on Ru (0001)," Arxiv preprint arXiv:1006.3686 (2010).

[266] S. R. Chubb and W. E. Pickett, "First-principles determination of giant adsorption-induced surface relaxation in p(11) O/Fe(001)," Phys. Rev. Lett. **58,** 1248 (1987).

[267] P. D. Johnson, A. Clarke, N. B. Brookes, S. L. Hulbert, B. Sinkovic, and N. V. Smith, "Exchange-Split Adsorbate Bands: The Role of Substrate Hybridization," Phys. Rev. Lett. **61,** 2257 (1988).

[268] J. Bansmann, L. Lu, and M. Getzlaff, "Magnetic dichroism in photoemission from oxygen atoms adsorbed on cobalt surfaces," Surf. Sci. **402-404,** 371–376 (1998).

[269] S. Pick and H. Dreysse´, "Model of gas adsorption on magnetic surfaces," Surf. Sci. **394,** 192–200 (1997).

[270] O. Isnard and V. Pop, "Effect of hydrogen as interstitial element on the magnetic properties of some iron rich intermetallic compounds," J. Alloy. Comp. In Press, Corrected Proof .

[271] G. Wiesinger, G. Hilscher, and K. Buschow, "Chapter Five Magnetism of Hydrides," in *Chapter Five Magnetism of Hydrides* (Elsevier, 2007), Vol. Volume 17, pp. 293–456.

[272] T. Mitsui, M. K. Rose, E. Fomin, D. F. Ogletree, and M. Salmeron, "Dissociative hydrogen adsorption on palladium requires aggregates of three or more vacancies," Nature **422,** 705–707 (2003).

[273] W. Moritz, R. Imbihl, R. J. Behm, G. Ertl, and T. Matsushima, "Adsorption geometry of hydrogen on Fe(110)," J. Chem. Phys. **83,** 1959 (1985).

[274] M. E. Bridge, C. M. Comrie, and R. M. Lambert, "Hydrogen chemisorption and the carbon monoxide-hydrogen interaction on cobalt (0001)," J. Catal. **58,** 28–33 (1979).

[275] K. M. E. Habermehl-Cwirzen, K. Kauraala, and J. Lahtinen, "Hydrogen on Cobalt: The Effects of Carbon Monoxide and Sulphur Additives on the D2/Co(0001) System," Physica Scripta p. 77 (2004).

[276] W. Lisowski, "Kinetics of hydrogen adsorption and desorption on thin platinum films," Appl. Surf. Sci. **31,** 451–459 (1988).

[277] C. Harrison, D. H. Adamson, Z. Cheng, J. M. Sebastian, S. Sethuraman, D. A. Huse, R. A. Register, and P. M. Chaikin, "Mechanisms of Ordering in Striped Patterns," Science **290,** 1558 –1560 (2000).

[278] J. de la Figuera, F. Léonard, N. C. Bartelt, R. Stumpf, and K. F. McCarty, "Nanoscale Periodicity in Stripe-Forming Systems at High Temperature: Au/W(110)," Phys. Rev. Lett. **100,** 186102 (2008).

[279] S. K. Streiffer, J. A. Eastman, D. D. Fong, C. Thompson, A. Munkholm, M. V. R. Murty, O. Auciello, G. R. Bai, and G. B. Stephenson, "Observation of Nanoscale 180° Stripe Domains in Ferroelectric PbTiO_3 Thin Films," Phys. Rev. Lett. **89,** 067601 (2002).

[280] O. Portmann, A. Vaterlaus, and D. Pescia, "An inverse transition of magnetic domain patterns in ultrathin films," Nature **422,** 701–704 (2003).

[281] J. Hauschild, U. Gradmann, and H. J. Elmers, "Perpendicular magnetization and dipolar antiferromagnetism in double layer nanostripe arrays of Fe(110) on W(110)," Appl. Phys. Lett. **72,** 3211 (1998).

[282] H. J. Elmers, J. Hauschild, and U. Gradmann, "Onset of perpendicular magnetization in nanostripe arrays of Fe on stepped W(110) surfaces," Phys. Rev. B. **59,** 3688 (1999).

[283] J. Shen, R. Skomski, M. Klaua, H. Jenniches, S. S. Manoharan, and J. Kirschner, "Magnetism in one dimension: Fe on Cu(111)," Phys. Rev. B. **56,** 2340 (1997).

[284] M. Hehn, K. Ounadjela, R. Ferre?, W. Grange, and F. Rousseaux, "Reorientational magnetic transition in mesoscopic cobalt dots," Appl. Phys. Lett. **71,** 2833 (1997).

[285] L. Belliard, J. Miltat, V. Kottler, V. Mathet, C. Chappert, and T. Valet, "Stripe domains morphology versus layers thickness in CoPt multilayers," J. Appl. Phys. **81,** 5315 (1997).

[286] L. D. Landau, L. P. Pitaevskii, and E. Lifshitz, *Electrodynamics of Continuous Media, Second Edition: Volume 8*, 2 ed. (Butterworth-Heinemann, 1984).

[287] G. Leaf, H. Kaper, M. Yan, V. Novosad, P. Vavassori, R. E. Camley, and M. Grimsditch, "Dynamic Origin of Stripe Domains," Phys. Rev. Lett. **96,** 017201 (2006).

[288] C. Won *et al.*, "Magnetic stripe melting at the spin reorientation transition in Fe/Ni/Cu(001)," Phys. Rev. B. **71,** 224429 (2005).

[289] J. Choi, J. Wu, C. Won, Y. Z. Wu, A. Scholl, A. Doran, T. Owens, and Z. Q. Qiu, "Magnetic Bubble Domain Phase at the Spin Reorientation Transition of Ultrathin Fe/Ni/Cu(001) Film," Phys. Rev. Lett. **98,** 207205 (2007).

[290] P. Bruno, "Spin-wave theory of two-dimensional ferromagnets in the presence of dipolar interactions and magnetocrystalline anisotropy," Phys. Rev. B. **43,** 6015 (1991).

[291] C. Chappert, K. L. Dang, P. Beauvillain, H. Hurdequint, and D. Renard, "Ferromagnetic resonance studies of very thin cobalt films on a gold substrate," Phys. Rev. B. **34,** 3192 (1986).

[292] Z. Zhang, L. Zhou, P. E. Wigen, and K. Ounadjela, "Angular dependence of ferromagnetic resonance in exchange-coupled Co/Ru/Co trilayer structures," Phys. Rev. B. **50,** 6094 (1994).

[293] J. M. MacLaren, T. C. Schulthess, W. H. Butler, R. Sutton, and M. McHenry, "Electronic structure, exchange interactions, and Curie temperature of FeCo," J. Appl. Phys. **85,** 4833 (1999).

[294] S. Gallego, "private communucation," .

[295] C. T. Chen, Y. U. Idzerda, H. Lin, N. V. Smith, G. Meigs, E. Chaban, G. H. Ho, E. Pellegrin, and F. Sette, "Experimental Confirmation of the X-Ray Magnetic Circular Dichroism Sum Rules for Iron and Cobalt," Phys. Rev. Lett. **75,** 152 (1995).

[296] "Ferromagnetism,", http://en.wikipedia.org/wiki/Ferromagnetism.

[297] M. Pajda, J. Kudrnovsky, I. Turek, V. Drchal, and P. Bruno, "Oscillatory Curie Temperature of Two-Dimensional Ferromagnets," Phys. Rev. Lett. **85,** 5424 (2000).

[298] O. Donzelli, D. Palmeri, L. Musa, F. Casoli, F. Albertini, L. Pareti, and G. Turilli, "Perpendicular magnetic anisotropy and stripe domains in ultrathin Co/Au sputtered multilayers," J. Appl. Phys. **93,** 9908 (2003).

[299] M. Speckmann, H. P. Oepen, and H. Ibach, "Magnetic Domain Structures in Ultrathin Co/Au(111): On the Influence of Film Morphology," Phys. Rev. Lett. **75,** 2035 (1995).

[300] M. Copel, M. C. Reuter, E. Kaxiras, and R. M. Tromp, "Surfactants in epitaxial growth," Phys. Rev. Lett. **63,** 632 (1989).

[301] M. H. von Hoegen, J. Falta, M. Copel, and R. M. Tromp, "Surfactants in Si(111) homoepitaxy," Appl. Phys. Lett. **66,** 487 (1995).

[302] C. Tölkes, R. Struck, R. David, P. Zeppenfeld, and G. Comsa, "Surfactant-Induced Layer-by-Layer Growth on a Highly Anisotropic Substrate: Co/Cu(110)," Phys. Rev. Lett. **80,** 2877 (1998).

[303] M. Izquierdo, M. E. Dávila, J. Avila, H. Ascolani, C. M. Teodorescu, M. G. Martin, N. Franco, J. Chrost, A. Arranz, and M. C. Asensio, "Epitaxy and Magnetic Properties of Surfactant-Mediated Growth of bcc Cobalt," Phys. Rev. Lett. **94,** 187601 (2005).

[304] Y. Bao, W. An, C. H. Turner, and K. M. Krishnan, "The Critical Role of Surfactants in the Growth of Cobalt Nanoparticles," Langmuir **26,** 478–483 (2010).

[305] G. Parteder, F. Allegretti, S. Surnev, and F. Netzer, "Growth of cobalt on a VO(1 1 1) surface: Template, surfactant or encapsulant role of the oxide nanolayer?," Surf. Sci. **602,** 2666–2674 (2008).

[306] J. Camarero, T. Graf, J. J. de Miguel, R. Miranda, W. Kuch, M. Zharnikov, A. Dittschar, C. M. Schneider, and J. Kirschner, "Surfactant-Mediated Modification of the Magnetic Properties of Co /Cu(111) Thin Films and Superlattices," Phys. Rev. Lett. **76,** 4428 (1996).

[307] J. Camarero, L. Spendeler, G. Schmidt, K. Heinz, J. J. de Miguel, and R. Miranda, "Surfactant-Induced Suppression of Twin Formation During Growth of fcc Co/Cu Superlattices on Cu(111)," Phys. Rev. Lett. **73,** 2448 (1994).

[308] W. Kuch, A. Dittschar, M. T. Lin, M. Salvietti, M. Zharnikov, C. M. Schneider, J. Kirschner, J. Camarero, J. J. de Miguel, and R. Miranda, "Direct evidence for complete antiferromagnetic coupling between Co films epitaxially grown on Cu(1 1 1) using Pb as surfactant," J. Magn. Magn. Matter. **170,** L13–L16 (1997).

[309] J. Camarero, J. Ferrón, V. Cros, L. Gómez, A. L. V. de Parga, J. M. Gallego, J. E. Prieto, J. J. de Miguel, and R. Miranda, "Atomistic Mechanism of Surfactant-Assisted Epitaxial Growth," Phys. Rev. Lett. **81,** 850 (1998).

[310] J. Ferrón, L. Gómez, J. Gallego, J. Camarero, J. Prieto, V. Cros, A. V. de Parga, J. de Miguel, and R. Miranda, "Influence of surfactants on atomic diffusion," Surf. Sci. **459,** 135–148 (2000).

[311] J. Camarero, M. N. no, D. F. acute accent]as, V. Cros, J. de Miguel, R. Miranda, A. Hernando-Mañeru, A. Asenjo, J. González, and M. Vázquez, "Surfactant control of growth

and interface quality in granular magnetic CoCu/Cu(1 1 1) superlattices," Surf. Sci. **482-485,** 1077–1082 (2001).

[312] K. Pehr, "Safety concept of an engine test rig with liquid hydrogen supply," Int. J. Hydrogen Energ. **18,** 773–781 (1993).

[313] M. Morjan, H. Züchner, and K. Cammann, "Contributions to a reliable hydrogen sensor based on surface plasmon surface resonance spectroscopy," Surf. Sci. **603,** 1353–1359 (2009).

[314] T. D. Lee, T. Goldenberg, and J. P. Hirth, "Effect of hydrogen on fracture of U-notched bend specimens of spheroidized AISI 1095 steel," Metallurgical Transactions A **10,** 199–208 (1979).

[315] H. Hänninen, K. Törrönen, M. Kemppainen, and S. Salonen, "On the mechanisms of environment sensitive cyclic crack growth of nuclear reactor pressure vessel steels," Corrosion Science **23,** 663–679 (1983).

[316] H. E. Hänninen, T. C. Lee, I. M. Robertson, and H. K. Birnbaum, "In situ observations on effects of hydrogen on deformation and fracture of A533B pressure vessel steel," Journal of Materials Engineering and Performance **2,** 807–817 (1993).

[317] "RKI Instruments,".

[318] "Storage Battery Systems, Inc.,".

[319] "The H2 Specific Hydrogen Detector,".

[320] "Hazardous gas detectors,".

[321] M. N. Baibich, J. M. Broto, A. Fert, F. N. V. Dau, F. Petroff, P. Etienne, G. Creuzet, A. Friederich, and J. Chazelas, "Giant Magnetoresistance of (001)Fe/(001)Cr Magnetic Superlattices," Phys. Rev. Lett. **61,** 2472 (1988).

[322] G. Binasch, P. Grünberg, F. Saurenbach, and W. Zinn, "Enhanced magnetoresistance in layered magnetic structures with antiferromagnetic interlayer exchange," Phys. Rev. B. **39,** 4828 (1989).

[323] B. N. Engel, M. H. Wiedmann, R. A. V. Leeuwen, C. M. Falco, L. Wu, N. Nakayama, and T. Shinjo, "Influence of structure on the magnetic anisotropy of Co/Pd (001) epitaxial superlattices," Appl. Surf. Sci. **60-61,** 776–780 (1992).

[324] M. Przybylski, L. Yan, J. Zdotukrowski, M. Nyvlt, Y. Shi, A. Winkelmann, J. Barthel, M. Wasacuteniowska, and J. Kirschner, "Topology-dependent interface contribution to magneto-optical response from ultrathin Co films grown on the (001), (110), and (111) surfaces of Pd," Phys. Rev. B. **73,** 085413 (2006).

[325] S. Kim, Y. Koo, V. A. Chernov, J. B. Kortright, and S. Shin, "Comparison of atomic structure anisotropy between Co-Pd alloys and Co/Pd multilayer films," Phys. Rev. B. **62,** 3025 (2000).

[326] J. Kohlhepp and U. Gradmann, "Magnetic surface anisotropies of Co(0001)-based interfaces from in situ magnetometry of Co films on Pd(111), covered with ultrathin films of Pd and Ag," J. Magn. Magn. Matter. **139,** 347–354 (1995).

[327] L. B. Lueck and R. G. Gilson, "Challenges and opportunities: The magnetic media industry in the 1990s," J. Magn. Magn. Matter. **88,** 227–235 (1990).

[328] L. Qiu, J. Shi, S. Piramanayagam, J. Chen, and J. Ding, "Nanocomposite magnetic films for high-density perpendicular magnetic recording media," Thin Solid Films **516,** 5381–5385 (2008).

[329] J. Kim, B. Lee, G. Park, M. Uchida, T. Kurosawa, S. Watanabe, J. Ariake, N. Honda, and K. Ouchi, "The effect of Pd buffer layers on magnetic exchange energy of Co/Pd multilayered films for perpendicular magnetic recording," J. Magn. Magn. Matter. **235,** 53–58 (2001).

[330] S. Piramanayagam and K. Srinivasan, "Recording media research for future hard disk drives," J. Magn. Magn. Matter. **321,** 485–494 (2009).

[331] R. L. White, "The physical boundaries to high-density magnetic recording," J. Magn. Magn. Matter. **209,** 1–5 (2000).

[332] J. Dorantes-Dávila, H. Dreyssé, and G. M. Pastor, "Magnetic Anisotropy of Transition-Metal Interfaces from a Local Perspective: Reorientation Transitions and Spin-Canted Phases in Pd Capped Co Films on Pd(111)," Phys. Rev. Lett. **91,** 197206 (2003).

[333] S. Nakagawa and H. Yoshikawa, "Effect of roughness and continuity of Co layers to magnetic properties of Co/Pd multilayers," J. Magn. Magn. Matter. **287,** 193–198 (2005).

[334] K. Munbodh, F. A. Perez, C. Keenan, D. Lederman, M. Zhernenkov, and M. R. Fitzsimmons, "Effects of hydrogen/deuterium absorption on the magnetic properties of Co/Pd multilayers," Phys. Rev. B. **83,** 094432 (2011).

[335] S. Okamoto, O. Kitakami, and Y. Shimada, "Enhancement of magnetic anisotropy of hydrogenated Pd/Co/Pd trilayers," J. Magn. Magn. Matter. **239,** 313–315 (2002).

[336] T. Duden and E. Bauer, "Influence of Au and Cu overlayers on the magnetic structure of Co films on W(110)," Phys. Rev. B. **59,** 468 (1999).

[337] F. E. Gabaly, K. F. McCarty, A. K. Schmid, J. de la Figuera, M. C. M. noz, L. Szunyogh, P. Weinberger, and S. Gallego, "Noble metal capping effects on the spin-reorientation transitions of Co/Ru(0001)," New J. Phys. **10,** 073024 (2008).

[338] H. Herlt and E. Bauer, "A very low energy electron reflection study of hydrogen adsorption on W(100) and W(110) surfaces," Surf. Sci. **175,** 336–368 (1986).

[339] B. Santos, J. Puerta, J. I. Cerda, T. Herranz, J. de la Figuera, and K. F. McCarty, "The role of CO in hydrogen absorption into ultra-thin Pd films," In preparation (2011).

List of Figures